

Dissertation

Photoelectrochemical Porosification of Silicon Carbide for MEMS

Zur Erlangung des Grades

des Doktors der technischen Wissenschaften

der Fakultät für Elektrotechnik und Informationstechnik

am Institut für Sensor- und Aktuatorssysteme E366

der Technischen Universität Wien

Dipl.-Ing. Markus Leitgeb

Matrikelnummer: 0728046

Wien, 2018

Verteidigung: Wien, 27. April 2018

Betreuer:

Univ.-Prof. Dr.rer.nat. Ulrich Schmid
Technische Universität Wien, Österreich

Gutachter:

Univ.-Prof. Dr.rer.nat. Helmut Seidel
Universität des Saarlandes, Deutschland

Univ.-Prof. Dr.sc. Silvan Schmid
Technische Universität Wien, Österreich

Abstract

In this thesis metal assisted photochemical etching (MAPCE) and photoelectrochemical etching (PECE) of single crystalline 4H-silicon carbide (SiC) are investigated with the emphasis of possible application scenarios of those techniques in the field of microelectromechanical systems (MEMS). Both methods allow in principle the porosification of 4H-SiC, but MAPCE was not a reliable method before the start of this thesis and also pure PECE was not controllable such that the degree of porosity could be adjusted for specific application scenarios. Being able to fabricate porous SiC layers in a controlled and reproducible manner is a promising goal, since they could be used in harsh environments where other porous semiconductors like porous silicon cannot be used or need to be protected for operation. Therefore, in the beginning of this thesis the fundamentals of MAPCE and PECE were investigated. During MAPCE the surface of a 4H-SiC wafer is partly covered with a Platinum (Pt) thin film utilizing sputter deposition. This wafer is immersed in an etching solution and irradiated with UV light. The UV light generated holes cause oxidation of the bare 4H-SiC surface and the oxide is dissolved by hydrofluoric acid in the etching solution leading to a porous structure of 4H-SiC. The UV light generated electrons leave via the Pt/4H-SiC interface where they are accepted by an oxidizing agent in the etching solution, to restore charge balance during MAPCE. Decreasing the contact resistance at the Pt/4H-SiC interface with annealing and surface near doping leads to reproducible experimental outcomes of MAPCE experiments even with samples having different bulk resistivity values. This finding allowed for the first time a detailed investigation of MAPCE of 4H-SiC. It was found that the porous structure is coated with functional groups stemming from the etching process, causing protection from further etching. However, at long etching times this stabilization is lost, and also total dissolution of the porous structure is possible. Additionally, it could be shown that the initiation of new pores and the growth of already existing pores during MAPCE are two different processes with the latter being energetically favored. This enabled the fabrication of highly porous and homogenous layers with MAPCE.

The findings concerning MAPCE also contributed to the investigation and improvement of PECE. PECE is similar to MAPCE with the difference that an external voltage is necessary for etching. On the other hand, Pt deposition and an oxidizing agent in the etching solution are not necessary. During this thesis it was found that MAPCE is a reasonable method for producing porous thin films with thicknesses up to 2 μm while 30 μm thick porous layers could be achieved with PECE. A common problem of PECE was the inhomogeneity of the resulting porous layers. This was solved by providing a starting porous layer with MAPCE for PECE. When the voltage is switched on the pore tips from the starting layer act as initiation sites for the PECE process. By doing so the homogeneity of PECE formed porous SiC could be enhanced. Further experiments showed that PECE can be described in terms of dielectric breakdown. This means that the resulting degree of porosity does not depend on the current density throughout an experiment but on the applied voltage. The current density, however, has an

impact on the experimental outcome; with decreasing current density the etching rate decreases. These findings lead to so called charge-controlled etching.

The degree of porosity is controlled by the applied voltage, but the thickness of a porous layer is adjusted by the transported charge and not the etching time. This enabled the fabrication of stacked porous SiC layers with alternating degree of porosity.

After the investigation of MAPCE and PECE potential application scenarios in the field of MEMS were targeted. MAPCE was utilized for the local porosification of 4H-SiC. The Pt was removed with aqua regia and afterwards polycrystalline SiC was deposited on the whole sample with low pressure chemical vapor deposition. In a second annealing step, the porous SiC underneath the polycrystalline SiC collapsed, leaving behind a cavity with defined pressure inside. Such cavities have potential application as a SiC based MEMS pressure sensor. Another approach was to tailor MAPCE such that a defined line of breakage forms underneath a highly porous layer. By depositing compressively stressed amorphous SiC:H on top of such porous areas a buckling membrane could be fabricated, which could in principle also be used as a pressure sensor.

Furthermore, MAPCE allowed the fabrication of porous anti-reflection layers as well as highly uniform porous layers on 4H-SiC substrates, showing thin-film like reflection behavior. The former has the potential to be applied in LEDs or UV sensors while the latter can be useful in optical sensors relying on the reflectance shift when the pores are filled a liquid medium.

The charge-controlled PECE method allowed the fabrication of stacked porous SiC layers with alternating degree of porosity. This, in turn, allowed the fabrication of porous SiC rugate mirrors exhibiting sharp peaks in the reflection spectrum. Such mirrors can be used in optical sensors for harsh environments or in the field of bio-analytics.

Altogether the principle of MAPCE and PECE were investigated thoroughly which allowed in turn to fathom possible MEMS application scenarios for those methods. Hopefully this will stimulate the future development of porous SiC based MEMS devices.

Kurzfassung

In dieser Arbeit wurden Metall-unterstütztes photochemisches Ätzen (engl. metal assisted photochemical etching – MAPCE) und photoelektrochemisches Ätzen (engl. photoelectrochemical etching – PECE) von Siliciumcarbid (SiC) mit Hinblick auf mögliche Anwendungen in Mikrosystemen (engl. microelectromechanical system - MEMS) untersucht. Im Prinzip eignen sich beide Methoden zur Herstellung von porösem SiC, wobei MAPCE vor Beginn dieser Arbeit nicht reproduzierbare experimentelle Ergebnisse lieferte und PECE es nicht erlaubte den Porositätsgrad gezielt auf mögliche Anwendungsgebiete einzustellen. Ziel dieser Arbeit ist es diese Probleme zu lösen, da poröses SiC in aggressiven Umgebungen eingesetzt werden kann, wo andere poröse Halbleiter -wie zum Beispiel poröses Silicium- nicht eingesetzt werden können oder mit einer Schutzschicht überzogen werden müssen. Daher wurden zuerst die grundlegenden Prinzipien von MAPCE und PECE untersucht. Während eines MAPCE Prozesses wird die Oberfläche eines 4H-SiC Wafers teilweise mit einem Platin-Dünnsfilm mittels Kathodenzerstäuben bedeckt. Danach wird der Wafer in eine Ätzlösung getaucht und parallel einer UV Bestrahlung ausgesetzt. Durch den UV-Einfluss werden Löcher im Halbleiter generiert, die zur Oxidation von nicht mit Pt bedecktem SiC führen. Anschließend wird dieses Oxid durch Flusssäure (HF) in der Ätzlösung aufgelöst. Letztendlich bleibt eine poröse Struktur von SiC zurück. Um Ladungsneutralität zu wahren, verlassen die durch UV-Licht generierten Elektronen den Halbleiter über den Pt/4H-SiC Kontakt, wo sie vom Oxidationsmittel aufgenommen werden. Das Herabsetzen des Kontaktwiderstandes an dieser Grenzfläche durch oberflächennahes Dotieren führte dazu, dass die experimentellen Ergebnisse von MAPCE für Proben mit unterschiedlichen spezifischen Widerstandswerten reproduzierbar wurden. Diese Entdeckung erlaubte erstmals eine detaillierte Untersuchung von MAPCE. Dabei stellte sich heraus, dass die poröse Struktur mit funktionellen Gruppen bedeckt ist, die diese in der Ätzlösung stabilisieren und vor vollständiger Auflösung schützen. Bei langen Ätzzeiten geht dieser Schutzmechanismus verloren, sodass letztendlich auch die vollständige Auflösung des porösen SiC ermöglicht wird. Weiters stellte sich heraus, dass die Bildung neuer Poren und das Wachstum bereits existierender Poren zwei unterschiedliche Prozesse sind, wobei letzterer eine niedrigere Aktivierungsenergie hat. Diese Erkenntnis erlaubte die Herstellung von hochporösen und homogenen porösen SiC-Schichten mit MAPCE.

Diese Erkenntnisse trugen auch zur Untersuchung und Verbesserung des PECE-Prozesses bei. Im Unterschied zu MAPCE wird bei PECE eine externe Spannung benötigt, die den Stromfluss während des Ätzens bedingt. Deshalb werden kein Oxidationsmittel in der Ätzlösung und kein Pt-Dünnsfilm benötigt. Es stellte sich heraus, dass MAPCE sich gut eignet, um poröse Dünnsfilme mit Schichtdicken bis zu 2 µm herzustellen, während mit PECE bis zu 30 µm dicke poröse Schichten realisiert werden konnten. Ein typisches Problem in Verbindung mit PECE war, dass es zur Ausbildung inhomogener poröser Schichten kam. Dieses Problem wurde durch eine poröse Startschicht behoben, die mit MAPCE auf der Oberfläche eines Wafers erzeugt wurde.

Die Porenspitzen der MACPE Startschicht dienen als Initiationsstellen für den PECE-Prozess, was zu homogenen porösen PECE-Schichten führte. Weitere Untersuchungen zeigten, dass PECE dem Materialversagen bei dielektrischem Durchbruch ähnelt. Das heißt, dass der resultierende Porositätsgrad nicht von der gewählten Stromdichte, sondern von der angelegten Spannung abhängt. Der Einfluss der Stromdichte manifestiert sich in der resultierenden Schichtdicke. Das führte zu der Anwendung eines Ladungs-kontrollierten Ätzmodus. Der Porositätsgrad wird über die angelegte Spannung und die Schichtdicke über die geflossene Ladungsmenge eingestellt. Das ermöglichte die Herstellung von übereinander angeordneten, individuellen SiC-Schichten mit alternierendem Porositätsgrad.

Nach der grundlegenden Untersuchung von MAPCE und PECE wurden mögliche Anwendungsgebiete dieser Methoden für MEMS-Bauelemente ausgelotet. MAPCE wurde dabei zur lokalen Herstellung von porösem SiC genutzt. Das Pt wurde nach dem Ätzen mit Königswasser entfernt und anschließend wurde auf der ganzen Probe polykristallines SiC mittels chemischer Gasphasenabscheidung abgeschieden. Nach einem zusätzlichen Temperaturschritt kollabierte das nun mit poly-SiC bedeckte poröse SiC, sodass eine geschlossene Kavität zurückblieb. Solche Kavitäten haben potentielle Anwendung in SiC-basierten MEMS-Drucksensoren. Ein weiterer Ansatz bestand darin eine Sollbruchstelle unter der hochporösen MAPCE Schicht zu erzeugen. Durch Abscheiden einer druckverspannten amorphen SiC:H Schicht konnte eine sich beulende Membran hergestellt werden, die ebenfalls in MEMS-Drucksensoren eingesetzt werden kann.

Weiters war es möglich mit MAPCE poröse Anti-Reflexions-Beschichtungen und homogen poröse Schichten auf 4H-SiC Substraten zu erzeugen, die Reflexionseigenschaften wie Dünnschichten zeigen. Erstere könnten in LEDs oder UV-Sensoren eingesetzt werden, wobei letztere eine mögliche Anwendung in optischen Sensoren haben, die auf einer Änderung der Reflexion beruhen, wenn die Poren mit z.B. gasförmigem oder flüssigem Medium befüllt werden.

Ladungs-kontrolliertes PECE erlaubte die Herstellung von gestapelten porösen SiC Schichten mit unterschiedlichem Porositätsgrad. Das erlaubte wiederum die Herstellung von porösen Rugate Spiegeln, die scharfe Peaks im Reflexionsspektrum zeigen. Solche Spiegel haben potentielle Anwendung in optischen Sensoren für aggressive Umgebungen und im Bereich der Bioanalytik.

Zusammenfassend wurden MAPCE und PECE für das photoelektrochemische Porösifizieren von 4H-SiC sowohl experimentell als auch theoretisch untersucht. Mit den in dieser Arbeit vorgestellten Ergebnissen wurden die notwendigen Grundlagen gelegt, um poröse 4H-SiC Schichten reproduzierbar in MEMS Bauelemente zu integrieren.

Acknowledgements

First of all I would like to thank Prof. Ulrich Schmid for giving me the opportunity to perform this PhD thesis and Dr. Tobias Frischmuth who motivated me to perform a PhD thesis at the institute of sensor- and actuator-systems. I had the great opportunity to work in a multi-disciplinary field, containing elements of chemistry, physics, electrical engineering and computer science. Therefore, I was able to improve my skills in all of these subjects, which is for me the most valuable thing. I would like to thank everyone at the institute for creating and maintaining such a positive working environment where unconventional thinking is allowed and encouraged.

There are a few people who I especially want to mention here. Manuel Dorfmeister, MSc who was my office-mate and always interested in scientific discussions. Christopher Zellner, who performed a lot of experiments for me. He really helped me in pushing things forward during this thesis. Moreover, I would like to thank my bachelor-students Markus Lukschanderl and Christoph Hufnagl, Georg Pfusterschmied, MSc for performing chemical vapor deposition experiments and Dr. Michael Schneider for the scientific discussions and helpful advice.

I also thank all the people on edx.org and coursera.org for pushing online classes forward and sharing their passion for teaching with the world. You guys rule. Furthermore, I highly respect all Wikipedia authors for sharing their knowledge for free. These sources were really helpful when it was necessary to build up new skills. Last but not least I am grateful for the high quality education in schools and universities here in Austria which was available for free.

This project has been supported by the COMET K1 centre ASSIC Austrian Smart Systems Integration Research Center. The COMET – Competence Centers for Excellent Technologies-Programme is supported by BMVIT, BMWFW and the federal provinces of Carinthia and Styria.

Finally, I would like to thank my family, my neighbors, all of my friends and my girlfriend Jennifer for making life valuable and for being there when I needed them.

Table of Contents

1	Introduction.....	11
2	Basics and state of the art.....	12
2.1	Silicon Carbide.....	12
2.2	Photoelectrochemical Etching	14
2.2.1	Semiconductor-electrolyte junction	15
2.2.2	Theories of porous layer formation.....	27
2.3	Metal assisted (photo)chemical Etching	32
2.4	Porous silicon and silicon carbide: properties and devices.....	34
2.5	Specific task in this thesis	35
3	Experimental methods.....	37
3.1	Porous silicon etching chamber	37
3.2	Sputter deposition	38
3.3	Chemical vapor deposition	40
3.4	Scanning electron microscopy	42
3.5	Image analysis.....	44
3.6	Infrared spectroscopy.....	45
3.7	Secondary ion mass spectrometry.....	48
3.8	Thin film reflectance.....	49
3.9	Additional equipment and measurement techniques	50
3.9.1	Electrical characterization.....	50
3.9.2	Photometric measurement.....	50
3.9.3	White light interferometry	51
3.9.4	UV light power measurement	51
3.9.5	Redox potential measurement.....	51
4	Fundamental investigations on MAPCE and PECE	52
4.1	Role of the metal semiconductor junction during MAPCE	52
4.2	Porous SiC from PECE without skin and cap layer.....	55
4.2.1	Effect of a prior MAPCE step on PECE	57
4.2.2	Etching of an already existing porous layer with MAPCE.....	65
4.3	Preparation of highly porous and uniform porous SiC thin layers with MAPCE.....	72
4.3.1	Evolution of the porous layer.....	74
4.3.2	Chemical composition of the porous layers.....	92
4.4	Cellular automaton simulation of MAPCE.....	98
4.4.1	Experimental observations.....	98
4.4.2	Implementation details.....	100

4.4.3	Comparison with real experiments	102
4.4.4	Conclusiones	105
4.5	Preparation of stacked porous layers with alternating degree of porosity	106
4.5.1	Current controlled experiments.....	107
4.5.2	Voltage controlled experiments	118
4.5.3	Similarity to dielectric breakdown.....	128
4.5.4	Chemical analysis	130
4.5.5	Summary	139
5	Micromachined devices based on porous SiC	140
5.1	Membrane fabrication.....	140
5.1.1	Sintering approach	140
5.1.2	Buckling approach	142
5.2	Optical devices.....	144
5.2.1	Antireflective and homogeneous thin films.....	144
5.2.2	Porous SiC based, optical mirrors fabricated with PECE.....	148
6	Summary and Outlook	156
7	References	158
8	Abbreviations	166
9	Appendix	169
9.1	SEM micrographs of PECE transition regions from section 4.5.1	169
9.2	Curriculum Vitae	171

1 Introduction

The first porous semiconductor which was fabricated out of single crystalline wafers was porous silicon (pSi). It was discovered by Arthur and Ingeborg Uhlir at the Bell Laboratories, who observed colored films after electrochemical micromachining of silicon. Both researchers, however, did not consider further investigation of this phenomenon and just noted their observations in a laboratory journal [1].

After this initial discovery of pSi, the scientific community did not pay much attention to this material until the 1990's, when it was found that pSi shows fluorescence due to quantum confinement effects [2,3]. Since then the research effort devoted to pSi has increased drastically. This led to new pSi based device concepts such as optical Bragg mirrors [4], gas sensors [5], or super-capacitors [6]. Furthermore, pSi has found application in the field of microelectromechanical systems (MEMS), where it is used as sacrificial layer during device fabrication [7,8]. This demonstrates that pSi is a promising material for a wide range of application scenarios due to its outstanding properties. Therefore, scientists have also tried to produce pSi also via other routes than electrochemical etching. As a very popular approach metal assisted etching of Si-wafers has been established in the scientific community as an alternative method [9]. This method shows great potential since it does not need an externally applied voltage and it also allows positive patterning of Si by just depositing a metal film on the surface of Si. However, the theoretical principles of this method are still under debate [10].

These achievements show that pSi has great potential for future applications. Nevertheless, it has also some disadvantages when it comes to application scenarios in harsh environments, in corrosive electrolyte solutions or biological sensing. In such cases pSi has to be covered with a dense protection layer, which prevents pSi from chemical degradation or dissolution [11]. These drawbacks of pSi led to the investigation of other porous semiconductors like gallium nitride (GaN) [12], indium phosphide (InP) [13] or silicon carbide (SiC) [14], fabricated with the before mentioned methods. Due to its chemical inertness and stability at high temperatures, pSiC could replace pSi in several challenging application scenarios. However, before such attempts can be made the theoretical basics of pSiC formation have to be better understood. This is necessary because at the beginning of this thesis a specific adjustment of basic porous layer properties such as the degree of porosification and an acceptable homogeneity within a layer with respect to the targeted application scenario was not possible. Due to this lack of knowledge it is the objective of this thesis to reveal the theoretical principles of the photoelectrochemical pSiC formation. Based on a tailored degree of porosity and a substantial increase in homogeneity within the porous layer, the potential of pSiC is evaluated for novel MEMS device architectures.

2 Basics and state of the art

2.1 Silicon Carbide

Silicon carbide (SiC) is a compound material consisting of silicon (Si) and carbon (C). The primary building block of SiC is a tetrahedron based on a C atom placed in the middle and Si atoms in the corners (see Figure 1). Both, the C as well as the Si atoms form sp^3 hybridized orbitals, such that there are covalent bonds between the Si and C atoms. The Si-C bond has a binding energy of 6.34 eV which is considerably higher than that of the Si-Si binding energy of 4.63 eV [15]. Furthermore the Si-C bond is polarized due to the higher electronegativity of carbon. This results in a higher electron density at the C atoms [16].

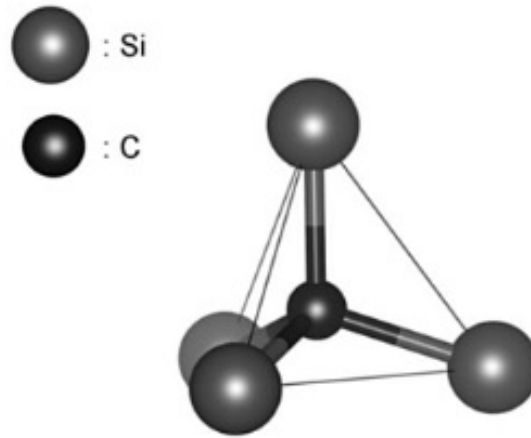


Figure 1: SiC Tetrahedron Taken from [17].

The high binding energy of the Si-C bond explains the high melting point of SiC (3100 K) [18] and the high chemical inertness of SiC in comparison to Si. Moreover the band gap of all crystal variations of SiC is higher than that of Si and also the electron mobility is lower with respect to Si. A comparison of several key material parameters is shown in Table 1. Besides the differences between Si and SiC mentioned before, also the differences between three crystal variations of SiC (i.e. 3C, 4H and 6H) are shown. Figure 2 shows schematically the atomic structure of these variations, called polytypes. These polytypes differ in their Si-C bilayer stacking sequences along the c-axis of a hexagonal unit cell. In the case of 3C-SiC the bilayer stacking sequence can be described with three consecutive, different bilayers called A, B and C. Hence the notation 3C, where C represents in this context the cubic symmetry of this polytype. In contrast to this the unit cell of 3C-SiC shown in Figure 2 is not primitive; the hexagonal structure is chosen for comparison reasons with the other polytypes. The 4H and 6H polytypes of SiC can be constructed from the 3C stacking sequence by inserting additional layers. This leads to the stacking sequences ABCB and ABCACB, respectively. The insertion of a layer requires

a twist of the lattice by 60° , which can be imagined by a rotation of the tetrahedron building blocks along the horizontal axis (see Figure 1). For 4H-SiC, twisting occurs at the C bilayer because the insertion of a B layer on top requires a rotation of 60° (see Figure 2 – black arrow).

Material parameter	Si	3C-SiC	4H-SiC	6H-SiC
Lattice constant a at 300 K [\AA]	5.43	4.35	3.08	3.08
Lattice constant c at 300 K [\AA]			10.05	15.08
Density at 300 K [g/cm^3]	2.33	3.21	3.21	3.21
Thermal conductivity [$\text{W}/(\text{cm}\cdot\text{K})$]	1.49	3.2	4.9	4.9
Band gap energy at 300 K [eV]	1.12	2.35	3.28	3.08
Electron mobility [$\text{cm}^2/(\text{V}\cdot\text{s})$] @ $N_D=10^{16} \text{ cm}^{-3}$	1430	800	\parallel c-axis: 900 \perp c-axis: 800	\parallel c-axis: 60 \perp c-axis: 400

Table 1: Properties of Si compared with those of 3C, 4H and 6H polytypes of SiC. Material properties are taken from [19].

Such bilayers, where twisting causes a change of the nearest neighbors compared to 3C-SiC, are denoted as hexagonal lattice sites, as they cause the overall hexagonal crystal structure of 4H and 6H SiC. The other bilayers are called cubic lattice sites [20].

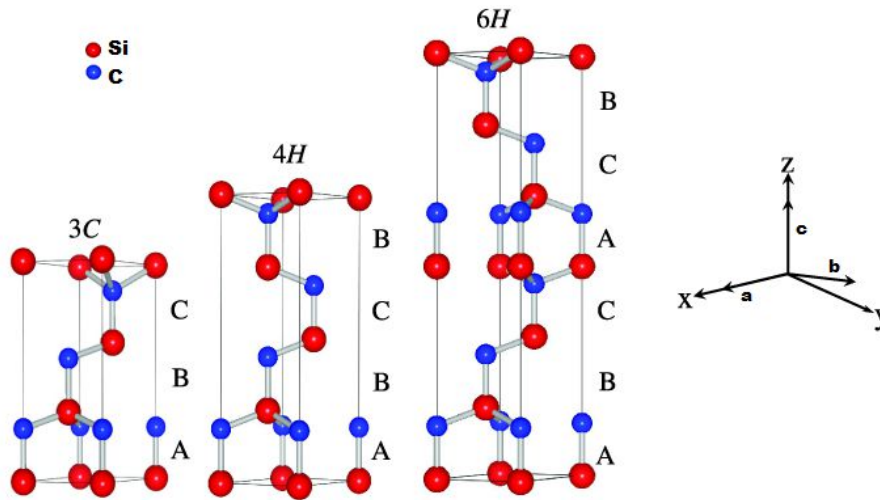


Figure 2: Schematic structures of SiC polytypes. Taken from [21].

This means that 3C-SiC has just cubic lattice sites while only one half and two thirds of the lattice sites of 4H-SiC and 6H-SiC are cubic. In conclusion the different polytypes of SiC are

characterized by their differences in the stacking sequence along the c-axis. This manifests also in different physical properties of SiC polytypes, as can be seen in Table 1. The electron mobility is anisotropic for 4H and 6H-SiC and the band gap increases with the amount of hexagonal lattice sites from 3C to 4H-SiC [22].

Another intrinsic property of SiC is the occurrence of different faces. Basically, a Si-face and a C-face can be defined. This is exemplarily illustrated in Figure 3. One can see the bonding structure of a hexagonal polytype with the (0001) and (000 $\bar{1}$) faces defined as Si and C-face, respectively. The occurrence of these two different faces is due to energy minimization. The solid favors a state minimizing the density of dangling bonds, which can only be realized by Si-dangling bonds on one side and C-dangling bonds on the other side of the structure, shown in Figure 3. The C and Si-face have different chemical reactivity, surface energy and electronic properties due to the polar nature of the Si-C bond [22].

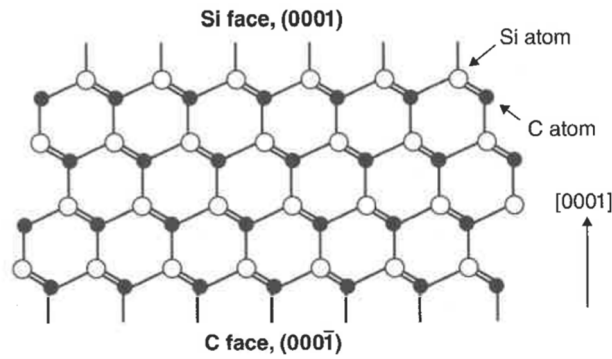


Figure 3: Schematic illustration of a hexagonal SiC polytype. Normal to the [0001] axis the C as well as the Si face are defined. Taken from [22].

Altogether SiC in its crystalline form is a semiconductor, which can appear in several different polytypes. Due to its chemical inertness, high temperature stability and high band gap, it is suitable for application scenarios in harsh environments [23].

2.2 Photoelectrochemical Etching

Photoelectrochemical etching is a method for the micromachining of semiconductors or for the preparation of porous semiconductors. Its principle is shown in Figure 4. A semiconductor electrode and an inert counter electrode are immersed in an electrolyte solution.

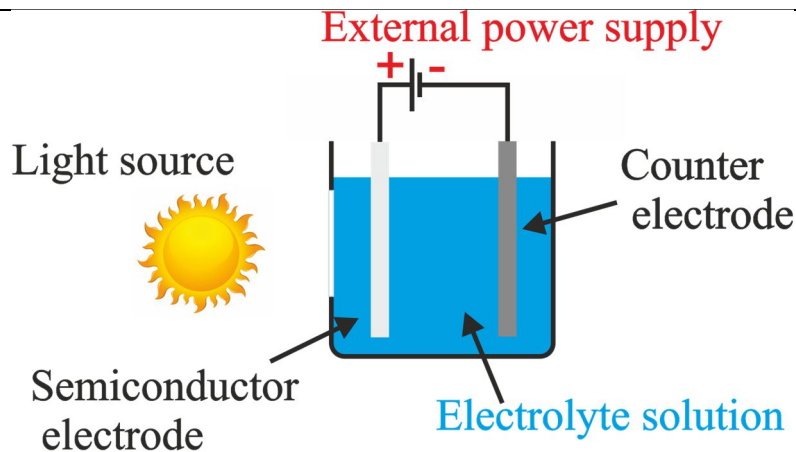


Figure 4: Schematic depiction of the photoelectrochemical etching approach.

When an external power supply is switched on chemical reactions at the semiconductor surface cause dissolution of the electrode. Optionally illumination with a light source is done to support the dissolution process. In the following sections the theoretical basics of this process are derived with a special emphasis on silicon because it is the best investigated reference material and silicon carbide.

2.2.1 Semiconductor-electrolyte junction

In this section the semiconductor-electrolyte junction properties are explained for the case of an n-type semiconductor. Analogous conclusions can be made for a p-type semiconductor, which are briefly discussed afterwards.

2.2.1.1 Semiconductor and electrolyte before contact

A semiconductor-electrolyte junction forms when the surfaces of both materials are brought into contact. To derive the electrical properties of this junction, first the energetic properties of both phases are briefly introduced [24–27].

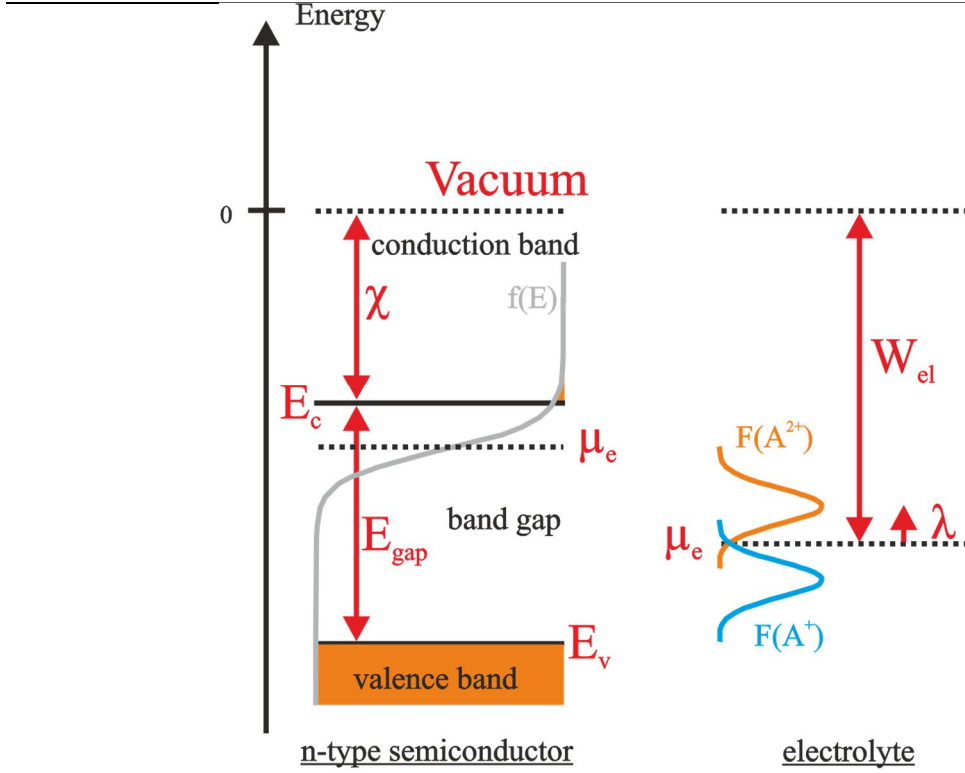


Figure 5: Energy diagrams of an n-type semiconductor and an electrolyte solution.

Figure 5 shows the energy diagrams of an n-type semiconductor and an electrolyte solution on an energy axis where vacuum is set as reference point to be zero. The semiconductor is characterized by a conduction and valence band exhibiting electronic states that can be occupied by electrons. Between the valence and conduction band lies the band gap, where in the ideal case no electronic states are present. The upper edge of the valence band and the lower edge of the conduction band are denoted with E_c and E_v , respectively. The band gap energy is E_{gap} while χ represents the electron affinity of the semiconductor. The available electronic states are filled with electrons according to Fermi-Dirac distribution function which is given in Equation [2-1] and illustrated by the grey curve in Figure 5 [28].

$$f(E) = \frac{1}{\exp\left(\frac{E - \mu_e}{k_B T}\right) + 1} \quad [2-1]$$

The probability that an electronic state having energy E is occupied depends on the chemical potential of the electrons μ_e and the thermodynamic temperature T while k_B is Boltzmann's constant. This is graphically illustrated in Figure 5. The chemical potential of the electrons represents the turning point of the Fermi-Dirac distribution. Its value depends on temperature. For room temperature this dependence is small, and the chemical potential of the electrons is often approximated by the Fermi energy, which is the value of the chemical potential when the temperature goes to zero Kelvin [27]. The states of the valence band are almost all occupied

with electrons (represented by the orange area) while in the conduction band the probability for occupying an electronic state is significantly lower. Thus most of the electronic states in the conduction band are empty allowing the electrons to move under the influence of an external electric field. The turning point of the Fermi-Dirac distribution is given by the chemical potential of the electrons which is defined in Equation [2-2] as the partial derivative of the free energy F with respect to the amount of electrons N in the semiconductor.

$$\mu_e = \frac{\partial F}{\partial N} = \mu_e^{\circ} + k_B T \ln \left(\frac{n_b}{n_i} \right) \quad [2-2]$$

The given definition can be expanded into two terms. The first term μ_e° represents the chemical potential of the undoped semiconductor, while the second term on the right side takes doping as well as temperature dependence of the chemical potential of the electrons into account.

The concentration of free electrons in the semiconductor is given by n_b while the intrinsic free electron concentration is given by n_i . This means that by increasing n_b through doping of the semiconductor with donator atoms, the chemical potential of the electrons is shifted upwards in the band gap. Furthermore, the chemical potential increases with temperature which is due to a higher amount of electrons that are thermally excited into the conduction band from energetically lower states.

Mathematically the chemical potential of the electrons is the energy at which the probability to find an electron in this state is 0.5. Physically the chemical potential of the electrons characterizes the average energy that is needed to transfer an electron from the bulk semiconductor to infinity assuming that there are no electric fields present. This also means that in equilibrium the chemical potential of an electron is constant throughout space, because the system tries to minimize its total energy.

The chemical potential of the electrons can also be defined for a redox couple in an electrolyte solution. This is explained in the following paragraphs. First the distribution of electronic states in an electrolyte solution is explained and afterwards the chemical potential of the electrons for a redox couple is introduced. The equilibrium reaction of an arbitrary redox couple is stated in Equation [2-3]. The oxidized and reduced form of a species in solution are denoted by A^{2+} and A^+ while e^- represents an electron.



This equilibrium condition is also graphically illustrated in Figure 5. The amount of particles of the oxidized and reduced form show a Gaussian distribution $F(A^{n+})$ with respect to energy. This Gaussian profile is due to polarization fluctuations in the solvent which perturb the electronic states of the ions in the solution. A measure for this perturbation is the reorganization

energy λ , which is the energy difference between the chemical potential of the electrons and the maximum of a Gaussian distribution function [24].

Compared to the semiconductor, the states of the oxidized form can be interpreted as empty states that can be occupied by electrons. Therefore they are higher in energy than the states of the reduced form.

In analogy to the semiconductor there is also a chemical potential of the electrons that can be defined for the redox couple. The equilibrium condition given in Equation [2-3] can also be stated in terms of chemical potentials as it is done in Equation [2-4]. The individual chemical potentials of the oxidized and reduced form can be expressed in terms of their concentrations. Instead of the free electron concentration n_b in the semiconductor (compare with Equation [2-2]), the concentration of the species ($[A^+]$ or $[A^{2+}]$) enters the logarithmic term. In the denominator the intrinsic free electron concentration n_i is replaced by the concentration of the ionic species at standard conditions which is per definition set to 1 mol/L. Coming from a chemical point of view one could also say that free electron concentration in the semiconductor at standard conditions is n_i .

$$\mu_{A^{2+}} + \mu_e = \mu_{A^+} \quad [2-4]$$

This leads to an expression for the electrochemical potential of the electrons in the electrolyte solution:

$$\mu_e = \mu_{A^+}^\ominus - \mu_{A^{2+}}^\ominus + kT \ln \left(\frac{[A^+]}{[A^{2+}]} \right) \quad [2-5]$$

The first two terms at the right side of Equation [2-5] are the chemical potentials of A^+ and A^{2+} at standard conditions and independent of concentration. The logarithmic term describes the dependence of the chemical potential on the concentration of the reduced and oxidized species.

So, in summary the chemical potential of the electrons is now also defined for a redox couple in an electrolyte solution. It can be interpreted the same way as for the semiconductor. The two Gaussians in Figure 5 can be thought of a density of states for electrons with the reduced form as filled and the oxidized form as empty states. In the middle of this density of states lies the electrochemical potential of the electrons, describing the energy at which the probability to find an electron is one half. Furthermore the chemical potential of the electrons for a redox couple characterizes the average energy needed to remove an electron from the electrolyte solution. Therefore its absolute value equals the work function $W(E)$ of the electrolyte solution. Here it is also assumed, that no electric fields, (e.g. stemming from a surface dipole) are present. So the chemical potential is in both, the semiconductor and the electrolyte a quantity that describes

the distribution of occupied and unoccupied states. It is therefore useful when both phases come into contact and equilibrium conditions need to be described [29].

2.2.1.2 Semiconductor and electrolyte contact formation

After having introduced the chemical potential of the electrons for the semiconductor and the electrolyte, the process of equilibration when their surfaces are brought together can be discussed [24–27].

At first the contact formation is discussed for the special case which is illustrated in Figure 5 (n-type semiconductor, lower chemical potential of the electrons in the electrolyte). Afterwards, based upon the derived relationships, the contact formation behavior for other cases will be explained.

When the n-type semiconductor is brought into contact with the electrolyte solution, electrons start to occupy the states of the oxidized form A^{2+} in the electrolyte solution in this special case. This way, the system of semiconductor and electrolyte can minimize its free energy but analogously also an electric field forms because locally charge neutrality is not preserved anymore. The semiconductor is depleted of electrons and forms a positively charged region with total charge Q_{sc} (see Figure 6a). To restore net charge balance a negatively charged region in the electrolyte builds up having total charge $Q_{el} = -Q_{sc}$. In this description it is assumed that the charge density is constant within the different phases which is only an approximation but is sufficient to derive the properties of the semiconductor-electrolyte junction. The width of the charged region in the semiconductor w (space charge region) is much larger than the width of the charged region in the electrolyte (Helmholtz layer) because the density of states in the semiconductor is lower than in the electrolyte. Typical values of w range between 10 and 1000 nm while the Helmholtz layer has a thickness of about 0.5 nm [24].

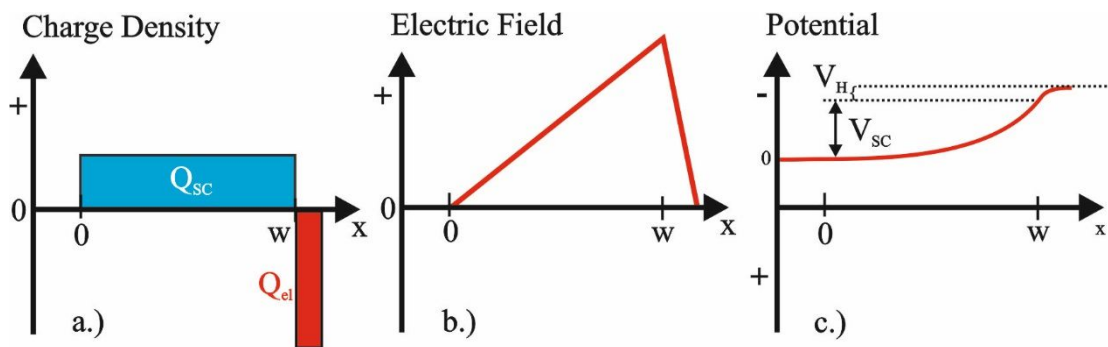


Figure 6: Properties of the semiconductor-electrolyte junction as a function of distance. The distance w denotes the semiconductor-electrolyte phase border. a.) charge density distribution. b.) resulting electric field strength and c.) characteristics of the electric potential.

Having established the space charge layer in the semiconductor as well as the Helmholtz layer it is possible to derive an expression for the electric field strength E as a function of distance. This is done by using the one dimensional Gaussian law $\frac{dE}{dx} = \frac{\rho}{\varepsilon}$ with the static dielectric constant ε of the corresponding material. The resulting electric field strength in the semiconductor is stated in Equation [2-6], where the charge density ρ is written in terms of the donator doping atom concentration N_D and the elementary charge q .

$$E(x) = \frac{qN_D}{\varepsilon}x \quad (0 \leq x \leq w) \quad [2-6]$$

By using the relation $\frac{d\varphi}{dx} = -E(x)$ it is possible to derive the electric potential φ characteristics within the semiconductor (see Equation [2-7]). In this equation the electric potential at point zero is the reference point, which is arbitrarily set to be zero.

$$\Delta\varphi = V(x) = -\frac{qN_D}{2\varepsilon}x^2 \quad (0 \leq x \leq w) \quad [2-7]$$

Similar expressions can be derived for the electrolyte and a schematic of the overall electric field strength and electric potential characteristics is given in Figure 6. It can be seen that most of the electric potential drops across the space charge region (V_{SC}) while the potential drop in the electrolyte V_H is significantly lower. This is due to the low thickness of the Helmholtz layer compared to the width of the space charge layer and high dielectric constants of electrolyte solutions. Therefore in the following it is assumed that all of the electric potential drops in the space charge layer, which makes derivations easier but does not lead to less physical insight.

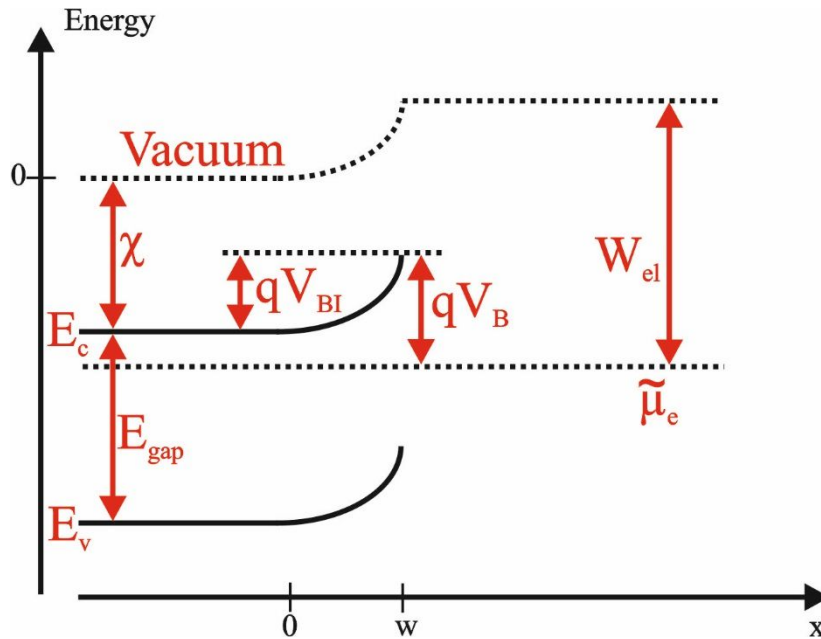


Figure 7: Energy band diagram of the n-type semiconductor-electrolyte junction.

Now that an expression for the characteristics of the electric potential across the semiconductor-electrolyte junction has been derived, this result can be incorporated into the energy band diagram of Figure 5. To account for the effect of the electric potential the band energies are summed with the potential energy $W_{pot} = -qV(x)$. The resulting band diagram is illustrated in Figure 7, where the band edges in the semiconductor are bent upwards towards the phase border which is located at $x = w$. The energy difference of a band edge at the phase border compared to the bulk semiconductor value is given by qV_{BI} . This is the total amount of potential energy due to the equilibration process. The quantity V_{BI} is called the built-in potential and V_B is called the barrier height.

By comparison of Figure 7 with Figure 5 it can be noticed that the chemical potential of the electrons μ_e is replaced with the electrochemical potential of the electrons $\tilde{\mu}_e$ and is constant throughout the semiconductor and the electrolyte due to the equilibration process. This is now explained in detail.

The chemical potential of the electrons (or any other species) was defined as partial derivative of the free energy F (see Equation [2-2]). When just chemical energies need to be considered, a change in the free energy can be written as $dF = \sum \mu_i dN_i$ where the subscript i denotes a species in the system and dN_i is the change of particles of species i . So when building the partial derivative with respect to the amount of electrons in the system one gets the chemical potential of the electrons.

When bringing the semiconductor and the electrolyte together, a gradient in the chemical potential of the electrons is initially present. The system tries decrease its energy until this gradient vanishes. This is for example the reason of diffusion of uncharged particles until the concentration is everywhere the same.

However in the described case charge particles (electrons) are considered. Thus the equation of the free energy must also account electrical energies. This means that for each species an extra term $q\phi dN_i$ must be added, where ϕ is the electrical potential in the phase, where the particle is located. Now when taking the partial derivative with respect to the amount of electrons, one gets the electrochemical potential of the electrons: The chemical potential plus the electrical energy that is needed to insert an electron in the corresponding phase.

$$\tilde{\mu}_e = \mu_e - q\phi \quad [2-8]$$

So during the equilibration process at the semiconductor-electrolyte junction, at first diffusion of electrons takes place which is due to chemical energy minimization. This effect is counter-balanced by the built up of an electric field. This is accounted for in the electrochemical potential. So when electric fields are present the chemical potential of a species has to be replaced by

its electrochemical potential, describing its average energy in the considered system. Thus at equilibrium the electrochemical potential is constant throughout all phases.

This definition of the electrochemical potential helps to derive an expression for the built-in voltage V_{BI} at the semiconductor-electrolyte junction [30]. The electrochemical potential at the point $x = 0$ in Figure 7 can be written as $\tilde{\mu}_e = \mu_{e,x=0} - q\varphi_{x=0}$. The same procedure can be done for the electrochemical potential at the point $x = w$, which leads to the following equations because of constant $\tilde{\mu}_e$ throughout all phases:

$$\mu_{e,x=0} - q\varphi_{x=0} = \mu_{e,x=w} - q\varphi_{x=w} \quad [2-9]$$

$$\varphi_{x=w} - \varphi_{x=0} = \frac{\mu_{e,x=w} - \mu_{e,x=0}}{q} \quad [2-10]$$

The term on the left hand side can be identified as the built in voltage, while the chemical potential of the electrons at $x = 0$ and $x = w$ are equal to the chemical potentials before contact formation because there is no net charge at these positions. Thus the built-in voltage is determined by difference of the chemical potential of the electrons before semiconductor and electrolyte are brought together. Because both quantities can be adjusted (e.g. by altering the electrolyte composition or the doping level in the semiconductor), also the built-in voltage can be deliberately manipulated.

2.2.1.3 Current voltage characteristics

Now that the electrical properties of the electrolyte semiconductor junction at equilibrium have been introduced it is possible to discuss its characteristics when an external voltage is applied [25]. In equilibrium the forward and backward reactions corresponding to Equation [2-3] take place at the same rate. The rate equations for the forward and backward reactions at the semiconductor-electrolyte interface are given in Equations [2-11] and [2-12], respectively. In this approach it is assumed, that all electron transfers between the oxidized and reduced species take place via the semiconductor.

$$\frac{d[A^+]_s}{dt} = k_{et}[A^{2+}]n_s \quad [2-11]$$

$$-\frac{d[A^+]_s}{dt} = k_{et}^{-1}[A^+] \quad [2-12]$$

The concentration of electrons at the surface of the semiconductor is given by n_s , while k_{et} and k_{et}^{-1} represent the forward and backward rate constants. Furthermore $[A^+]_s$ represents the surface concentration of A^+ in units of mol/cm^2 to account for the flux across the unit area. The

amount of states that can be occupied by electrons in the semiconductor is regarded as constant and therefore incorporated into k_{et}^{-1} . In equilibrium (absolute forward and reverse reaction rate are equal) the electron concentration at the interface is replaced by its equilibrium concentration $n_{s,eq}$.

$$k_{et}[A^{2+}]n_{s,eq} = k_{et}^{-1}[A^+] \quad [2-13]$$

The net forward reaction rate is the difference between the rate equations and by using the Equations [2-11] to [2-13] it can be expressed as follows:

$$\frac{d[A^+]_s}{dt} = k_{et}[A^{2+}](n_s - n_{s,eq}) \quad [2-14]$$

The surface electron concentration of the semiconductor is determined by the energy difference of electrons in the bulk and at the surface. In equilibrium this energy difference is given by the potential energy due to the build-in potential qV_{BI} (see Figure 7). When an external voltage V_{ext} is applied the potential energy is given by $q(V_{BI} + V_{ext})$. Now the concentration of electrons at the surface of the semiconductor can be approximated with a Boltzmann function using the concentration of electrons in the bulk semiconductor n_b .

$$\frac{d[A^+]_s}{dt} = k_{et}[A^{2+}] \left(n_b e^{-\frac{q(V_{BI}+V_{ext})}{kT}} - n_b e^{-\frac{qV_{BI}}{kT}} \right) \quad [2-15]$$

To obtain the electrical current I in forward reaction, Equation [2-15] has to be multiplied with the electrode's area A and the negative elementary charge $-q$, because electrons are considered. This leads to Equation [2-16], with the exchange current I_0 , where all constants are incorporated.

$$I = I_0 \left(e^{-\frac{qV_{ext}}{kT}} - 1 \right) \quad [2-16]$$

Figure 8 - curve 1 shows a typical current voltage characteristic according to Equation [2-16]. In the forward direction (i.e. the considered electrode under test is at negative potential relative to a reference electrode having a constant electrical potential) the current increases exponentially with the voltage while the current in the reverse direction becomes rather constant with increasing voltage. This is because in forward direction the external voltage decreases the potential energy barrier in Figure 7 while in reverse direction it is increased, hindering electrons to pass the interface.

The exchange current I_0 determines the slope of the current voltage characteristics and is given by Equation [2-17] [26]. It is noticed that the current voltage characteristic can be influenced by the composition of the electrolyte solution, as well as the doping level of the semiconductor

since n_b , $[A^{2+}]$ and consequently V_{BI} determine I_0 . A steeper curve in forward direction is obtained by decreasing the built-in potential energy barrier.

$$I_0 = -n_b q A k_{et} [A^{2+}] e^{-\frac{qV_{BI}}{kT}} \quad [2-17]$$

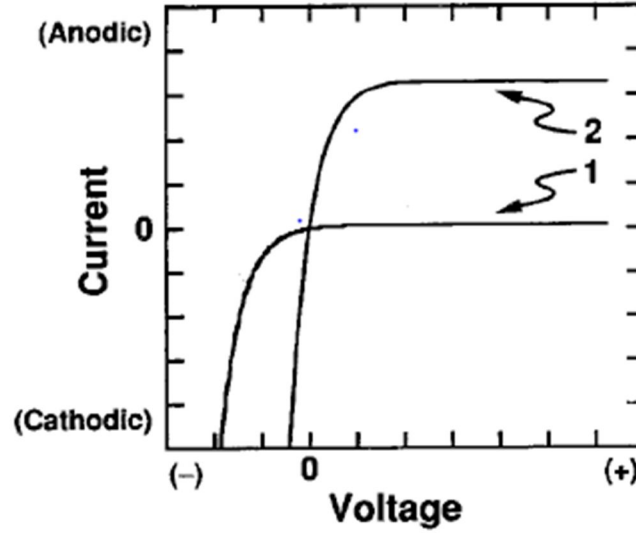


Figure 8: Current voltage characteristics of a semiconductor electrolyte junction. 1.) under dark conditions 2.) under illumination with light. Taken from [25].

The presented current voltage characteristics are similar to the current voltage characteristics of a diode, but there are physical differences. To illustrate them, the electron transfer rate constant k_{et} in Equation [2-17] is described in greater detail: [24,31]

$$k_{et} = Z \kappa e^{-\frac{-(E_c - \tilde{\mu}_e + \lambda)^2}{4k_B T \lambda}} \quad [2-18]$$

Here Z is the frequency factor and quantifies the attempts to cross the potential energy barrier qV_{BI} , which is analogous to the thermionic emission theory for metal semiconductor junctions. The exponential term in Equation [2-18] stems from the Gaussian probability distribution shown in Figure 5, but here the case after contact formation is considered. The center of the $[A^{2+}]$ energy distribution is given by $\tilde{\mu}_e + \lambda$ and the probability of charge transfer is proportional to the value of the distribution function evaluated at the conduction band edge at the phase border. This means that, the higher the probability to find a $[A^{2+}]$ state near the conduction band edge, the higher the probability for charge transfer in forward direction. This probability is lower compared to a metal-semiconductor junction, because of the relatively higher density of states in a metal. κ is called the transmission coefficient and can take values between 0 and 1. This parameter describes the interaction between the electronic wave function of the electron in the semiconductor electrode and of the acceptor state in the electrolyte solution.

When the interaction is strong charge transfer is enhanced, because of the formation of a high and low energy wave function similar to chemical bonding in molecules. Finally k_B is Boltzmann's constant and T is the thermodynamic temperature. All these effects do not appear in metal-semiconductor junctions and hence the exchange current I_0 is lower for electrolyte semiconductor junctions, compared to metal semiconductor interfaces [24,31].

Beside physical differences also the notation in electrochemistry is different. The voltage axis describes the potential of the semiconductor electrode relative to an electrode at fixed potential. This is different in common electric circuit testing, where the reference is the ground, arbitrarily set to zero volt. In addition also negative charge carriers are considered in electrochemical notation, instead of positive charge carriers in technical current direction. Therefore the current voltage characteristics in electrochemistry is inversed compared to common electrical circuit analysis.

Finally the behavior of the semiconductor-electrolyte junction under light illumination is discussed [32]. When the semiconductor electrode is illuminated with light having higher energy than the band-gap energy, valence band electrons are excited to the conduction band. The missing electron in the valence band is treated as a positively charged particle, called a hole. This electron hole pair is separated in the space charge layer because of the electric field that is present. The holes are accelerated to the semiconductor electrolyte phase border while electrons are accelerated into the bulk of the semiconductor electrode. This means that under light illumination an additional current I_{photo} opposing the forward direction current is generated (see Equation [2-19]).

$$I = I_0 \left(e^{-\frac{qV_{ext}}{kT}} - 1 \right) + I_{photo} \quad [2-19]$$

The effect of this photocurrent is illustrated in Figure 8— curve 2. There is a constant offset in the current voltage characteristics compared to the situation when the junction is under dark conditions. Considering more details, this constant offset is an approximation, namely that all the charge generated holes contribute to the photocurrent, which is justified for most semiconductor-electrolyte junctions [25]. A more detailed analysis just considering monochromatic light illumination takes into account, that holes are generated in the space charge layer, as well as in the bulk material. The photocurrent from the former is mostly determined by the light absorption coefficient α of the material, while the latter depends on the diffusion length L_h of holes in the given material. These relationships are described by Equation [2-20], where Φ is the incident photon flux and w is the thickness of the space charge layer.

$$I_{photo} = q\Phi \left(1 - \frac{e^{-\alpha w}}{1 + \alpha L_h} \right) \quad [2-20]$$

So the photocurrent increases with increased absorption coefficient, and diffusion length (lifetime) of holes in the semiconductor. Furthermore I_{photo} depends on the width of the space charge layer w , which is increased when voltage is applied in the reverse direction. So the photocurrent also depends on the applied voltage and is increased when the semiconductor electrolyte is at positive potential relative to the reference electrode [32].

2.2.1.4 Case of accumulation

So far only the special case for an n-type semiconductor with charge depletion has been considered. When the chemical potential of the electrons in the electrolyte solution has a higher value than in the semiconductor electrons will diffuse into the semiconductor during contact formation. Now also a positive and negative net charge forms at both sides of the interface, but because of the high density of states in the conduction band, the width of the charged region in the semiconductor is comparable to the one in the electrolyte.

This behavior is illustrated in Figure 6. In the case of accumulation the net charge in the semiconductor has opposite sign and is located near the interface. Therefore also the thickness of the potential barrier narrows. The probability of electrons that can tunnel through the potential energy barrier is increased, eventually leading to an ohmic current voltage characteristics when an external voltage is applied because neither the forward or reverse reaction are favored in the tunneling process [25].

2.2.1.5 Case of a p-type semiconductor

Similar considerations as were done for an n-type semiconductor can be made when a p-type semiconductor comes into contact with an electrolyte solution. This is not elaborated here in detail but the final results are presented. Charge depletion occurs when the chemical potential of the electrons is initially higher in the electrolyte solution than in the semiconductor. When during the equilibration process electrons diffuse into the semiconductor, they can occupy the acceptor states from the p-type dopants. This leads to a negatively charged space charge layer and a positive net charge in the electrolyte; the opposite behavior as for the n-type semiconductor case.

The resulting band diagram is illustrated in Figure 9, showing energy band downward bending at the interface.

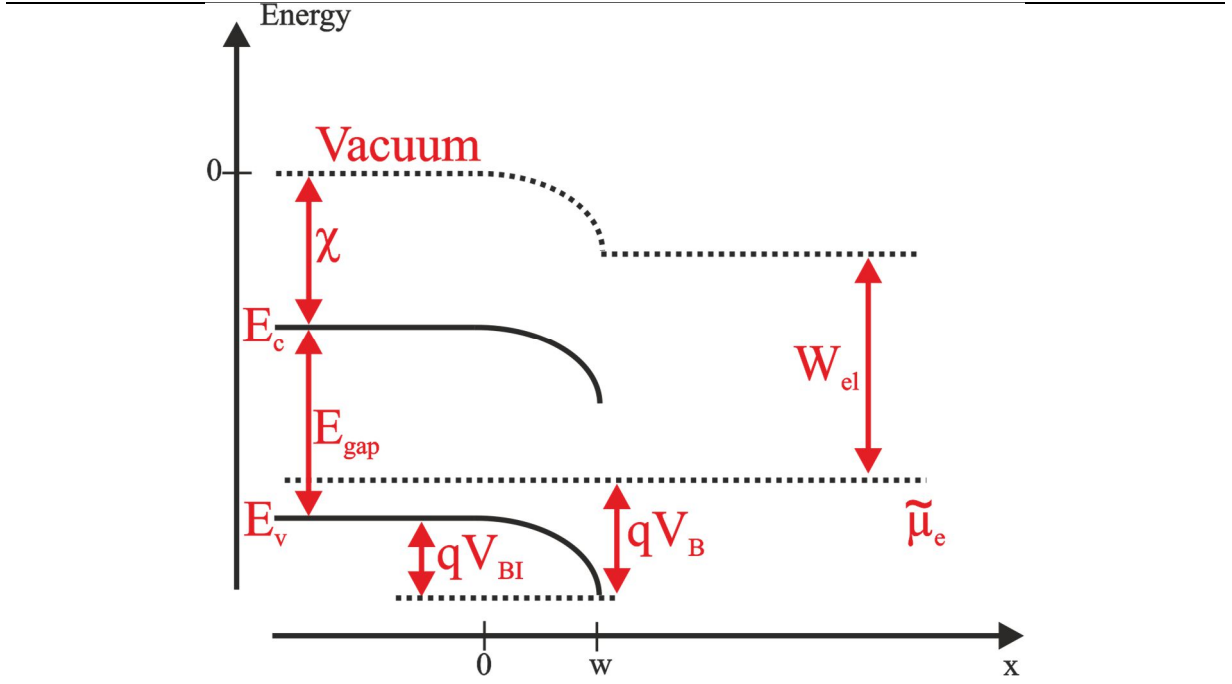


Figure 9: Energy band diagram of the p-type semiconductor-electrolyte junction.

In contrast to n-type semiconductors where electrons in the conduction band are the majority free charge carriers, positively charged holes in the valence band are the majority charge carriers in p-type semiconductors. The built-in potential energy decreases the concentration of holes at the interface. Thus the band bending represents an energy barrier for the transport of holes from the bulk semiconductor to the interface, similarly to the energy barrier for electrons in the case of an n-type semiconductor. Consequently the p-semiconductor electrolyte junction in the depletion case shows the same current voltage characteristic as for the n-type semiconductor but forward direction is given when the semiconductor is at positive electrical potential relative to a reference electrode.

Finally, also the case of accumulation can occur when a p-type semiconductor is connected with an electrolyte solution, namely when the chemical potential of the electrons is at lower energy in the electrolyte solution prior to contact formation [25,26].

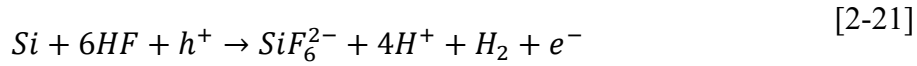
2.2.2 Theories of porous layer formation

In the former section, the ideal behavior of a semiconductor electrolyte junction under light illumination and under applied voltage has been discussed. In this section the formation of porous silicon in hydrofluoric acid (HF) containing electrolyte solutions under externally applied voltage is described by means of the before derived expressions.

2.2.2.1 Chemical interpretation of the etching mechanism

In the section 2.2.1 charge carrier transfer across the semiconductor electrolyte junction was introduced, neglecting the possibility that the semiconductor electrode material itself can be involved in the chemical reactions. In the electrochemical micromachining as well as in the preparation of porous semiconductors exactly this is utilized. The semiconductor electrolyte is attacked by the electrolyte and dissolved. Silicon is the most investigated material, hence the topic is introduced with this type of material.

Figure 10 shows a chemical interpretation of the porous silicon formation. First a hole \oplus is generated in the bulk of the semiconductor (1). Such a hole can be interpreted as a weak bond which is prone to attack by nucleophilic species in the electrolyte solution. So when the hole moves to the surface due to the space charge layer electric field or an externally applied voltage, the weakened bond is attacked by a fluoride ion F^- . This polarizes the back bonds of the silicon atom, thus favoring further F^- attack, while an electron from the conduction band \ominus leaves the semiconductor through the back side contact (2). In the steps (3) and (4) the back bonds of the silicon atom become more and more polarized until SiF_4 is detached from the silicon electrode, while H^+ and H_2 are created. Finally SiF_4 reacts with HF molecules to form dissociated silicic acid and a hydrogen terminated silicon surface is left behind (5). For this reaction a net equation can be stated as follows: [33]



This reaction is only one possible reaction path during electrochemical etching of silicon in HF based solutions but the essential point is illustrated. Etching of silicon always requires at first a hole in the valence band, for initial polarization of the $Si - H$ bond [3,33].

These initial considerations also show that p-type semiconductors can be etched when the semiconductor electrolyte junction is biased in forward direction, because the required holes are the majority carriers. Contrarily, n-type semiconductors must be etched under reverse bias and light illumination is required to create holes in the valence band.

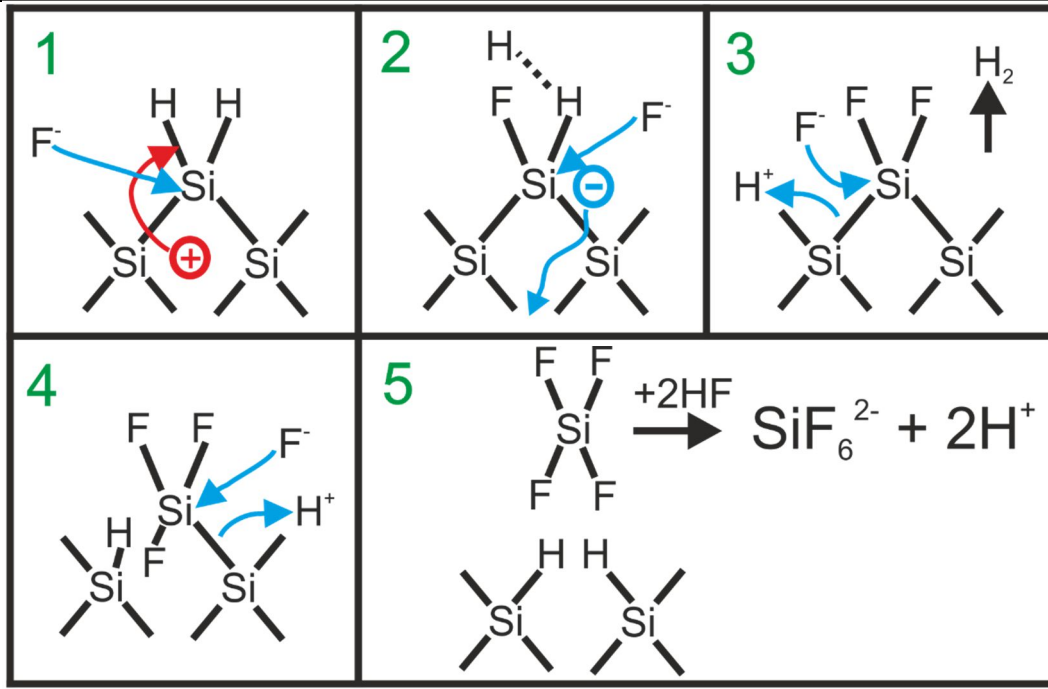
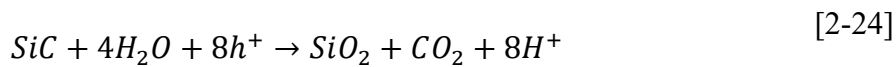
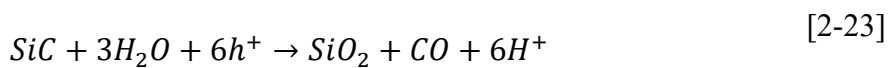
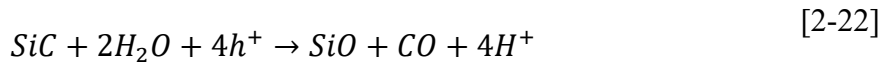
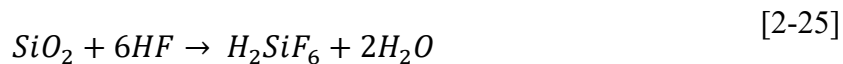


Figure 10: Chemical reactions taking place during the etching of silicon in HF containing electrolyte. Reproduced from [3].

The same principles are valid for electrochemical etching of SiC in HF based solutions. Holes in the conduction band are needed for etching [14,34,35]. However, there are only speculations of a dissolution mechanism [33], but the majority of the published articles state that the dissolution of SiC is a two-step process. First SiC is oxidized according to the reactions [2-22] to [2-24] [36].



In a second step the oxide is removed with HF according to equation [2-25].



There are also reaction paths proposed where no intermediate oxide is formed and fluoride acts as nucleophile species. According to those reports this becomes more likely when the HF concentration is increased and when organic solvents such as ethanol are added [34,37]. Overall the processes during electrochemical etching of SiC are still poorly understood.

2.2.2.2 Pore formation theories

In the previous paragraph the basic theory for the electrochemical etching of Si and SiC has been presented. This does not answer the question why a porous material remains during etching, when a certain current density is not exceeded. So there must be a passivating effect that prevents the semiconductor from total dissolution. In the following text currently proposed theories are presented.

First the quantum confinement theory of porous silicon is introduced [3]. During the dissolution of silicon small fibers of the bulk material remain. Electronically this means that less orbitals contribute to the band structure of the remaining material, causing a decrease in electronic states in both the valence and the conduction band. Furthermore, according to a linear combination of atomic orbitals approach also the band gap energy increases [38]. Such a behavior results in an energy band structure as is shown in Figure 11. The band gap increases and band bending occurs at the bulk to porous material transition.

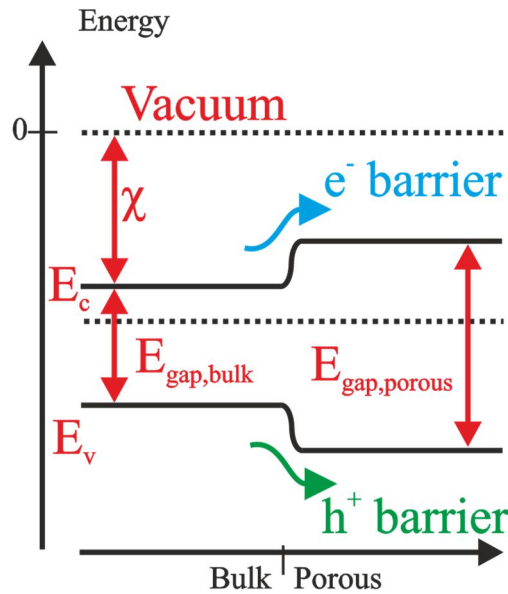


Figure 11: Quantum confinement effect at the transition from bulk material to porous material in a semiconductor.

As already discussed in section 2.2.1.3 upward bands represent a potential energy barrier for electron e^- flow and downward bands are a barrier for hole h^+ transport. Both is the case when the dimension of the silicon crystal is reduced. From an electronic perspective, this means that the charge transport from the bulk semiconductor to the porous material is hindered and no etching of the porous fibers takes place.

There exist also other theories of porous Si formation taking into account other phenomena. For example the diffusion limited model states that the diffusion of holes h^+ from the bulk to the

porous structure is responsible for the formation of porous silicon. It is assumed that holes move randomly from the bulk to the porous Si structure until they cause dissolution. In simulations that obey this assumption a porous structure could be obtained [39]. There exist several other formation theories for porous silicon, which often share several elements but none of them can explain all experimental observations. A summary can be found in [40]. In comparison to porous Si, there are only a few publications available about the formation mechanism of porous SiC. Most of the research has been done with n-type 4H or 6H-SiC under UV light illumination. Konstantinov *et al.* stated that quantum confinement cannot explain the formation of porous SiC, because the fiber size in their experiments was too large for a significant increase in the band gap energy. Instead they proposed that the space charge layer at the SiC electrolyte interface fills out the porous structure, thus having an insulating effect that protects the porous structure from total dissolution. Furthermore they stated that the electrochemical potential of the electrons is pinned. This means that there are allowed energy levels in the band gap due to functional groups at the SiC electrolyte interface. These states can also exchange electrons with the bulk semiconductor, thus the position of the electrochemical potential in the bulk SiC becomes relatively independent of the composition of the electrolyte solution.

The whole situation is depicted schematically in Figure 12. In the middle valence as well as conduction band edge of a single fiber of porous SiC are illustrated. The band bending is due to the space charge layer that fills out the fiber. Furthermore surface states are present, which pin the electrochemical potential of the electrons at a constant level, since electrons from inside the fiber occupy them [41]. This basic theory was adopted by Shishkin *et al.* [34] and by Ke [42] in their works.

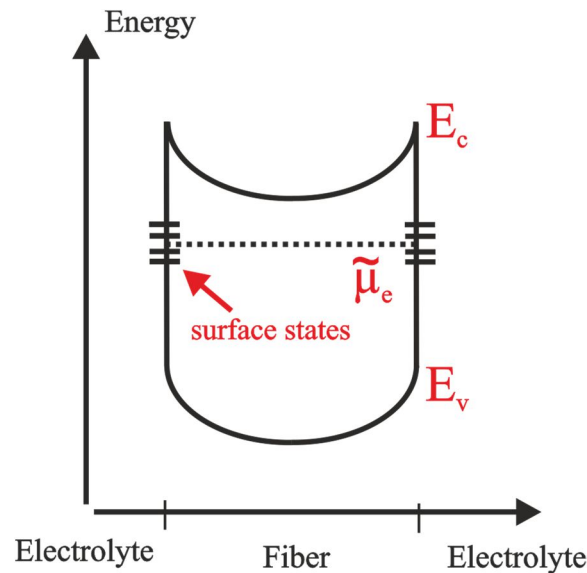
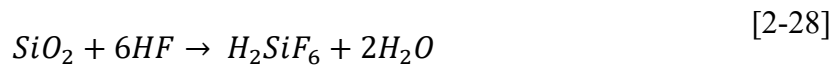
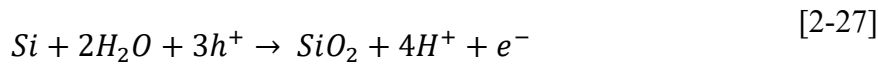
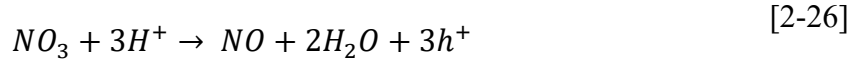


Figure 12: Energy band diagram of a porous SiC fiber.

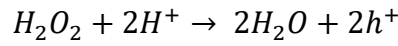
In the latter study the behavior of the C and Si-face under UV light assisted electrochemical etching was studied. Ke found that a columnar porous structure is obtained when the C-face is etched while a dendritic porous layer results from Si-face etching experiments. This behavior was explained with the different electronegativities of silicon and carbon, resulting in a positive polarization of the Si-face and a negative polarization of the C-face (see Figure 3 for the different faces). In the adjacent Helmholtz layer the electric field will therefore point in the direction of the electric field generated by the external power source, favoring etching along the field lines. The opposite is true for the Si-face. The electric field in the Helmholtz layer has opposite direction than the one from the external power source. This means that the effectively applied voltage is decreased and properties of the crystal, such as etch stop planes [34] are dominant at when the Si face is etched [42,43].

2.3 Metal assisted (photo)chemical etching

Another method for the preparation of porous semiconductors is metal assisted chemical etching (MACE). This method is an enhancement of stain etching, where an oxidizing agent such as HNO_3 is added to the HF -containing electrolyte solution (etching solution). In stain etching, a porous layer forms on the surface of silicon when a wafer is immersed in an etching solution. Both, anodic (see Equation [2-27] and [2-28]) and cathodic ([2-26]) reactions take place during stain etching.



To increase the etching rate during stain etching the silicon wafers were covered with aluminum thin films and heat treated before etching, to catalyze the cathodic reaction [44]. In later developments the aluminum thin film was replaced by noble metal particles as is illustrated in Figure 13-1a. Furthermore the oxidizing agent HNO_3 was replaced by H_2O_2 , because it is known that its decomposition is catalyzed in the presence of noble metals (gold, platinum) [45]. Eventually the cathodic reaction ([2-29]) is enhanced in the vicinity of the noble metal particles. Holes are injected into the valence band of silicon. This is thermodynamically justified because the electrochemical potential of a H_2O_2 containing etching solution is below the valence band edge of silicon. Thus holes will be generated in silicon, independent of its doping type.



[2-29]

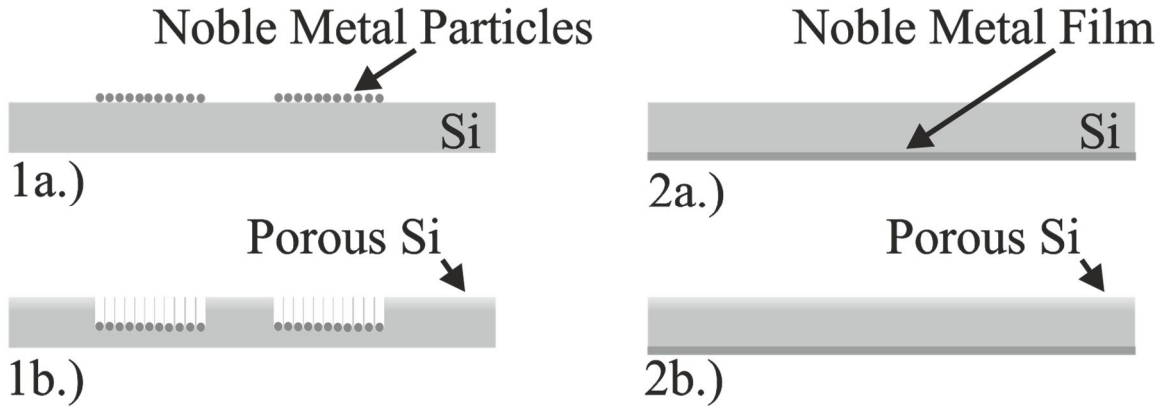
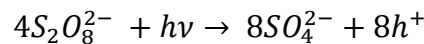


Figure 13: Realizations of metal assisted etching of silicon. 1.) original version: a – before etching, b- after etching 2.) galvanic etching: a- before etching, b- after etching

Because of the locally enhanced hole generation, also the dissolution of silicon is more localized. This leads to selective etching of silicon as is indicated in Figure 13 – 1b. Beside this also porous silicon forms across the whole surface of the wafer. With a lower conductivity of the substrate also the rate of porous silicon formation decreases because charge transport to the noble metal particles is hindered [9,10]. This method allows the direct transfer of a desired pattern into a silicon wafer in a simple manner without external power supply. A different form of metal assisted etching is so called galvanic etching, as is illustrated in Figure 13-2a and 2b. First a dense noble metal film is deposited on a silicon wafer. After immersion in an etching solution the same reactions take place, but porous silicon forms on the other side of the wafer [46].

Metal assisted etching of silicon carbide was also investigated in literature [47]. A thin film of platinum (10 nm) was deposited on the surface of 4H and 6H-SiC wafers. During metal assisted etching a porous layer formed in those regions which had not been covered with Pt. Furthermore UV light illumination having energy larger than the band gap was necessary and reasonable etching was only possible with $K_2S_2O_8$ as oxidizing agent. Experiments with H_2O_2 were not successful. This observation could not be explained with standard theories [48]. The underlying principles of metal assisted photochemical etching (MAPCE) of SiC are not well understood. Currently it is hypothesized that $K_2S_2O_8$ in the presence of Pt and UV ($h\nu$) light is capable of injecting holes into the valence band of SiC according to Equation [2-30].



[2-30]

Furthermore it is assumed that the created holes lead to oxide formation, which is in turn dissolved by HF , as was already described in Section 2.2.2.1. The formation of porous layers on SiC with MAPCE turned out to be not reproducible [47,48]. Moreover, controlling the etching depth for MAPCE of 6H-SiC is still an unresolved issue, while the formation of a porous structure on 4H-SiC is limited to surface regions in the nanometer range [48,49].

2.4 Porous silicon and silicon carbide: properties and devices

In this section an overview of the properties of porous Si and porous SiC are given. This is not an exhaustive treatment but some of the most important facts are presented.

In section 2.2.2.2 the reason for pore formation instead of total dissolution during etching of Si in HF electrolytes was given by a quantum confinement effect, which causes an increase of the band gap energy. This in turn also shifts the photoluminescence, as well as the electroluminescence of porous Si to shorter wavelengths compared to bulk Si (sub band-gap light emission) [50,51]. Consequently, pSi can be used for the realization of light emitting diodes, which emit light in the visible range [52]. Such experiments were conducted with porous SiC as well but no sub band gap light emission was found. Contrarily a shift to higher wavelengths was found. It was reasoned that surface states are responsible for the shift to higher wavelengths in photo- and electroluminescence experiments [53–55]. The porous nature does not only cause changes in the light emission properties of porous Si, but also the reflectance can be changed. This is for example utilized in antireflection coatings, where on top of a Si wafer a layer with continuously decreasing degree of porosity is generated with metal assisted etching or stain etching [56,57]. Doing so, a smooth refractive index gradient is introduced from the surface to the bulk material. The reflectance is positively correlated to the gradient in the refractive index and less sharp transitions in this property decrease the reflectance [58]. Such antireflective coatings are used in solar cells, to improve their efficiency [59].

Since the degree of porosity governs the effective refractive index of the material also other optical devices such as Bragg mirrors can be realized with porous Si [60]. Here electrochemical etching is applied for fabrication. When the current density is varied periodically during etching, a stack of layers with alternating refractive index is formed. This Bragg mirror selectively reflects visible light. When the pores are filled with a different material, such as a solution containing an analyte, the reflection spectrum changes. Thus such a porous Si Bragg mirror is utilized in sensor applications [61].

The last two applications have not been realized with wet etching methods for SiC. Porous SiC antireflective coatings could be used in UV sensors and porous SiC Bragg mirrors are especially interesting because porous Si is a chemically not stable material and has to be protected with a

dense cover layer before application in harsh environments or alkaline electrolyte solutions can be targeted [11].

Beside these optical properties, porous Si and porous SiC also have a high surface to volume ratio, which makes them interesting in the field of super-capacitors. Porous Si has been successfully implemented as electrode material in super-capacitors, utilizing an ionic liquid as electrolyte [6]. As mentioned before porous Si is chemically not stable so it has to be protected with a dense cover layer for applications in super-capacitors. In this particular case it was done with a graphene coating. There are no reports available about porous SiC super-capacitor electrodes which have been synthesized via an electrochemical route. As for Bragg mirrors, porous SiC created from single crystalline wafers could be used without further protection. Furthermore a high conductivity of the substrate is desired in such applications. By creating a porous layer with a highly doped SiC substrate also this requirement could be fulfilled.

Lastly porous Si is also used in the field of microelectromechanical systems (MEMS). The first application was as sacrificial material. In particular porous Si was locally generated with electrochemical etching and afterwards thin film structures were deposited on top of it. Finally the porous Si is removed with an alkaline electrolyte such as a potassium hydroxide solution. By using this approach, free standing cantilevers and bridges could be realized in surface micromachining [7]. Beside this, electrochemically fabricated porous Si is also utilized in pressure sensor fabrication. There porous Si is also locally generated and afterwards epitaxial Si is deposited on top such that the porous Si is fully covered. Finally in an annealing step the porous Si reorganizes, due the minimization of surface energy. Finally, a free standing membrane on top of a closed cavity is obtained. When the pressure in the environment varies, the silicon membrane deflects accordingly. This is the basic building block for a MEMS pressure sensor [8]. Also in this field porous SiC has not been applied so far.

2.5 Specific tasks in this thesis

In this chapter the properties of porous Si and porous SiC were introduced. Currently a lot of application scenarios have been realized for porous Si, while there is little work available for porous SiC. This is due to the high cost of SiC wafers, which makes experiments expensive but there are also unsolved issues in the electrochemical fabrication of porous SiC. For example some authors report about the formation of a skin layer on top of the porous structure, just exhibiting a few pores in the nm-dimension [42,62]. This skin layer is followed by a cap layer, which exhibits an irregular porous structure [42,63,64]. The skin and cap layer are cumbersome for application scenarios where the electrolyte solution has to be in contact with the surface of the porous material, such as in super-capacitors or chemical sensors. Moreover controlling the

degree of porosity during electrochemical etching has not yet been achieved, being of utmost importance especially in the preparation of optical devices such as Bragg mirrors.

Furthermore the realization of porous SiC based application scenarios in the field of MEMS requires the ability to etch locally defined regions of porous SiC. So far this issue has not been realized and not even targeted in current literature.

Besides these unsolved issues in electrochemical etching of SiC, the photochemical etching is still not reproducible [48]. This means that the governing factors of this method are so poorly understood that no predictions about the etching behavior can be made.

In this thesis the investigation of possible application scenarios of porous SiC is aimed, as it could replace porous Si in micromachined devices operated in harsh environments due to its chemical inertness and high band gap.

But before particular application scenarios can be targeted, the before mentioned issues of photochemical and (photo)electrochemical etching have to be solved such that a reliable and a locally defined formation of porous SiC is possible. Afterwards, depending on the properties of the obtained porous SiC several application scenarios such as Bragg mirrors or pressure sensors can be realized.

3 Experimental methods

3.1 Porous silicon etching chamber

For electrochemical etching experiments a porous silicon etching chamber from AMMT GmbH was used. A schematic illustration is shown in Figure 14. A wafer is mounted between two isolated compartments, meaning that no fluid exchange between them takes place. The total volume of electrolyte solution is 1.5 L while the front chamber where the cathode is integrated contains approximately 150 mL. There is also the possibility to illuminate the wafer through a sapphire window also located at the front side. The anode is fixed in the back chamber. Anode as well as cathode are made of a Pt grid, such that light illumination through them is possible.

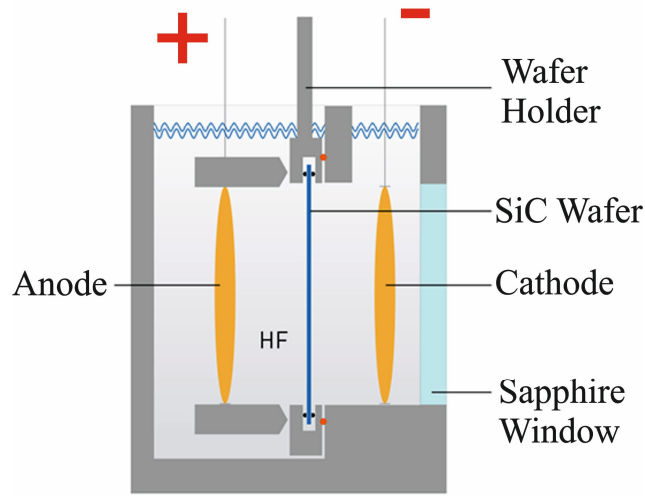
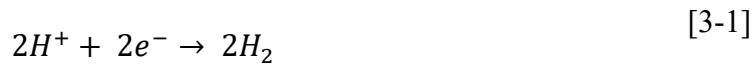


Figure 14: Porous silicon etching chamber. Taken from [65].

The theoretical details have already been presented in section 2.2, so here only a brief description of photoelectrochemical etching (PECE) with the etching chamber is given. When electrons flow from the cathode to the anode, charge transport has to take place through the SiC wafer. When a HF containing etching solution is utilized, porous SiC forms at the front side of the wafer according to Equations [2-22] to [2-25]. A special feature of the used equipment is that no metallic back side on the wafer is necessary. The electrons simply leave at the back side of the wafer according to Equation [3-1].



Electrons are accepted from H^+ ions in the etching solution. Eventually hydrogen gas forms at the back side of the wafer during current flow.

In all performed experiments n-type 4H-SiC wafers were used, so holes had to be generated at the front side of the wafer with UV light illumination. Therefore, a 250 Watt ES280LL mercury arc lamp at full spectrum was used. The distance between the wafer and the UV light source was approximately 3 cm. For PECE experiments, different etching solutions were used, either containing HF and ethanol or $\text{Na}_2\text{S}_2\text{O}_8$ and HF. The detailed concentrations are given when the experimental results are discussed. Finally two different power supplies were utilized within this thesis. Either a PS2-36V12A Porous Silicon Power Supply delivered from AMMT GmbH or a CPX400DP Dual 420 watt power supply from Aim-TTi - Thurlby Thandar Instruments Limited were used. The maximum voltages of the two components are 36 V and 60 V, respectively.

3.2 Sputter deposition

Sputter deposition is a well-established method for the synthetization of thin films. These thin films can be made of different kinds of materials, such as metals, semiconductors or even polymers [66].

The sputter deposition of conducting materials can be realized with direct current (DC) sputtering. In this method a potential difference of several 100 volts is applied between two electrodes in parallel plate configuration. One of these electrodes consists of the substrate which is intended to be covered with a thin film. The other one is called target and is made of the desired thin film material. Both electrodes are inside a vacuum chamber, containing the sputter gas. The pressure inside the vacuum chamber typically ranges between 10^{-1} to 10^{-3} mbar. The applied potential difference causes the ionization of sputter gas atoms and eventually a steady state current between target and substrate builds up. The whole situation is depicted in Figure 15. The target is at negative and the substrate at positive potential.

Electrons are directed towards the substrate while plasma ions move towards the target. When a plasma ion hits the target, its momentum is transferred to the target atoms. A collision sequence is initiated in the target, where energy is dissipated into the target at each step of the sequence. When the direction of the momentum is inversed and the transferred energy during collision is still higher than the binding energy of the atoms in the target, then an atom leaves the target surface (green particle). These so called neutral deposits collide with plasma ions in the vacuum chamber as well as with other neutral deposits. Their direction of momentum shows a cosine shaped angular distribution. Therefore sputter deposition is even a useful method, when the substrate topography not flat and smooth. This results in an overall enhanced coverage characteristics of e.g. edges from patterned structures of previous mask steps with a thin film compared to other methods (for example thermal evaporation), where the neutral deposits show a narrow angular distribution of momentum.

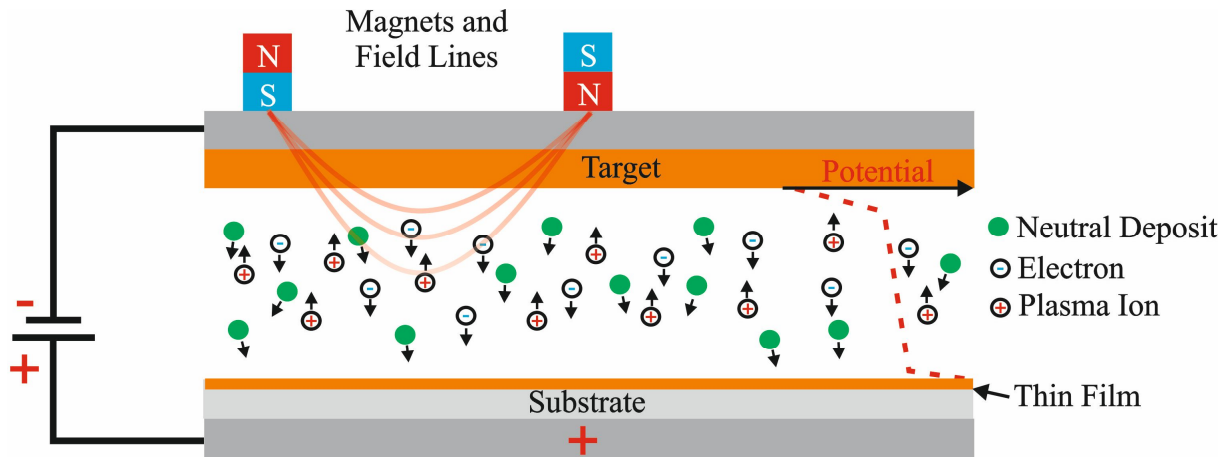


Figure 15: Schematic depiction of magnetron DC sputtering.

Figure 15 also shows the trend of the electric potential between substrate and target. Most of the potential drop occurs near these electrodes, because a net charge builds up at their vicinities. Around the target there is a net positive charge. Electrons are ejected from the target and gain kinetic energy with increasing distance until they are capable of ionizing the sputter gas atoms. Consequently free electrons and positively charged plasma ions are generated. Because of their mass difference electrons are accelerated faster away from the substrate than plasma ions can move towards it. When moving even further away from the target, more and more electrons are generated. Thus the energy of a single electron decreases and no further ionization takes place. This means that the positive ions that are responsible for knocking out the atoms from the target are created in the vicinity of the target.

Similarly there is a region of negative net charge surrounding the substrate because plasma ions are repelled by the applied negative potential while electrons are attracted. In the middle between the two regions of potential drop, there is an electrically almost neutral region with equal amount of positive ions and electrons, providing a high conductivity for electrical current [67].

The fact that most of the plasma ions are generated near the target is already convenient for a high material ablation per time (sputtering rate). A method to further increase the sputtering rate is by positioning magnets on top of the target (see Figure 15). The Lorentz force guides the electrons in circular paths around the field lines. This increases the retention time of the electrons and in turn also increases the ionization rate of neutral sputtering gas atoms. Consequently the sputtering rate is increased. This effect is mostly pronounced where the field lines are parallel to the target because the Lorentz' force magnitude has its highest value there.

Also, reactive gases can be admixed to the sputter gas. When the ionized sputter gas atoms react with the neutral deposit particles, compound materials are synthesized on the substrate. This method is called reactive sputter deposition [68].

In this thesis a LS730S Von Ardenne sputter deposition equipment was used. In addition to sputter deposition also sputter cleaning of samples was performed. Therefore the sample (substrate) was on negative potential; thus the ionized sputter gas atoms were used for cleaning. In this cleaning procedure, Argon served as sputter gas and the pressure inside the chamber was adjusted to 6 μ bar. The plasma power and the cleaning were different throughout the performed experiments and are reported at the corresponding results.

Also sputter deposition was done throughout this thesis. Platinum was sputter deposited at nominally unheated substrate conditions at a plasma power of 150 W, a sputter gas pressure of 3 μ bar and a sputter gas flow (Argon) of 60 sccm. The distance between the target and the substrate was 75 mm, while the sputter rate was 1 nm/s.

Furthermore titanium nitride was sputter deposited at again at nominally unheated substrate conditions at a sputter rate of 0.5 nm/s. The plasma power was 500 W, the sputter gas (nitrogen) pressure was 8 μ bar and the nitrogen flow was 60 sccm. The distance between the target and the substrate was 75 mm.

3.3 Chemical vapor deposition

Chemical vapor deposition (CVD) is a method which is capable of producing thin films on a given substrate. The principle is to initiate a chemical reaction at a gaseous-solid interface by providing the necessary energy for the chemical reaction. This can be done by local heating of a given substrate; optionally the ionization of gas particles by applying an external voltage (compare with section 3.2) can reduce the necessary temperature.

Figure 16 shows a schematic illustration of a plasma enhanced (PE) CVD equipment used for the deposition of amorphous silicon carbide thin films in this thesis. The reactant gases silane SiH_4 and methane CH_4 are provided through a gas inlet. The substrate is heated and thus deposition of SiC takes place according to Equation [3-3]. Gaseous silane and methane react to solid silicon carbide (SiC) containing due to the low deposition temperatures a high amount of hydrogen both in atomic and molecular form.

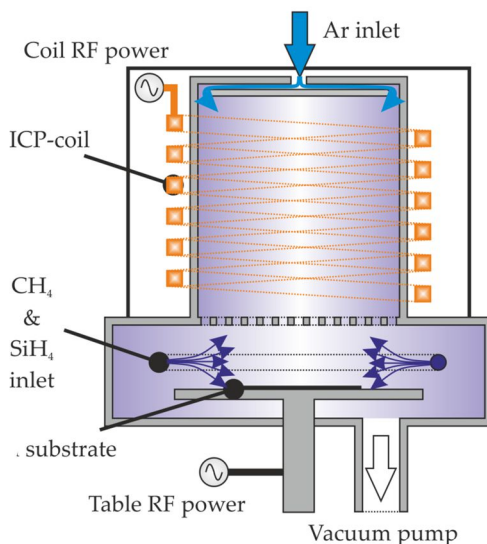
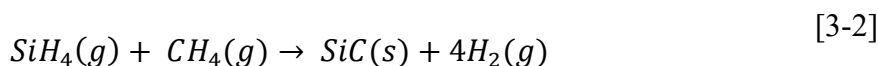


Figure 16: Schematic illustration of the used plasma enhanced chemical vapor deposition (PECVD) equipment. Taken from [69].



In the described system in Figure 16, the carrier gas and consequently also the reactant gases are ionized with an inductively coupled plasma (ICP) coil. This increases the reactivity of the educt molecules and thus the necessary temperature for thin film deposition is lowered. In addition, the educt molecules can also be influenced by the table RF power, further lowering the activation energy of the deposition reaction. During a PECVD process a vacuum pump steadily removes the reaction products, maintaining a steady state condition throughout thin film deposition [69].

Such PECVD processes lead to amorphous thin films. This is because of the comparably low substrate temperature in relation to other deposition techniques and of the high reactivity of the educt molecules. When they arrive at the substrate they immediately react, which favors high entropy in the deposited thin film. When poly- or even single-crystalline thin films need to be deposited, higher substrate temperatures are used. Furthermore the pressure inside the chamber is reduced. This gives educt molecules that adsorb at the substrate the necessary surface mobility to diffuse to thermodynamically favorable locations. Altogether this enhances the crystallinity in the deposited thin film. This method is called low pressure (LP) CVD [70].

In this thesis PECVD and LPCVD processes were used for the deposition of silicon carbide. Both were operated with silane and methane as reactive gases.

Amorphous, hydrogenated SiC (a-SiC:H) thin films were obtained by utilizing a PECVD Oxford Instruments PlasmaLab 100 ICP-CVD reactor. The reactive gas flow ratio of methane was 0.675 at a total reactant flow of 20 sccm, the ICP coil power was set to 2000 W, no RF table

power was applied and the substrate temperature was set to 250°C. Finally, the chamber back pressure was regulated to 8 μ bar at an argon flow rate of 50 sccm additionally to the reactant gases. The resulting deposition rate was 13.6 nm/min.

Polycrystalline SiC films were deposited with a hot wall LPCVD furnace from FirstNano. The SiC films were deposited at 1050 °C using gas flows of 1 sccm silane, 60 sccm methane and 500 sccm hydrogen as background gas.

3.4 Scanning electron microscopy

A scanning electron microscope (SEM) utilizes electrons instead of light for the generation of magnified images [71]. Figure 17 shows schematically the optics for the electrons, which is operated in high vacuum. First electrons with a kinetic energy in the keV range are generated in an electron gun. The electrons are emitted from a heated material such as lanthanum hexaboride LaB_6 , or from a sharp tungsten tip and afterwards accelerated in an electric field. In the latter approach no heat is applied. To enable electrons to tunnel out of the material a small tip having a diameter less than 100 nm is used. In contrast to a tipless configuration a lower electric field strength is needed for tunneling, as the effective work function barrier is decreased more effectively by the local concentration of the electric field [72].

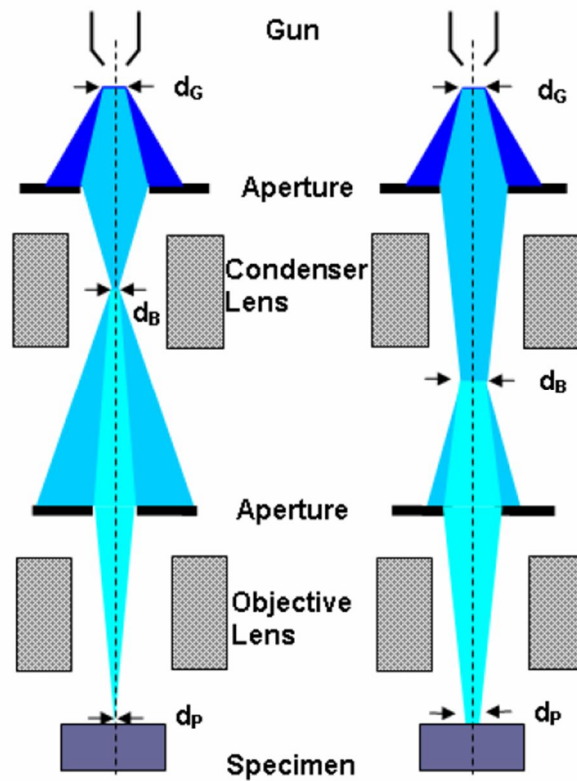


Figure 17: Schematic depiction of a scanning electron microscope. A low beam diameter d_B (left image) is compared with a high beam diameter (right image). Taken from [71].

The emitted electrons then pass an aperture where part of them are blocked in front of the condenser lens. The condenser lens usually consists of a coil of copper wires inside an iron pole piece. When an electric current is sent through the copper wires a magnetic field is created which deflects the trajectory of incoming electrons. The higher the current the smaller is the resulting spot size d_B . After passing a second aperture, the objective lens focusses the electron beam onto the sample. The objective lens is usually also a magnetic lens. The final spot size on the sample d_p is adjusted with the condenser lens.

When the electron beam interacts with the specimen, several signals are created (see Figure 18). Auger electrons are emitted from a depth of several nanometers, while secondary electrons have an escape depth between approximately 5-50 nm. Therefore the secondary electrons (SE) just have a kinetic energy of less than 50 eV, which is much lower than the incident electron beam's electrons [71]. Due to their distinct energy range the intensity of the generated SE can be detected very precisely. Since the intensity depends on the topography of the sample (i.e. edges show a higher SE intensity and areas that are averted to the detector show a lower SE intensity), a projection of the specimen can be created by moving the electron beam along the surface in a virtual raster. Every point on that raster creates a detector signal with a surface topography dependent intensity. This is called topography contrast.

Back scattered electrons can escape from a depth a hundred times greater than the SE and from an even greater depth, characteristic X-rays leave the specimen. The intensity of the backscattered electrons depends on the atomic number of the material. In this case an image can be formed due to material contrast, by moving the electron beam along the sample surface.

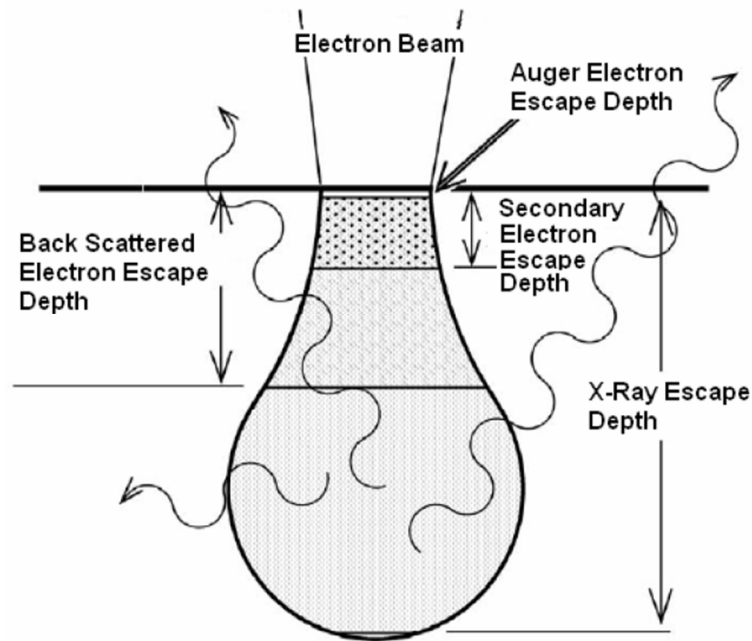


Figure 18: Electron beam – specimen interactions. Taken from [71].

Finally in scanning electron microscopy the magnification is given by the ratio of the area of the obtained image and the area of the scanned region on the sample. Magnifications up to 800000:1 can be achieved with SEM. At such high magnifications the spot size of the electron beam is in the dimension of 1 nm. The quality of the resulting image is determined by both, the magnification and the achievable contrast [71].

In this thesis a Hitachi SU8030 scanning electron microscopy was used, with acceleration voltages ranging between 1 and 5 kV.

3.5 Image analysis

The degree of porosity and the pore size distribution of the SEM micrographs was estimated with image processing methods. Therefore adaptive Gaussian image thresholding was utilized [73,74]. In common image thresholding an 8 bit grey-scale image is converted into a black and white image. Pixels above a defined value are converted into black (value 255) and the other pixels are converted into white (value 0). In adaptive Gaussian image thresholding the weighted average of a pixel's surrounding is calculated with a Gaussian window function. The thresholding value which determines the pixel to be converted to black or white is determined by subtraction of a constant value from the weighted average. Adaptive image thresholding has the advantage over common image thresholding that changing background illumination does not affect the result. In the particular case of investigating SEM micrographs, contaminations are a common problem in image thresholding [71]. This is illustrated in Figure 19. The SEM micrograph on the left side shows a varying value of the grayscale due to surface contaminants. These artefacts do not appear in the black and white image due to the weighting in adaptive image thresholding.

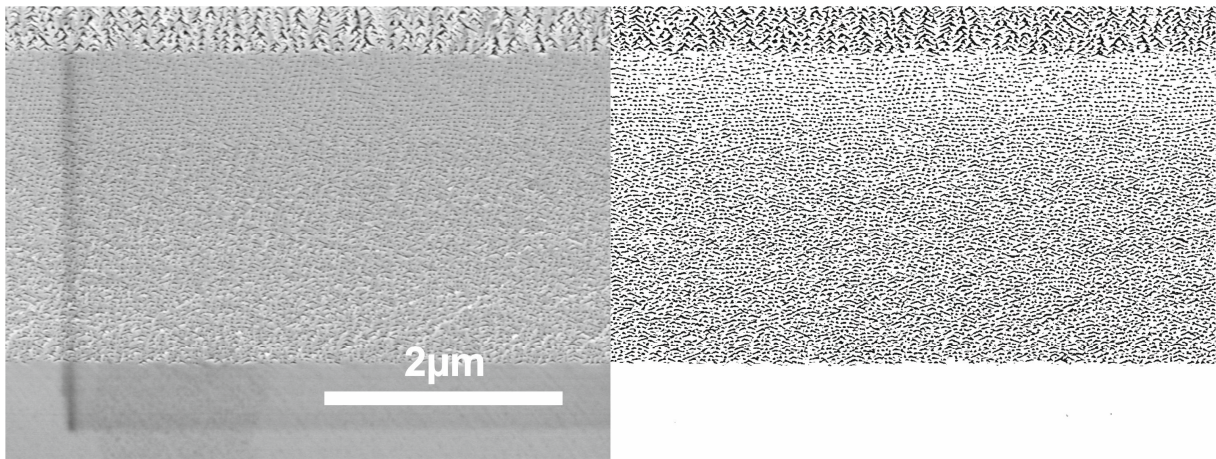


Figure 19: Cross-sectional SEM micrograph of a porous SiC sample and the corresponding black and white image, obtained from adaptive Gaussian image thresholding.

The obtained black and white images can be used to estimate the resulting degree of porosity as well as the pore size distribution. The former is simply given by the ratio of black and white pixels in a row and the pore size can be evaluated from the amount of pixels contributing to a black cluster. The physical length l_{pixel} of a pixel on the black and white image is given by Equation [3-3]. dpi_{image} is the dpi-value of the black and white image and M is the length of an object in the SEM micrograph divided by its real physical length. The constant in the numerator is due to the conversion from inch to microns.

$$l_{pixel} = \frac{2.54 \cdot 10^4 \mu m}{dpi_{image} \cdot M} \quad [3-3]$$

To analyze the SEM micrographs, a program was written in the Python programming language [73]. With the obtained information from image analysis, the degree of porosity as a function of depth as well as the pore size distribution were evaluated.

3.6 Infrared spectroscopy

In infrared (IR) spectroscopy the interaction of matter with infrared radiation is utilized for chemical analysis. The IR radiation can induce molecular and crystal lattice vibrations in a material, provided that there is a permanent or induced dipole moment [75].

In classical chemical analysis molecules are studied with IR spectroscopy to determine their structure. In the simplest case such a molecule consists of two atoms. The oscillation can be approximated by the quantum mechanical harmonic oscillator. Its discrete energy values are given by Equation [3-4]

$$E_n = \hbar\omega \left(n + \frac{1}{2} \right) \quad [3-4]$$

where \hbar is the reduced Planck's constant and ω the angular frequency of the harmonic oscillator. The quantum number is given by n and can only take on positive integer values including zero. Since the allowed energy values are discrete, energy can just be absorbed in discrete values, given by the difference of two allowed energy states. This means that the absorbed IR radiation can only have certain frequencies ν_{abs} according to Equation [3-5].

$$\nu_{abs} = \frac{1}{2\pi} \sqrt{\frac{k}{\mu}} \quad [3-5]$$

Here k is the spring constant and μ is the reduced mass. The spring constant describes the strength of the chemical bond, while μ is given by Equation [3-6], with m_1 and m_2 being the masses of the molecule's atoms.

$$\mu = \frac{m_1 m_2}{m_1 + m_2} \quad [3-6]$$

In summary, the frequency of the absorbed IR radiation depends on the bond strength and the masses of the atoms that oscillate. This is also true for more complex oscillations. In crystals, such as single crystalline 4H-SiC, vibrations can also be induced by IR radiation. Such collective lattice oscillations are called phonons [28,76].

In this thesis two different kinds of IR spectroscopy modes are utilized: Transmission mode and attenuated total reflection (ATR) mode. In former the amount of light that is transmitted through the sample is measured (see Figure 20a). The sample is irradiated with IR light having the intensity I_0 . The sample absorbs some of the IR radiation and the decreased light intensity I is measured by a detector. In ATR-IR radiation is guided through a crystal with high refractive index, such that at its edges total reflection takes place (see Figure 20b). Despite total reflection, the amplitude of the electric field does not abruptly decay to zero at the interface, but shows an exponential decrease. This is called an evanescent field. When this takes place several times and there is a sample at the interface, IR radiation is considerably absorbed by the sample. The penetration depth of this evanescent field is in the range of a fifth of the wavelength of the incident light. So the ATR method is more surface sensitive than transmission IR [75].

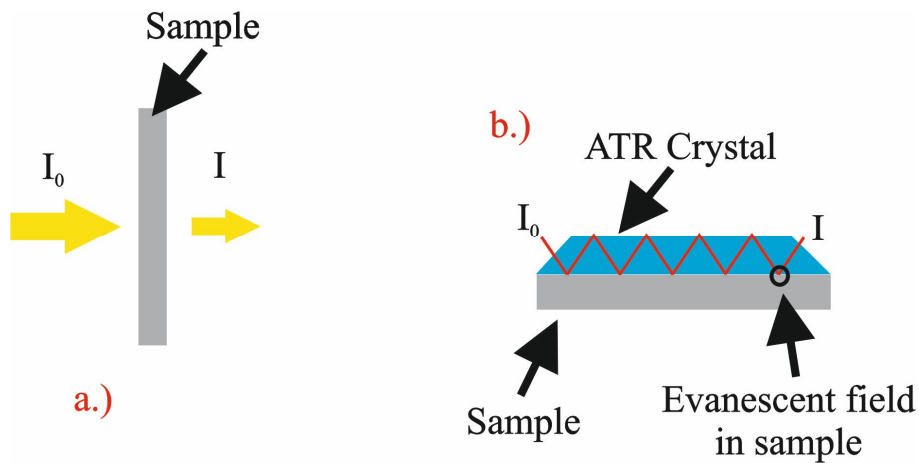


Figure 20: Modes of IR spectroscopy: a.) Transmission IR, b.) ATR-IR

In both approaches the Fourier transform technique was used for data analysis (see Figure 21). First, IR light hits a beam splitter. One beam is reflected back at a fixed mirror, whereas the second beam is reflected back at a moving mirror. The movement of one mirror introduces an optical path difference when the two beams are combined at the beam splitter again. This optical path difference causes positive and destructive interference in the light arriving at the detector.

When monochromatic light is used, the detector records a sinusoidally varying signal as a function of the moving mirror's position or time. When a polychromatic light source is used, the signal recorded at the detector contains the sum of all sinusoids corresponding to the different wavelengths of the polychromatic light. This recorded signal as a function of time is called the interferogram [75].

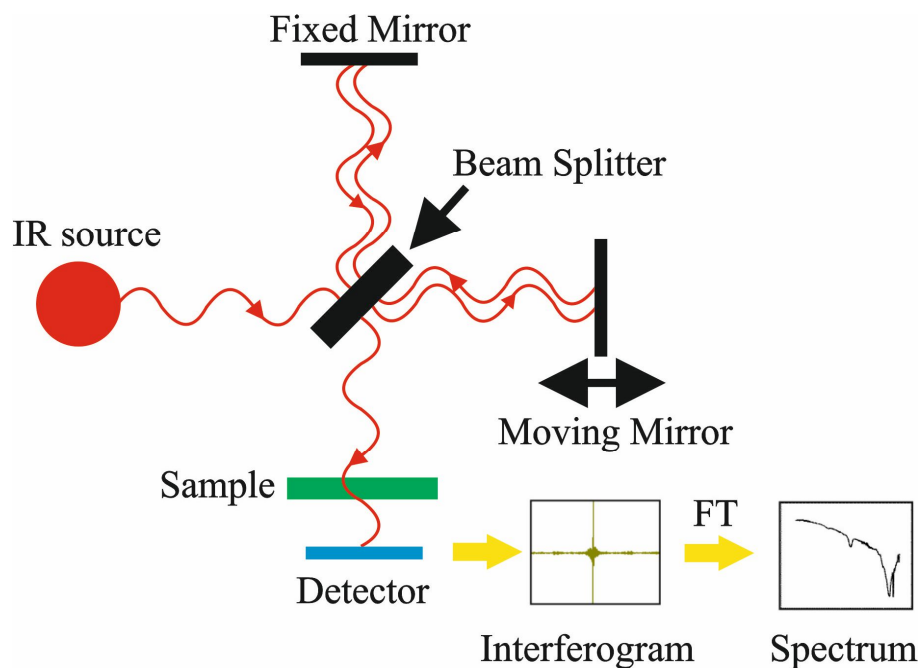


Figure 21: Principle of Fourier transform (FT) IR spectroscopy.

A sample, which can absorb IR radiation at specific wavelengths, in the optical path causes the decrease of the corresponding sinusoids in the interferogram. By applying a Fourier transform (FT) to the interferogram, the transmission T of the sample as a function of frequency is calculated.

The transmission is defined as the ratio between the intensity that is transmitted through the sample I and the initial intensity I_0 used for irradiation. Both quantities need to be defined at the same wavelength λ .

$$T(\lambda) = \frac{I(\lambda)}{I_0(\lambda)} \quad [3-7]$$

Often the absorption $A(\omega)$ is used instead of the transmission. It can be calculated according to Equation [3-8]. Often the absorption is plotted as a function of the wavenumber, which is the inverse of the wavelength.

$$A(\lambda) = -\log(T(\lambda))$$

[3-8]

In this thesis two different Bruker Tensor FT-IR spectrometer were used. One contained an ATR assembly utilizing a diamond crystal as the high refractive index material. The other IR spectrometer allowed measurements in transmission mode.

3.7 Secondary ion mass spectrometry

Secondary ion mass spectrometry (SIMS) is an analytical method that allows to determine the elemental composition of a given sample [77]. In contrast to other methods all elements of the periodic table, including hydrogen, can be detected. SIMS requires, like SEM a high vacuum atmosphere to exclude any impact of impurities with the analytes.

To do so an ion beam is focused onto the sample utilizing a so called primary ion gun. The impact of these primary ions causes a collision cascade in the sample and secondary particles leave the sample. Some of them are ionized, the so called secondary ions.

They can be categorized with a time of flight (ToF) detector according to Equation [3-9].

$$\frac{m}{q} = \frac{2Vt^2}{L^2} \quad [3-9]$$

In such a detector the secondary ions are accelerated in a potential difference V along a given distance L ; the detector length. The mass to charge ratio of a secondary ion $\frac{m}{q}$ is proportional to the time of flight t needed to cover the detector length.

A higher mass to charge ratio means longer time of flight, hence the secondary ions can be categorized by their mass to charge ratio.

In addition to the primary ion gun, a secondary ion gun is utilized for sputtering. This allows the removal of the upper atom layers of the sample and thus depth profiling of the sample can be performed. The primary and secondary ion gun therefore are used in alternating mode. The total time of both ion guns being active is called a cycle.

Furthermore, the sample shows charging effects upon the generation of secondary ions, with increasing electrical resistivity. To counterbalance this charging an electron gun is used to maintain charge balance during the measurement [77].

In this thesis ToF SIMS depth profiles were acquired using a TOF-SIMS 5 (IonTof GmbH, Münster, Germany). A 25 keV Bi^+ primary ion beam was used for analysis (high current bunched mode [78]). For sputtering a 2 keV Cs^+ beam was used. The analysis area was set to 50

x 50 μm with a pixel resolution of 128 x 128 and the crater size to 400 x 400 μm . The measurements were carried out in negative ion mode using the interlaced mode with a cycle time of 100 μs . Low energy electron flooding (21 V) was applied.

3.8 Thin film reflectance

A thin film in the μm dimension shows interference phenomena when it is illuminated with light. To illustrate this behavior, at first the superposition of two electromagnetic waves in vacuum is considered [79]. The resulting intensity I_{sum} is given by Equation [3-10].

$$I_{sum} = I_1 + I_2 + \epsilon_0 c E_1 E_2 \cos(\delta) \quad [3-10]$$

The intensities of the two electromagnetic waves are given by I_1 and I_2 , ϵ_0 is the permittivity of free space, c the speed of light and E_1 and E_2 are the electric field amplitudes of the electromagnetic waves.

The delta term δ represents the total phase difference of the two electromagnetic waves and is given by Equation [3-11], with λ being the wavelength at which the intensity is considered.

$$\delta = \frac{2\pi}{\lambda} (\Delta_{path} + \Delta_{phase}) \quad [3-11]$$

The total phase difference has two contributions, namely the path difference Δ_{path} and the phase difference Δ_{phase} . In the case of a thin film on a substrate, the former is given by Equation [3-12], when the angle of incidence is zero. Here n is the refractive index of the thin film and d is its thickness.

$$\Delta_{path} = 2nd \quad [3-12]$$

The phase difference Δ_{phase} arises from the boundary between the thin film and the substrate. When the refractive index of the substrate is higher than that of the thin film a phase shift of 90° takes place. If this is the case then $\Delta_{phase} = \frac{\lambda}{2}$ or zero otherwise.

Figure 22a shows a measurement of the reflection from a porous SiC thin film prepared during this thesis, as a function of wavelength. The intensity shows the behavior discussed above. It varies between minima and maxima as it is predicted from Equation [3-10] and [3-11]. The effect of this thin film reflection is further illustrated in Figure 22b. Light that hits the porous layer—having uniform refractive index n and a thickness d —is reflected at the porous layer/substrate interface. The back reflected light interferes with the reflected light at the thin film/air interface, causing minima and maxima in the reflectance due to the introduced optical path difference. However, the intensity of the reflectance does not go down to zero or up to hundred

percent. This is because the back reflected light from the thin film/substrate interface has a lower amplitude according to Fresnel's equations. Furthermore multiple reflections have not been considered in this straightforward explanation, which also slightly alters the reflection properties. An exhaustive discussion of this topic can be found in [58].

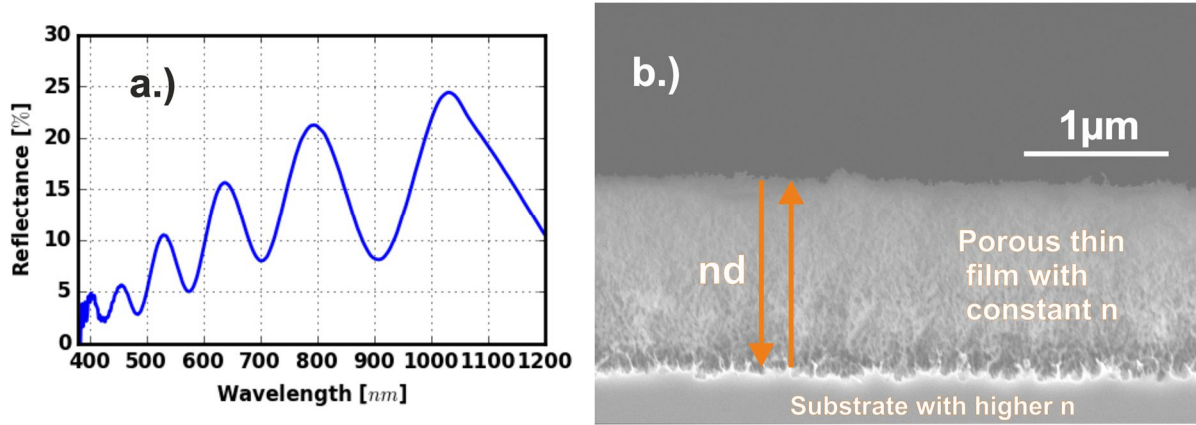


Figure 22: Thin film reflection. a.) Measured reflection from a porous thin film. b.) Porous thin film.

In this thesis a Filmetrics F20-UVX spectral reflectometer was used. The angle of light incidence was 90° during every measurement and a silicon wafer was used as reference material with known reflectance.

3.9 Additional equipment and measurement techniques

In this section devices and experimental details are introduced which are not discussed in detail.

3.9.1 Electrical characterization

For electrical characterization the Agilent B2911A Precision Source/Measure Unit was used. An array of circular Pt/TiN/Pt tri-layered pads was sputter deposited onto 1 cm^2 square samples. The diameter of the pads was 1 mm and the distance between them was 1 mm. The thickness of the Pt and TiN films at the top and bottom was 300 nm and 150 nm, respectively. Current voltage characteristics between adjacent pads were recorded.

3.9.2 Photometric measurement

In this thesis the absorption of solutions containing $\text{Na}_2\text{S}_2\text{O}_8$ was measured. For these photometric measurements a UV-1800 spectrophotometer from Shimadzu was used.

3.9.3 White light interferometry

For measuring the deflection of a buckling membrane a Polytec MSA-400 white light interferometer operated in in phase-shift mode was used.

3.9.4 UV light power measurement

For measuring the UV light power density a UV-Meter from Kühnast Strahlungstechnik was used with a sensor responding to wavelengths ranging from 315 to 400 nm.

3.9.5 Redox potential measurement

The redox potentials were recorded using a Pt wire that touched the sputter deposited Pt on the samples. This served as sensing electrode. As reference a mercury/mercurous-sulfate electrode filled with saturated K_2SO_4 was used. The redox potentials were measured under room light conditions if not stated otherwise.

4 Fundamental investigations on MAPCE and PECE

In this section the current problems of electrochemical porous SiC fabrication are addressed. First, the unreliability of MAPCE is discussed and overcome in the sub-chapter 4.1. Then, in 4.2 the origin of the inhomogeneous porosity/depth profiles usually obtained from PECE are revealed. Finally the detailed mechanisms of MAPCE and PECE are investigated.

4.1 Role of the metal semiconductor junction during MAPCE

Parts of this section have been published in [80].

In this section the reliability of MAPCE is addressed. In the current state of the art, neither controlling the etching depth nor the porosification of substrates with different bulk resistivities has been achieved (see section 2.3 for details). Moreover, MAPCE is not reliable, meaning that it is not ensured at the beginning whether an experiment will show the predicted behavior. Therefore, experiments were conducted in analogy to Rittenhouse *et al.* and successively modified [48].

As substrates, n-type 4H-SiC wafers with low and high resistivity (i.e. $\rho = 0.02 \text{ } \Omega \cdot \text{cm}$ and $\rho = 0.106 \text{ } \Omega \cdot \text{cm}$) were purchased from CREE. Square samples of these substrates with an area of 1 cm^2 were used for experiments. Then, a 300 nm thin Pt layer was sputter deposited on the samples while a $0.7 \times 0.7 \text{ cm}^2$ square silicon piece in the center of the sample served as shadow mask. Prior to Pt deposition, the samples were cleaned *in situ* using an inverse sputter etching procedure with Argon plasma for 60 s at 1000 W. Finally the samples were placed in an etching solution containing 0.04 mol/L $\text{Na}_2\text{S}_2\text{O}_8$ and 1.31 mol/L HF for 2 hours under UV irradiation, utilizing the etching chamber from AMMT GmbH (see section 3.1 for details). All etching experiments in this section were performed on the Si-face.

The first samples obtained from pure MAPCE experiments showed non-uniform etching characteristics. The samples having lower resistivity showed etching depths ranging from 0.5 μm to just surface roughening, even on the same area. The samples having higher resistivity showed mostly surface roughening; local parts with etching depths up to 1.3 μm could be observed, featuring a sharp border to the not porous regions. Both samples were etched in the regions not covered with Pt unlike metal assisted etching of Si where etching is mainly enhanced underneath a noble metal catalyst deposited at the surface. For etching to occur, oxidation and reduction reactions are necessary. This means that electrons need to flow from the anode (i.e. 4H-SiC) to the cathode (i.e. Pt). Because the electrical current has to pass the Pt/4H-SiC interface, a low contact resistance should increase the etch rate and the uniformity of the

porous layers. Annealing metal layers deposited on silicon carbide is a standard approach to form low ohmic contacts [81,82].

The MAPCE experiment was carried out again with the difference that after Pt deposition the samples were annealed for 5 minutes under Argon flow of 40 L/h at 1100°C with a prior temperature ramp starting at 800°C that lasted for 30 minutes. After 2 hours of MAPCE a porous layer with a more uniform depth of $(1.11 \pm 0.14) \mu\text{m}$ was observed at the samples with a resistivity of $\rho = 0.02 \Omega \cdot \text{cm}$. A top down and cross-sectional view of the obtained porous structure are shown in Figure 23, demonstrating that a porous layer has formed. Figure 24a shows the current voltage characteristics recorded across two contact pads of a sample having a resistivity of $\rho = 0.02 \Omega \cdot \text{cm}$ before and after annealing. The pads used for the measurements consisted of Pt/TiN/Pt layers, because partial dewetting of pure Pt pads took place during high temperature annealing under argon flow, which lead to unreproducible results in electrical characterization. Due to the high melting point and chemical inertness of TiN, dewetting was prevented. It demonstrates that the contact resistance at the Pt/4H-SiC junction had decreased due to the annealing, thus enhancing the formation of a porous layer during MAPCE process.

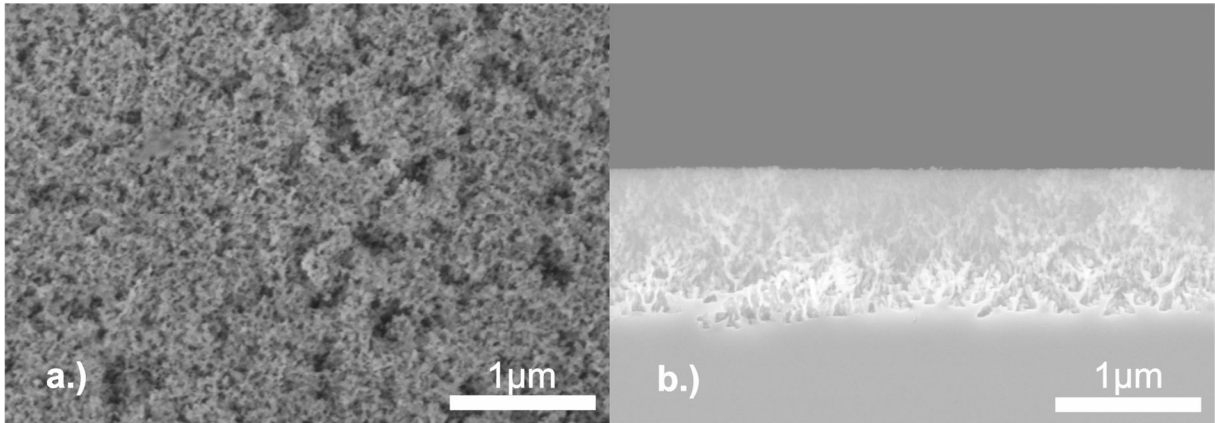


Figure 23: SEM micrographs of an n-type 4H-SiC ($\rho = 0.02 \Omega \cdot \text{cm}$) sample after MAPCE. a.) top down view b.) cross-sectional view.

The same experiments were not successful when using the samples with higher bulk resistivity of $\rho = 0.106 \Omega \cdot \text{cm}$. This means that just surface roughening or occasional formation of a thin porous layer was observed. At higher resistivity and thus lower dopant concentration the contact resistance is increased at the metal/semiconductor junction. This explains why for the samples with higher resistivity no reproducible porous layer formation was observed even when the samples were annealed. To decrease the contact resistance further, a sample with $\rho = 0.106 \Omega \cdot \text{cm}$ was doped with phosphorous surface-near according to a method developed by Mendis *et al.* [83]. Therefore, 0.1 mL of a solution consisting of 50 mL absolute ethanol and 20 mL phosphoric acid (85%) were placed on the sample surface. Next, the sample was annealed in air at 650°C for 30 minutes and in a second step in air at 1100°C for 2 hours. Finally, the sample

was cleaned in buffered oxide etch to remove oxidation products, Pt was sputter deposited and annealed like in the previous experiments. These samples showed the formation of a porous layer with uniform depth of $(0.78 \pm 0.07) \mu\text{m}$ homogeneously across the sample after 2 hours of MAPCE. A top down and a cross-sectional micrograph of the obtained porous layer are shown in Figure 25. Due to the increased dopant concentration near the surface, the resistance at the Pt/4H-SiC contact decreased substantially, thus enabling the MAPCE process. This is verified by current voltage measurements between two pads of differently processed samples (see Figure 24b), demonstrating the expected impact of annealing and additional doping on contact resistance.

It has to be noted that the aim was to increase the electron flow across the Pt/4H-SiC junction by annealing. It was not necessary to verify whether ohmic or Schottky type contacts were achieved. So one Pt/4H-SiC junction may always be operated in reverse direction during measurements. This means that the measured current characteristics give a qualitative proof that a lowered contact resistance increases the etching rate in MAPCE but the absolute current values of samples with different initial dopant concentration cannot be compared directly among each other

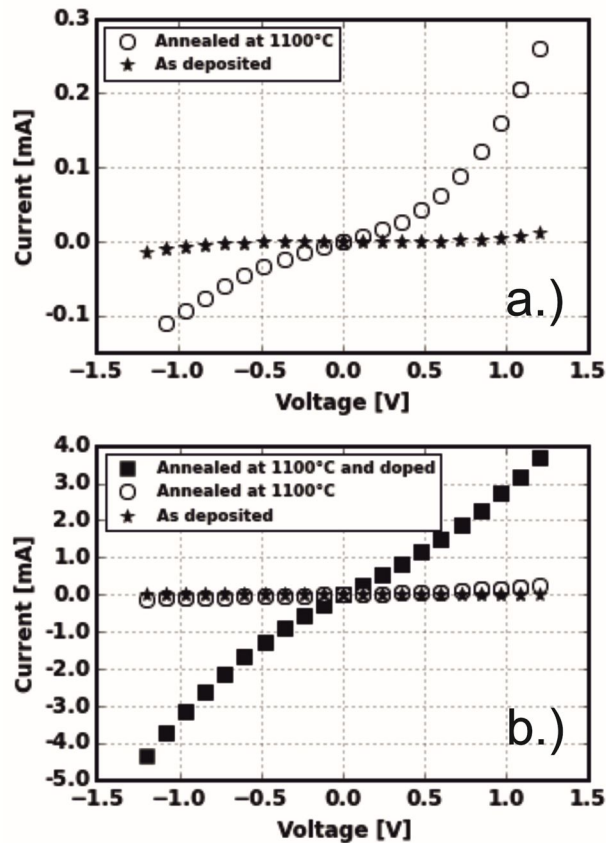


Figure 24: Current-voltage characteristics recorded between two adjacent circular pads of Pt/TiN/Pt stacked tri-layers on n-type 4H-SiC before and after annealing. a.) Sample with a resistivity of $\rho = 0.02 \Omega\text{-cm}$. b.) Sample with a resistivity of $\rho = 0.106 \Omega\text{-cm}$ including an additional measurement showing the current-voltage characteristics after surface near phosphorous doping.

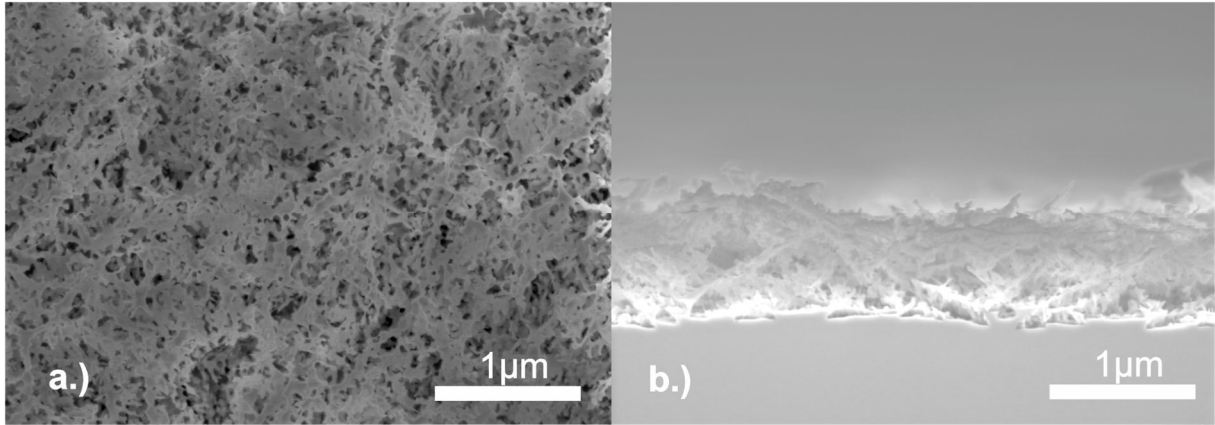


Figure 25: SEM micrographs of an n-type 4H-SiC ($\rho = 0.106 \Omega\cdot\text{cm}$) sample after MAPCE. a.) top down view b.) cross-sectional view.

The observed etching depth for the surface near doped sample with $\rho = 0.106 \Omega\cdot\text{cm}$ is large compared to the reported diffusion depth of phosphorous atoms in SiC of about $0.1 \mu\text{m}$ during annealing [84]. This means that not additionally doped 4H-SiC was also etched. These observations show that there are three interfaces of interest in Pt assisted photochemical etching of 4H-SiC which determine the performance of the etching process. One is the Pt/4H-SiC junction for which a low contact resistance is needed. Next, persulphate is reduced at the Pt/etching solution interface. Lastly, in the space charge region of the 4H-SiC/etching solution interface holes are generated and injected into the valence band of 4H-SiC by UV light which are needed to increase the etching rate.

In this section the metal assisted photochemical etching (MAPCE) of n-type 4H-SiC in a solution of $\text{HF}/\text{Na}_2\text{S}_2\text{O}_8$ with Pt as catalytic metal was investigated. It was shown that the Pt/4H-SiC interface plays a crucial role in this process. Decreasing the contact resistance at the Pt/4H-SiC junction by annealing the samples was sufficient to allow photochemical etching of specimens with low bulk resistivity, while additional surface near doping with phosphorous was mandatory for samples having high resistivity to enable the porosification process. Furthermore, UV light illumination is necessary to generate electron-hole pairs in the space charge layer of the etching solution/4H-SiC interface.

4.2 Porous SiC from PECE without skin and cap layer

Parts of this section have been published in [85].

In the last section the reliability of MAPCE could be enhanced and also 4H-SiC wafers with different bulk resistivity values could be porosified. In this section the attention is turned to PECE. As was pointed out in section 2.2, there is the problem of cap and skin layer formation

during PECE of SiC. This, in turn, causes the formation of an inhomogeneous profile of the porous SiC layer.

To address these problems a combination of MAPCE and PECE was utilized. The basic idea was that the pore tips generated first in the porous SiC layer by MAPCE could act as initiation sites for a subsequent PECE process. Therefore, prior to PECE MAPCE was performed as is illustrated schematically in Figure 26. The process flow was chosen according to the findings presented in section 4.1, with the experimental parameters being similar.

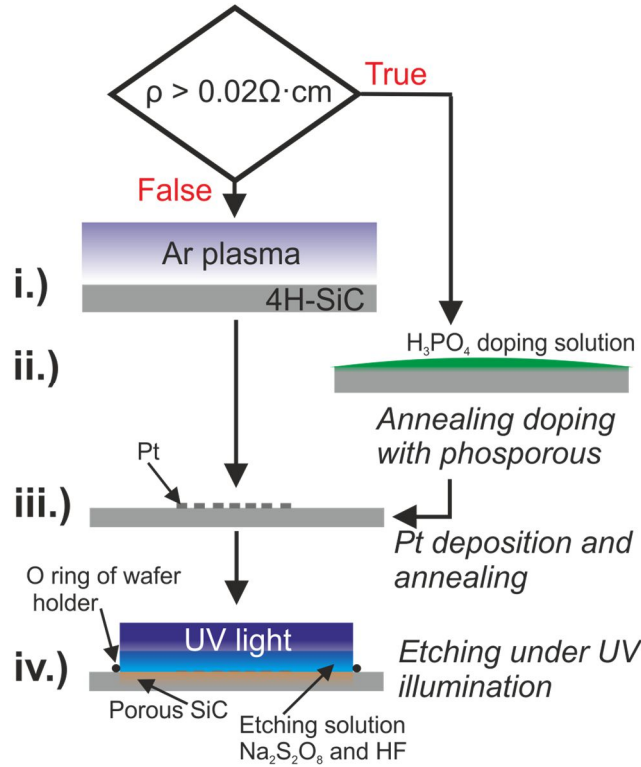


Figure 26: Process flow of metal assisted photochemical etching (MAPCE).

Samples with a bulk resistivity lower than $0.02 \Omega \cdot \text{cm}$ were cleaned with inverse sputter etching (step i). Afterwards MAPCE was performed as it is basically described in section 4.1. One difference was that Pt pads were sputter deposited in the middle of the sample (step iii). The total area of the Pt pads was 55 mm^2 . Moreover the sample size was $2.5 \times 2.5 \text{ cm}$. After annealing the samples were etched as described in 4.1 in the AMMT etching cell (step iv).

Samples with a higher resistivity than $0.02 \Omega \cdot \text{cm}$ were etched the same way, except phosphorous doping was done instead of sputter cleaning (step ii). The details of the doping process can be found in section 4.1.

For the PECE experiments in this section an aqueous solution containing 5.7 mol/L HF and 1.7 mol/L ethanol was used. If a different etching solution was used, the corresponding concentrations are stated alongside the experimental results. The theoretical details of PECE are presented in section 2.2 while the specific experimental parameters can be found in section 3.1.

4.2.1 Effect of a prior MAPCE step on PECE

4.2.1.1 Experiments on the Si-face of 4H-SiC

First, the influence on pore homogeneity is studied when MAPCE is applied prior to PECE. This was done because with MAPCE it is possible to generate highly porous layers on 4H-SiC samples up to a depth in the μm range. The pore tips from these layers act as initiation sites for subsequent PECE, leading to homogeneous porous SiC layers obtained from PECE. This effect is illustrated in an experiment with two samples having a bulk resistivity of $0.106 \Omega \cdot \text{cm}$ where the Si-face was etched. At one sample PECE was performed, while at the other sample first MAPCE and then PECE was performed.

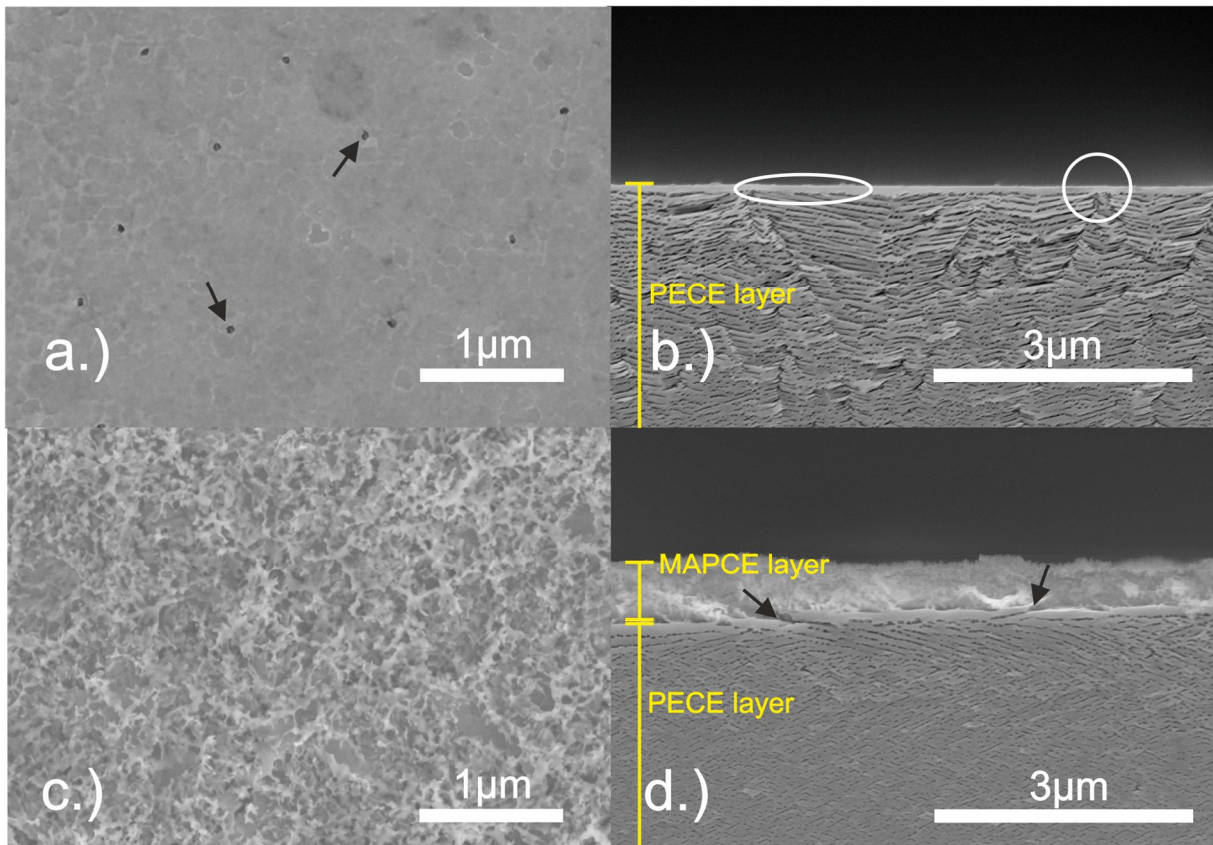


Figure 27: SEM micrographs 4H-SiC samples where the Si-face was etched. Sample resistivity of $0.106 \Omega \cdot \text{cm}$. a.) top down view after pure PECE b.) cross-sectional view after pure PECE c.) top down view after MAPCE and PECE d.) cross-sectional view after MAPCE and PECE.

Figure 27 shows in top down and in cross sectional views both samples after etching. One can see that the sample where only PECE was performed shows small singular pores at the surface (Figure 27a – black arrows). In the corresponding cross-sectional view (Figure 27b) a skin layer (white ellipse) at the very surface followed by an irregular porous structure is detected. The white circle indicates a surface pore that formed at the beginning of PECE. These features are not present when a MAPCE step was carried out prior to PECE. Figure 27c shows the top down view of the sample that was subjected to MAPCE and PECE, where a highly porous structure is generated by MAPCE. The corresponding cross-sectional view is given in Figure 27d. A highly porous top layer stemming from MAPCE is followed by the porous layer formed with PECE. It can be seen that the porous layer formed with PECE shows an increased regularity in the nano-sized pore formation when MAPCE is performed prior to PECE. Also no skin layer is observed.

This behavior is explained with the expected effect that the pore tips of the porous layer from MAPCE act as initiation sites for pore formation at the beginning of PECE (black arrows in Figure 27d). In particular, the pore initiation takes place at the concave-shaped pore edges of the dendritic porous MAPCE layer. This is due to an increased field strength at locations with high curvature, resulting in a higher dissolution rate [40]. Because of the provided initiation sites for MAPCE also the regularity of the PECE layer increased. The white circle in Figure 27b shows a branched porous structure originating at a surface pore when MAPCE is not done prior to PECE. Surface pores are starting points for porous layer formation at the beginning of PECE. A low amount of surface pores (“surface defects”) leads to an inhomogeneous porous layer because pore propagation takes place statistically in different directions. A MAPCE step performed prior to PECE increases the amount of initiation sites at the surface. Therefore the homogeneity of the porous layer increases [40].

Beside the increased regularity of the porous structure due to the MAPCE step prior to PECE, also the etching behavior is enhanced. This is illustrated in Figure 28. Both samples were etched in a current controlled mode with a current density of 22.3 mA/cm^2 . Without a MAPCE pre-treatment a region with the maximum possible voltage output of 36 V from the power source is present at the beginning. During this stage, which is attributed to skin layer formation, the current flow was very low until a strong voltage drop is detected. Furthermore without MAPCE the desired current density could not be maintained throughout the whole process. This was the case for voltage regions where the maximum voltage of 36 V was present. When MAPCE had been performed prior to PECE different current and voltage characteristics were obtained. A constant current density of 22.3 mA/cm^2 was observed from the very beginning of the PECE process and the voltage increased continuously with etching time. The continuously rising, but stable voltage evolution when the MAPCE assisted process is applied in advance is attributed

to the lack of a skin layer and the subsequent formation of a more regular porous structure during PECE.

If a skin layer is present it basically acts as a diffusion barrier throughout PECE. The out-diffusion of reaction products and the in-diffusion of reaction educts into the porous layer is hindered. This leads to an accumulation of reaction products and to a depletion of reaction educts in the porous layer. In general the necessary voltage for an electrochemical reaction increases with the concentration of the educts and decreases with the concentration of the products. When there is no skin layer present, diffusion in the porous layer is enhanced. Therefore the current density could be maintained for a longer time when MAPCE was performed prior to PECE. This finding is also of high interest when targeting the realization of porous SiC based chemical sensors. When diffusion in the porous layer is enhanced during its preparation, it is also enhanced in the final porous layer. This is regarded as a most desirable feature, especially when analytes have to come in contact with the increased surface provided by the porous layer.

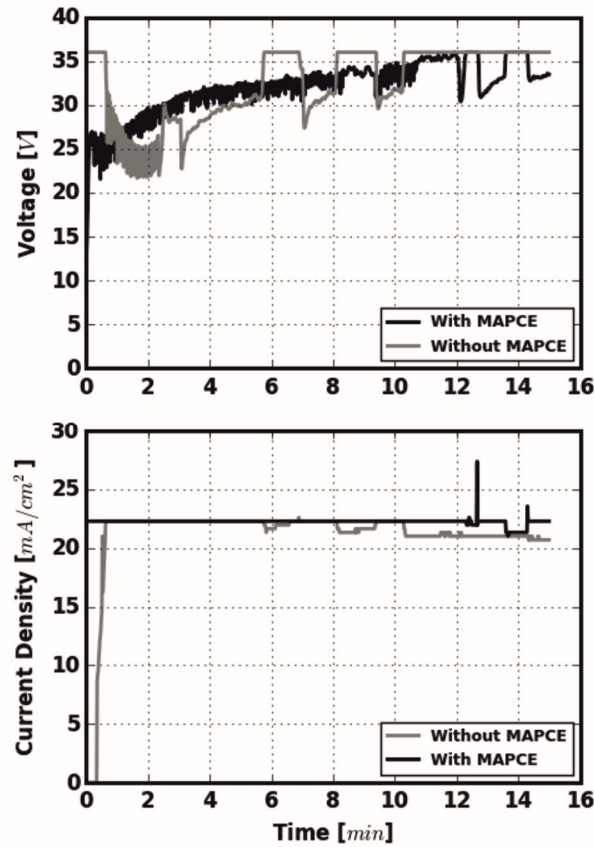


Figure 28: Voltage and current density characteristics during Si-face PECE of a 4H-SiC sample having a bulk resistivity of $0.106 \Omega\text{-cm}$ with and without MAPCE pre-treatment.

4.2.1.2 Influence of etching mode

So far it has been demonstrated that the porous layer formed with MAPCE provides initiation sites for PECE. The result is an enhanced etching behavior during PECE, which manifests in a porous layer with high uniformity. Next the influence of the etching conditions during PECE was studied. Therefore MAPCE was performed on samples with a bulk resistivity of $0.157 \Omega \cdot \text{cm}$. Afterwards, PECE was performed. One experiment was conducted in a current controlled mode, the other one in a voltage controlled mode. Additionally the influence of the bulk sample resistivity is discussed.

Figure 29 shows a cross sectional SEM micrograph of a sample with a resistivity of $0.157 \Omega \cdot \text{cm}$ which was treated with MAPCE and PECE. PECE was performed in a current controlled mode. It can be seen that the porous layer generated with MAPCE provided initiation sites for PECE (black arrows) like in the experiment with the sample having a resistivity of $0.106 \Omega \cdot \text{cm}$. The porous layer stemming from PECE shows a regular structure but the degree of porosity decreases significantly with depth. This is due to the high resistivity of the sample. Figure 30 shows the corresponding current and voltage characteristics during PECE. The experiment was performed in a current controlled mode with a desired current density of 51 mA/cm^2 . There is no region of very low current density (compare with Figure 28 – without MAPCE) at the beginning of PECE, due to the initiation sites provided by the highly porous layer from MAPCE. However, due to the high resistivity of the sample the desired current density could not be maintained throughout the experiment. Thus the degree of the porosity drops drastically with depth.

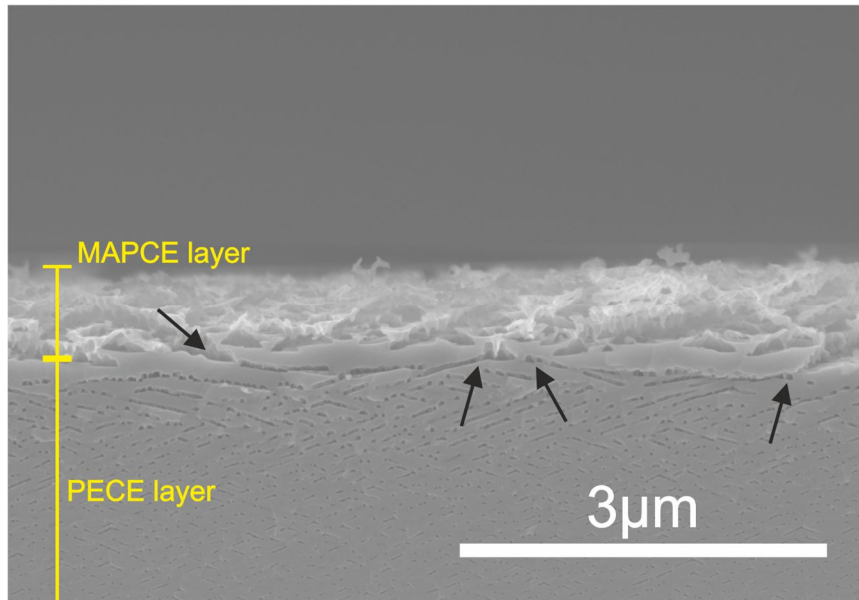


Figure 29: Cross-sectional view on a 4H-SiC sample with a bulk resistivity of $0.157 \Omega \cdot \text{cm}$ after MAPCE and PECE. PECE was performed in a current controlled mode.

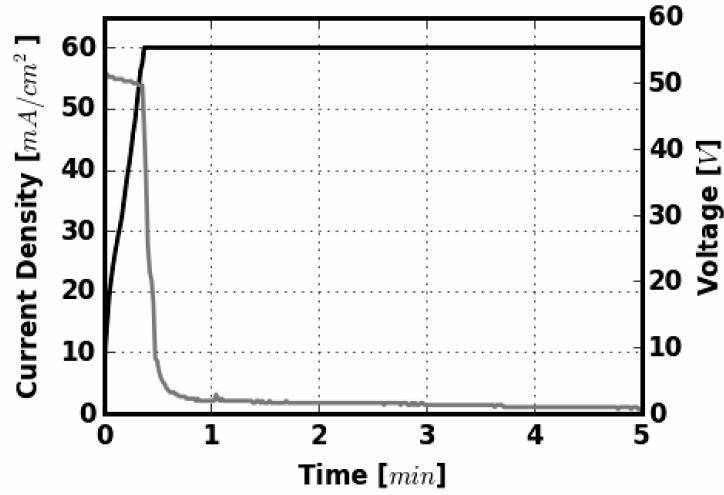


Figure 30: Current density and voltage evolution during current controlled Si-face PECE of a 4H-SiC sample having a bulk resistivity of $0.157 \Omega\cdot\text{cm}$ with MAPCE pre-treatment.

Figure 31 shows a cross sectional view of a sample where PECE was performed after MAPCE in a voltage controlled mode. As discussed, the porous layer from MAPCE provides initiation sites for PECE (indicated by black arrows). In contrast to the current controlled experiment, the porous layer formed with PECE shows a different structure. The uniformity of the porous layer is reduced and pore growth has taken place preferentially into depth.

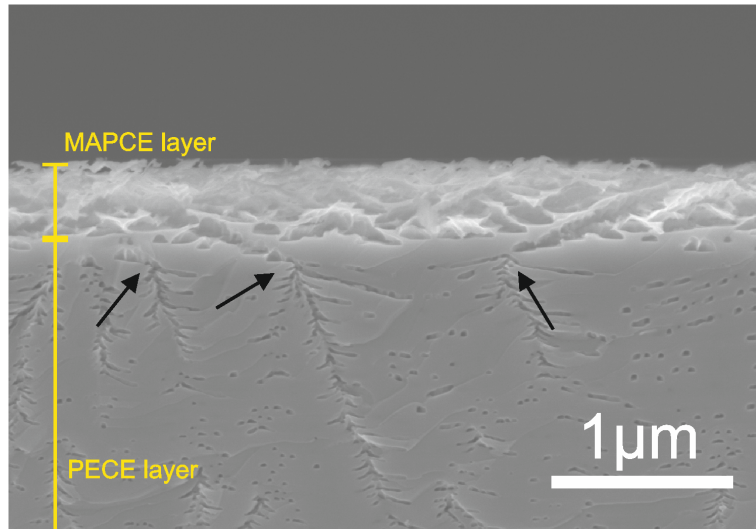


Figure 31: Cross-sectional view on a 4H-SiC sample with a bulk resistivity of $0.157 \Omega\cdot\text{cm}$ after MAPCE and PECE. PECE was performed in a voltage controlled mode.

This is due to an initially higher voltage at the beginning of the voltage controlled PECE (see Figure 32). The initial voltage influences the whole course of a PECE experiment. When comparing Figure 30 with Figure 32 it can be seen that the current density was lower during current

controlled PECE, despite the maximum voltage was measured after 1 minute and was afterwards on average higher than during the voltage controlled experiment. So the same or an even higher voltage leads to a significantly lower current density in this period.

This counter-intuitive behavior can be explained with the following gedanken-experiment: When MAPCE is performed prior to PECE, the etching result of PECE is enhanced. Sites with high curvature aid the initiation of the first PECE pores and also diffusion is enhanced. So the initial current-voltage conditions have a strong impact on the entire PECE process. The current voltage-conditions during PECE when a new pore is formed have a similar impact on the whole PECE process. The shape and hence, the curvature of the initially formed pores is determined by the applied voltage. But, the local electric field strength at the semiconductor/electrolyte junction at the pore tip depends on this latter parameter [40]. Therefore pore propagation will take place in different directions for differently shaped pores. This leads to an overall different morphology of the porous layer and also different current voltage characteristics during PECE.

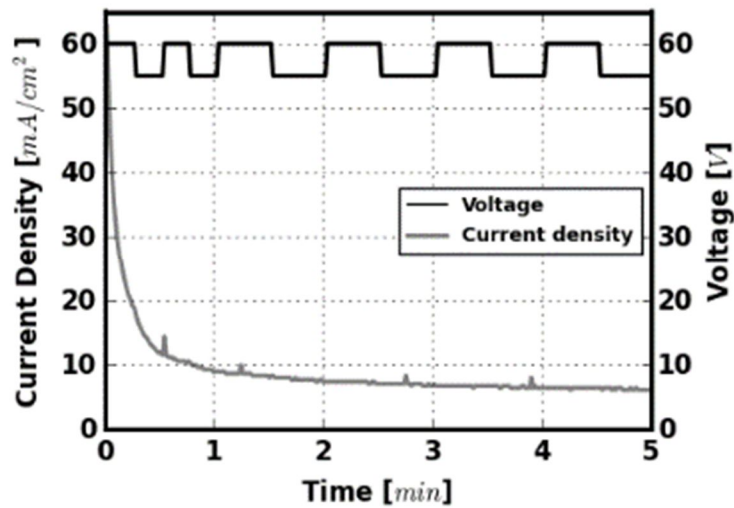


Figure 32: Current density and voltage evolution during voltage controlled Si-face PECE of a 4H-SiC sample having a bulk resistivity of 0.157 $\Omega\cdot\text{cm}$ with MAPCE pre-treatment.

In summary it can be stated that the combination of MAPCE and PECE can be applied to 4H-SiC samples with different bulk resistivity values. Furthermore, PECE can be performed in a current and voltage controlled mode. In both cases the pore tips from the MAPCE generated porous layer act as initiation sites for PECE. The higher the voltage during PECE the more pronounced is the pore initiation at sites with high curvature.

4.2.1.3 Experiments on the C-face of 4H-SiC

Experiments were also carried out with the C-face of the sample exposed to the etching solution. It was found that MAPCE can be performed also on the C-face of 4H-SiC which has not been reported so far. A combination of MAPCE and PECE was successfully applied to samples having bulk resistivities of $0.057 \Omega \cdot \text{cm}$, Figure 33a shows a sample with a resistivity of $0.057 \Omega \cdot \text{cm}$ where a combination of MAPCE and PECE was carried out with an etching solution containing $0.17 \text{ mol/L Na}_2\text{S}_2\text{O}_8$ and 1.8 mol/L HF . During PECE a constant voltage of 40 V was applied for 10 minutes. Again, the pore tips from the porous layer prepared with MAPCE act as initiation sites for pore initiation in PECE (black arrows in Figure 33a) such that no skin and cap layer resulted.

Figure 33b shows a cross-sectional SEM micrograph from a sample etched with the same experimental conditions but without a MAPCE step. A skin layer formed (white ellipse) which is followed by a cap layer exhibiting an irregular porous structure.

The nature of the porous layer formed with MAPCE is displayed in the current density evolution during PECE shown in Figure 34. Without a MAPCE step prior to PECE the current density at the onset of the porosification process increases with time, but is considerably lower than in the experiment with MAPCE. First the current density is very low due to surface pore initiation and cap layer formation. After surface pore initiation the current density increases up to a certain point until accumulation of reaction products and depletion of fresh etching solution in the porous structure cause a drop in the current density. In contrast, when performing a MAPCE step prior to PECE initial pore formation is enhanced and the resulting pores are better aligned to the field direction. This leads to a higher electrical field strength at the pore tips throughout PECE. Furthermore the absence of a skin layer enhances diffusion in the whole porous layer. So, increased electric field strength at the pore tips and enhanced diffusion in the porous layer lead to an overall higher current density when MAPCE was performed prior to PECE. In addition, this increase in current density favors a higher etching depth of about $50 \mu\text{m}$, while for the sample etched without a MAPCE step an etching depth of only $5 \mu\text{m}$ was observed.

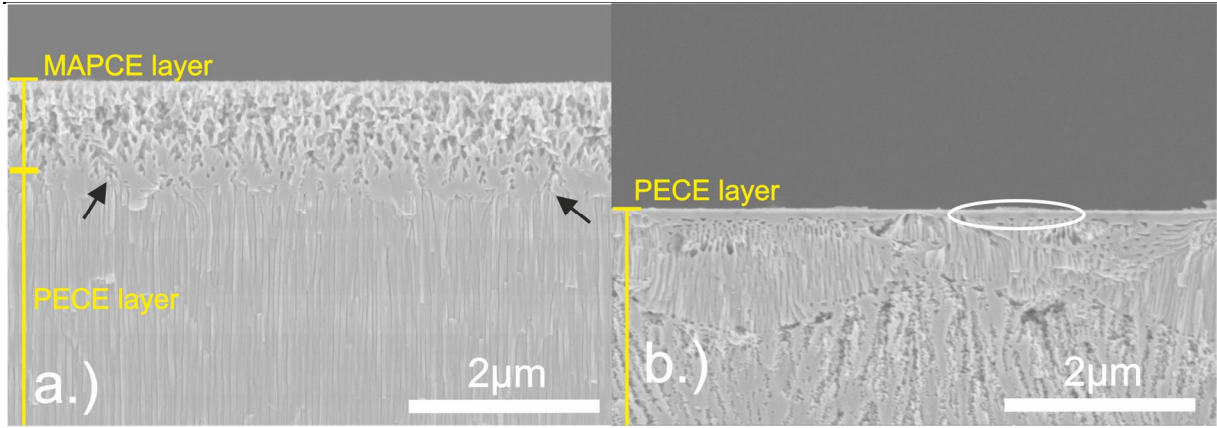


Figure 33: Cross-sectional view of 4H-SiC samples with a bulk resistivity of $0.057 \Omega\cdot\text{cm}$, where the C-face was photoelectrochemically etched a.) with MAPCE b.) without MAPCE pre-treatment.

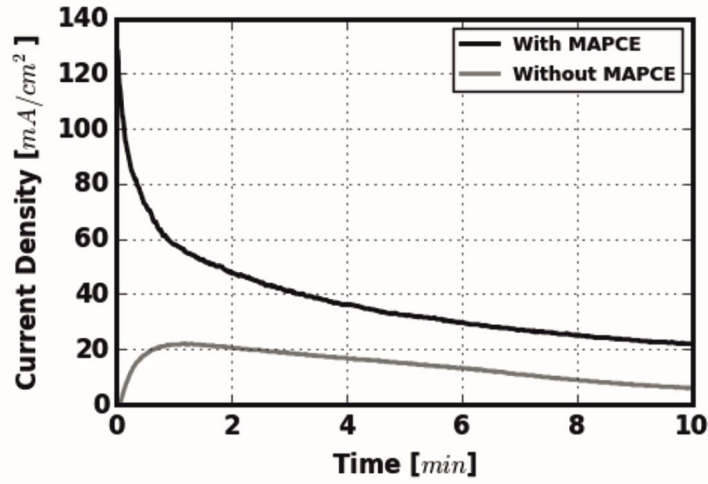


Figure 34: Current density evolution at a constant voltage of 40 V during PECE on the C-face of a 4H-SiC sample having a bulk resistivity of $0.057 \Omega\cdot\text{cm}$ with and without a MAPCE pre-treatment.

The different morphologies of the porous layers obtained from C-face and Si-face experiments can be attributed to both their different oxidation behavior and to different directions of the Helmholtz layer fields at the solution/SiC junction [42]. Nevertheless in both cases the initial conditions when PECE is started are crucial for the course of the whole experiment. Pore initiation at the beginning PECE takes place at regions with the highest curvature. The shape of these first pores determine the morphology of the whole porous layer.

The observed results have also in common that the porous layers resulting from MAPCE show a higher porosity than that prepared with PECE. The voltage generated with the redox reactions during MAPCE can be assumed much lower [86] than that applied during PECE. Therefore pore propagation into depth is less pronounced and a higher degree of porosity results. This statement is confirmed in the next section.

4.2.2 Etching of an already existing porous layer with MAPCE

Based on the important result that PECE is most suitable combined with MAPCE to increase the local homogeneity of the porous structure, it was then aimed to increase the porosity of the whole layer formed during PECE. Therefore, a second MAPCE step was performed after PECE (post treatment). Like in the previous sections prior to PECE a pre MAPCE step was carried out in all experiments of this section.

Underneath the originally deposited Pt pads porous SiC had been formed during the first MAPCE and PECE step. Since the electrical conductivity of porous SiC is lower than the corresponding bulk value [87] the necessary electron transport for MAPCE is diminished according to the findings of section 4.1. Therefore, a 300 nm thin Pt layer was deposited at regions of the sample where no porous layer had been formed and annealed. This enabled a second MAPCE step, because the newly sputter deposited Pt was not isolated by a porous SiC layer underneath

The first experiment with this approach was carried out with a sample having a bulk resistivity of $0.02 \Omega \cdot \text{cm}$, whereas the Si-face was exposed to the etching solution. First, MAPCE was performed for two hours. Then PECE was carried out with the targeted current density of 22.3 mA/cm^2 using the same etching solution. A porous layer with an average thickness of $10.5 \mu\text{m}$ was obtained, with a standard deviation of $\pm 1 \mu\text{m}$. Finally, a second MAPCE step was applied for 2 hours (post treatment). The result of the experiment is demonstrated by comparing the etching fronts at the bottom of the porous layer, before and after the second MAPCE step, as shown in Figure 35. In addition also black and white images from image thresholding are given. The micrographs correspond to different regions of the sample. The two etching fronts shown, correspond to etching depths of 9.7 and $9.5 \mu\text{m}$, respectively. Compared to a standard MACE/PECE combination shown in Figure 35a, an additional etching with MAPCE, as illustrated in Figure 35b, a smoother morphology profile is present. Hence it is assumed that no further etching into the depth occurred, because the pore morphology strongly depends on the etching conditions. When driving the etch front even further into the bulk with the MAPCE post treatment there should be a region with distinct pore morphology and degree of porosity at the bottom of the porous layer. (This assumption is proven by investigations presented below in Figure 40). Therefore, it can be concluded, that the difference in etching depth is due to etching depth variations originating from the PECE process and not due to further etching into depth during the second MAPCE step.

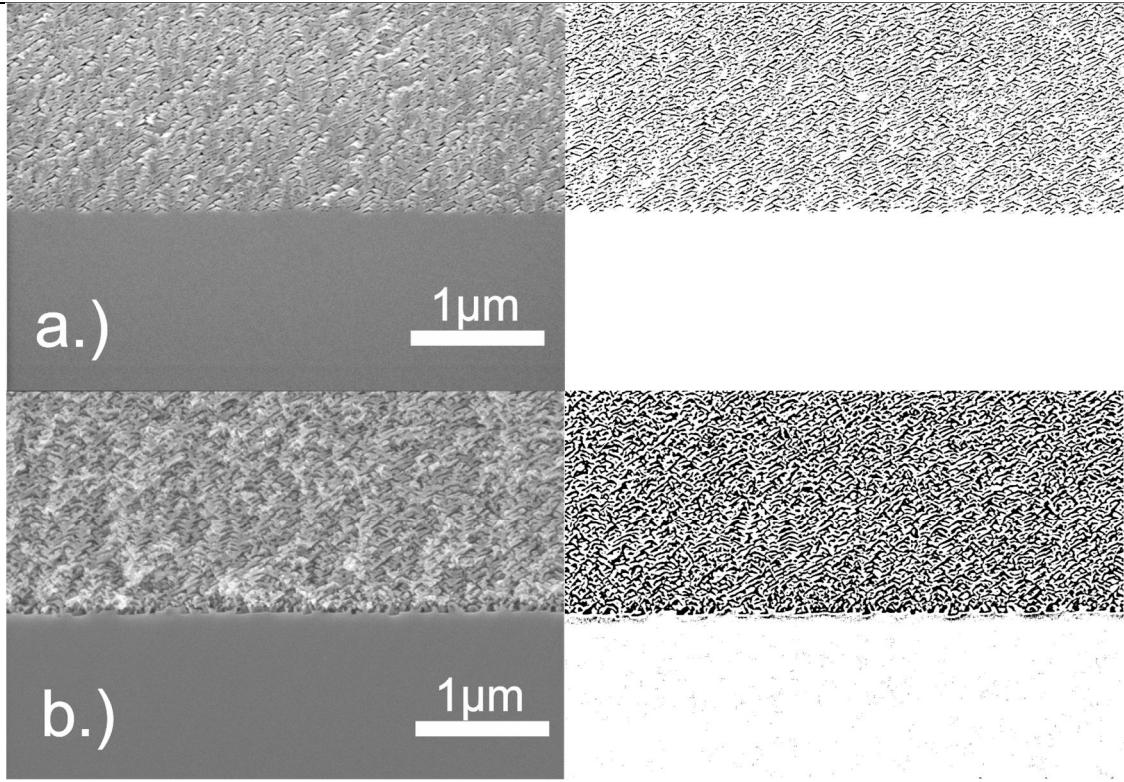


Figure 35: Comparison of etch fronts before and after MAPCE of a porous 4H-SiC layer electrochemically formed in a sample with a bulk resistivity of $0.02 \Omega\cdot\text{cm}$ a.) before MAPCE with black and white image, b.) after 2 hours of MAPCE post-treatment with corresponding black and white image

The values from image thresholding allowed to estimate the magnitude of porosity within the layer as a function of etching depth. To obtain reproducible values the image processing parameters were adjusted such that the porosity of the region below the porous layer is zero. Furthermore, the porous layers originating from the MAPCE process before PECE were not considered due to a too high porosity to allow a reasonable evaluation by this approach. This allowed the analysis of the trend of the porosity depth profile for each sample. The results are displayed in Figure 36. The gray curve represents the data obtained from image thresholding, while the black curve represents the corresponding smoothened values.

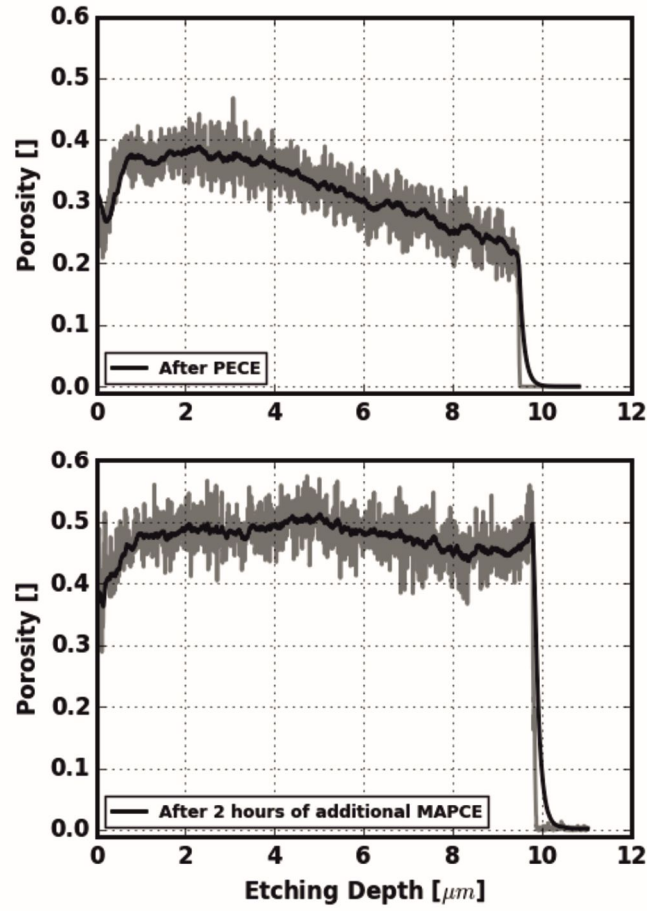


Figure 36: Degree of porosity in 4H-SiC formed in a sample having a bulk resistivity of $0.02 \Omega\text{-cm}$ before and after a post-treatment with MAPCE.

Basically, after PECE the porosity of the layer increases up to a depth of approximately $1 \mu\text{m}$, then stays constant up to approximately $3 \mu\text{m}$ and then continuously decreases down to the bottom of the porous layer. This allows several conclusions about the characteristics of the PECE process. The current density during the experiment was constant at 22.3 mA/cm^2 (see Figure 37), but the porosity is not equally distributed across the porous layer.

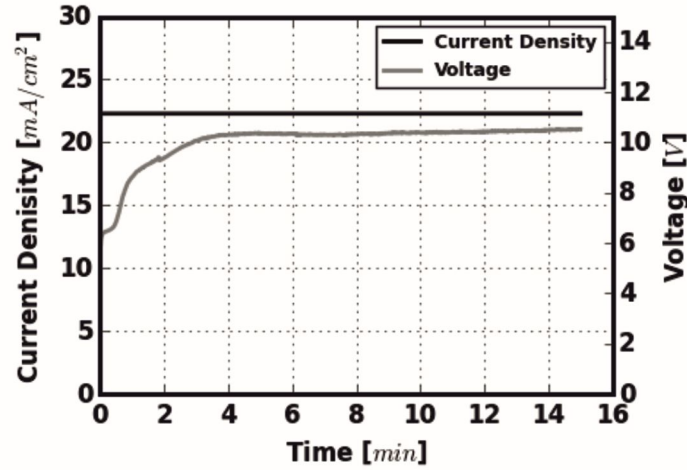


Figure 37: Current density and voltage evolution during Si-face PECE of a 4H-SiC sample having a bulk resistivity of $0.02 \Omega\text{-cm}$ with MAPCE pre-treatment.

Figure 37 also shows that at the beginning of the experiment the voltage increased until it became rather constant. Also the porosity at the top of the porous structure shows an increasing trend, which is shown in Figure 36 (after PECE). So an increasing voltage also led to an increasing porosity at constant current density. This can be explained with a higher pore initiation rate with increasing voltage. Thus the degree of porosity is increased with increasing voltage. A similar result is reported in literature, where an increasing pore size with etching depth is stated for 6H-SiC, which was anodized at constant current density under yellow light conditions [88].

At the later stages of the PECE experiment the current density as well as the voltage were rather constant. Contrarily, the tail of the porosity depth profile in Figure 36 (after PECE) shows a decreasing trend. This implies that etching did not only take place at the etching front. During the course of etching also already existing pores enlarged. A similar finding is reported in literature where surface near pores become larger with ongoing etching time [34]. These observations show that it is a challenging task to prepare homogenous and highly porous layers only with a pure PECE process. Later in this thesis this issue is addressed in more detail (see section 4.5).

After the MAPCE post treatment process the magnitude of the porosity was increased across the whole layer and relatively constant compared to the situation after PECE as can be seen in Figure 36. This is of technological interest because it allows in principle the formation of homogeneous porous 4H-SiC layers with a defined etching front independent of the electrical parameters during PECE. On the other hand these observations also provide new information to the mechanisms of PECE and MAPCE. The formation of a defined etching front confirms that the basal plane is an etch stop plane [34], while the other crystallographic planes in the

porous layer show a higher etching rate. Furthermore new pore initiation is energetically less favorable than etching of the crystallographic planes already exposed to the etching solution.

After having evaluated these data the same experiment was performed on the Si-face of a sample with a bulk resistivity of $0.057 \Omega \cdot \text{cm}$. The goal of this experiment was to show that a homogenous and highly porous layer can also be obtained independent of the sample resistivity. Furthermore one additional MAPCE post-treatment was carried out with an etching time of 3 hours.

Figure 38 shows a SEM micrograph after PECE and another one after 3 hours of MAPCE together with the corresponding black and white images from image processing. Further etching of this porous layer with MAPCE resulted in an increased porosity within the layer while the pore morphology was still preserved. Basically, the final degree of porosity as well as the pore morphology depend explicitly on each other when just PECE is performed. In contrast, when PECE is combined with MAPCE as post-treatment the situation is completely different. The pore morphology can be adjusted with the experimental parameters during PECE. Finally, the degree of porosity can be increased with MAPCE.

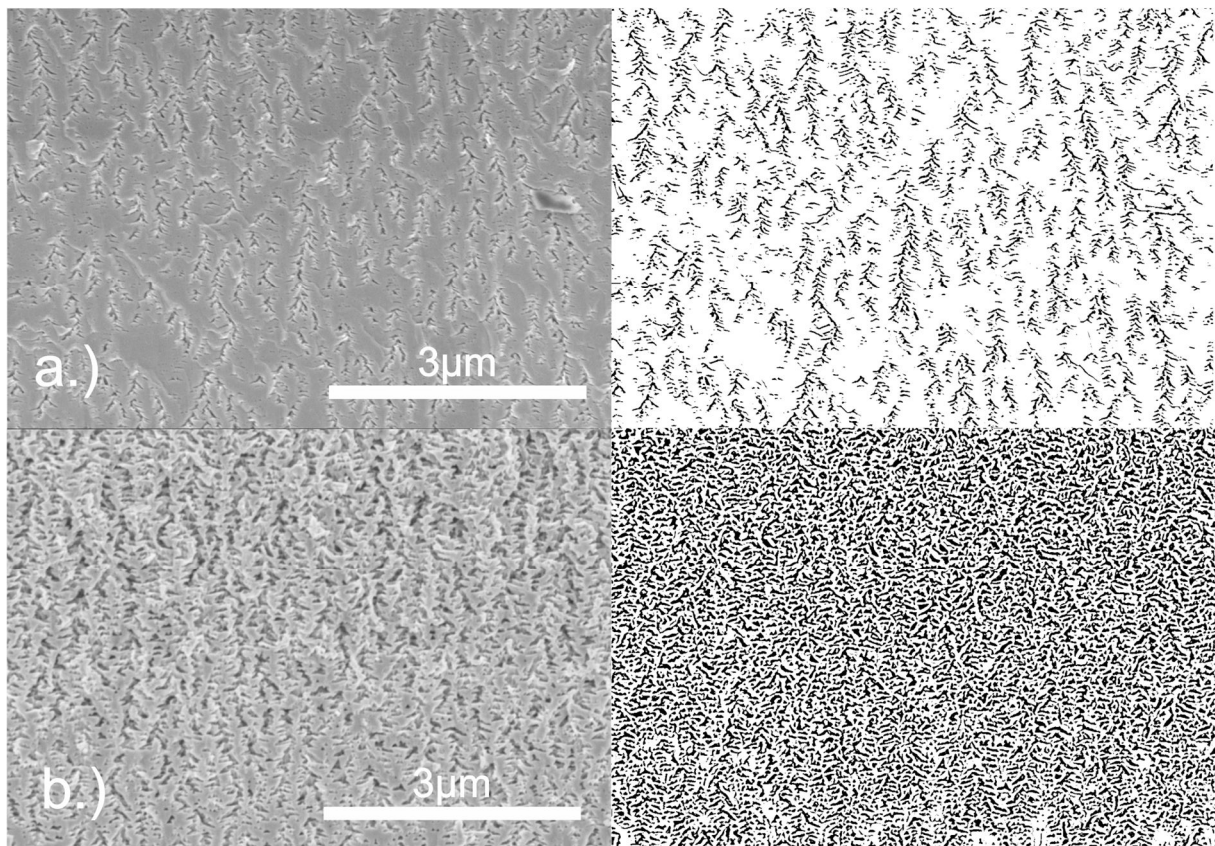


Figure 38: Comparison of porous 4H-SiC layers formed in a sample with a bulk resistivity of $0.057 \Omega \cdot \text{cm}$ at an etching depth of $9.6 \mu\text{m}$. a.) before MAPCE as post-treatment with corresponding black and white image, b.) after 3 hours of MAPCE as post-treatment with corresponding black and white image.

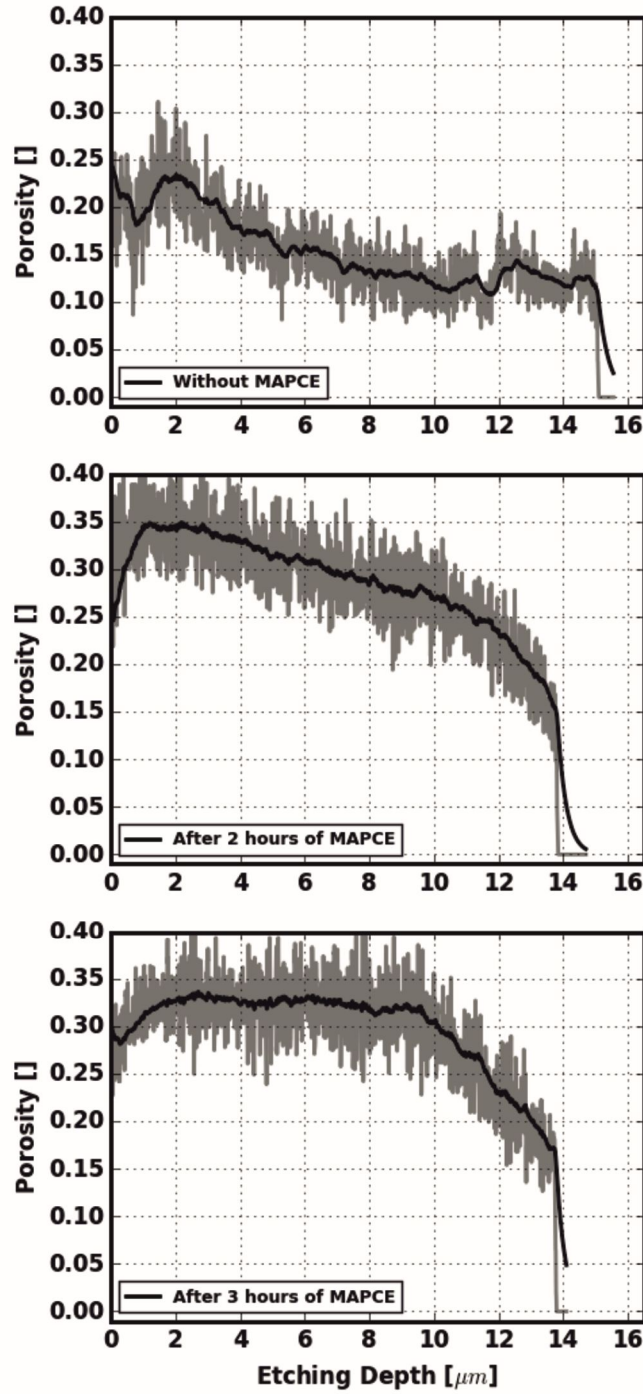


Figure 39: Depth characteristics of the porosity in 4H-SiC formed in a sample having a bulk resistivity of $0.057 \Omega\cdot\text{cm}$ before and after MAPCE as post-treatment.

Figure 39 shows the depth porosity characteristics of samples having a bulk resistivity of $0.057 \Omega\cdot\text{cm}$ after PECE and after a MAPCE as post-treatment. It can be seen that the porosity increases with increasing etching time and in the upper regions of the porous layer the value of the porosity becomes constant. This corresponds to the expected behavior, as the upper regions of the porous layer are etched first due to front side light irradiation during MAPCE. After a

certain time the resistivity of the upper regions of the porous layer increases, thus etching becomes energetically less favorable. This condition continuously moves into lower regions of the porous layer until a homogeneous degree of porosity is reached.

According to theory, the space charge regions cover more and more volume of the porous layer with increasing degree of porosity, thus introducing a masking effect [41]. After a certain time of MAPCE, further etching of the already existing porous layer becomes energetically less favorable. This was experimentally confirmed by applying MAPCE for 3 hours to the sample with a bulk resistivity of $0.02 \Omega \cdot \text{cm}$. The result of the experiment is illustrated in Figure 40a. It can be seen that new pore initiation took place at the etching front as it was expected. This could also be observed for the sample with a bulk resistivity of $0.057 \Omega \cdot \text{cm}$ after applying MAPCE for 4 hours as is shown in Figure 40b.

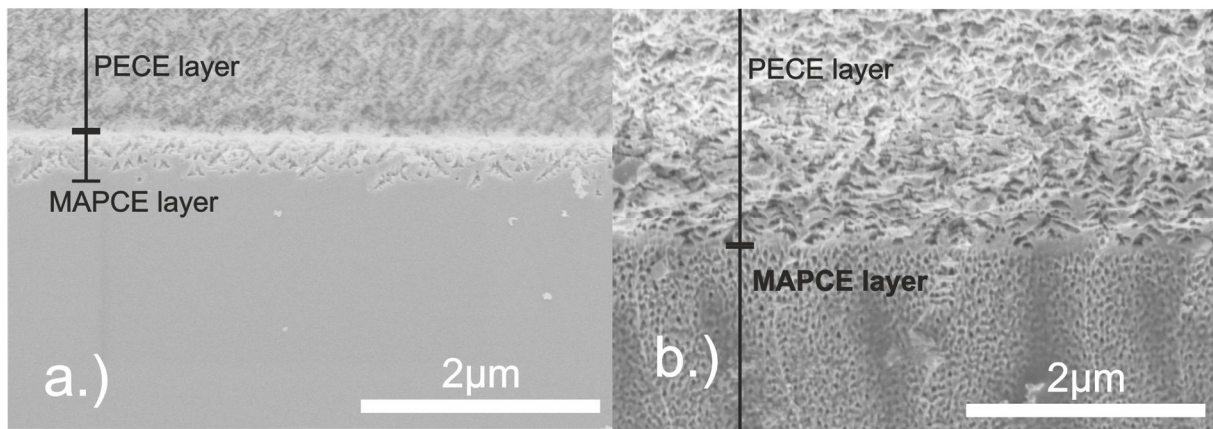


Figure 40: Etching fronts of porous 4H-SiC layers formed with a sequence of MAPCE, PECE and MAPCE. a.) Sample with a bulk resistivity of $0.02 \Omega \cdot \text{cm}$ after 3 hours of MAPCE post-treatment b.) Sample with a bulk resistivity of $0.057 \Omega \cdot \text{cm}$ after 4 hours of MAPCE post-treatment.

These findings can be summarized in a model describing the processes during MAPCE when starting with a pre-porositified 4H-SiC layer. A schematic illustration of the process is shown in Figure 41. Basically, persulphate ions ($\text{S}_2\text{O}_8^{2-}$) are reduced at the surface of Pt. This process is counterbalanced by oxidation of the porous layer that delivers electrons. The formed oxide is then dissolved by HF. The red arrows indicate the resulting electron flow from the surface of the porous layer via the Pt/SiC junction to the Pt/solution interface. This process slows down with increasing porosity because the space charge layer increasingly masks the porous structure and further etching becomes energetically less favorable. When the whole porous layer is occupied by the space charge layer new pore initiation at the etching front takes place because it becomes the energetically most favorable sub-process. These findings confirm the theory, that the space charge layer is responsible for the formation of porous SiC [41]. Furthermore, for the first time this knowledge is transferred and directly implemented in a technological process.

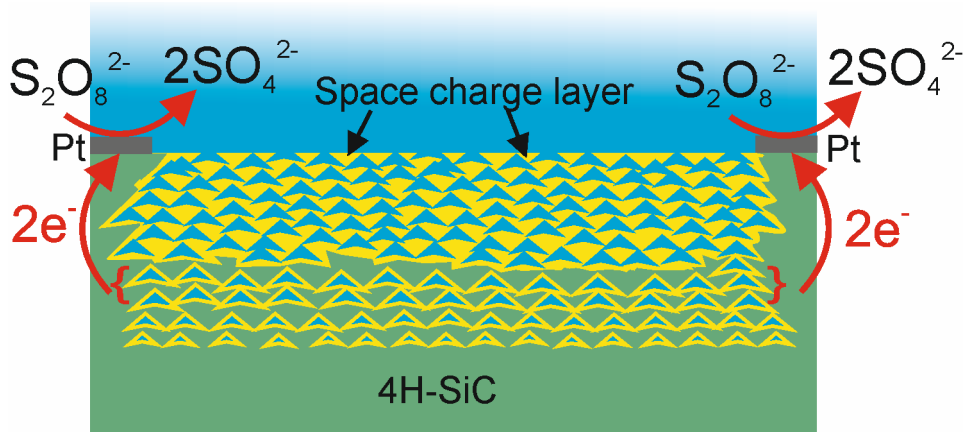


Figure 41: Schematic illustration of MAPCE as post-treatment carried out with a pre-porosified 4H-SiC layer.

The experimental evidences allow the tailored porosification of 4H-single crystal wafers. A homogeneous porosity-depth profile can be obtained. This is a challenging task when just PECE is utilized. Once a certain porosity profile is etched into the wafer, it is difficult to increase the porosity and homogeneity. Further increase of the degree of porosity is possible with methods like reactive ion etching, but the porous layer will be fully dissolved [63]. In contrast, when the degree of porosity is increased with MAPCE, a constant degree of porosity results across the layer. This is due to the electrochemical nature of MAPCE, as the space charge layer in the porous SiC prevents it from total dissolution.

4.3 Preparation of highly porous and uniform porous SiC thin layers with MAPCE

Parts of this section have been published in [89].

In the previous section it was found that an already existing porous layer levels out to a constant degree of porosity when MAPCE as post-treatment is applied; the space charge layer in the porous structure prevents the material from further etching. Furthermore the growth already existing pores is energetically more favorable than the initiation of new pores. This implies that uniform porous layers can be generated with MAPCE only when small volumes of etching are used, because in this case the oxidizing agent concentration decreases and the initiation rate of new pores should decrease while the growth rate of already existing pores is less decreased by the decreasing oxidizing agent concentration according to the findings presented in section 4.2.2.

With ongoing etching time most of the oxidant should be reduced. Thus the redox potential as an indicator for the electrochemical potential of the etching solution should decrease as explained in section 2.2.1. Pore formation should stop when all of the oxidizing agent is reduced. Furthermore it was assumed, that the resulting porous layer should have a homogenous porosity depth profile because the space charge layer limits the final degree of porosity. This would allow to control the degree of porosity across the porous layer, while the progress of the etching reaction could be recorded with redox potential measurements. The potential problem of heat generation due to the light source in mass production would be minimized with a low pressure mercury lamp that emits no infrared radiation. Moreover low etchant volumes are of economic interest, especially when highly toxic etching solutions are used.

To meet these requirements the experimental parameters of MAPCE had to be modified. The process flow of modified MAPCE is illustrated in Figure 42. Step *i* and step *ii* are essentially the same as in section 4.1. In step *ii* a single strip of Pt was sputter deposited at the edge of the sample, occupying approximately 10 % of the surface. Another modification is step *iii*: Pt was sputter deposited for a second time and structured with standard photolithography and lift off. By doing so, defined areas of porous SiC can be formed. This was done with possible application scenarios in mind, where the local definition of porous SiC is required.

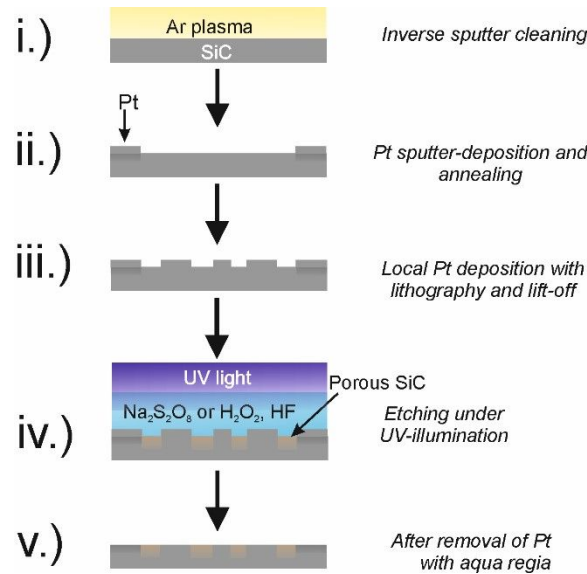


Figure 42: Process flow chart for metal assisted photochemical etching (MAPCE) of silicon carbide.

In step *iv* the sample is immersed in 1.2 mL of etching solution while UV light irradiation is done with a custom-built 18 W low pressure mercury UV-C source having its peak intensity at 254 nm. The experiments were carried out with either H₂O₂ or Na₂S₂O₈ to investigate the influence of the oxidizing agent type on MAPCE. The HF concentration in all performed experiments was 1.31 mol/L, while the concentrations of the oxidants varied.

Finally (step v) the Pt can be removed with aqua regia after etching, if needed for further processing.

First the evolution of the porous layer is studied when the modified MAPCE parameters are applied. In particular the influence of the oxidizing agent concentration and type was studied with respect to the resulting porous layer. The obtained results were interpreted with a chemical ToF-SIMS analysis of the porous SiC. All samples in this section had a size of 1 x 1 cm² and a nominal resistivity of (0.012 -0.025) Ω·cm.

4.3.1 Evolution of the porous layer

In this section the evolution of the porous layer during etching is presented with varying oxidizing agent types (H₂O₂ or Na₂S₂O₈) and concentrations. Porous layers were formed at 25 μm and 50 μm square areas defined by photolithography.

The porosified area of each sample was 0.11 cm². The etching times ranged between 15 and 150 minutes and during the first experiments the C-face was exposed to the etching solution. This was done because no reference data exists for such experiments and the initial experiments may be easier to interpret without the etch stop plane present during Si-face etching [34]. However, after the C-face experiments those experimental outcomes were compared with Si-face experiments basically showing the same results.

First the experimental results with H₂O₂ containing solutions are presented, then those with Na₂S₂O₈. Finally, all results are evaluated and discussed.

4.3.1.1 Experiments with H₂O₂

Figure 43 shows the evolution of the etching depth and the redox potential with respect to etching time. After 60 minutes the total etching depth, as well as the redox potential becomes relatively constant. This is attributed to the decay of H₂O₂ due to photolysis (see Equation [4-1]) [90] in the etching solution with time.



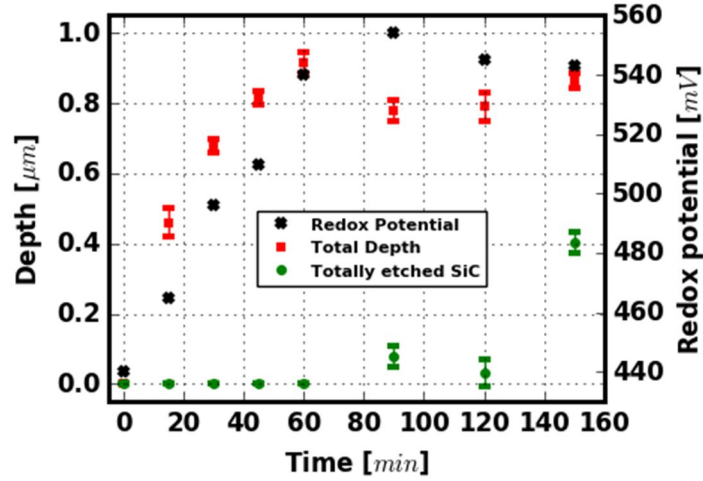


Figure 43: Etching depth and redox potential versus time. Etching solution: 1.2 mL of 0.04 mol/L H_2O_2 in 1.31 mol/L HF, while the C-face is exposed to the etchant. The error bars represent the standard deviation from 10 measurements.

When all the H_2O_2 is decomposed, no further etching into depth is observed. This behavior is illustrated in Figure 44. At first the total etching depth increases until it becomes relatively constant. This behavior is accompanied by the formation of a defined etching front. When the total etching depth does not increase anymore, total dissolution of porous 4H-SiC takes place. This is an unexpected behavior and is discussed below in this section after the presentation of additional results (see section 4.3.1.6).

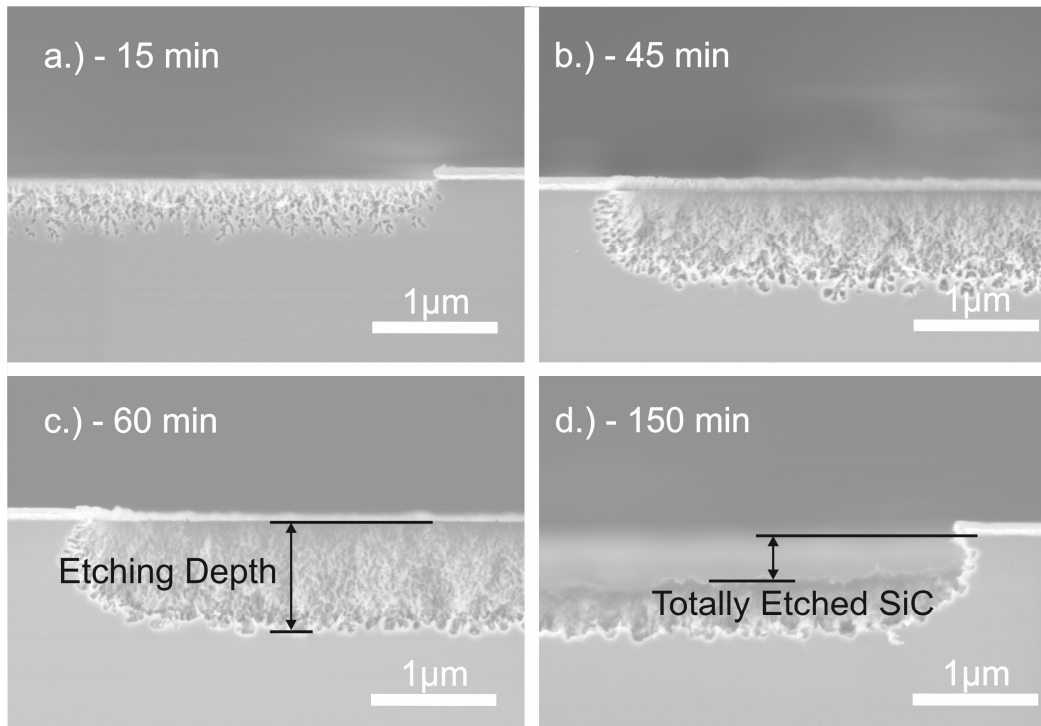


Figure 44: Evolution of the porous layer with increasing etching time. Etching solution: 1.2 mL of 0.04 mol/L H_2O_2 in 1.31 mol/L HF, while the C-face is exposed to the etchant.

Next, the influence of a higher H_2O_2 concentration (i.e. 0.15 mol/L instead of 0.04 mol/L) is presented. Qualitatively the same result was obtained as displayed in Figure 45 and Figure 46. The redox potential as well as the total etching depth become constant with ongoing etching time.

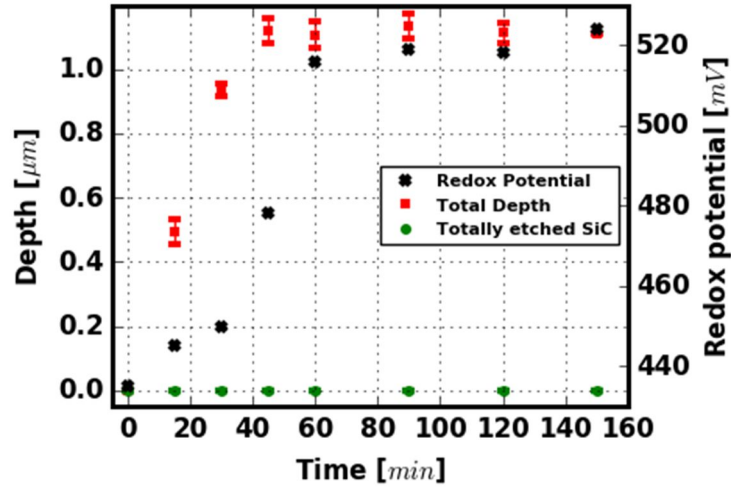


Figure 45: Etching depth and redox potential versus time. Etching solution: 1.2 mL of 0.15 mol/L H_2O_2 in 1.31 mol/L HF, while the C-face is exposed to the etchant. The error bars represent the standard deviation from 10 measurements.

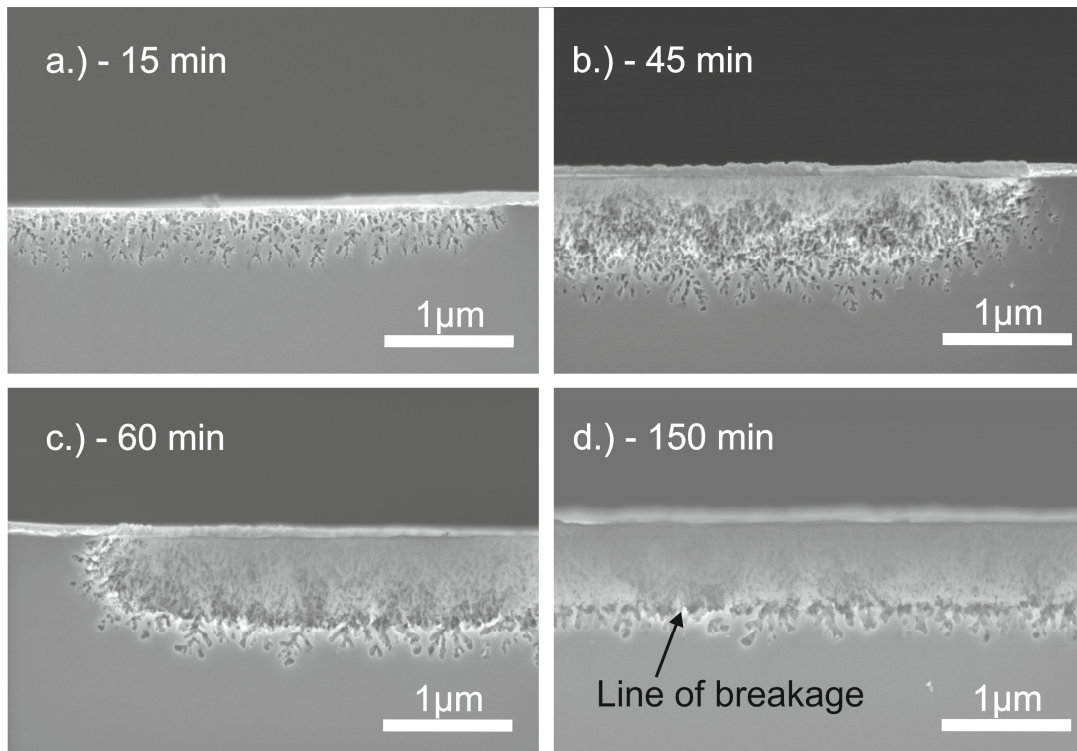


Figure 46: Evolution of the porous layer with increasing etching time. Etching solution: 1.2 mL of 0.15 mol/L H_2O_2 in 1.31 mol/L HF, while the C-face is exposed to the etchant.

Beside these similarities there are also differences when the H_2O_2 concentration is increased. At longer etching times a so-called line of breakage forms (see Figure 46d). This means that total dissolution takes place at the bottom of the porous layer, instead at the top surface. So the upper porous layer is protected from further etching because total dissolution starts at its bottom.

4.3.1.2 Experiments with $\text{Na}_2\text{S}_2\text{O}_8$

Now the results with $\text{Na}_2\text{S}_2\text{O}_8$ as oxidizing agent are presented. The etching depth and redox potential characteristics are illustrated in Figure 47 (0.04 mol/L $\text{Na}_2\text{S}_2\text{O}_8$) and Figure 49 (0.15 mol/L $\text{Na}_2\text{S}_2\text{O}_8$). The corresponding SEM micrographs are shown in Figure 48 and Figure 50.

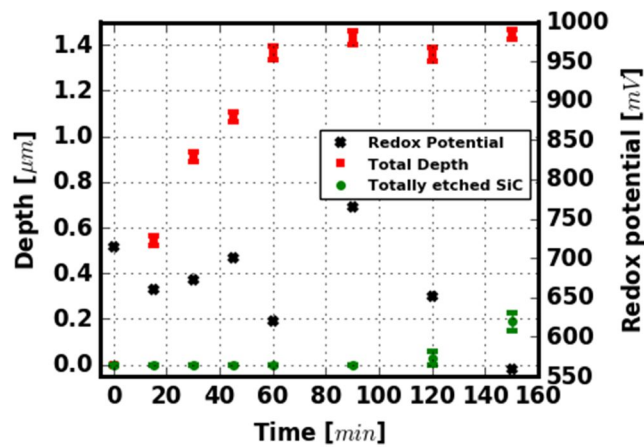


Figure 47: Etching depth and redox potential versus time. Etching solution: 1.2 mL of 0.04 mol/L $\text{Na}_2\text{S}_2\text{O}_8$ in 1.31 mol/L HF, while the C-face is exposed to the etchant. The error bars represent the standard deviation from 10 measurements.

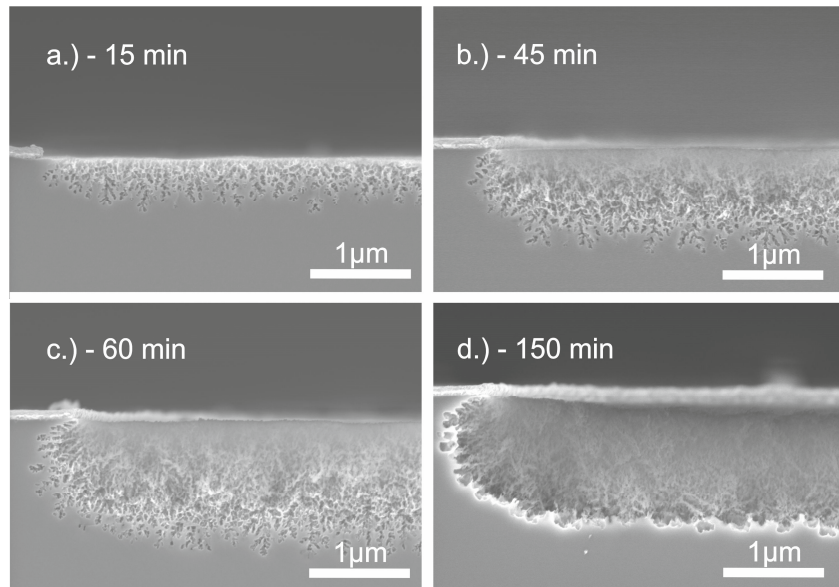


Figure 48: Evolution of the porous layer with etching time. Etching solution: 1.2 mL of 0.04 mol/L $\text{Na}_2\text{S}_2\text{O}_8$ in 1.31 mol/L HF, while the C-face is exposed to the etchant.

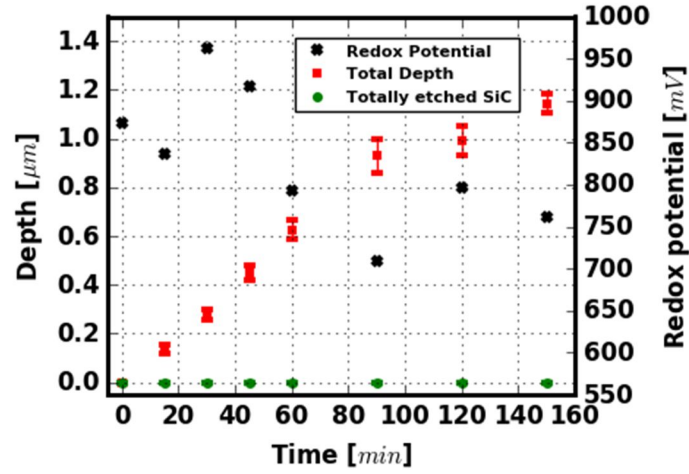


Figure 49: Etching depth and redox potential versus time. Etching solution: 1.2 mL of 0.15 mol/L $\text{Na}_2\text{S}_2\text{O}_8$ in 1.31 mol/L HF, while the C-face is exposed to the etchant. The error bars represent the standard deviation from 10 measurements.

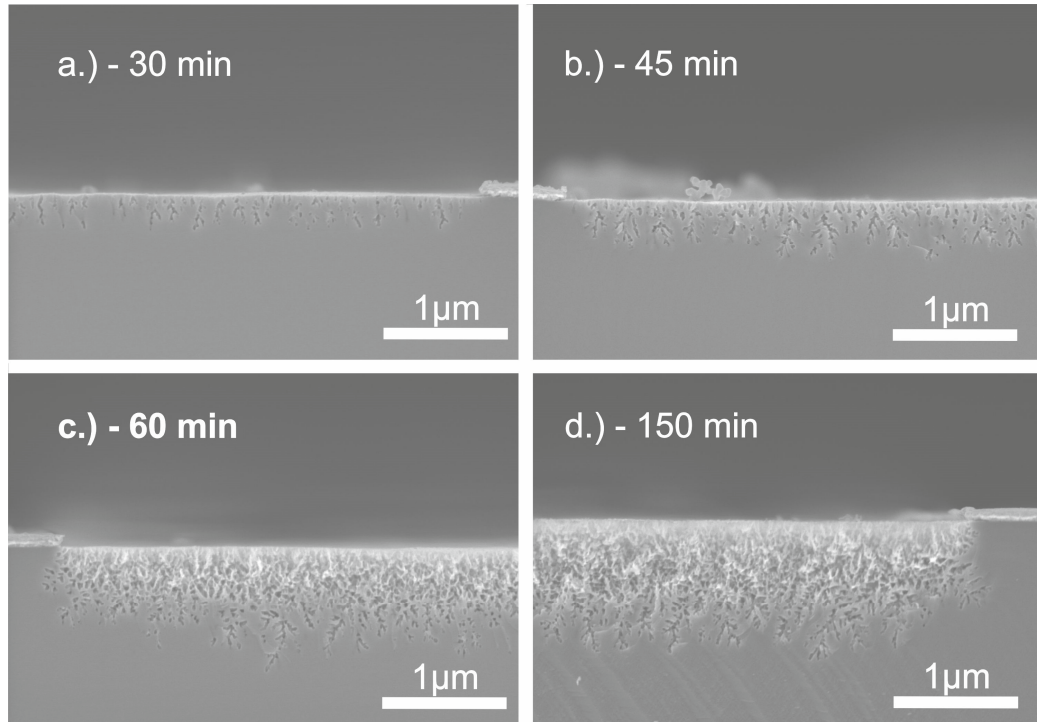


Figure 50: Evolution of the porous layer with etching time. Etching solution: 1.2 mL of 0.15 mol/L $\text{Na}_2\text{S}_2\text{O}_8$ in 1.31 mol/L HF, while the C-face is exposed to the etchant.

The same statements as for the samples etched with H_2O_2 based etchants (see section 3.2.1) can be made. After a certain time all the oxidizing agent is consumed due to photolysis (see Equation [4-2]) [91] and the total etching depth does not increase anymore (see Figure 47). During the experiment with 0.15 mol/L $\text{Na}_2\text{S}_2\text{O}_8$ also a decrease of the redox potential is determined. This indicates the decay of $\text{Na}_2\text{S}_2\text{O}_8$ in the etching solution. This is contrary to the samples

etched with H₂O₂, where the redox potential increased. This phenomenon has been studied and the results are shown in section 4.3.1.3.



After pore formation into depth had stopped, total dissolution of the porous layer started. In contrast, in no experiment with Na₂S₂O₈, the formation of a line of breakage could be observed. An increase of the Na₂S₂O₈ concentration from 0.04 mol/L to 0.15 mol/L yielded an etching process still ongoing into depth after 150 minutes, so that total dissolution was not observed (see Figure 49 and Figure 9). This is attributed to the presence of a not reduced oxidizing agent in the etching solution. However, etching at the top surface of the porous layer stopped, as is shown by an analysis of the pore size distribution in this region.

The pore size distribution on the top of the porous layers was estimated using image processing as described in section 3.5. Exemplarily results are shown in Figure 51. The column corresponding to Figure 51a shows the top down SEM micrograph, the corresponding black and white image after image processing and the corresponding pore cross section distribution after 30 minutes of MAPCE in an etching solution containing 0.15 mol/L Na₂S₂O₈. The column corresponding to Figure 51d shows the same information but for an etching time of 90 minutes.

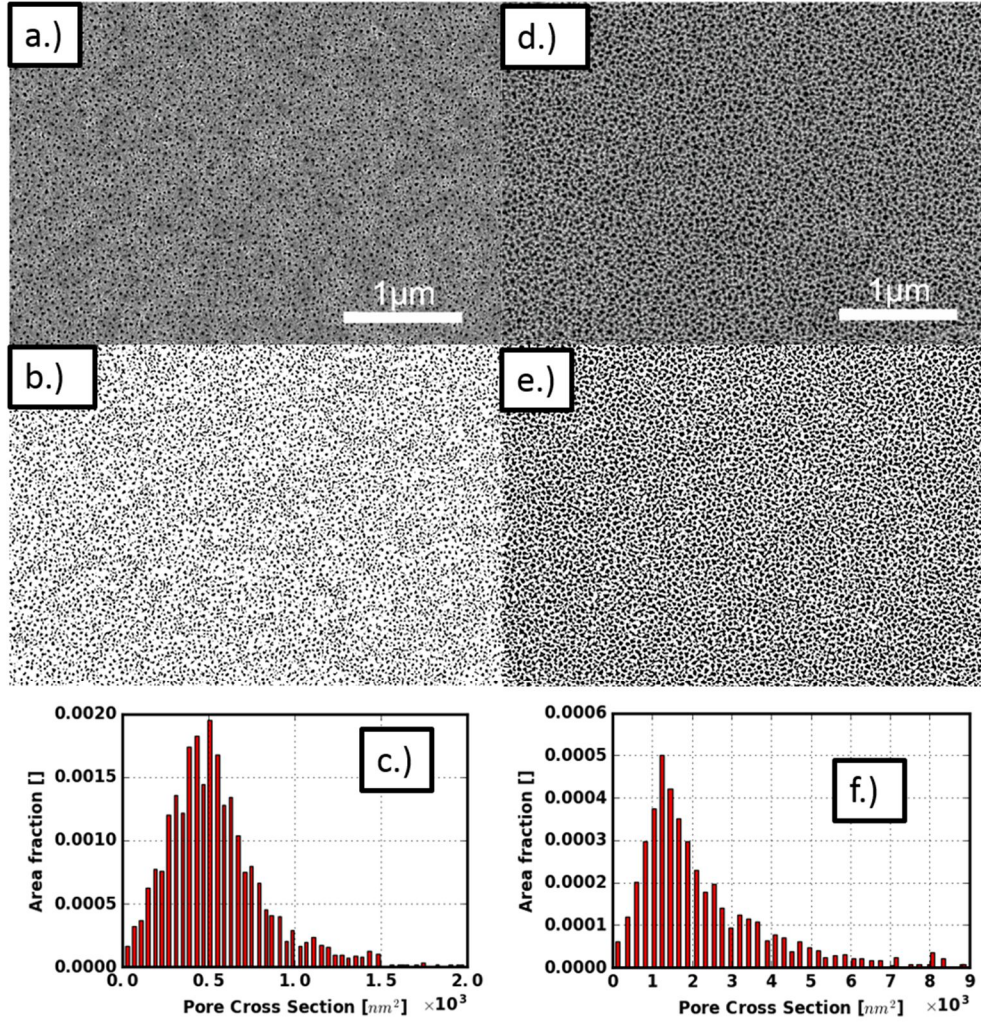


Figure 51: SEM micrographs in top view of porous 4H-SiC after different etching times. a.) 30 minutes of MAPCE d.) 90 minutes of MAPCE. The corresponding black and white images after image processing are shown in b.) and e.) while c.) and f.) illustrate the corresponding pore area distributions. Etching solution: 1.2 mL of 0.15 mol/L $\text{Na}_2\text{S}_2\text{O}_8$ in 1.31 mol/L HF, while the C-face is exposed to the etchant.

After 90 minutes of MAPCE the pores had connected and thus the average pore size has increased significantly. The cumulative pore area distributions have been fitted with Fisk distribution curves (Equation [4-3]) [92] with the fitting parameters α and β . The value of α is also the median of Fisk distributions.

$$F(x; \alpha, \beta) = \frac{1}{1 + \left(\frac{x}{\alpha}\right)^{-\beta}} \quad [4-3]$$

The modal pore areas were calculated according to Equation [4-4].

$$Mode = \alpha^{\beta} \sqrt{\frac{\beta - 1}{\beta + 1}} \quad [4-4]$$

Figure 52 shows the modal pore area (i.e. the pore area that appears most often in the pore distribution) after different etching times for the experiments with 0.15 mol/L $\text{Na}_2\text{S}_2\text{O}_8$ (see Figure 49 and Figure 9). At first the modal pore area increases almost linearly with time. The sharp increase represents individual pores that connect to larger clusters. From this characteristic point on, the pore size stays relatively constant, indicating a drastic drop of the etching rate. This demonstrates that etching of the porous layer stops at the highly porous regions at the top while pore formation into depth still proceeds.

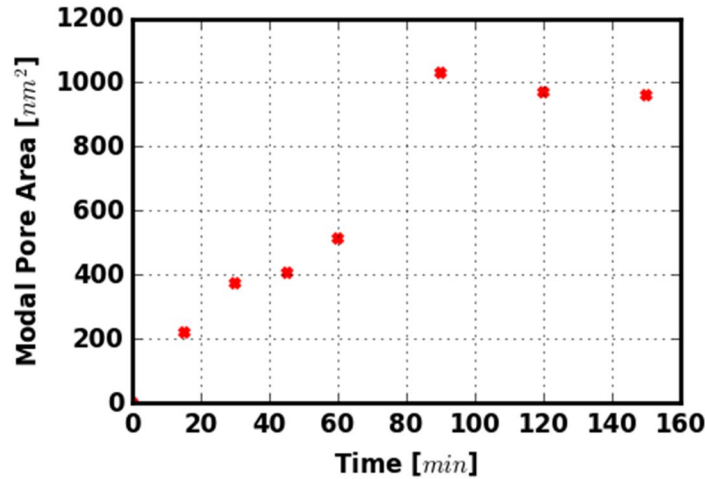


Figure 52: Modal pore area after different etching times. Etching solution: 1.2 mL of 0.15 mol/L $\text{Na}_2\text{S}_2\text{O}_8$ in 1.31 mol/L HF, while the C-face is exposed to the etchant.

The collected fitting data are shown in Table 2 and the corresponding probability density functions are given in Figure 53. The median as well as the mode first increase and then show a jump. This is attributed to surface pores that are connected with ongoing etching. After this jump, the median and the mode are relatively constant, showing a drastically decreased etching rate. The value of β is the shape parameter of a Fisk distribution, describing the width of a Fisk function for a given median value. Altogether the width of the probability density functions increases drastically at an etching time of 90 minutes and stays constant at higher etching times. This is also attributed to the connection of individual pores and the subsequent stop of the etching reaction at the surface of the sample.

Time [min]	Median [nm^2]	β []	Mode [nm^2]
0	0.0	0,0	0.0
15	331.7	2.3	220.2
30	456.7	3.2	374.0
45	465.7	3.8	403.8
60	580.8	4.0	510.7
90	1643.0	2.2	1030.1
120	1379.1	2.4	967.8
150	1305.1	2.6	961.9

Table 2: Collected fitting data for the pore size distribution of samples etched with 1.2 mL of 0.15 mol/L $\text{Na}_2\text{S}_2\text{O}_8$ in 1.31 mol/L HF, while the C-face is exposed to the etchant.

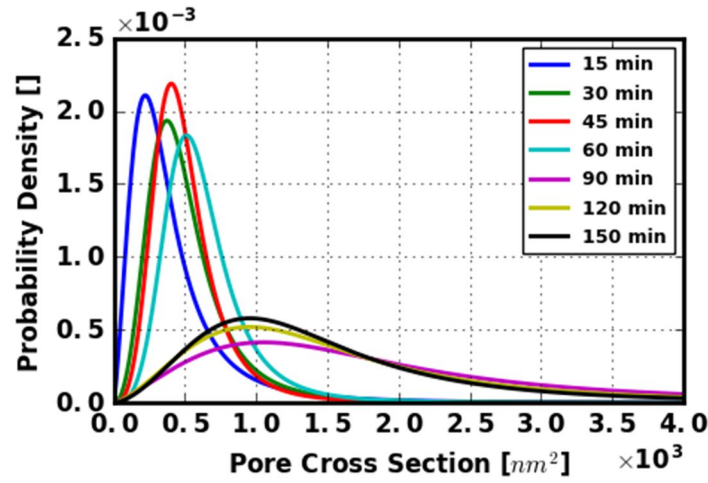


Figure 53: Fisk probability density functions corresponding to Table 2.

4.3.1.3 Influence of UV light intensity

So far, it has been proven that there is a limiting factor that restricts the final degree of porosity during etching and furthermore leads to homogeneous porous layers. With increasing porosity the insulating effect of the space charge layer becomes more dominant and the etching rate slows down. This passivating effect can be related to the space charge layer at the electrolyte semiconductor junction but it is also reasonable that an increased UV light intensity causes total dissolution.

The total dissolution of porous 4H-SiC is accompanied by the decay of oxidizing agent which in turn increases the amount of UV light that hits the sample. In this chapter the influence of the UV light intensity on the process of total dissolution is clarified.

Therefore transmission spectra of $\text{Na}_2\text{S}_2\text{O}_8$ solutions in water as well as the emission spectrum of the 18 W UV source were measured. As expected the UV source shows a maximum intensity peak at 254 nm (see Figure 54). The corresponding transmission values of the $\text{Na}_2\text{S}_2\text{O}_8$ solutions are shown in Figure 55. At 254 nm, the transmission T drops drastically with increasing $\text{Na}_2\text{S}_2\text{O}_8$ concentration. The measurement points are fitted with an exponential relationship being a function of the concentration c (see Equation [4-5]). The physical path d length of the light was 1 cm and the value of the absorption coefficient α was found to be $38.748 \text{ L}/(\text{cm} \cdot \text{mol})$. The upper curve represents the calculated transmission for a path length d of 4 mm.

$$T(c) = \exp(-adc) \quad [4-5]$$

This curve is shown because the etching solution covered the samples with this height during MAPCE. It shows that the light intensity increases drastically during MAPCE when the oxidizing agent concentration decreases.

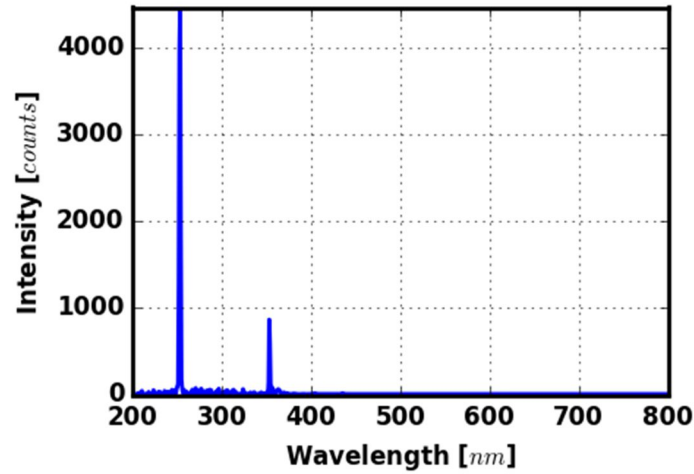


Figure 54: Measured emission spectrum of the 18W UV source.

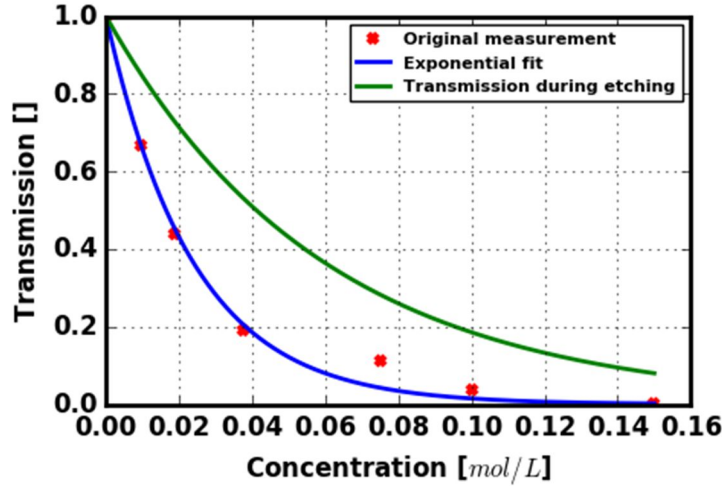


Figure 55: Transmission values of aqueous $\text{Na}_2\text{S}_2\text{O}_8$ solutions at a wavelength of 254 nm for different concentrations c and a fixed path length of the light of 1 cm. The experimental data points are fitted according to Equation [4-5]. The upper curve represents the calculated transmission for $d = 4$ mm; the same as during MAPCE experiments.

To evaluate whether the process of total dissolution necessarily requires an increased light intensity hitting the sample surface, the following experiment was conducted. MAPCE was performed for 90 minutes with an etching solution containing 0.04 mol/L $\text{Na}_2\text{S}_2\text{O}_8$. Then the distance between the sample and the UV source was increased from 7 mm to 20 mm. According to measurements of the UV light power density (0.4 mW/cm^2 at 7 mm and 0.2 mW/cm^2 at 20 mm), the light intensity was decreased to 50 % of the value present after 90 minutes of etching. Then etching was continued for 2 hours. Still total dissolution could be observed, despite the decreased light intensity, as illustrated in Figure 56.

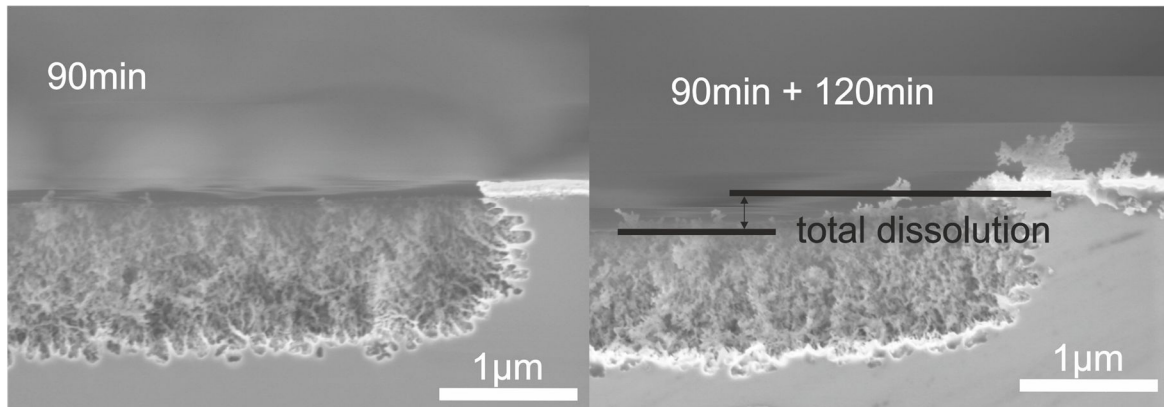


Figure 56: Cross-sectional SEM micrographs of porous 4H-SiC after 90 minutes and 90 minutes + 120 minutes of MAPCE. During the period of 120 minutes, the distance between the sample and UV source was increased to 20 mm. Etching solution: 1.2 mL of 0.04 mol/L $\text{Na}_2\text{S}_2\text{O}_8$ in 1.31 mol/L HF, while the C-face is exposed to the etchant.

This is in accordance with other experimental observations. The highest light intensity can be achieved with no oxidizing agent in the etching solution, but such an experiment showed no

formation of a porous layer. Also the formation of a line of breakage during experiments with H_2O_2 based solutions cannot be explained with total etching caused by an increased light irradiance. Furthermore pore formation into depth should be increased as well when the light intensity increases, which is not the case.

However the increased light intensity must play a role during etching. Indeed this can be seen in the experiments illustrated in Figure 47 and Figure 49 (section 4.3.1.2). An increased oxidizing agent concentration decreases the etching rate because the amount of light that hits the sample is decreased. So two effects control the etching behavior: the light intensity and the oxidizing agent concentration. UV light is needed for h^+ generation and the oxidizing agent is required for maintaining charge balance through electron transfer at the Pt electrode.

The presented results are in line with the current theory reported in literature. A space charge layer electrically insulates the porous layer from further etching. In the performed experiments there must be some effect that decreases this surface-near passivation. It may be related to the composition of the etching solution, as the light intensity could be ruled out as responsible factor. In accordance with these statements, it could be shown that an already partially dissolved porous SiC layer is stable in fresh etching solution. The corresponding SEM micrographs are illustrated in Figure 57. MAPCE for 15 minutes leads to a thin porous layer (see Figure 57a). After 60 minutes of etching total dissolution is already observed (see Figure 57b). Exposing a sample to 60 minutes of MAPCE and subsequently to a 15 minute etching step with fresh etching solution shows that the highly porous layer is stabilized (see Figure 57c).

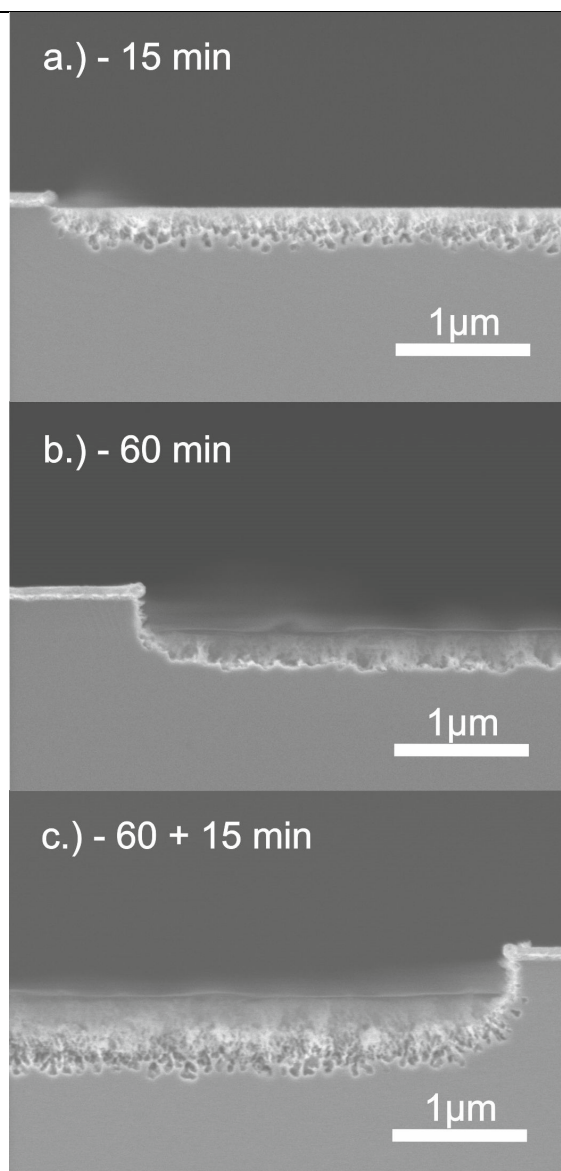


Figure 57: Comparison of differently etched samples. a.) Etching time of 15 minutes b.) Etching time of 60 minutes c.) Sample etched for 60 minutes and then etched in fresh etching solution for again 15 minutes. Etching solution: 1.2 mL of 0.08 mol/L $\text{Na}_2\text{S}_2\text{O}_8$ in 1.31 mol/L HF, while the C-face is exposed to the etchant.

4.3.1.4 Redox potential evolution of H_2O_2 and $\text{Na}_2\text{S}_2\text{O}_8$ solutions

Experiments showed that the redox potential decreases when applying an etching solution containing $\text{Na}_2\text{S}_2\text{O}_8$, which is in accordance with the Nernst Equation [76]. With less oxidizing agent in the solution, also the capability to accept electrons (the redox potential) is decreased. Etching solutions containing H_2O_2 showed the opposite behavior.

To study this in detail, the redox potential as a function of time was measured under UV light illumination. The UV light irradiation was done with the 18 W source, while as sensing electrode only a Pt wire was used (no 4H-SiC sample was immersed in the etching solution during these experiments). Also an increased volume of etching solution (22 mL) was necessary. At first a solution with a $\text{Na}_2\text{S}_2\text{O}_8$ concentration of 0.04 mol/L was investigated. The recorded values are shown in Figure 58. At the beginning, the UV source was switched on for approximately 4 minutes. As a consequence, an increase in the redox potential is measured which is attributed to the formation of $\text{SO}_4^{\bullet-}$ radicals. Next, the UV light was switched off, resulting in a decay of the redox potential. This shows that the chemical reactions initiated at the Pt/etching solution interface are reversible. Finally, in a third step, UV light was switched on again for four minutes and the redox potential increased again until a steady state condition was reached.

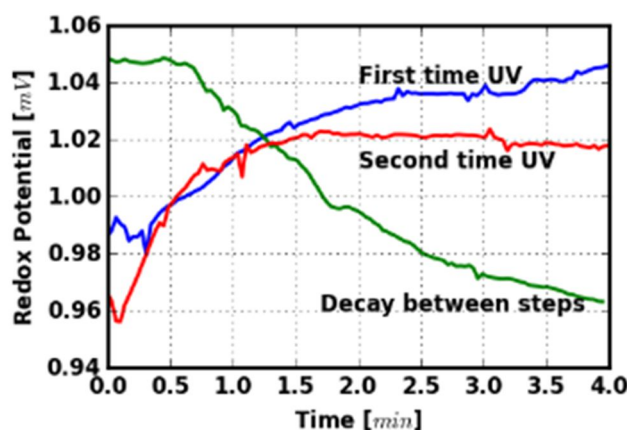


Figure 58: Redox potential characteristics of a solution with a $\text{Na}_2\text{S}_2\text{O}_8$ concentration of 0.04 mol/L in 1.31 mol/L HF as a function of time. First UV light was switched on for approximately 4 minutes, then switched off for 4 minutes (decay between steps) and then switched on again for 4 minutes (second time UV).

In the case of H_2O_2 the situation is different as shown in Figure 59. The experimental conditions were the same as for the experiment with $\text{Na}_2\text{S}_2\text{O}_8$. The H_2O_2 concentration was 0.04 mol/L. During the first UV illumination step, the redox potential decreased. Between steps, however, the UV source was switched off and the value of the redox potential stayed rather constant. During the second UV illumination period the redox potential slightly decreased until a constant value was reached.

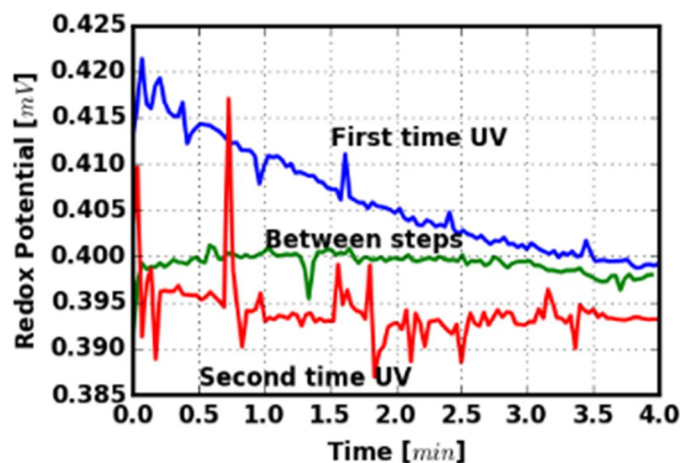


Figure 59: Redox potential characteristics of a solution with a H_2O_2 concentration of 0.04 mol/L in 1.31 mol/L HF as a function of time. First UV light was switched on for approximately 4 minutes, then switched off for 4 minutes (decay between steps) and then switched on again for 4 minutes (second time UV).

This can be explained with the adsorption of OH^\bullet radicals on the Pt surface which has been reported for Pt nanoparticles [93]. This leads to passivation and thus, the UV light induced reactions in the solution cannot be detected anymore. Such a behavior is reflected in the recorded characteristics of the redox potential shown in Figure 59. With increasing time more and more OH^\bullet radicals are adsorbed onto the surface of the Pt electrode. Finally the measured redox potential does not change anymore. This can explain the increasing redox potential observed during etching experiments. During etching, the H_2O_2 concentration drops because it is reduced at the sputter deposited Pt. With decreasing H_2O_2 concentration also the coverage of Pt with OH^\bullet radicals decreases and the measured redox potential increases. Finally, when all H_2O_2 is consumed the redox potential becomes constant at approximately the same value that was measured for pure 1.31 M HF solution (555 mV) (see section 4.3.1.1). This leads to the question whether H_2O_2 or not serves as oxidant during the total dissolution of the porous layer at later stages of etching. If H_2O_2 is not involved in the process, other species originating from a different source must serve as oxidant. A measurement of the redox potential under UV light illumination was performed with a solution containing 1.31 mol/L HF. The measured values are illustrated in Figure 60. It can be seen that the redox potential decreases during UV illumination and that there is a less pronounced recovering tendency in the dark. This is a similar behavior as has been observed for the solution containing 0.04 mol/L H_2O_2 .

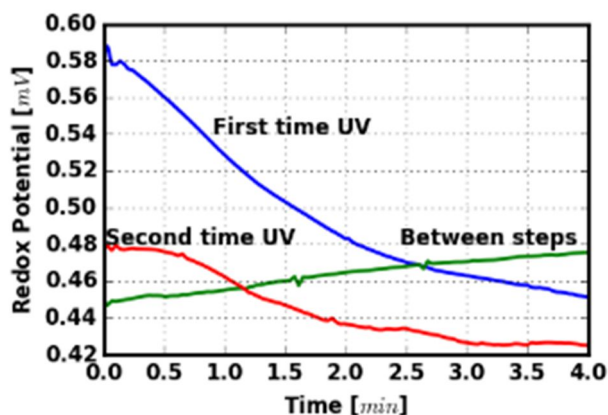


Figure 60: Redox potential characteristics of a solution with a HF concentration of 1.31 mol/L HF as a function of time. First UV light was switched on for approximately 4 minutes, then switched off for 4 minutes (decay between steps) and then switched on again for 4 minutes (second time UV).

This indicates that the Pt electrode also gets covered with UV light generated species. Regarding the total dissolution of the porous layer this indicates that oxidants originating from a different source than H_2O_2 can participate in the etching reaction. Possible species are oxygen dissolved in the etching solution like it is reported in studies focusing on metal assisted etching of silicon [94]. Moreover hydroxide radicals can be produced in the presence of Pt in a process similar to photocatalytic water splitting [95].

4.3.1.5 Experiments with the Si-face

In this section experiments with the Si-face are presented. The goal was to confirm whether the principles revealed in the previous sections are also valid when the Si-face is etched. Figure 61 shows the corresponding etching depth and redox potential evolution when $\text{Na}_2\text{S}_2\text{O}_8$ is used as oxidizing agent. The corresponding SEM micrographs are illustrated in Figure 62. Like it was the case for etching of the C-face a decreasing redox potential is accompanied by a decreasing etching rate. Moreover, also total dissolution of the porous layer takes place at the later stages of etching.

So in principle, MAPCE of the Si-face exhibits the same characteristic features as MAPCE of the C-face. After having confirmed this, the collected findings are discussed and interpreted in the next section.

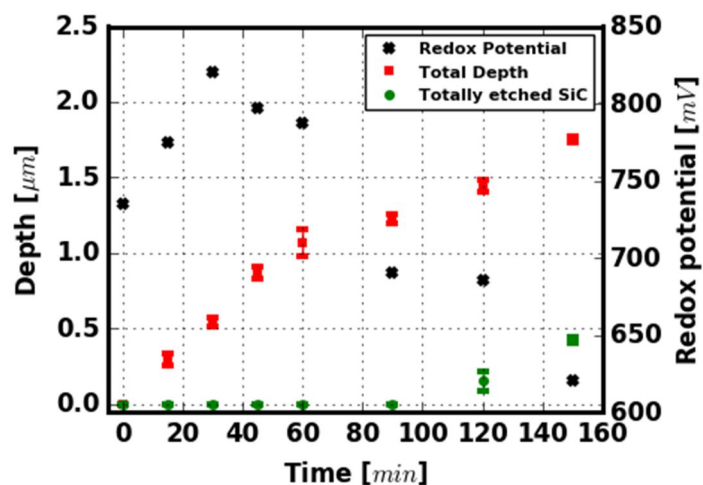


Figure 61: Etching depth and redox potential versus time. Etching solution: 1.2 mL of 0.08 mol/L $\text{Na}_2\text{S}_2\text{O}_8$ in 1.31 mol/L HF, while the Si-face is exposed to the etchant. The error bars represent the standard deviation from 10 measurements.

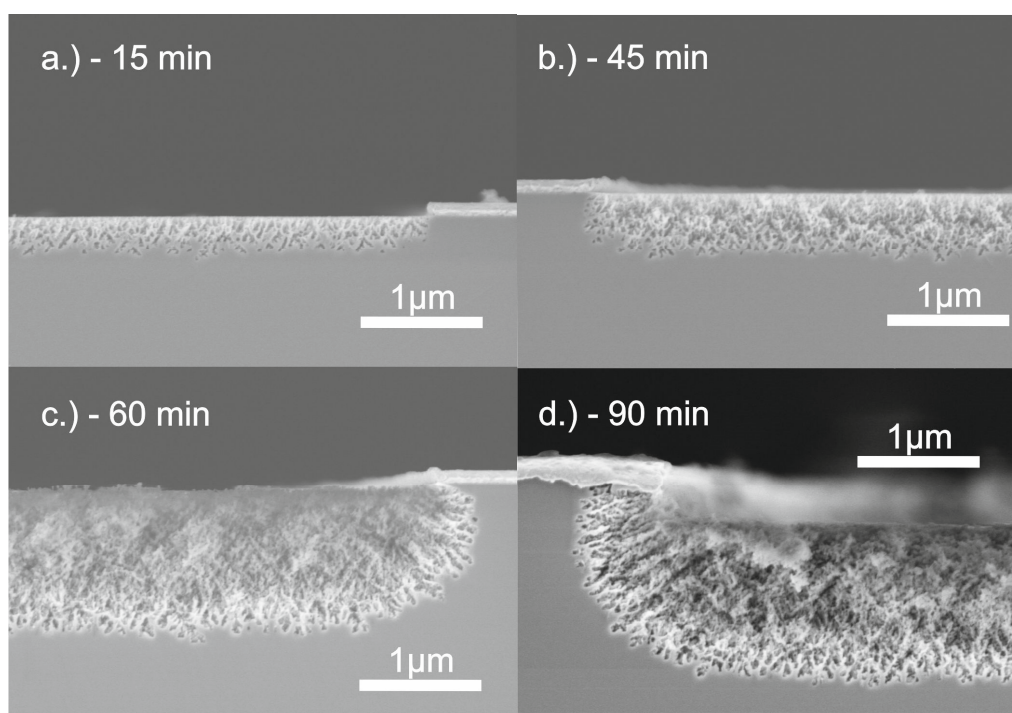


Figure 62: Evolution of the porous layer with increasing etching time. Etching solution: 1.2 mL of 0.08 mol/L $\text{Na}_2\text{S}_2\text{O}_8$ in 1.31 mol/L HF, while the Si-face is exposed to the etchant.

4.3.1.6 Discussion

So far the experimental data allow several statements about MAPCE of 4H-SiC. No increased etching depth was observed near the deposited Pt. Furthermore, when UV light is focused onto the sample with a light-wave cable, the etching depth is lower in the vicinity of the sputter deposited Pt, in contrast to regions being further away, in the focus of the UV light. So it can be concluded that the electron hole pair generation is done by the UV light irradiation. The UV light generated h^+ initiate the oxidation of SiC according to the Equations [2-22] to [2-24]. The formed oxide is then dissolved by HF (see Equation [2-25]).

This is in contrast to metal assisted etching of other semiconductors like silicon [10] or InP [13] where the oxidant creates h^+ in the semiconductor and etching is enhanced near the metallic cathode.

Despite this difference, the role of the deposited Pt is to serve as anode; without Pt no etching could be observed. The oxidizing agent serves as electron consumer during etching and takes up electrons at the Pt/etching solution interface. In agreement with this assumption, an etching experiment with deposited Pt and just HF in the etching solution showed only surface roughening (see Figure 63).

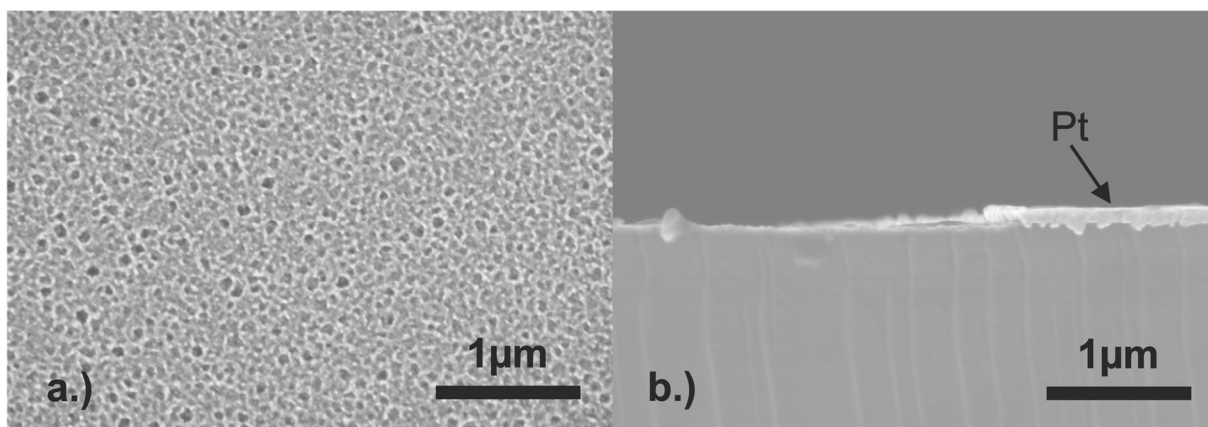


Figure 63: Sample of 4H-SiC after 60 minutes of MAPCE without oxidizing agent. Etching solution: 1.2 mL of 1.31 mol/L HF, while the C-face is exposed to the etchant. a.) Top view b.) Cross sectional view.

Altogether the following statements can be made: the UV light irradiation generates electron hole pairs. When the holes are responsible for the oxidation of SiC, charge balance must be maintained for etching to proceed. This is done by the oxidizing agent at the Pt cathode, which is reduced and takes up electrons as is shown in Equation [4-6].



Basically, the etching depth is lower for experiments performed with higher $Na_2S_2O_8$ (compare Figure 47 with Figure 49) concentration. This is explained with a decreased UV light intensity

that hits the sample, due to a higher oxidizing agent concentration. So the oxidizing agent concentration and the UV light intensity are the main factors competitively controlling the etching rate during MAPCE.

Prior to the experiments presented in this study, it was assumed, that with proceeding etching time the porosity in the layers should become more homogeneous and uniform; the space charge layer formed at the electrolyte semiconductor junction should limit the final degree of porosity. This was confirmed with our experiments, as can be seen in Figure 44, Figure 46 and Figure 48.

Furthermore, an evaluation of the surface pore size showed that there is a passivating effect that protects the upper part of the porous layer from further etching. This passivating effect can also be attributed to the space charge layer at the electrolyte semiconductor junction. With increasing porosity the insulating effect of the space charge layer becomes more dominant and the etching rate slows down.

The experiments have also revealed that this passivating effect is only present under certain experimental conditions. At the later stages of etching when the oxidizing agent concentration is low, total dissolution occurs and the passivating effect is lost.

This indicates that the oxidizing agent concentration is the main factor that is responsible for total dissolution of porous SiC. When the oxidizing agent concentration decreases, the chemical potential of the etching solution increases. As a consequence, the width of the space charge layer decreases in n-type SiC and thus the insulating effect is reduced. Another explanation is that with increased oxidation rate the amount of surface states is enhanced as well. Konstantinov *et al.* [41] claimed that the surface states pin the Fermi level during anodic etching of SiC and control the width of the space charge layer. This theory is supported by the formation of a line of breakage when using H₂O₂. The total dissolution starts at the bottom of the porous layer (see Figure 46). Such an underetching of the porous layer can only be explained by a chemical passivation of the surface of the porous material.

In summary, it can be concluded that MAPCE of n-type SiC is controlled by two competing factors: the oxidizing agent concentration and the UV light intensity. The effect of total dissolution can be explained with a decreased width of the space charge layer in the porous SiC with increasing etching time.

4.3.2 Chemical composition of the porous layers

Since little knowledge about MAPCE of 4H-SiC is available, the chemical composition of the prepared porous layers was investigated. Furthermore in the previous section it was stated that surface states are responsible for the effect of total dissolution. A chemical analysis of the porous layers can give information about their surface terminations. The etched area during the

experiments presented in this section was 0.9 cm^2 . First ATR-FTIR measurements were performed to investigate which functional groups are generated during MAPCE. Next, TOF-SIMS depth profiling was carried out to assign the observed peaks in the IR spectra. MAPCE was done in time intervals of 30 minutes. After each interval the old etching solution was replaced by a fresh one to prevent total dissolution. By doing so, the thickness of the porous layers could be increased and clearly identifiable peaks in the IR spectra were obtained. Experiments were performed with H_2O_2 or $\text{Na}_2\text{S}_2\text{O}_8$ as oxidizing agent while the concentration was in both cases 0.15 mol/L .

4.3.2.1 Experiments with H_2O_2

In Figure 64a, the IR spectra (after baseline subtraction) of samples are presented where MAPCE was performed with H_2O_2 as oxidizing agent, while Figure 64b and Figure 64c allow enlarged views on the same spectra. The not etched 4H-SiC sample shows characteristic peaks at 810 cm^{-1} and 950 cm^{-1} which are assigned to the TO SiC phonons and LO SiC phonons [96]. The small peaks at 1972 cm^{-1} , 2030 cm^{-1} and 2157 cm^{-1} are assigned to multi phonon absorptions [97,98]. These features vanish with increasing etching time and new peaks appear, due to the MAPCE process. There is a peak at around 1020 cm^{-1} and a triple peak in the region of 2900 cm^{-1} . To assign the peaks to functional groups, a TOF-SIMS depth profile was recorded from a sample that had been etched for 180 minutes (see Figure 65). F^- as well as O^- related signals were detected. Both characteristics tend to decrease with depth before a relative maximum occurs. Finally the signal intensity almost vanishes for both F^- and O^- . The $^{30}\text{Si}^-$ isotope signal is given for comparison reasons, reflecting the degree of porosity as a function of depth qualitatively. There is no clear maximum in the $^{30}\text{Si}^-$ characteristics.

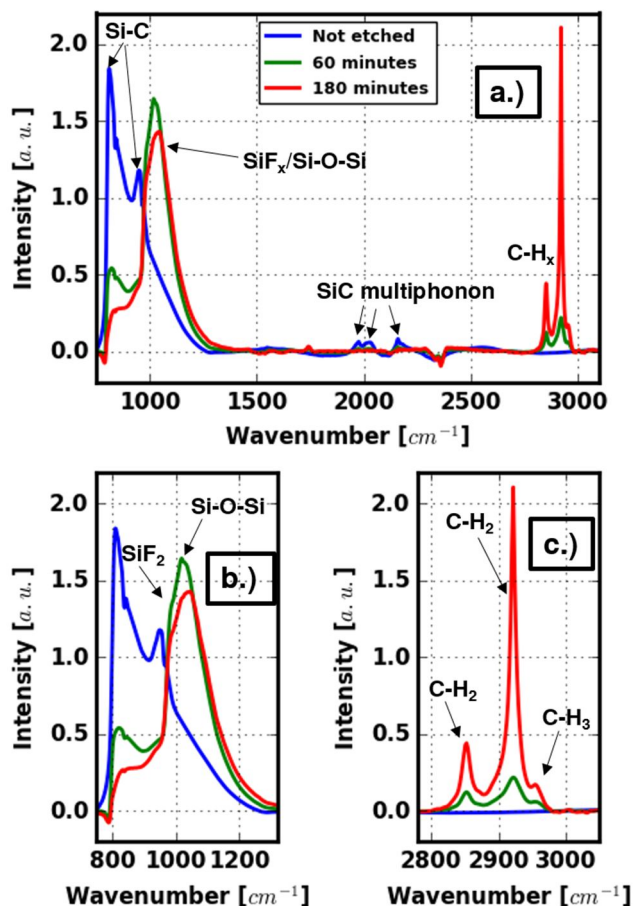


Figure 64: ATR-FTIR spectra of 3 samples, each of them etched in 30 minute MAPCE periods. Etching solution: 1.2 mL of 0.15 mol/L H_2O_2 in 1.31 mol/L HF. During etching, the C-face was exposed to the etchant, while the etched area was 0.9 cm^2 . a.) Overview of all three spectra. b.) Enlarged view of the Si-C, SiF_2 and Si-O-Si vibrations c.) Enlarged view of the C- H_x vibrations.

The observed features can be interpreted as follows: the F^- as well as the O^- signal decreases with sputter time because the surface-near regions were exposed to the etching solution for a longer time. The local maxima at approximately 50 minutes of sputter time are related to the active zone during etching. This is shown in Figure 66. At the surface-near regions of the porous layer, the MAPCE etching rate is low due to the passivating effect of the space charge layer. Below this protected region an active etching zone begins, thus peaks related to O^- and F^- are detected due to the chemical reactions which take place during MAPCE. Simultaneously the intensity of the $^{30}\text{Si}^-$ signal decreases because of a gradually decreasing porosity within the active zone. The decrease of the $^{30}\text{Si}^-$ is attributed to a higher sputter rate of porous SiC compared to bulk SiC. This is in agreement with findings presented in the previous section; at the top of the porous layer etching stops while pore formation into depth still takes place (see Figure 49 and Figure 52). The Si^- as well as the C^- related ion signals were in the upper detector compliance limit (not shown in Figure 65). Hence it can be reasoned that most of the porous layer

is still SiC. With this elemental information, peak assignment of the spectra in Figure 64 is done. The first peak at around 1020 cm^{-1} is assigned to Si-O-Si stretching vibrations [99]. This peak has a shoulder at 985 cm^{-1} which is assigned to SiF₂ stretching vibrations [100,101]. The triple peak centered at around 2900 cm^{-1} is due to sp^3 C-H₂ stretching (i.e. 2852 cm^{-1} symmetric and 2921 cm^{-1} asymmetric) and sp^3 C-H₃ asymmetric stretching (2956 cm^{-1}) [99].

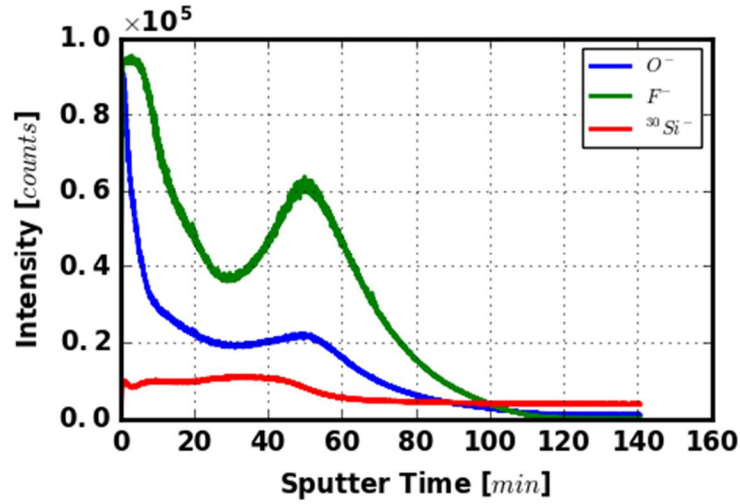


Figure 65: TOF-SIMS depth profile of a sample that was etched for 180 minutes (30 minute periods) in 1.2 mL of 0.15 mol/L H₂O₂ in 1.31 mol/L HF. During etching, the C-face was exposed to the etchant, while the etched area was 0.5 cm².

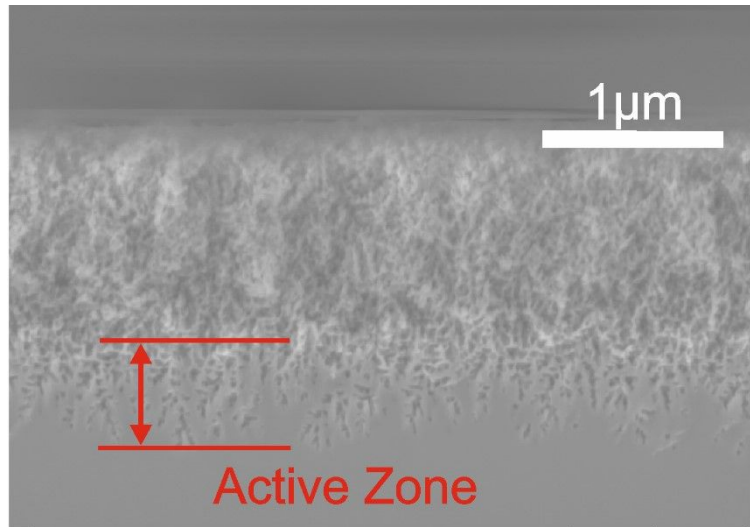


Figure 66: Cross-sectional SEM micrograph of a porous 4H-SiC sample corresponding to the TOF-SIMS experiment illustrated in Figure 65.

The findings support the stated mechanism of MAPCE described in section 2.2.2.1 since Si-O-Si vibrations are identified in the IR spectra and O⁻ peaks were found during the SIMS meas-

urements which cannot be due to oxidation with atmospheric oxygen. According to the proposed mechanism, silicon carbide is first oxidized and then dissolved by HF. So far, this has been just a hypothesis, but not proven by experiments [47]. The results also show that there is fluoride present in the porous layer after etching. Based on this knowledge it is now possible to formalize a detailed mechanism of MAPCE, but it is possible that in addition to H_2O , F^- serves as nucleophilic species during oxidation and direct dissolution of SiC like in the case of Si (see section 2.3). Such a behavior has been suggested by Lauermaun *et al.* for anodic etching of SiC [102]. Finally, the C-H_x vibrations are interpreted as follows: Once the oxidation products are dissolved, the pure SiC surface remains, but terminated with hydrogen.

Furthermore, no indications for the presence of a carbon rich layer could be found, which is often mentioned in reports related to electrochemical etching of SiC [96,103]. Peaks between 1200 cm^{-1} and 1800 cm^{-1} in the IR spectrum are attributed to C-C vibrations [104] while other authors label them as N-H vibrations (nitrogen from the doping of SiC) [54]. Such peaks could not be observed during the presented experiments. This shows that the surface termination is different from the one obtained from pure electrochemical etching of SiC. It is also in agreement with the finding of Rittenhouse *et al.*, that porous SiC obtained from MAPCE shows different photoluminescence than porous SiC obtained from pure electrochemical etching [53]. The photoluminescence is attributed to surface states, so a different surface termination is expected.

4.3.2.2 Experiments with $\text{Na}_2\text{S}_2\text{O}_8$

Next, the experimental results with $\text{Na}_2\text{S}_2\text{O}_8$ as oxidizing agent are presented. Figure 67 shows the corresponding IR-spectra while Figure 68 presents the TOF-SIMS depth profile. The same elements were found during the TOF-SIMS analysis and the same functional groups were identified in the IR spectra. A major difference is the relative intensity of the C-H_x peaks and the Si-O-Si peak compared to the experiments with H_2O_2 . By comparison of Figure 64 with Figure 67 one can see that the intensity of the C-H_x peaks relative to the Si-O-Si peak is higher for the samples which were etched with H_2O_2 . This indicates that the C-H_x functional groups at the surface are responsible for the passivating effect observed during MAPCE. The passivating effect is more pronounced with H_2O_2 as oxidizing agent (see Figure 46 – formation of line of breakage). Since the C-H_x intensity is increased as well when H_2O_2 is used, it is reasoned that those functional groups contribute predominantly to the observed passivating effect. This means, in turn, that they are responsible for Fermi level pinning during etching.

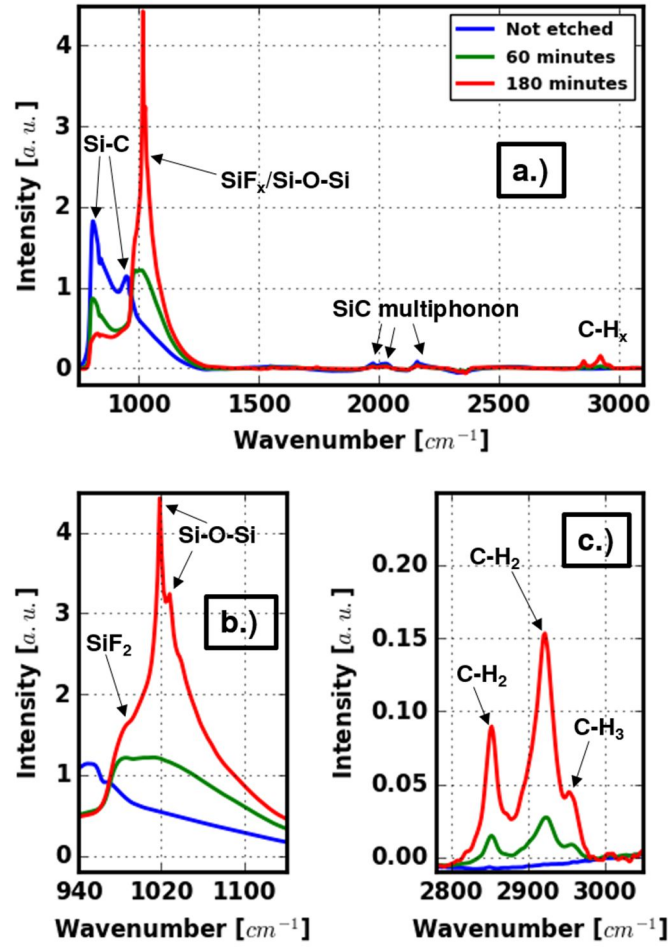


Figure 67: ATR-FTIR spectra of 3 samples, each of them etched in 30 minute MAPCE periods. Etching solution: 1.2 mL of 0.15 mol/L $\text{Na}_2\text{S}_2\text{O}_8$ in 1.31 mol/L HF. During etching, the C-face was exposed to the etchant, while the etched area was 0.9 cm^2 .

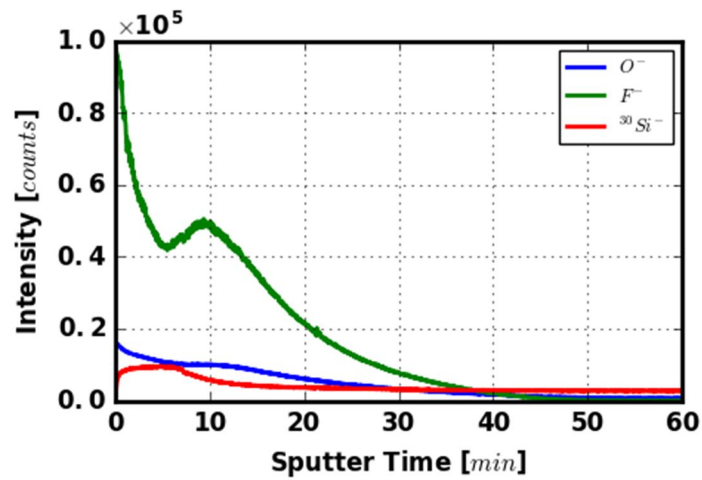


Figure 68: TOF-SIMS depth profile of a sample that was etched for 180 minutes (30 minute periods) in 1.2 mL of 0.15 mol/L $\text{Na}_2\text{S}_2\text{O}_8$ in 1.31 mol/L HF. During etching, the C-face was exposed to the etchant, while the etched area was 0.9 cm^2 .

4.4 Cellular automaton simulation of MAPCE

In this section a cellular automaton (CA) [105] based model of MAPCE is implemented. This was done to evaluate whether MAPCE can be reproduced by a discrete stochastic model based on the findings of sections 4.2 and 4.3. Furthermore this allows the investigation of experimentally not quantifiable parameters, such as the time evolution of oxidizable sites.

4.4.1 Experimental observations

First, data derived from the previous chapter are introduced, as basis for the following discussion. Figure 69 shows two cross-sectional SEM micrographs of porous SiC which had been generated with MAPCE. In both cases the etching time was 120 min. and $\text{Na}_2\text{S}_2\text{O}_8$ served as oxidizing agent. In the case of an initial $\text{Na}_2\text{S}_2\text{O}_8$ concentration of 0.15 mol/L an active zone length of approximately 0.5 μm could be observed. It was found that the etching reaction takes place mostly in this region while the upper highly porous layer is protected from total dissolution by a space charge layer insulating the material. The active zone length increases when the etching rate is relatively constant between 15 and 90 min. of etching time as is illustrated in Figure 70. When the etching rate drops the active zone length becomes constant as a function of etching time (see also Figure 70).

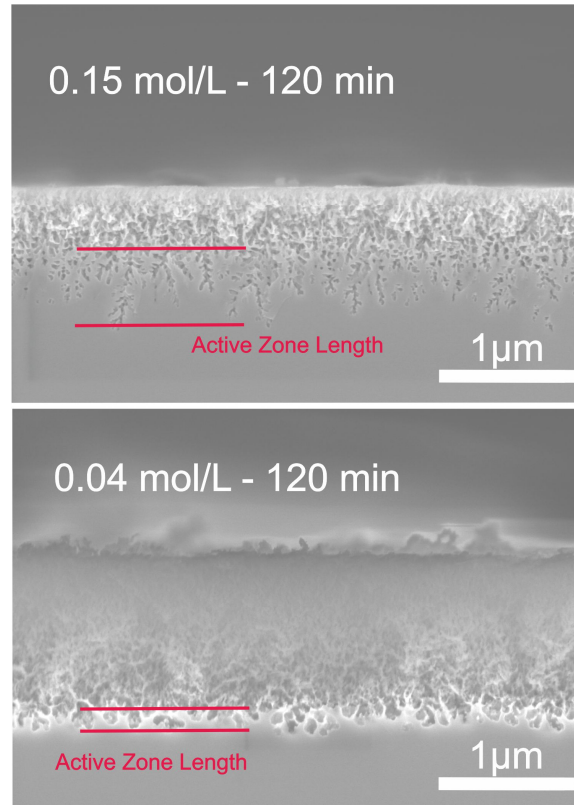


Figure 69: Cross-sectional SEM micrographs of MAPCE generated porous SiC after the same etching times, but different oxidizing agent concentrations. An etching solution containing 0.15 mol/L $\text{Na}_2\text{S}_2\text{O}_8$ yields a higher active zone length than a solution containing 0.04 mol/L $\text{Na}_2\text{S}_2\text{O}_8$.

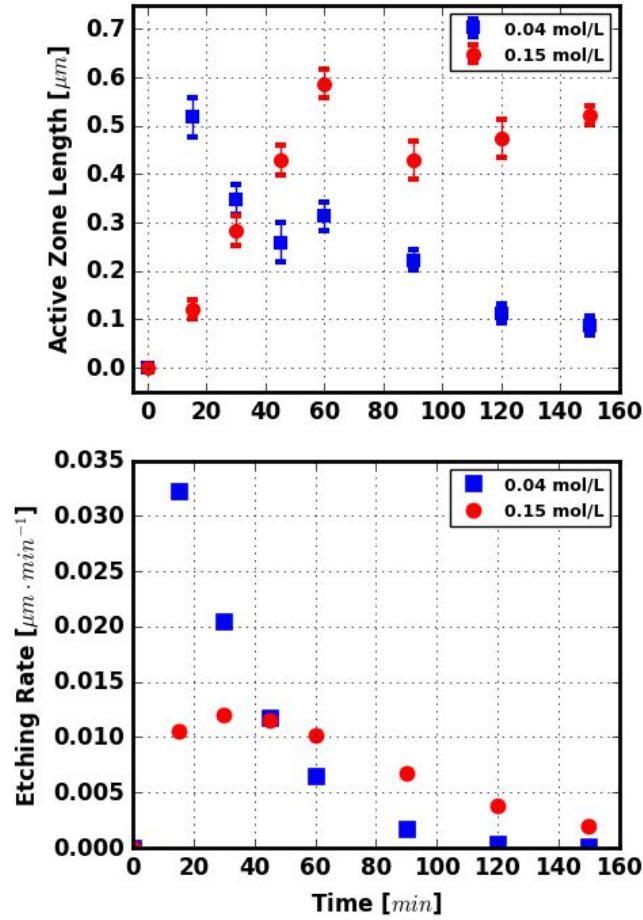


Figure 70: Active zone length and etching rate as a function of etching time for different initial oxidizing agent concentrations.

The situation is different when the initial oxidizing agent concentration is decreased to 0.04 mol/L as can be seen in Figure 69 as well as in Figure 70. In this case the etching rate drops to zero, which is accompanied by a significant decrease of the active zone length. The drop in etching rate in both cases is explained with the consumption of $\text{Na}_2\text{S}_2\text{O}_8$ throughout MAPCE and thus a decreased oxidation rate.

In summary it can be stated that a constant etching rate causes an increasing active zone length. When the etching rate drops the active zone length becomes constant as a function of etching time or even goes to almost zero.

These experimental observations lack a theoretical explanation. Therefore a straightforward cellular automaton (CA) simulation was implemented to mimic MAPCE and to evaluate the measurement results with the theoretical predictions.

4.4.2 Implementation details

First a 2-dimensional grid of cells is defined, whereas a different particle type is assigned to each cell. Then the time is increased in discrete steps. During each step every particle type can interact with its surrounding, following certain pre-defined rules.

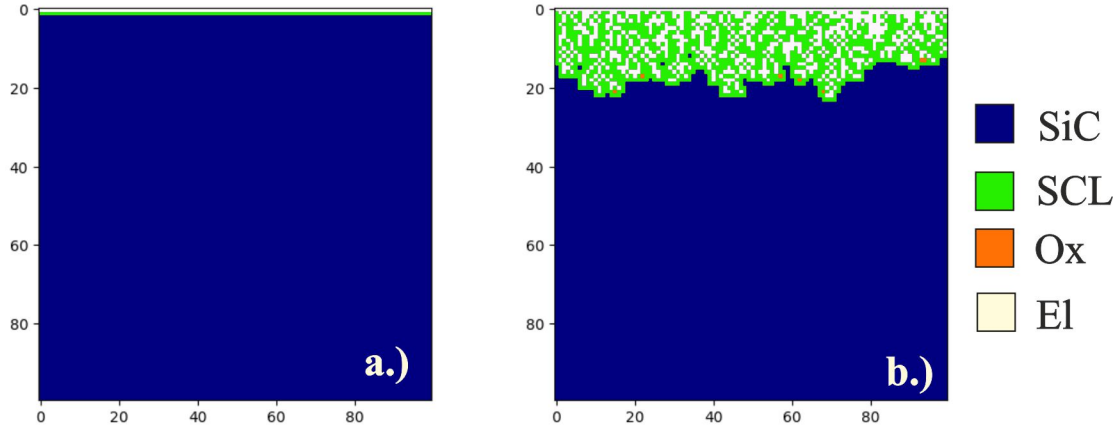


Figure 71: Graphical visualization of the implemented cellular automaton with a legend of the defined particle types a.) Initial conditions b.) Snapshot after start of the simulation.

After this rather abstract definition the concrete details of the implemented CA are given. Four different particle types were used in analogy to the experimental observations of the previous sections. These are silicon carbide (*SiC*), space charge layer (*SCL*), Oxide (*Ox*) and Elektrolyte (*El*). Initially all the cells of the 2D grid are of the type *SiC*, except the two top rows which are of type *SCL* and *El* (see Figure 71a). This mimics a *SiC* wafer immersed in an etching solution, where at the phase border a semiconductor-electrolyte junction forms.

According to the findings in the previous sections, *SiC* is oxidized and the oxide is afterwards dissolved by HF when etching takes place. To mimic this behavior in the CA all the defined particle types need to obey defined rules when the time is increased.

First the *SCL* particles are discussed. In the implemented CA this particle type can be oxidized, meaning that the cell status can only switch from *SCL* to *Ox*. To be oxidizable, an *SCL* particle has to be surrounded by *SiC* and *El* particles in a specific way, which is now explained. Every particle *P* has a set of surrounding elements *S* (see Figure 72 and Equation [4-7]). For an *SCL* particle to be oxidizable, opposing cells of the surrounding need to be of the type *SiC* and *El*, respectively.

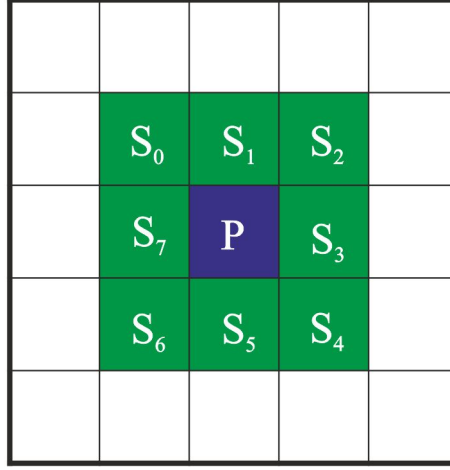


Figure 72: Particle P on the 2D CA grid and its surrounding cells S_n .

$$S = \{S_n | n \in \{0,1,\dots,8\}\} \quad [4-7]$$

This necessary condition for an SCL particle for being oxidizable is generalized in Equation [4-8]. Starting from any cell $S_n = S_{m \bmod 8}$ in the surrounding of an SCL particle, the opposing cell $S_{(m+4) \bmod 8}$ needs to be of type SiC when the n^{th} cell is of type El and *vice versa*. For instance when S_2 is of type SiC , S_6 has to be of type El . This condition was chosen because in reality the direction of the electric field is perpendicular to the etching front and a hole necessary for oxidation is accelerated in this direction.

$$S_{m \bmod 8} == El \text{ and } S_{(m+4) \bmod 8} == SiC \quad [4-8]$$

Furthermore when oxidation takes place in the CA as described, all the cells of type SiC in the surrounding of the newly defined Ox particle are switched to the status SCL .

When a cell of type SiC is oxidized its type changes to Ox . This type also has certain pre-defined properties. When there is an El particle in the surrounding, the original cell of type Ox can change its status to El as well. This corresponds to the dissolution of oxide in real experiments.

To start the CA simulation a defined percentage of all oxidizable SCL particles on the 2D grid are randomly oxidized in a first step (oxidations rate). In a second step a defined percentage (dissolution rate) of the generated Ox particles which can be dissolved are dissolved as previously described. These two processes (oxidation and dissolution) are carried out on the 2D grid until a certain average etching depth is reached. The result of such a simulation is shown in Figure 71b. A porous layer, fully covered by SCL particles (space charge layer) is followed by an active zone with decreasing degree of porosity. There, Ox particles are statistically distributed. This is in accordance with the findings of section 4.3. So the implemented CA qualitatively resembles real MAPCE experiments.

4.4.3 Comparison with real experiments

In this section the numerical results from the CA are presented. Figure 73 shows a typical outcome of a performed simulation. All the following statements are valid, independent of variation of the simulation parameters. In the presented CA run the oxidation rate was set to 40 %, the dissolution rate to 20 % and the grid size was 200 x 200 grid units. Finally the simulation was programmed to terminate at an etching depth of 180 grid units.

Throughout the whole simulated experiment the average etching depth increased because of constant oxidation and dissolution rates. The etching depth within a column is defined as the highest value x_i of a cell of type electrolyte. The average etching depth \bar{x} is thus given by Equation [4-9], where N is the number of columns defined for the CA.

$$\bar{x} = \frac{1}{N} \sum_{i=1}^N x_i \quad [4-9]$$

The etching rate decreases throughout the CA run until it becomes constant. This is similar to the experimental result when an etching solution containing 0.15 mol/L $\text{Na}_2\text{S}_2\text{O}_8$ was used (see Figure 70 and Figure 49).

Indeed there are further similarities between the CA model and the experimental findings. The standard deviation from the average etching depth is a measure of the active zone length in the CA simulation. The corresponding graph in Figure 73 resembles the active zone length graph in Figure 70 (0.15 mol/L). Both curves show at first a positive slope until they become almost constant. This indicates that the CA simulations qualitatively mimic the trends of MAPCE as long as the etching rate does not drop significantly. This is also in accordance with a slight increase of the standard deviation in the CA analysis. In the real experiment the active zone length does not increase anymore, due to an already decreasing etching rate.

An analysis of the amount of oxidizable and oxide particles as a function of simulation time (see Figure 73) shows that an on average constant standard deviation of the etching depth is accompanied by a constant level of these quantities. So it is reasoned, that the constant thickness of the active zone length at a constant etching rate is due to a steady state condition which is reached after a transient phase at the beginning of MAPCE. Furthermore, this demonstrates that MAPCE is governed mainly by time stochastic processes when the etching rate is constant.

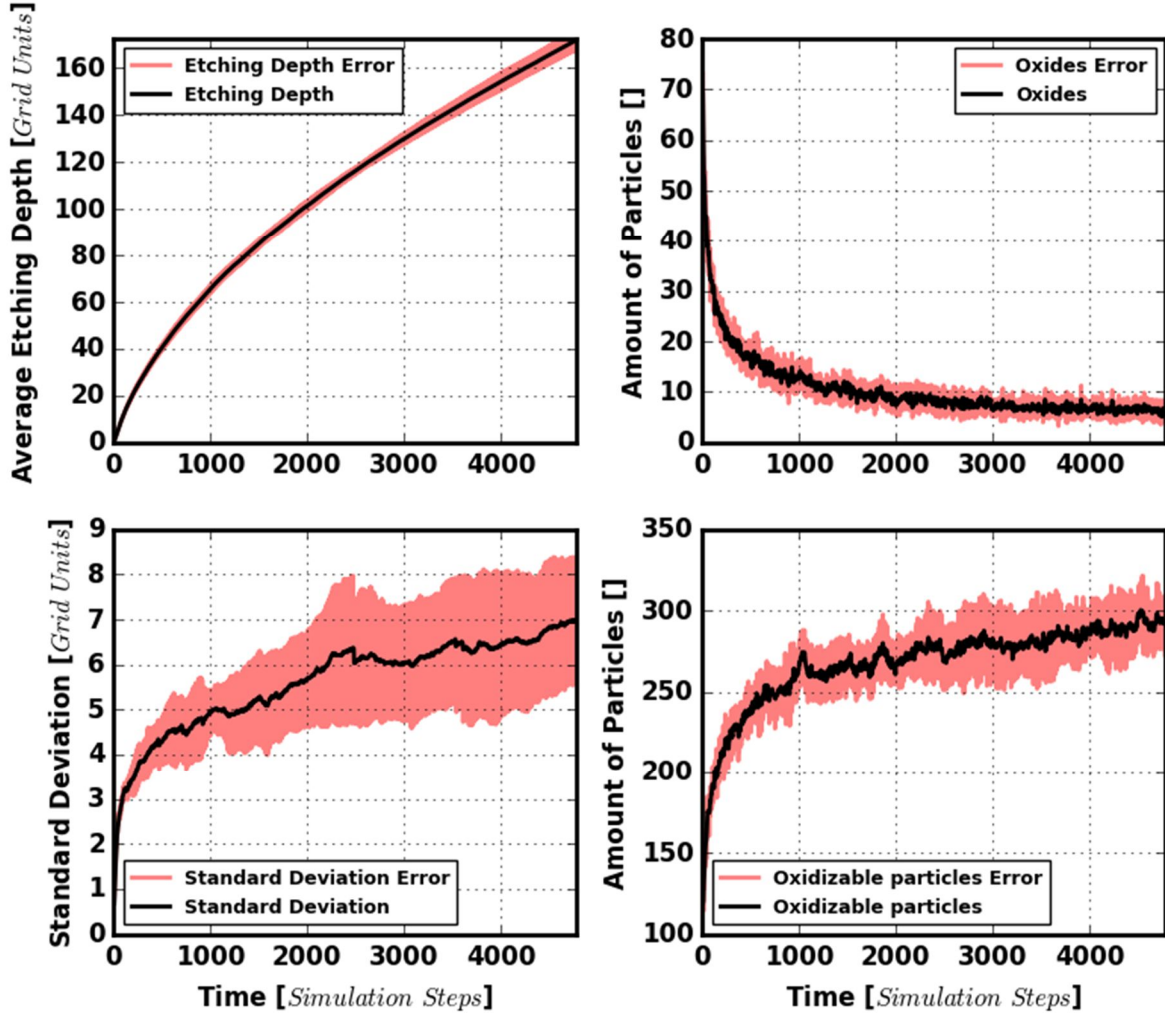


Figure 73: Results from a CA simulation utilizing an oxidation rate of 0.4, a dissolution rate of 0.2 and a grid size of 200 x 200 grid units. The presented values represent the average from 10 performed CA runs. The red error areas represent the standard deviation from 10 individual CA runs. .

In the case of a not constant etching rate, when the oxidizing agent concentration considerably decreases throughout MAPCE, the active zone length decreases and a sharp interface between porous layer and bulk material forms. This was the case during the MAPCE experiment performed with 0.04 mol/L $\text{Na}_2\text{S}_2\text{O}_8$ (see Figure 70).

To consider this significant decrease in etching rate, the oxidation rate in the CA was implemented as a function of time according to Equation [4-10]. The initial oxidation rate is given by Ox_0 , k represents the steepness of the curve and t_0 is its turning point.

$$Ox(t) = Ox_0 \left[1 - \frac{1}{1 + e^{-k(t-t_0)}} \right] \quad [4-10]$$

These functions are known as logistic functions [106] and were chosen in the CA because of the sigmoid-like tail of etching rate with time found in real experiments (see Figure 70). Figure 74 shows the evolution of the oxidation rate for different values of k obtained from CA simulations. The initial oxidation rate was 0.3 in every case, the turning point was set to 5000 simulation steps and the grid size was 200 x 200 grid units. The number for the initial oxidation rate was chosen such that there is a remarkable standard deviation of the etching front which can drop when the oxidation rate decreases. If the CA model correctly predicts the decrease of active zone length, as seen in the experiment, the standard deviation of the etching depth as a function of k should show an increasing tendency. This is not the case as can be seen in Figure 75. The steepness of the oxidation rate k is varied over several orders of magnitude without substantially affecting the final standard deviation of the average etching depth.

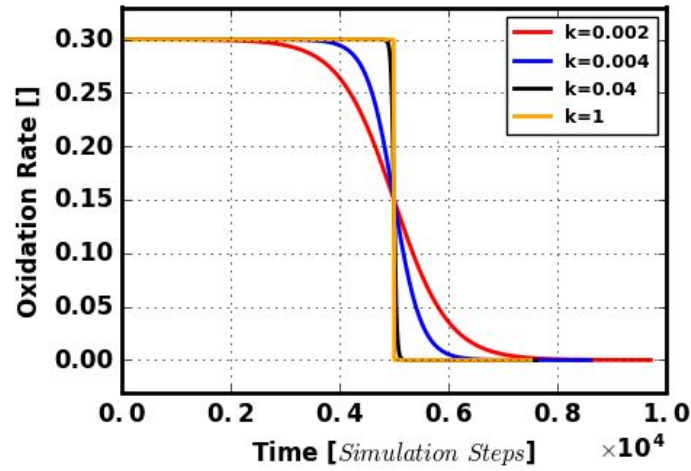


Figure 74: Oxidation rate during CA simulations for different steepness factors.

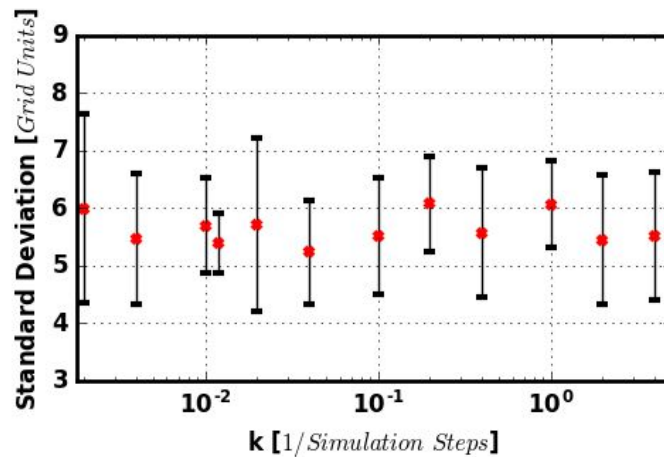


Figure 75: Standard deviation of the average etching depth versus steepness of the oxidation rate. The error bars represent the standard deviation resulting from 10 CA runs.

This discrepancy between the experimental results and those from the CA can be explained with the experimental observations reported in section 4.2.2. There it was found that when a porous PECE layer is subjected to a MAPCE post treatment, a constant degree of porosity is realized in the layer. When MAPCE is carried out the degree of porosity of the already existing PECE layer increases. Further pore growth into depth does not take place before a constant degree of porosity is achieved. This indicates that the formation of new pores is energetically less favorable during MAPCE than etching of already existing pores.

Moreover, in section 4.3 it was found that MAPCE is capable of producing highly porous and uniform layers when small volumes of etchant are used, causing a significant drop of etching rate with time. The given data from the CA simulations and section 4.2.2 indicate that this homogenous porosity obtained in experiments is due to a decreasing pore formation rate into depth and the energetically more favorable etching of already existing pores. Put differently, a statistical process with equal probabilities –like simulated in the CA- cannot yield a decreased active zone because no site is preferentially etched. However in reality this is indeed the case. When the oxidizing power of the solution decreases already existing pores are further etched, while the initiation of new pores slows down. These two effects lead to the formation of homogeneous porous layers with a defined etching front in the bulk material.

4.4.4 Conclusions

In this section CA simulations of MAPCE have been performed. It could be shown that MAPCE can be described theoretically by this simple statistical model, when assuming a constant oxidation rate. However, when the oxidation rate considerably drops as occurring in the experiments an evaluation with the CA approach fails. This is because in the experiments new pore initiation into depth is not the dominant effect and already existing pores are preferentially etched. Despite this drawback in describing the latter effect, the CA model confirms the findings and results of the previous sections on a qualitative level.

4.5 Preparation of stacked porous layers with alternating degree of porosity

Parts of this section have been published in [107].

In the previous sections the fundamentals of MAPCE have been investigated and PECE could be optimized, such that skin and cap layer formation can be avoided. In this section the influence of the electrical parameters during PECE on the resulting degree of porosity is investigated. Tailoring the degree of porosity as a function of depth is important for several device applications such as filters for proteins [108] or optical mirrors [61].

The work performed in this section aims to create a process serving as technological basis for the preparation of porous SiC layers that can be used within e.g. optical Bragg filters. In particular, this requires the capability to produce individual porous layers with alternating degree of porosity, while the porosity within each sub layer is constant. Beside these technological issues, this work also intends to contribute to the fundamental knowledge of PECE of SiC which is necessary for the implementation as a reliable process technology.

In detail, current as well as voltage controlled experiments were conducted. First the current controlled experiments are presented and afterwards the results from the voltage controlled experiments are shown.

During all experiments the Si-face was porosified. For the PECE experiments in this section an aqueous solution containing 5.7 mol/L HF and 1.7 mol/L ethanol was used. MAPCE experiments for the pre-treatment of the 4H-SiC substrate were performed as described in Figure 76. The steps *i* (substrate cleaning with Argon plasma) and *ii* (surface near doping with phosphoric acid solution) were performed like in section 4.2. Until section 4.5.2 MAPCE was continued as described by the steps *iii* and *iv*. This is also the same procedure as presented in section 4.2. Pt pads were sputter deposited in the middle of the sample and then etching was performed in the AMMT etching chamber while the 250 W UV source was used. The experiments after section 4.5.2 were conducted with a MAPCE pre-treatment similar to the one described in section 4.3 (steps *iiia* and *iva*). In this route only 10 mL of etching solution were necessary and the 18 W UV source was used. This was done to modify the etching process. The reason for this modification is explained in section 4.5.2 as well as the detailed experimental parameters.

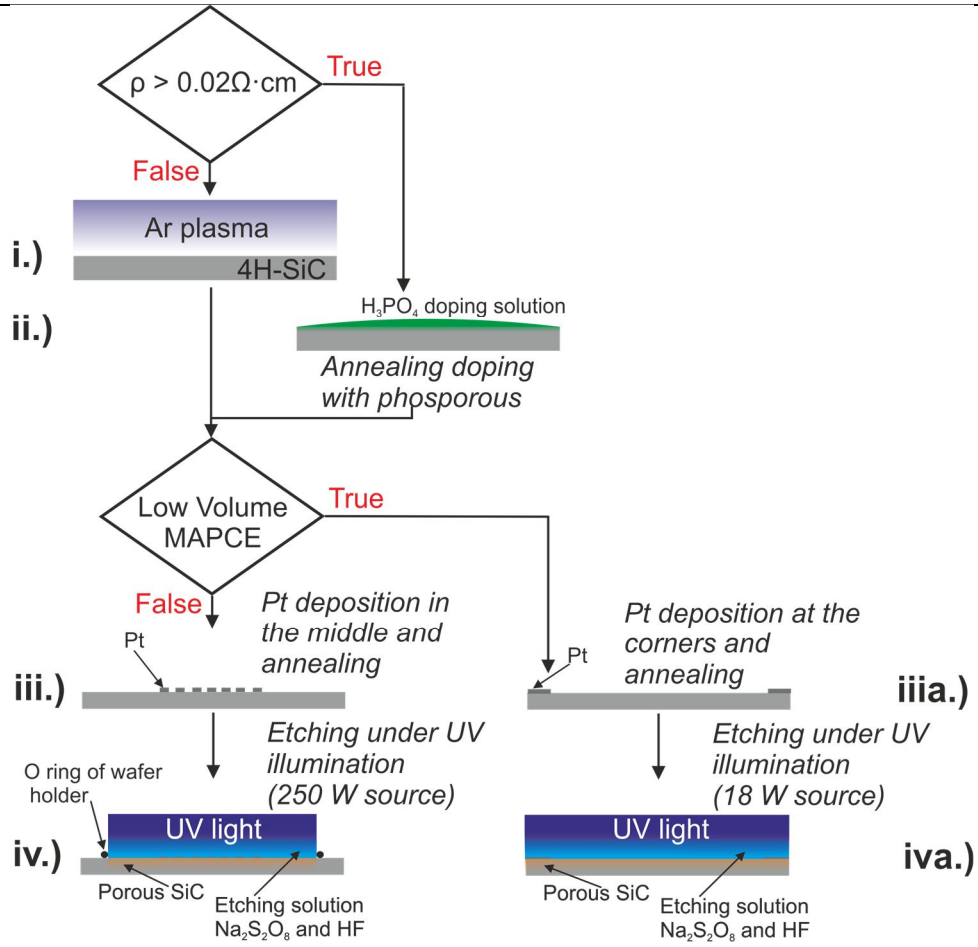


Figure 76: Process flow of metal assisted photochemical etching (MAPCE).

Also samples with different bulk resistivity values were used during experiments. The corresponding values are stated for each experiment in the following chapters.

4.5.1 Current controlled experiments

To generate a stack of layers with alternating degrees of porosity, while the porosity within each sub-layer had to be constant, the effect of changing electrical conditions during PECE is investigated in the first part of this section. This means that the power source was programmed to carry out a sequence of changing current densities. The applied sequence with the corresponding time intervals is given in Table 3.

Periode	Duration [min]	Targeted current density [mA/cm ²]
1	3	50.9
2	3	33.7
3	3	25.5
4	3	9.5
5	3	50.9
6	3	33.7
7	3	25.5
8	3	9.5

Table 3: Programmed sequence of changing current densities during PECE of a 4H-SiC sample with a bulk resistivity of 0.02 $\Omega\cdot\text{cm}$.

The first sample that was subjected to the described sequence of current densities had a bulk resistivity of 0.02 $\Omega\cdot\text{cm}$. The corresponding voltage and current density characteristics during the PECE experiment are illustrated in Figure 77. Basically, the programmed current density could be maintained throughout the whole experiment, except at the beginning of period 5, where it was lower than the targeted value for a short period. Simultaneously to this decreased current density, a sharp increase to the maximum possible voltage of 60 V was observed. At all other steps the voltage increased at the beginning until an almost constant value was reached.

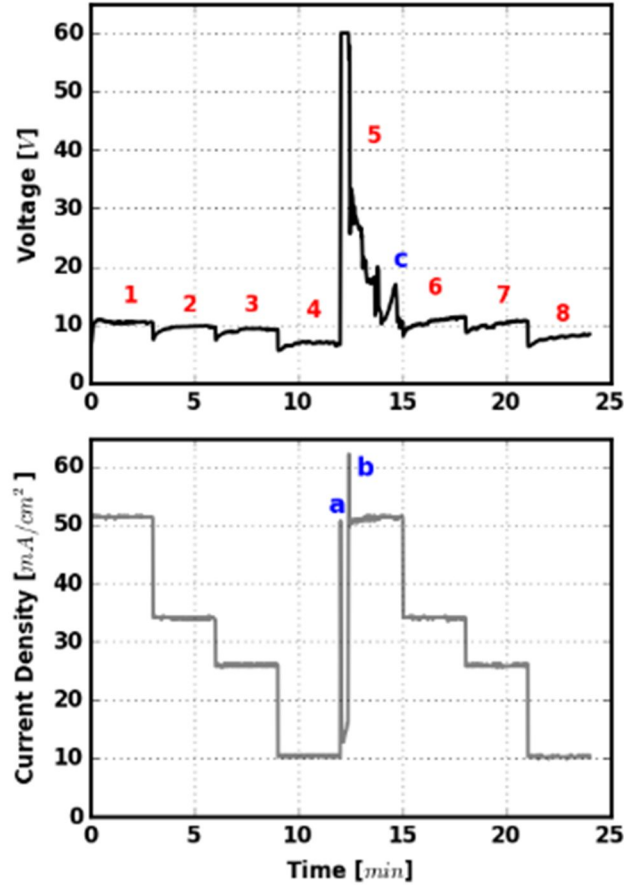


Figure 77: Voltage and current density characteristics during current controlled PECE of a 4H-SiC sample with a bulk resistivity of $0.02 \Omega\cdot\text{cm}$.

After etching, the sample was cracked for scanning electron microscope analysis. During cracking an approximately $20 \mu\text{m}$ thick, porous film detached from the bulk sample (the principle of thin film detachment is illustrated in Figure 87 while an example of a detached film is shown in Figure 94). A cross-sectional SEM micrograph of this film is shown in Figure 78. In this micrograph several layers are identified. On top there is a porous sub-layer which was generated during the MAPCE pre-treatment process. This layer is followed by 4 other sub-layers which can be assigned to the first four current density periods in Figure 77. The other 4 remaining sub-layers from the current density periods 5 - 8 were found in the cross-sectional analysis of the bulk sample.

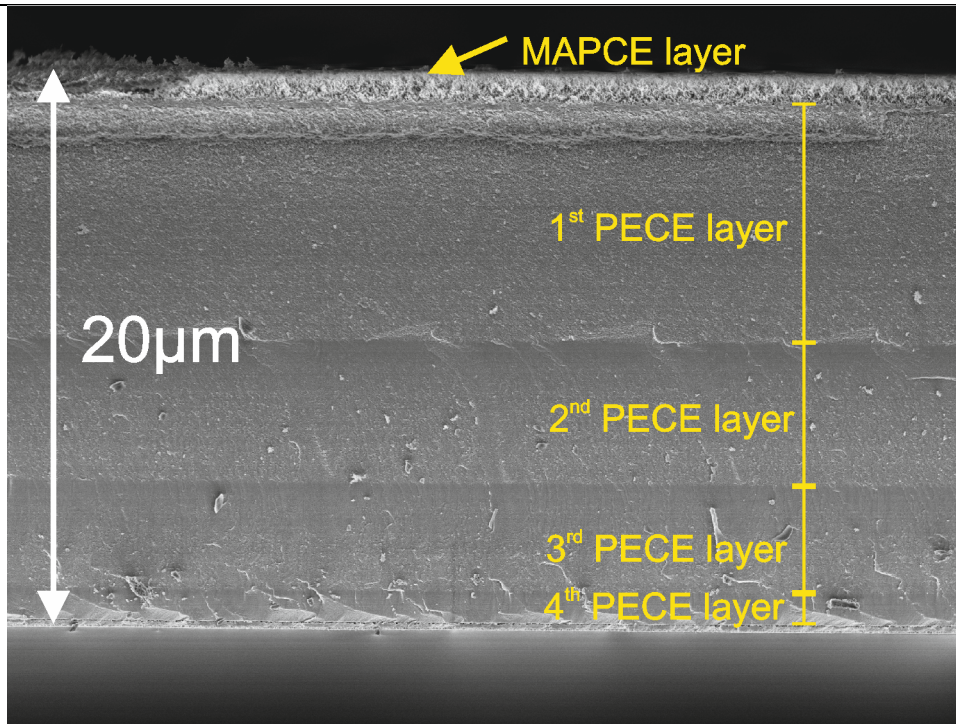


Figure 78: Detached porous 4H-SiC film after MAPCE and PECE of a sample with a bulk resistivity of 0.02 $\Omega\cdot\text{cm}$.

An examination of the bottom of the detached film and the top of the porous substrate material showed that lines of breakage had been created on the detached film. This is illustrated in Figure 79. In Figure 79a it can be seen that there is a first line of breakage after the fourth porous PECE sub-layer. This line of breakage is followed by a thin porous sub-layer and a second line of breakage at which separation took place during cracking of the sample. The lines of breakage can be assigned to specific events in the current density and voltage characteristics, shown in Figure 77. The first line of breakage is attributed to the very beginning of the fifth period where the current density shows a single peak (marked with an “a”). Then a region with decreased current density follows which is assigned to the very bottom layer in Figure 79a. Finally, the line of breakage which caused separation can be assigned to the peak “b” in the current density evolution.

The porous region generated after the current density peak b could be identified at the top of the bulk sample which is illustrated in Figure 79b. At its end a third line of separation (indicated by yellow arrows) started to form. A corresponding peak (marked with c in Figure 77) is observed in the voltage evolution during etching, while the current density stayed relatively constant. So far the presented findings showed that the transition from a low to a high current density mode caused the formation of lines of breakage in the porous material. These lines of breakage are represented as peaks in either the current density (see Figure 77; peaks “a” and “b”) or the voltage characteristics (see Figure 77, peak “c”).

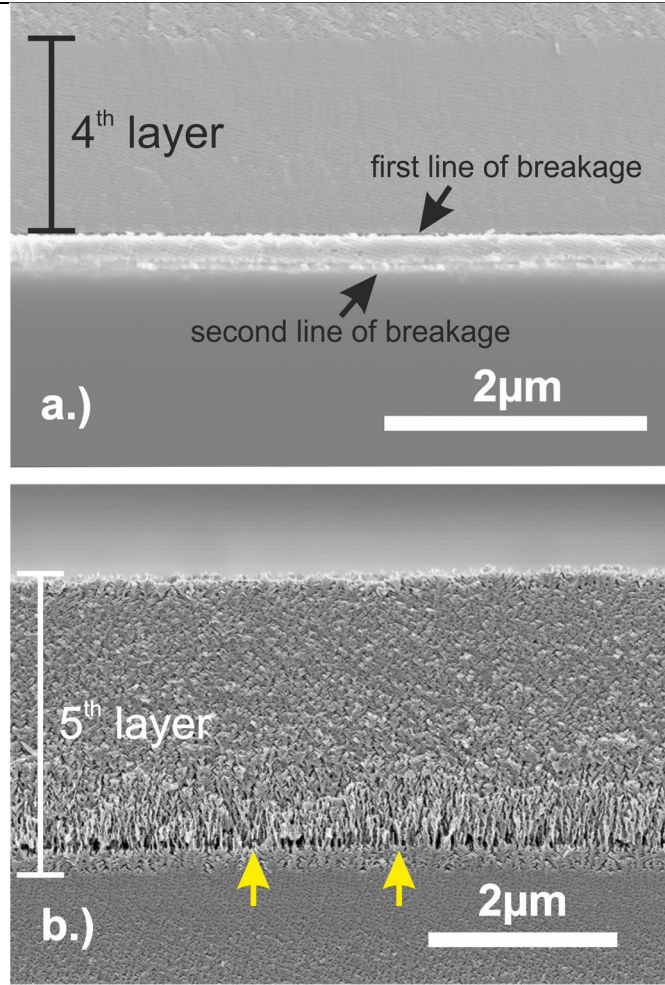


Figure 79: Cross-sectional view on a.) the bottom region of a detached porous 4H-SiC film and b.) the corresponding top region of the bulk material from which the film was separated. The bulk resistivity of the sample was $0.02 \Omega\text{-cm}$.

To further analyze this behavior, also the porous layers generated during the remaining current density periods were investigated. Therefore, the porosity of the porous layers was estimated with image processing. Typical results are shown in Figure 80, where the original SEM micrographs and the black and white images are presented to illustrate the trend in porosity. In particular, the porous regions resulting from the current density period transitions $1 \rightarrow 2$ and $7 \rightarrow 8$ are displayed. SEM micrographs of the other transition regions can be found in the Appendix (section 9 - Figure 122). Basically, the porosity decreases at the beginning of a new current density period until it becomes relatively constant. This is similar to the voltage characteristics during each period of constant current density (see Figure 77 – voltage characteristics). For a direct comparison of the voltage characteristics and the resulting porosity both quantities were plotted in Figure 81. The degree of porosity was determined with the black and white images obtained from image processing. Each number in Figure 81 represents a current density period as defined in Table 3.

Independent of the current density level, the porosity and the voltage drop at the onset of a new current density period. Afterwards both quantities increase and in most cases they show a saturation behavior.

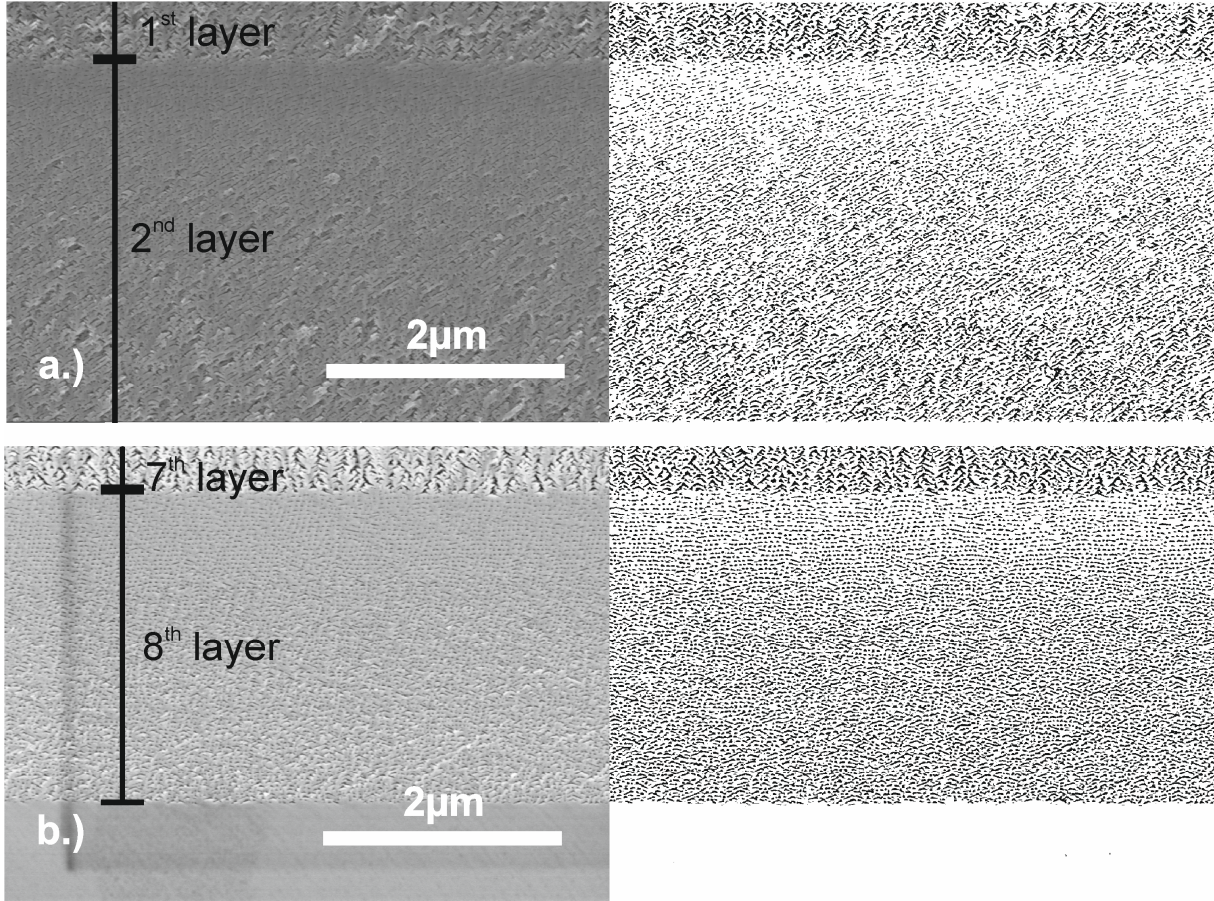


Figure 80: SEM micrographs of a 4H-SiC sample with a bulk resistivity of $0.02 \Omega\text{-cm}$ after MAPCE and PECE with corresponding black and white images obtained with image processing. a.) Transition from period 1 to 2. b.) Transition from period 7 to 8.

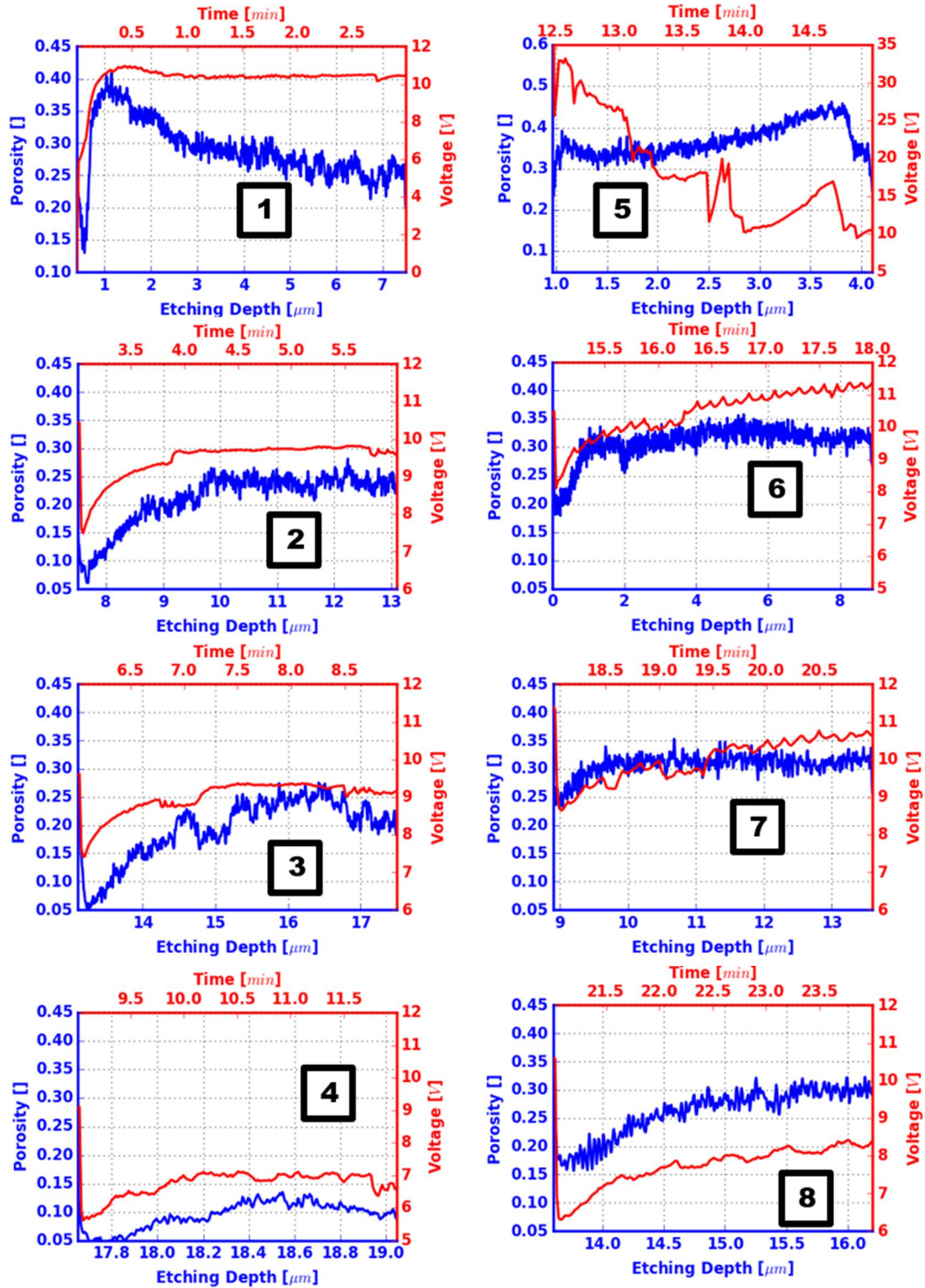


Figure 81: Degree of porosity (blue) and voltage (red) characteristics during each current density step. The numbers correspond to the current density periods shown in Figure 77.

To investigate whether this behavior is also true for samples with higher bulk resistivity values, a similar experiment was performed with a sample having a bulk resistivity of $0.106 \Omega \cdot \text{cm}$. The programmed current density periods for this experiment are shown in Table 4. The periods 5 to

8 were programmed with a lower current density to avoid the formation of lines of separation and subsequent separation of a porous film like in the previous experiment. The corresponding current density and voltage characteristics are illustrated in Figure 82. The different current periods are indicated by red numbers. At the beginning of the periods 1 to 4 the voltage tends to increase. During the periods 3 and 4 the voltage becomes rather constant like it was in the case for the sample with a bulk resistivity of $0.02 \Omega \cdot \text{cm}$. This indicates that the etching process turned into a steady state condition. During the periods 1 and 2 the voltage still increased at the end of the period or the maximum possible voltage had been reached. Here a steady state condition could not be reached because of the higher desired current density at the maximum possible voltage of 60 V.

During the periods 5 and 7 the desired current density could not be maintained by the power supply. This is accompanied by a voltage increase to the maximum possible value.

Periode	Duration [min]	Targeted current density [mA/cm^2]
1	3	50.9
2	3	33.7
3	3	25.5
4	3	9.5
5	3	25.5
6	3	9.5
7	3	25.5
8	3	9.5

Table 4: Programmed sequence of changing current densities during PECE of a 4H-SiC sample with a bulk resistivity of $0.106 \Omega \cdot \text{cm}$.

To estimate the impact on the degree of porosity the latter parameter and the voltage characteristics were plotted as done for the sample with a bulk resistivity of $0.02 \Omega \cdot \text{cm}$ (see Figure 83).

Basically, the porosity shows a similar trend as the voltage. This is essentially the same result as has been obtained for the sample with a bulk resistivity of $0.02 \Omega \cdot \text{cm}$. One difference, however, can be seen in the current density characteristics during period transitions $4 \rightarrow 5$ and $6 \rightarrow 7$, respectively. Here the current density stayed relatively constant (see Figure 82) while the voltage raised to the maximum possible value. This instantaneous change in voltage was accompanied by a sudden increase in the resulting porosity, at an almost constant current density. The corresponding SEM micrographs together with their black and white images are given in Figure 84. In both cases the pore morphology as well as the degree of porosity changes instantaneously.

SEM micrographs of the other transition regions corresponding to this experiment can be found in the Appendix (section 9 -Figure 123).

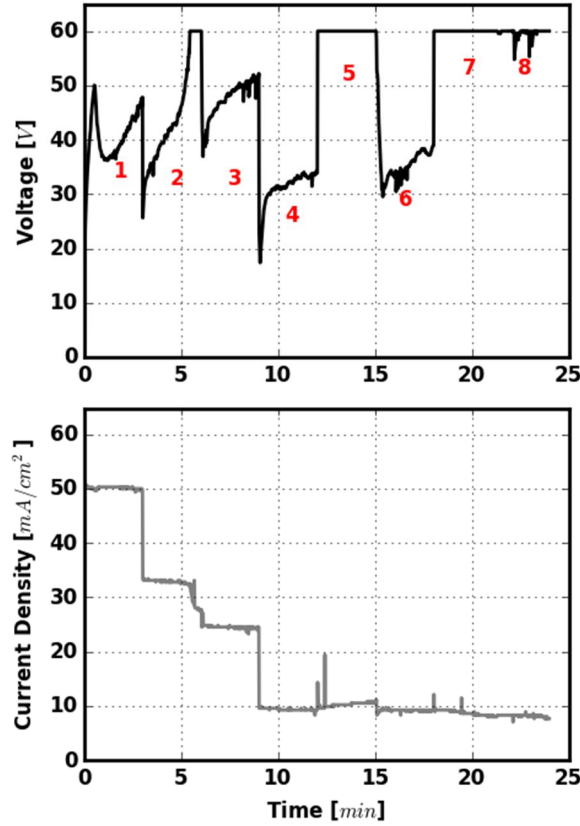


Figure 82: Voltage and current density characteristics during current controlled PECE of a 4H-SiC sample with a bulk resistivity of $0.106 \Omega\cdot\text{cm}$.

The collected data in current controlled mode showed that the resulting porosity as well as the pore morphology are predominantly determined by the applied voltage and not by the current density. In most cases the voltage and the resulting degree in porosity increase in one period of constant current density until they become almost constant. This indicates that a period of constant current density starts with a transition phase until a steady state condition is reached. Later in this thesis possible factors that determine this behavior are given (see section 4.5.4). On the other hand, when the voltage increased at a relatively constant current density the resulting porosity also increased instantaneously. This shows that changes in the pore morphology as well as the degree of porosity are determined by the applied voltage and do not necessarily require a change in current density. For the sample with a bulk resistivity of $0.02 \Omega\cdot\text{cm}$, the increase in porosity was so high that even the separation of a porous 4H-SiC film could be observed. This separation process is somewhat different from the other observations, since the second line of breakage was not accompanied with a voltage peak. This case is discussed in more detail in the chapter 4.5.3. These initial results showed that a current controlled PECE

process is not suitable for the preparation of stacked porous SiC layers that can be utilized as e.g. optical Bragg filter since the degree of porosity needs to be constant throughout every sub-layer of the stack.

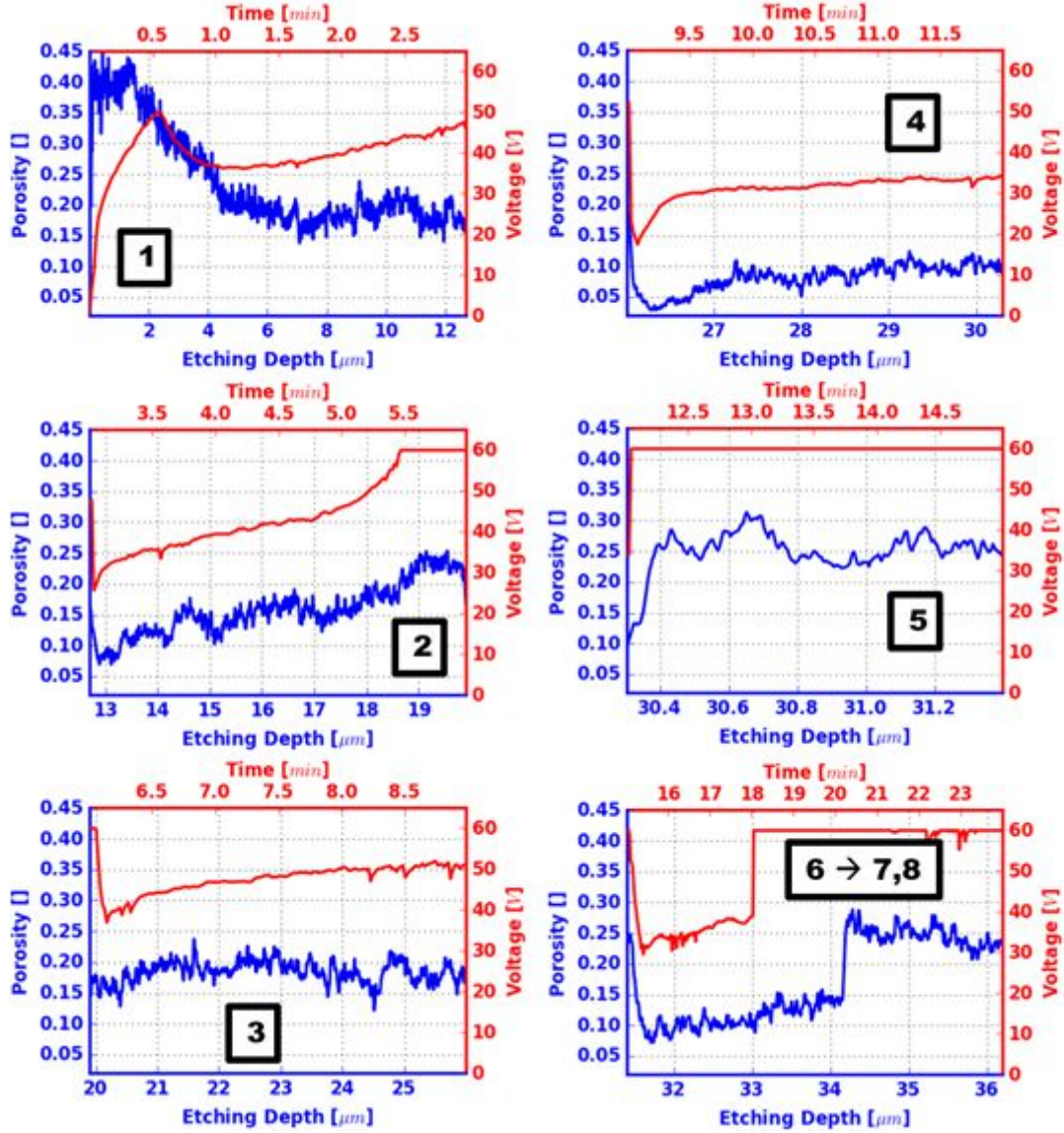


Figure 83: Degree of porosity (blue) and voltage (red) characteristics during each current density step. The numbers correspond to the current density periods shown in Figure 82.

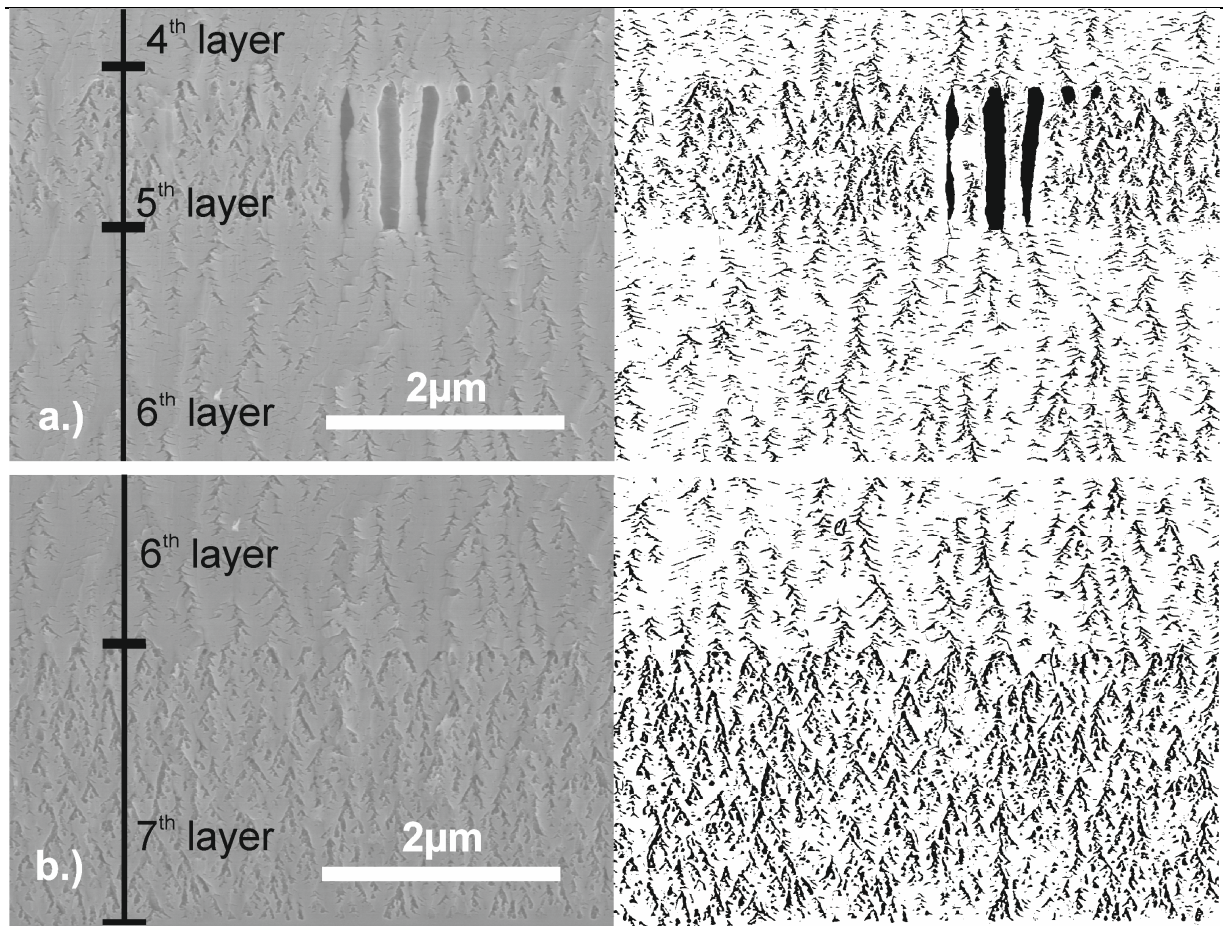


Figure 84: SEM micrographs of a 4H-SiC sample with a bulk resistivity of $0.106 \Omega\text{-cm}$ after MAPCE and PECE with corresponding black and white images obtained with image processing. a.) Transition from period 4 to 5. b.) Transition from period 6 to 7. The 7th layer was generated during the current density periods 7 and 8 (see Figure 82).

4.5.2 Voltage controlled experiments

The experimental observations so far showed that the degree of porosity and etching rate strongly depend on the applied voltage. Thus a sample with a bulk resistivity of $0.02 \Omega \cdot \text{cm}$ was etched under voltage controlled conditions. The performed sequence of voltage steps is shown in Table 5. The values of the voltages were chosen such that they were similar to the observed voltage values during the first current controlled experiment, before lines of breakage occurred (see Figure 77).

Periode	Duration [min]	Voltage [V]
1	3	11.5
2	3	10.5
3	3	9.5
4	3	8.5

Table 5: Programmed sequence of voltages during PECE of a 4H-SiC sample with a bulk resistivity of $0.02 \Omega \cdot \text{cm}$.

The evolution of the voltage and the current density as well as the resulting porosity is shown in Figure 85. The current density tends to decrease in every period of constant voltage. The porous layer generated during the first voltage period showed a decreasing tendency in porosity with depth. The porous layers generated during the voltage periods 2, 3 and 4 showed a slightly increasing porosity, despite a simultaneously decreasing current density. In contrast to the experiments in current controlled mode, the degree of porosity is relatively constant with depth. This is exemplary illustrated in Figure 86, where the transition from the third to the fourth porous layer is shown. In addition, the porosity drops only slightly at the beginning of a new voltage period.

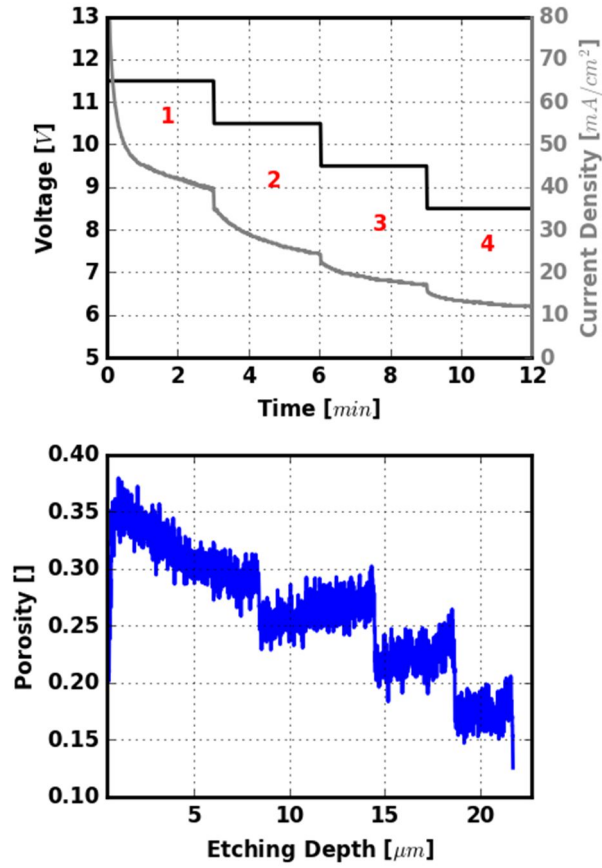


Figure 85: Voltage and current density characteristics during voltage controlled PECE of a 4H-SiC sample with a bulk resistivity of $0.02 \Omega\text{-cm}$.

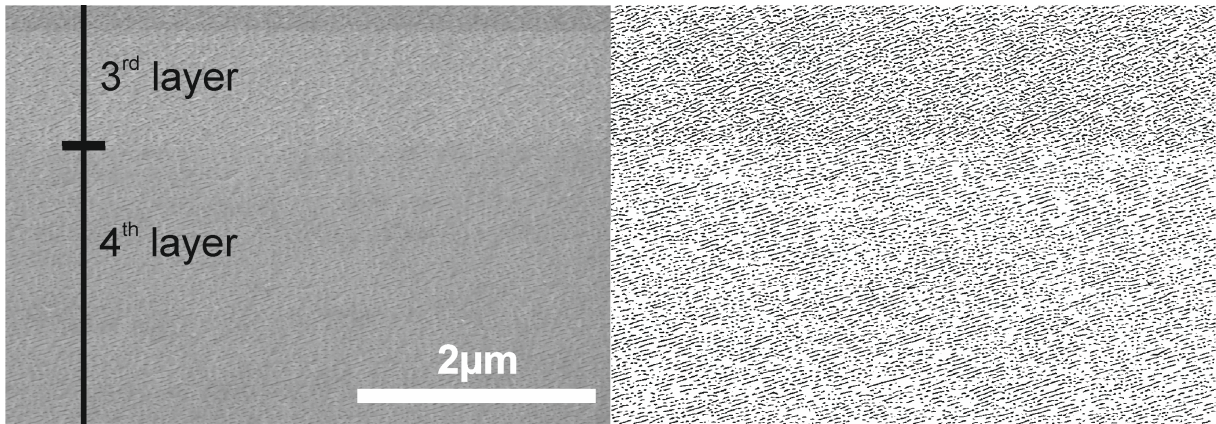


Figure 86: Cross-sectional SEM micrograph of a 4H-SiC sample with a bulk resistivity of $0.02 \Omega\text{-cm}$ after voltage controlled PECE with a corresponding black and white image obtained with image processing.

These findings confirm that the resulting degree of porosity as well as the trend of the porosity with depth crucially depend on the applied voltage and not on the current density. From a practical point of view this means that voltage controlled experiments are preferred for the preparation of porous SiC layers with homogeneous porosity as requested for e.g. optical filters.

4.5.2.1 Experiments with alternating voltages

To demonstrate an alternating degree of porosity in subsequent layers further experiments were conducted with alternating voltages of 11.5 V and 8.5 V based upon the previous experiment. Furthermore it was aimed to separate after etching the porous layers from the bulk material with the formation of a line of breakage as it had been observed during current controlled experiments. Therefore, the experimental parameters for MAPCE were modified such that the Pt was sputter deposited at the corners of the sample. Furthermore, MAPCE was done similar to the experiments described in section 4.3. The volume of etchant was 10 mL (0.15M $\text{Na}_2\text{S}_2\text{O}_8$), the distance to the UV source approximately 1 cm and the etching time was 2 hours. The etching solution was replaced every 30 minutes with fresh one, to prevent the depletion of oxidizing agent. Figure 87 shows schematically the above mentioned principle of the targeted preparation process. When the Pt is sputter deposited at the edges of the sample, MAPCE can be performed again after the separation of the porous layer. Doing so, the sample can be re-used several times for further porous film preparation.

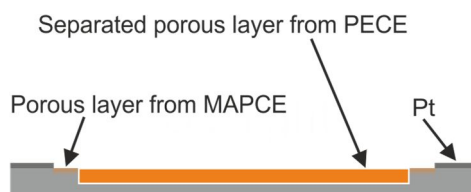


Figure 87: Principle of porous layer separation.

The first experiment with alternating voltages was carried out with a constant time interval of 1 minute as presented in Table 6. At the beginning a starting interval of 0.1 minutes was programmed. This was done because in pre-experiments it was found that the first layer shows significantly higher etching speed than the subsequent ones. This effect was also found during the following experiments and is discussed in section 4.5.3. Based on the data given in Table 6, the different periods at equal voltage level lead to different thicknesses of the porous sub-layers. This is explained with a decreasing current density with etching time as can be seen in Figure 88, where the voltage and the resulting current density are illustrated. On the other hand a clear distinction between the porous sub-layers could be achieved like in the first voltage controlled experiment, as shown in a cross-sectional SEM micrograph of the porous stack (see

Figure 89). In addition, as expected, the first period showed a significantly higher etching depth, despite the reduced time interval.

Periode	Duration [min]	Voltage [V]	Thickness [μm]
1	0.1	11.5	1.8
2	1	8.5	3.8
3	1	11.5	1.0
4	1	8.5	2.5
5	1	11.5	0.8
6	1	8.5	1.8
7	1	11.5	0.7
8	1	8.5	1.5
9	1	11.5	0.6
10	1	8.5	1.2
11	1	11.5	0.4

Table 6: Programmed sequence of alternating voltages during PECE of a 4H-SiC sample with a bulk resistivity of 0.02 $\Omega\text{-cm}$. Alternating etching periods with constant time and a starting period of 0.1 minutes.

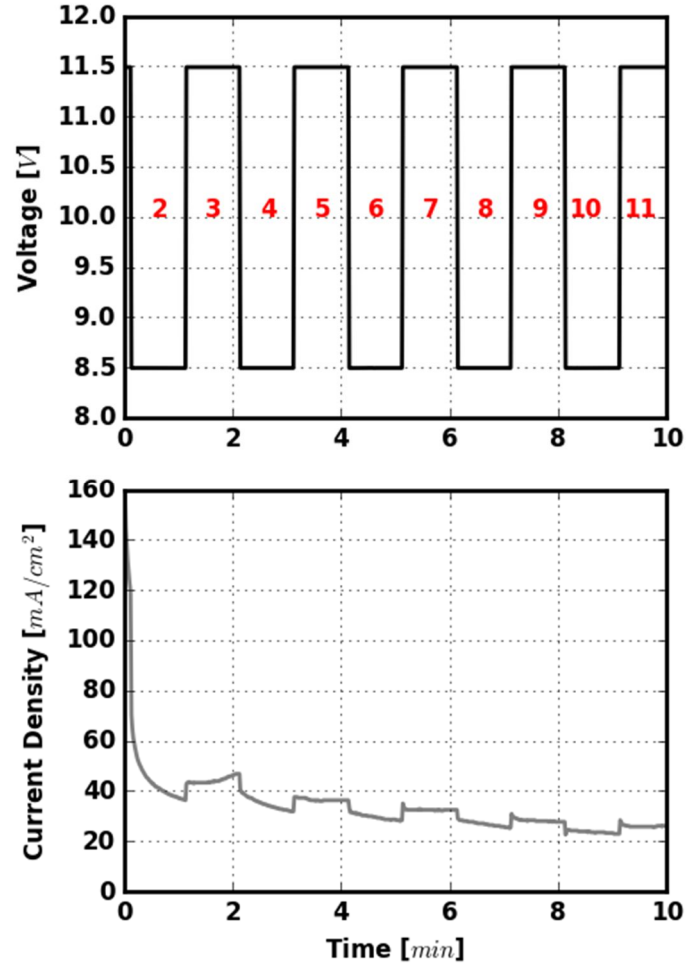


Figure 88: Voltage and current density characteristics during voltage controlled PECE of a 4H-SiC sample with a bulk resistivity of $0.02 \Omega\text{-cm}$. Alternating etching periods with constant time and a starting period of 0.1 minutes.

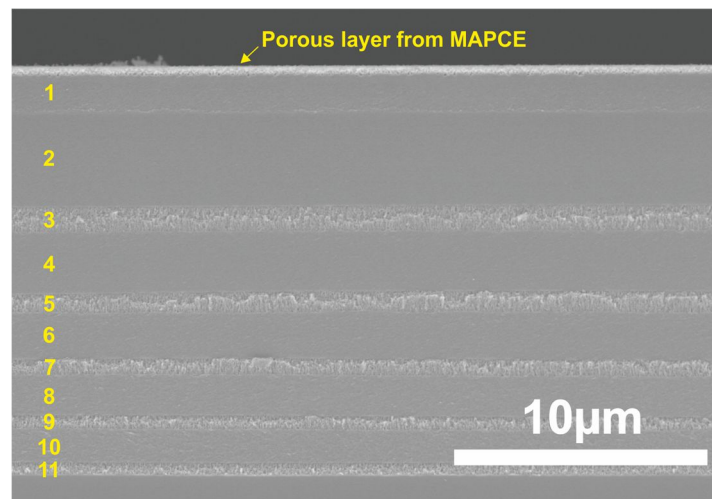


Figure 89: Cross-sectional SEM micrograph of a sample etched with alternating voltages of 11.5 V and 8.5 V. The samples bulk resistivity was $0.02 \Omega\text{-cm}$. Etching periods with constant time and a starting period of 0.1 minutes.

Since for the realization optical Bragg filters the thickness of the sub-layers with the same porosity has to be equal, the etching times during the experiment were modified with an empirical approach. In Figure 89 the porous sub-layers with decreasing thickness as a function of etching time are shown. To obtain equally spaced porous sub-layers the etching times for a sub-layer need to be larger at the end of the experiment than at the beginning. The adjusted etching times were calculated as follows: first, the thickness of the porous sub-layers as a function of voltage period number were fitted with a function $D_v(p)$, as is shown in Figure 90. The voltage period number p counts only the etching periods corresponding to a certain voltage level. This was done to make the fitting process easier. The thicknesses of the porous sub-layers generated with 11.5 V were fitted with a linear function (see also Equation [4-11]). The first data point corresponds to the starting period which lasted for only 0.1 minutes and was not considered. The thicknesses of the porous sub-layers generated with 8.5 V are fitted with an exponential relationship (see Equation [4-12]).

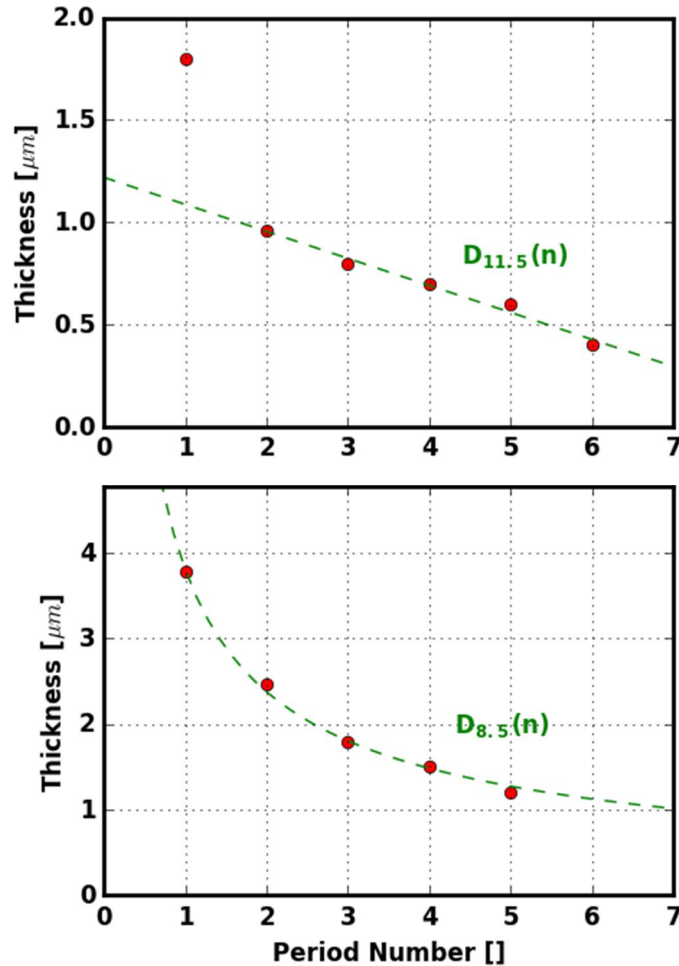


Figure 90: Etching depths of porous layers obtained with alternating voltages of 11.5 V and 8.5 V. The bulk resistivity of the sample was $0.02 \Omega\cdot\text{cm}$. Etching periods with constant time and a starting period of 0.1 minutes.

$$D_{11.5}(p) = -0.132p + 1.220 \quad [4-11]$$

$$D_{8.5}(p) = 3.8733p^{-0.7029} \quad [4-12]$$

To counterbalance the decreasing etching depth with ongoing etching time, the durations of the etching periods were decreased at the beginning of PECE and consecutively increased. For voltages with 11.5 V this increase was chosen linearly because Equation [4-11] showed a linearly decreasing behavior. For the calculation of the durations Equation [4-13] was used. The idea was to redistribute the etching times over the initially total time of 5 minutes by using the linear term from Equation [4-11]. First C was determined from Equation [4-13]. Then the first duration was found by integration from 4 to 5. The other time intervals were found by just moving the integration borders to lower values.

$$\int_0^5 (-0.132p + C) dp = 5 \text{ min} \quad [4-13]$$

$$\int_0^5 Ap^{-0.703} dp = 5 \text{ min} \quad [4-14]$$

The same approach was used for the calculations of the adjusted etching times corresponding to 8.5 V periods. For their calculation Equation [4-14] was applied.

The individual time intervals obtained for each period of the adjusted experiment, are illustrated in Table 7. The first period represents a starting period analogous to the experiment with fixed time intervals while the last period had the purpose to separate the porous layer from the substrate. The values for both, the porous layer thickness and the transferred charges are also shown in the same table. Their relationship is discussed in the section 4.5.3. The overall goal was to generate the same thickness for periods of the same voltage level. This has been partially fulfilled up to period 8. In the following layers, however, the resulting thickness values diverge.

Periode	Duration [min]	Voltage [V]	Thickness [μm]	Charge [C]
1	0.05	11.5	1.0	1.68
2	0.32	8.5	1.9	3.18
3	0.74	11.5	1.1	7.93
4	0.38	8.5	1.3	2.93
5	0.87	11.5	1.1	8.05
6	0.49	8.5	1.3	3.23
7	1	11.5	1.0	7.86
8	0.71	8.5	1.6	4.18
9	1.1	11.5	0.7	7.11
10	3.1	8.5	4.9	15.41
11	1.26	11.5	0.3	7.26
12	0.1	40		

Table 7: Programmed sequence of alternating voltages during PECE of a 4H-SiC sample with a bulk resistivity of 0.02 $\Omega\text{-cm}$. Alternating etching periods with adjusted time intervals and a starting period of 0.05 minutes.

The corresponding current and voltage characteristics are shown in Figure 91. The etching periods according to Table 7 are indicated in the current density plot. It can be seen that the current density decreases throughout the whole sequence until the voltage raises at the end implemented to separate the porous layer from the bulk sample. The resulting porosity is shown in Figure 92. Despite the decreasing current density throughout PECE, the porosity stayed relatively constant for a given voltage and changes instantaneously when the voltage is switched between 11.5 V and 8.5 V, as can also be seen in Figure 93. There the porous sub-layers corresponding to the etching periods 3, 4 and 5 are illustrated.

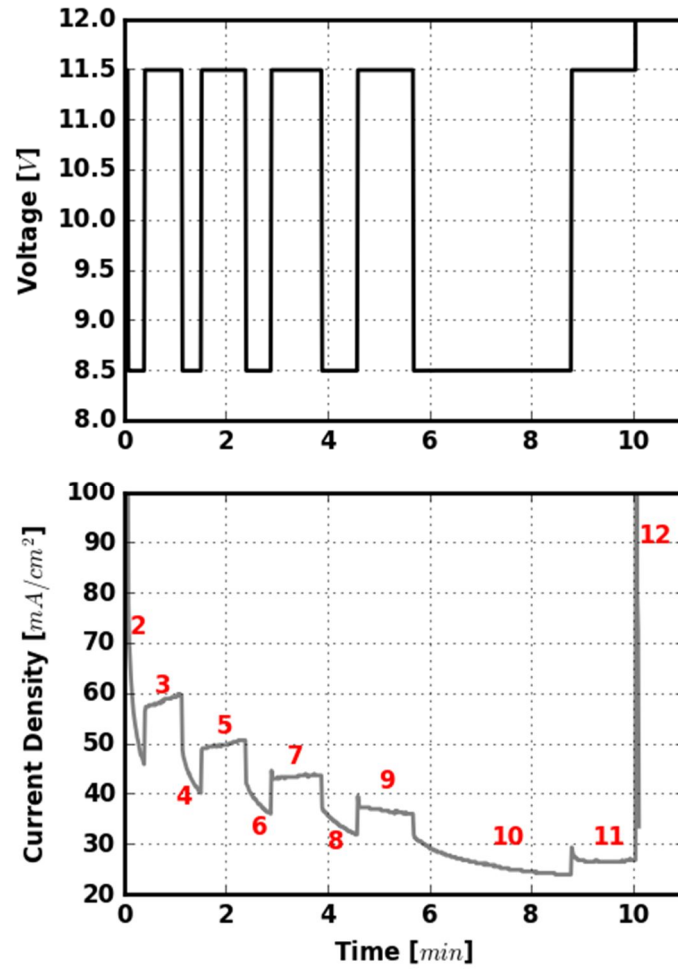


Figure 91: Voltage and current density characteristics comprising alternating etching periods with adjusted time intervals and a starting period of 0.05 minutes during voltage controlled PECE of a 4H-SiC sample with a bulk resistivity of $0.02 \, \Omega\text{-cm}$. At the end of the experiment the voltage is increased to separate the porous layer from the substrate.

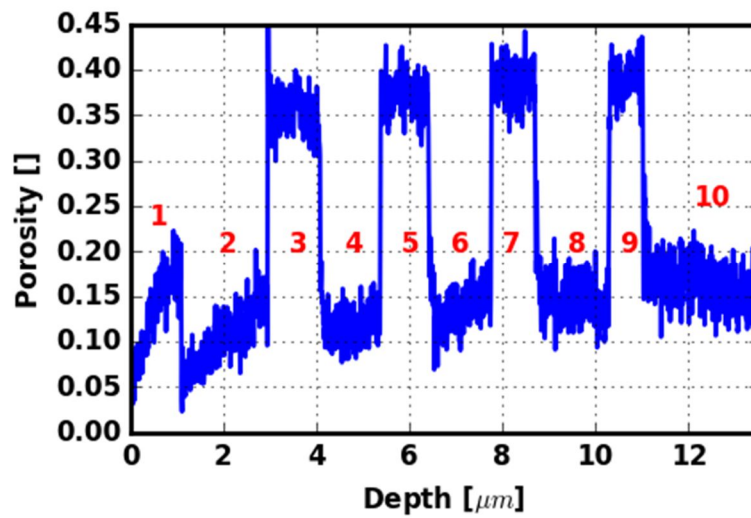


Figure 92: Porosity versus etching depth for a voltage controlled PECE of a 4H-SiC sample with a bulk resistivity of 0.02 $\Omega\text{-cm}$, based on alternating etching periods with adjusted time intervals and a starting period of 0.05 minutes.

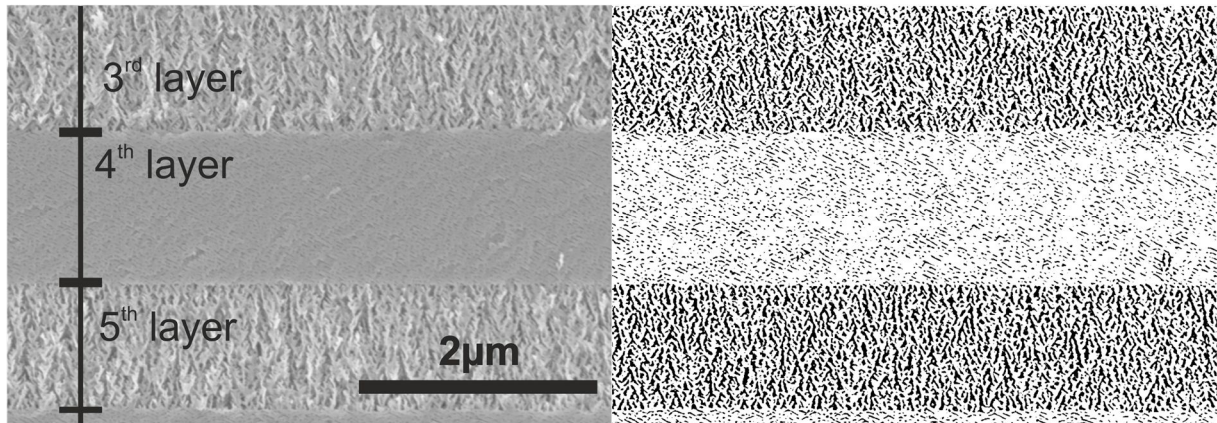


Figure 93: Cross-sectional SEM micrograph of a 4H-SiC sample after voltage controlled PECE comprising alternating etching periods with adjusted time intervals and a starting period of 0.05 minutes. The sample had a bulk resistivity of 0.02 $\Omega\text{-cm}$.

Finally, also the separation process during period 12 was successful. After removing the sample from the etching chamber, the etched porous layer easily detached from the bulk sample during cleaning with deionized water. Both, the sample and the detached porous layer are shown in Figure 94.

Beside these findings, it can also be seen that the etching rate was significantly higher during the first period (compare with Figure 89 and Table 6). This phenomenon is discussed in section 4.5.3.

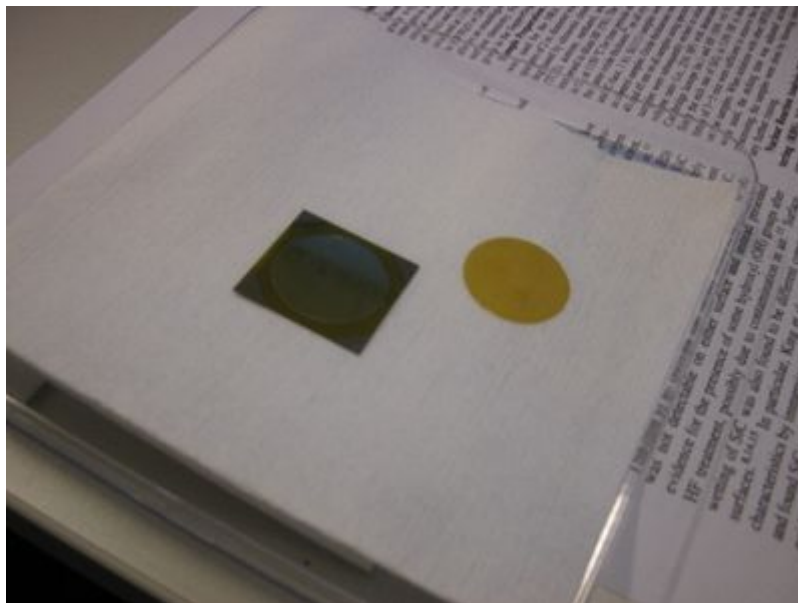


Figure 94: Detached porous layer of 4H-SiC after PECE and the corresponding 4H-SiC sample.

The resulting degree of porosity can be properly adjusted by a constant voltage during etching, relatively independent of the current density. Also sharp borders between the porous sub-layers can be formed by utilizing voltage controlled PECE. Furthermore the porous layer can be separated from the sample by a steep voltage increase.

4.5.3 Similarity to dielectric breakdown

Basically, the degree of porosity as well as the pore morphology are crucially influenced by the voltage while the current density shows no correlation with these properties. This observation indicates that the etching process can be described in a similar manner as fractal structures in solids obtained from dielectric breakdown [109]. In such processes, growth takes place along the pore tips where the electric field strength is higher compared to the surrounding regions. This argumentation is supported by the findings of section 4.2.1 where it was shown that a porous layer generated with MAPCE prior to PECE enhances the uniformity of the porous layer. In particular pores that are formed with PECE initiate at the pore tips of the previously formed porous MAPCE layer.

To further confirm the similarity between dielectric breakdown and PECE, an experiment with alternating voltages (10 V and 5V; 1 minute durations, see Figure 95) was performed.

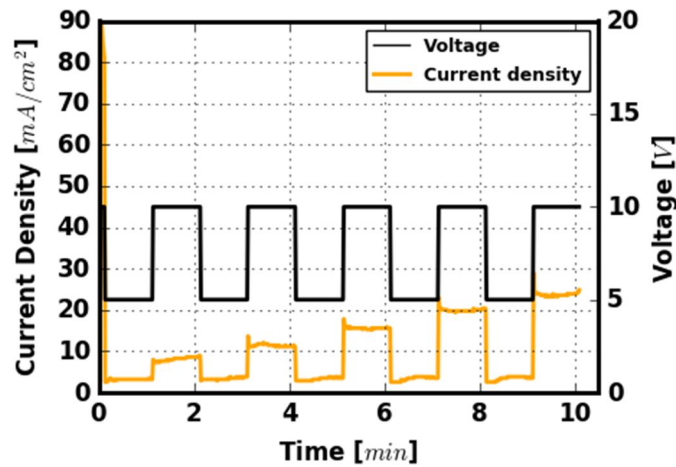


Figure 95: Voltage and current density characteristics during voltage controlled PECE of a 4H-SiC sample with a bulk resistivity of $0.02 \Omega \cdot \text{cm}$.

The intention was to decrease the porosity and thus the amount of pore tips during the periods of low voltage. Indeed, the result differed strongly from all the previously performed experiments, as can be seen in Figure 96. First, the etching fronts are not parallel to the sample surface. Such a behavior had not been observed for the samples prepared so far. This shows that for a uniform etching pattern the pore tip density is not allowed to drop below a certain critical value. This can also be seen by so-called Lichtenberg Figures (see black arrow in Figure 96). The

presence of such patterns is typical when dielectric breakdown has occurred, where the direction of the growth follows the regions of highest electric field strength [110].

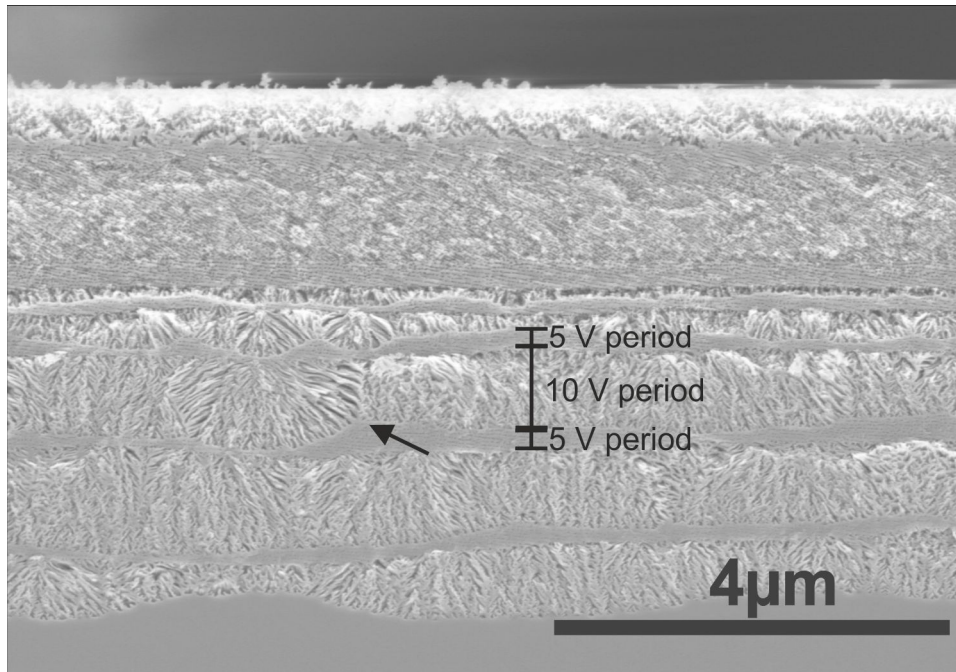


Figure 96: Cross-sectional SEM micrograph of a sample etched with alternating voltages of 10 V and 5 V. The samples bulk resistivity was $0.02 \Omega\text{-cm}$. Etching periods had a constant time interval of 1 minute.

From the experimental data it is reasonable to assume that at an increased voltage the active area at the pore tip is increased such that a higher porosity results. Figure 97 shows the thickness of the porous sub-layers versus the transferred charge obtained from the last PECE experiment performed in the section 4.5.2.1 (see Table 7) with adjusted time intervals.

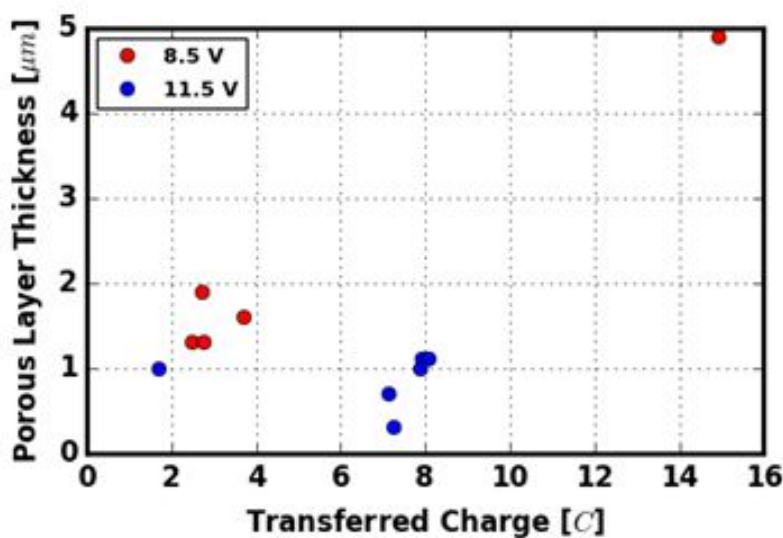


Figure 97: Transferred charge versus the porous layer thickness obtained from voltage controlled PECE. The transferred charge values are those given in Table 7.

Basically, a higher amount of transferred charge as well as a higher voltage lead to a decreased thickness of a single porous sub-layer. This confirms the statement that with increased voltage the active area at the pore tip is increased as well. It also matches the description of dielectric breakdown, where at higher electric fields the probability is higher that locally a larger area of material damage occurs [110]. In the case of PECE this means an increased degree of porosity. Altogether this is the reason why data points of constant voltage tend to be at the same position in Figure 97. The two data points corresponding to the highest and lowest transferred charge do not fit into this pattern. This can be explained as follows: the 11.5 V data point that groups with the 8.5 V data points represents the initial porous layer (period 1 in Table 7). The initial porous layers always showed an increased etching speed, which may be due to different starting conditions. The initiation sites for the first layer are the pore tips from the MAPCE layer and they are larger than the pores from PECE. This effect has not been studied in more detail, but explains why the data point corresponding to the lowest amount of transferred charge does not group with the other 11.5 V data points. The other data point that does not fit into the described pattern is the 8.5 V data point corresponding to a transferred charge of 15.4 C. Here the etching time and hence, the amount of transferred charge was significantly larger than for the other 8.5 V data points.

Finally the above discussion also allows an interpretation of the first layer separation process during current controlled PECE. The corresponding current and voltage evolution is shown in Figure 77. The peak “a” in the current density is also accompanied by a steep voltage increase and thus a line of separation occurred in the porous layer. The following decrease in current density can be explained with a decrease in the amount of pore tips, which are required for further etching. Such a phenomenon is also observed when no MAPCE is done prior to PECE (see section 4.2.1). So, also this phenomenon can be explained in terms of dielectric breakdown and accordingly fractal like pore growth.

4.5.4 Chemical analysis

Finally, the etching mechanism is discussed. During PECE, holes h^+ are consumed as described in section 2.2.2.1. There it is stated, that 4, 6 or 8 holes are required to oxidize one formula unit of SiC. The data presented so far, allows the estimation of the amount of holes h^+ that are needed to dissolve one formula unit of SiC during the porosification process.

The volume fraction of dissolved SiC v_{diss} during a current density step is the ratio between the porosity curve integral and the thickness of the porous layer d as is given in Equation [4-15].

$$v_{diss} = \frac{\int_0^d P(x)dx}{d} \quad [4-15]$$

The average amount of holes consumed during an etching step can be obtained by using Faradays law of electrolysis, which is illustrated in Equation [4-16]. Q is the amount of charge transferred during electrolysis, M is the molar mass of the deposited compound, F is Faradays constant and z represents the necessary amount of electrons to deposit a formula unit of the compound. With these quantities, the deposited mass m can be calculated.

$$m = \frac{QM}{zF} \quad [4-16]$$

Faradays law can be used to calculate the average amount of holes consumed during an etching period. The charge Q can be calculated by integration of the current during a period. The molar mass of SiC and Faradays constant are known. In the case of etching the deposited mass is substituted with the dissolved mass, which can be determined by multiplying v_{diss} with the area $A = 3.14 \text{ cm}^2$ enclosed by the O-ring of the wafer holder (see sections 3.1 and 4.2), the thickness of the porous layer d and the density of SiC ρ . Finally, z is substituted by the average amount of holes consumed h_{avg} during an etching period. The final expression for h_{avg} is given in Equation [4-17].

$$h_{avg} = \frac{M \int_{t_1}^{t_2} Idt}{FA d \rho v_{diss}} \quad [4-17]$$

As v_{diss} is loaded with noise, there is an uncertainty that propagates into the calculation of v_{diss} . According to the Gaussian law of error propagation [111] the uncertainty of h_{avg} can be calculated with Equation [4-18]. Δv_{diss} is the uncertainty in the dissolved volume fraction of SiC.

$$\Delta h_{avg} = \left| \frac{\partial h_{avg}}{\partial v_{diss}} \right| \cdot \Delta v_{diss} = \frac{h_{avg}}{v_{diss}} \cdot \Delta v_{diss} \quad [4-18]$$

This uncertainty was calculated as follows: the porosity/depth data points were exponentially smoothed (see Figure 98). The differences between the original data points and the solid curve obtained from the smoothening procedure were ordered in a histogram (error distribution) as can also be seen in Figure 98. The standard deviation of this error distribution represents the uncertainty of the dissolved volume fraction of SiC Δv_{diss} .

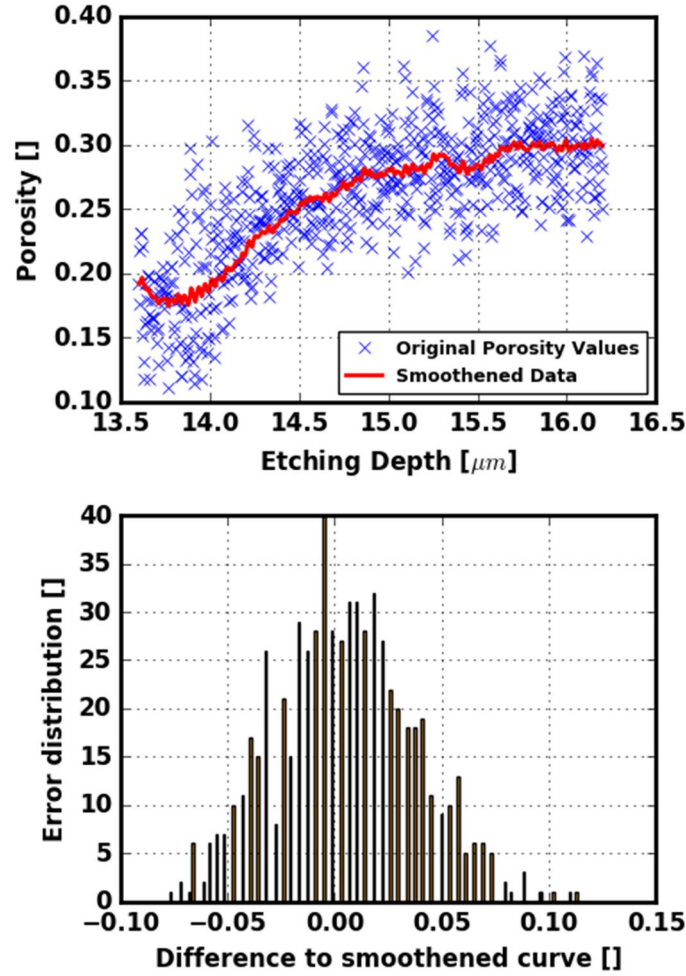


Figure 98: Distribution of errors for the obtained porosity data, including the original porosity data points and the corresponding exponentially smoothed curve. The differences between the smoothed curve and the original data points are plotted in a histogram.

Now, after having introduced the details of determining the needed holes, the data generated with the experimental results are presented. Figure 99 shows the amount of holes needed for the last experiment performed in section 4.5.2.1. The amount of holes needed is shown for the voltage controlled PECE experiment with adjusted times and alternating voltages (the corresponding experimental data are shown in Table 7 and Figure 91). It can be seen that the amount of holes changes with voltage as well as with increasing etching time. The former is reasonable because the electrochemical oxidation of SiC can be realized via several reaction paths [112] each with a different activation energy and different amount of holes needed. When the voltage is modified, the weighting of each reaction path contributing to the overall oxidation process changes. In particular, the generation of porous sub-layers with a higher degree of porosity requires a higher amount of holes to dissolve SiC (compare Figure 99 with Figure 92).

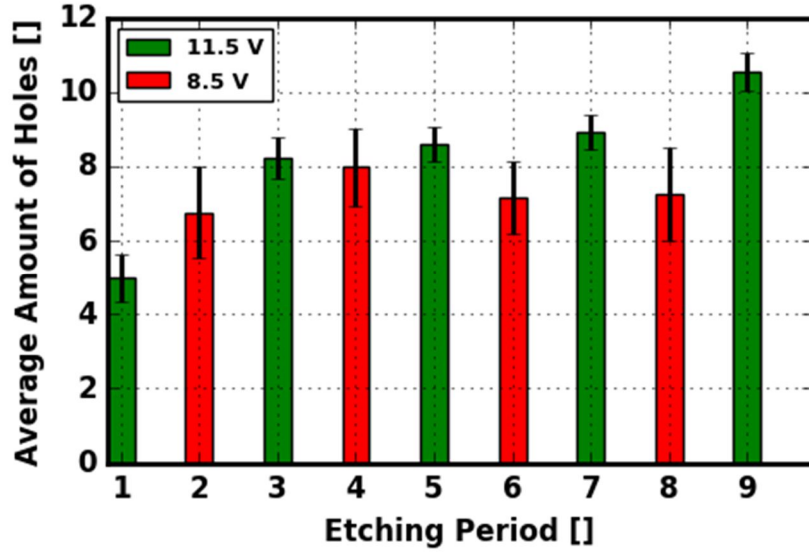


Figure 99: Average amount of holes needed to dissolve a formula unit of SiC during an etching period. The corresponding experimental data are illustrated in Table 7. The sample bulk resistivity is $0.02 \Omega\text{-cm}$.

The overall increase of the amount of holes with etching time is attributed to diffusion, could also be observed for the second current controlled (see Figure 100) and the first voltage controlled PECE experiment (see Figure 101). The corresponding experimental details can be found in section 4.5.1 (Table 4) and section 4.5.2 (Table 5), respectively.

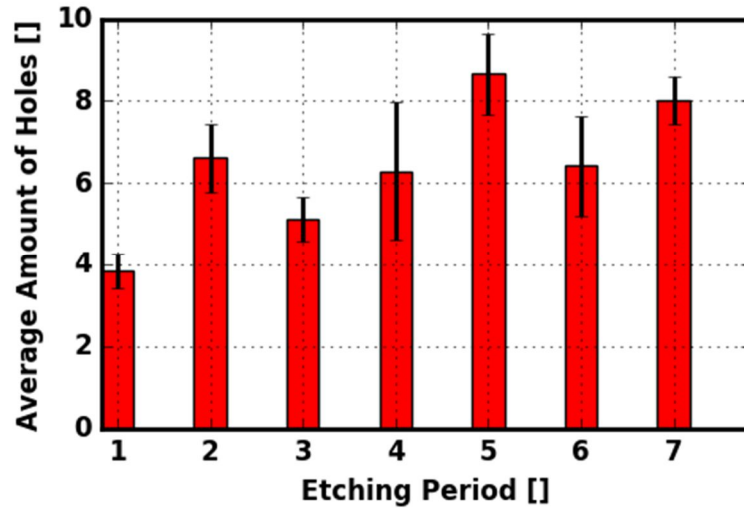


Figure 100: Average amount of holes needed to dissolve a formula unit of SiC during an etching period. Sample resistivity of $0.106 \Omega\text{-cm}$. PECE was performed under current controlled conditions.

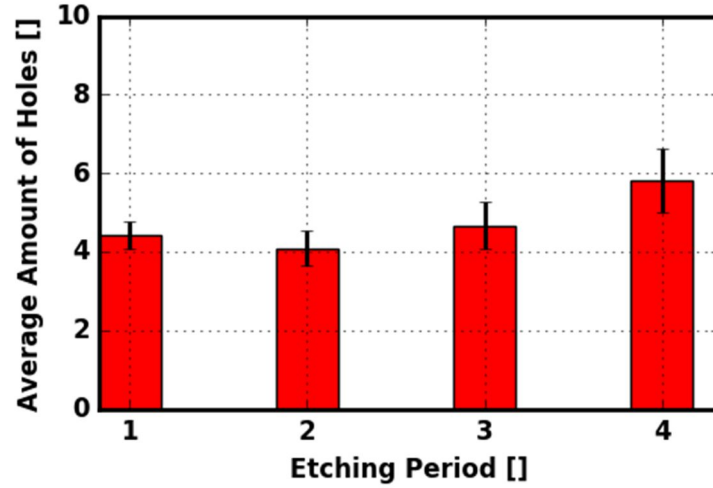


Figure 101: Average amount of holes needed to dissolve a formula unit of SiC during an etching period. Sample resistivity of $0.02 \Omega\text{-cm}$. PECE was performed under voltage controlled conditions.

An exception to this behavior was observed during the first current controlled PECE experiment presented in section 4.5.1. Figure 102 shows a plot of the holes needed corresponding to the first performed current controlled PECE experiment (see Figure 77 for the current and voltage characteristics). At the beginning of period 5 the porous film detached from the bulk sample (shown in Figure 78). Thus it is reasoned that the supply with fresh etching solution was improved during the following periods, which caused a decrease of the amount of holes needed for dissolution of a formula unit of SiC.

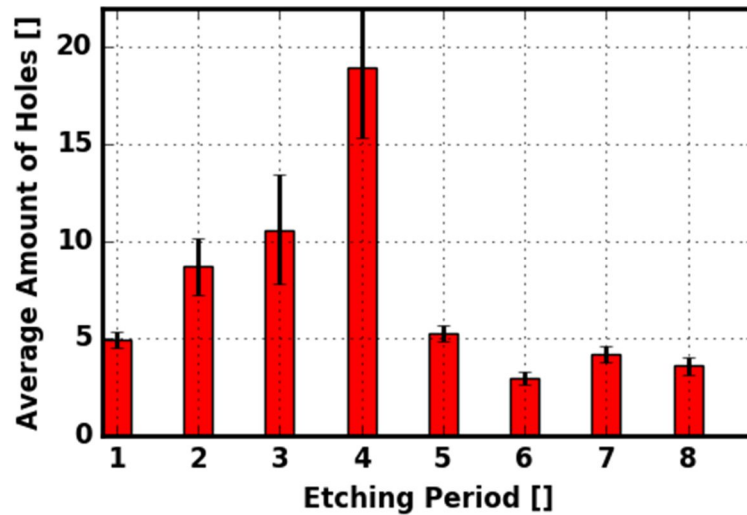


Figure 102: Amount of holes that are needed to dissolve a formula unit of SiC und current controlled conditions. The sample bulk resistivity is $0.02 \Omega\text{-cm}$. The corresponding current density and voltage characteristics are shown in Figure 77.

These observations show that the applied voltage as well diffusion through the porous layer are the main dominating factors. But, the amount of required holes is sometimes larger than those reported in literature. This may be due to an underestimation of the porosity because image thresholding provides only an approximation of this parameter. Furthermore the error in the calculation of the holes is larger when h_{avg} is substantially higher than 8, as can be seen in Figure 102.

In most of the experiments, a transient phase of the voltage and the porosity could be observed at the beginning of a new period of constant current density (see Figure 81 and Figure 83). This means that the electrolyte/semiconductor interfacial resistance (ESIR) increases with time until it becomes constant. This is at first counterintuitive because an increasing porosity (and thus an increased area for charge transport) should lower the resistance for charge transport. A chemical interpretation of the transient behavior, however, provides an adequate explanation. As stated in literature, the dissolution of SiC is a two-step process, involving the oxidation of SiC and subsequent dissolution of the oxide with HF (see section 2.2.2.1). It has been shown that the electrolytic oxidation of SiC generates an amorphous oxide layer on its surface, which is permeable for electrolyte solutions [102]. An amorphous layer has also been found on the surface of porous SiC prepared with PECE [42]. When the dissolution rate of the oxide is slower than its formation rate, the ESIR increases. In this case the voltage increases, which leads to a higher porosity and actively etched area. This, in turn, decreases the formation rate of the oxide layer per unit area because the same amount of charge can pass through a larger area. At some point, a steady state condition is reached.

The presence of an oxide layer on the surface of porous SiC is proven by Fourier transform infrared (FT-IR) spectroscopy and secondary ion mass spectrometry (SIMS) depth profiling. First the SIMS measurement are presented and then the results from FT-IR are discussed.

Figure 103 shows the SIMS depth profile of a sample that was etched with 300 alternating voltage values of 11.5 V and 8.5 V (see section 5.2.2 for preparation details). O^- , F^- as well as C_xH^- and CN^- fragments were identified in the mass spectrum. Oxygen and fluoride are present due to the etching process while nitrogen is due to the n-doping of the sample. The variation in the measured intensities in the depth profile is due to the porosity profile of the sample. The Si^- and C^- signals exceeded the limits of the detector, thus $^{30}Si^-$ and C_2H^- are plotted respectively.

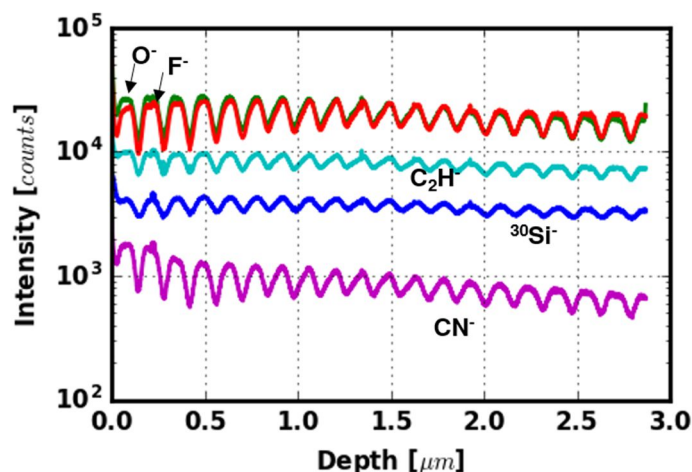


Figure 103: SIMS depth profile of a porous SiC sample with alternating layers of low and high porosity. The bulk resistivity of the sample is $0.02 \Omega\cdot\text{cm}$.

The FT-IR measurements were performed with a porous 4H-SiC film that was detached from a bulk sample. The resistivity of the bulk sample was $0.02 \Omega\cdot\text{cm}$. During PECE several thin films separated from the bulk sample. One was used for the FT-IR measurements. Figure 104 shows the corresponding current and voltage evolution during PECE while Figure 105 shows a cross-sectional SEM micrograph of the porous film used for the measurements.

The elemental information gained by the SIMS measurement can be used for interpretation of the IR spectra shown in Figure 106. The IR spectra were acquired in attenuated total reflection (ATR) and transmission mode. One can see three different spectra obtained from two samples. First the porous film is compared with a bulk sample of 4H-SiC. Secondly the ATR measurement of the porous film is compared with a measurement in transmission mode.

There is a significant difference between the ATR-IR spectra of a detached porous SiC film and the original bulk SiC (see Figure 106a). The spectrum of the latter sample shows two characteristic peaks of SiC at 800 cm^{-1} (TO phonon) and 975 cm^{-1} (LO phonon) [96,113]. The etched sample also shows these peaks together with a main peak at 1030 cm^{-1} which is attributed to Si-O-Si stretching vibrations [114]. The minor peak at 975 cm^{-1} can be assigned to Si-F₂ vibrations [100,101]. According to literature and in agreement with the SIMS results it is also possible that C-F vibrations contribute to this peak (C-F bending at 1100 cm^{-1}) [115]. Several peaks also appear at higher wavenumbers, which are due to functional groups attached during PECE. The peak at 1460 cm^{-1} can be assigned to C-H bending, while the two peaks at higher wavenumbers are probably due to N-H vibrations [54].

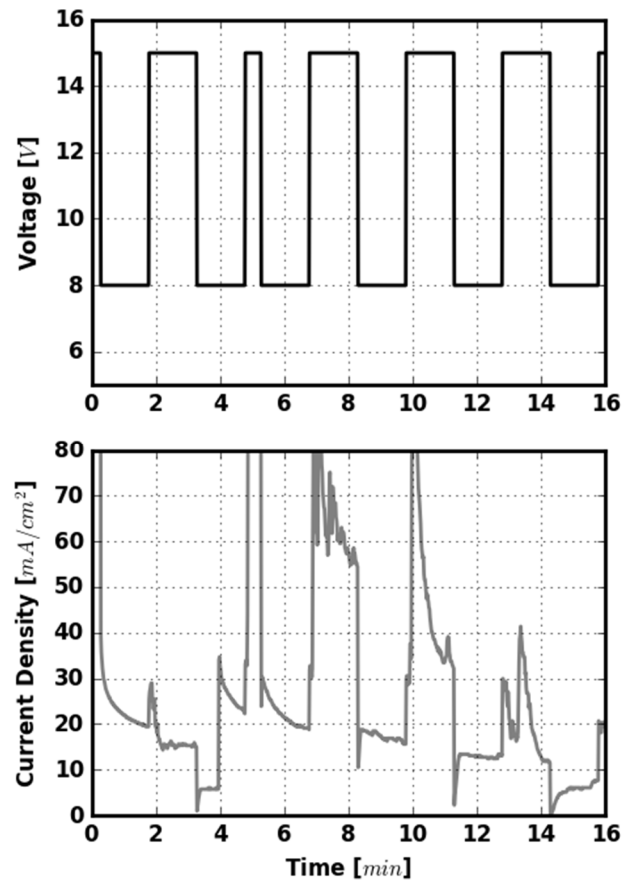


Figure 104: Voltage and current density characteristics during voltage controlled PECE of a 4H-SiC sample with a bulk resistivity of $0.02 \Omega\text{-cm}$. Separated thin films were used for FT-IR measurements.

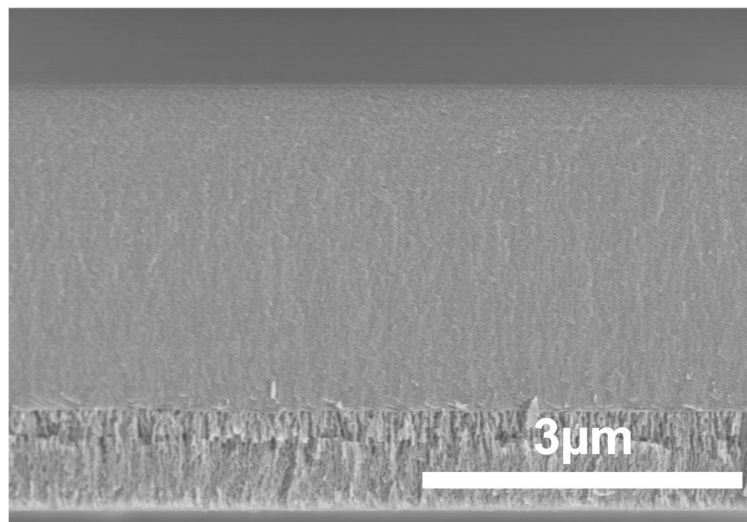


Figure 105: Cross-sectional SEM micrograph of a separated thin film that was measured with FT-IR.

The detached film had only a thickness of about 4 μm , so a measurement in transmission mode was also possible. The corresponding spectrum (see Figure 106b) shows two main peaks which can be attributed to SiC vibrations at 800 cm^{-1} (TO phonon) and 890 cm^{-1} (Si-C stretching) [99] but no peaks from an Si-O-Si stretching vibration or other functional groups at higher wave-numbers are detected. The small peaks at 1545 cm^{-1} and 1625 cm^{-1} are due to phonon overtones of SiC [96,113].

So, the measurement in transmission mode shows that the detached porous film still consists mainly of SiC. This is in accordance with the SIMS measurement where the C^- and Si^- signals exceeded the limits of the detector. The surface sensitive ATR measurement implies that the porous film is covered with an oxide layer and other functional groups.

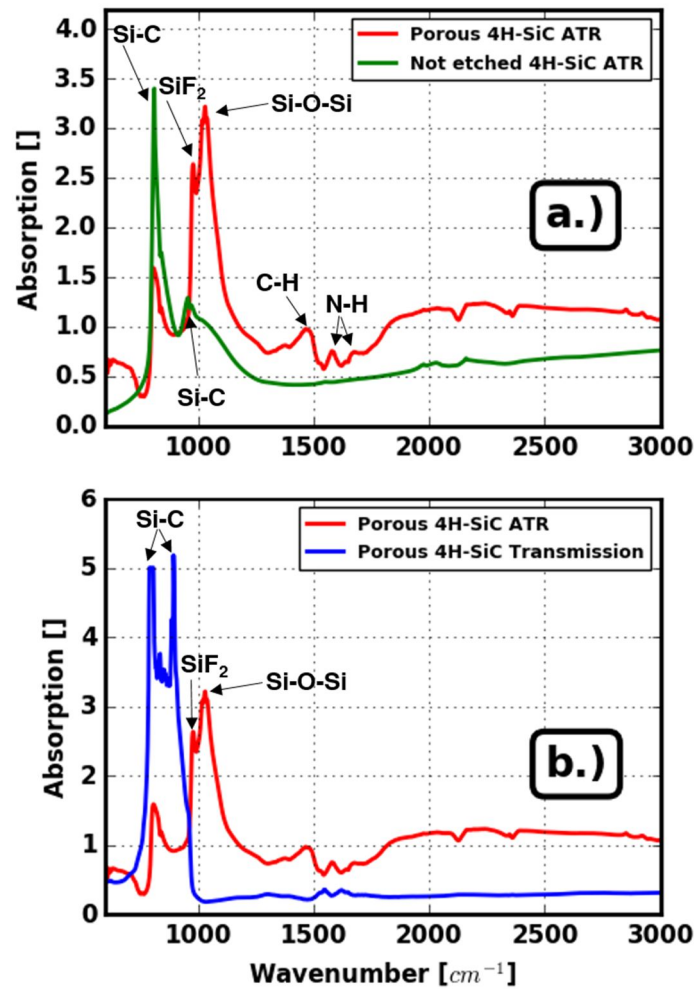


Figure 106: FT-IR spectra of a porous 4H-SiC sample detached from the substrate, measured in ATR mode and in transmission mode. a.) Comparison of etched and not etched sample with ATR method. b.) Comparison of an etched sample in transmission and ATR mode. All samples had a bulk resistivity of 0.02 $\Omega\text{-cm}$.

4.5.5 Summary

In this section basic investigations for a micromachining process were presented which can be used to prepare stacked layers of porous SiC with highly different degree of porosity. The initial aim was to achieve a constant degree of porosity within each sub-layer to a maximum degree such that the films could be used as e.g. optical Bragg filters. For this purpose photoelectrochemical etching (PECE) was utilized. The first samples were etched under current controlled conditions like it is done for the preparation of porous silicon optical filters. This approach proved to be inappropriate for porous SiC because the resulting degree of porosity turned out to be almost independent of the current density. In contrast, the degree of porosity shows similar trends as the voltage during experiments, both exhibiting a transient phase at the beginning of an etching step.

Therefore PECE was performed at constant voltage levels for the realization of each sub-layer. This proved to be an appropriate approach for preparing porous layers with sub-layers having a constant degree of porosity. The experimental results could be interpreted in terms of fractal growth like it is the case for dielectric breakdown in solids. The applied voltage determines the active region at the pore tips during etching and thus the resulting degree of porosity. It has also been shown that the etched porous layers can be detached from the bulk sample and by controlling the sub-layer thickness by the amount of transferred charge porous SiC optical filters can be prepared. This makes the presented results also economically interesting because costly SiC substrates can be re-used several times for porous layer preparation.

Furthermore, the average amount of holes needed to dissolve a formula unit of SiC is influenced by the applied voltage as well as by diffusion of fresh reactants into the porous layer. The transient phase during current controlled PECE is explained by the oxide growth counteracted by its dissolution rate due to the presence of HF.

In summary it could be shown that both the degree of porosity and the homogeneity is controllable in a wide range in 4H-SiC when applying a photo-electrochemical approach.

5 Micromachined devices based on porous SiC

In section 3.9.2 principal investigations on MAPCE and PECE were performed, having already possible application scenarios in mind. The local porosification of SiC is now possible by utilizing MAPCE while a combination of MAPCE and PECE allows tailored fabrication of porous SiC multilayers.

At first membrane fabrication processes are presented, then optical porous SiC devices are introduced.

5.1 Membrane fabrication

Parts of this section have been published in [116].

In this section the fabrication of membranes by utilizing MAPCE and chemical vapor deposition of silicon carbide thin films using both LPCVD and PECVD techniques is reported. First a method is shown that utilizes the reorganization of porous silicon carbide under high temperatures. Afterwards an approach is presented, that utilizes a compressively stressed amorphous SiC thin film. Such membranes can be used in pressure sensors for harsh environments because of the high chemical inertness of silicon carbide.

5.1.1 Sintering approach

At first membrane fabrication was performed by utilizing MAPCE and low pressure chemical vapor deposition. After depositing a polycrystalline SiC thin film on top of the porous layer, a high temperature treatment should cause re-organization of the underlying porous layer. This process is inspired by the work of Armbruster *et al.* [8], but has not been performed with SiC so far. Figure 107a shows MAPCE generated porous SiC directly after etching. Here the same experimental parameters as in section 4.3 were used for MAPCE. Square areas with side lengths of 50 and 100 μm were porosified. After removing the Pt thin film from the sample in boiling aqua regia, a polycrystalline SiC thin film was deposited with low pressure chemical vapor deposition (LPCVD), as is shown in Figure 107b. The polycrystalline SiC fully covers the porous layer without filling the pores.

To initiate re-organization of the porous structure samples with a polycrystalline SiC layer on top were subjected to a heat treatment for 2 hours in air at 1500 $^{\circ}\text{C}$. Such a treatment yielded two possible outcomes as can be seen in Figure 108. Some porous areas showed almost no reorganization of the porous layer. Only the pores at the bottom had vanished after thermal treatment (see Figure 108a). Contrarily several porous areas showed total re-organization as can be seen in Figure 108b.

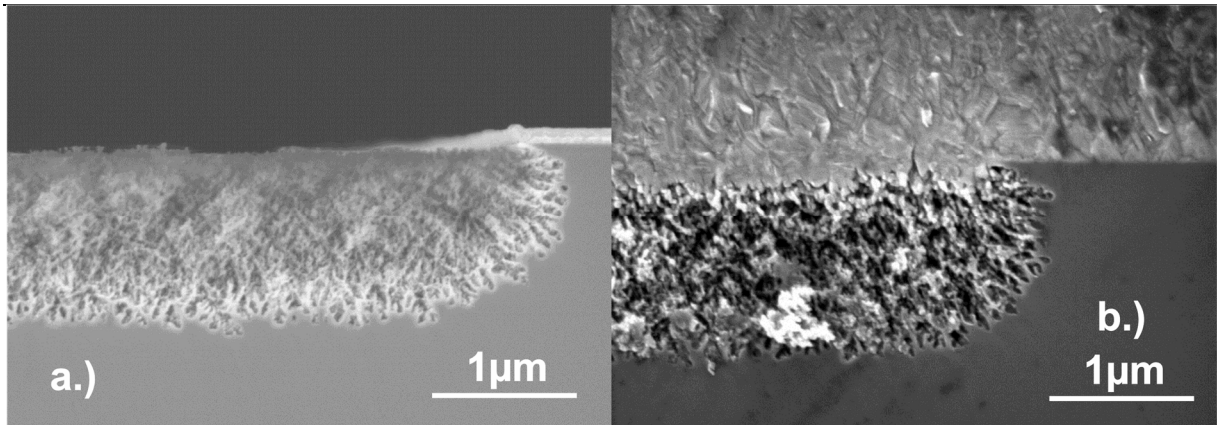


Figure 107: MAPCE generated porous SiC. a.) After etching with a solution containing 0.08 mol/L $\text{Na}_2\text{S}_2\text{O}_8$, utilizing the experimental parameters reported in section 4.3. The Si-face was exposed to the etching solution. b.) After removal of Pt with aqua regia and deposition of polycrystalline silicon carbide thin film.

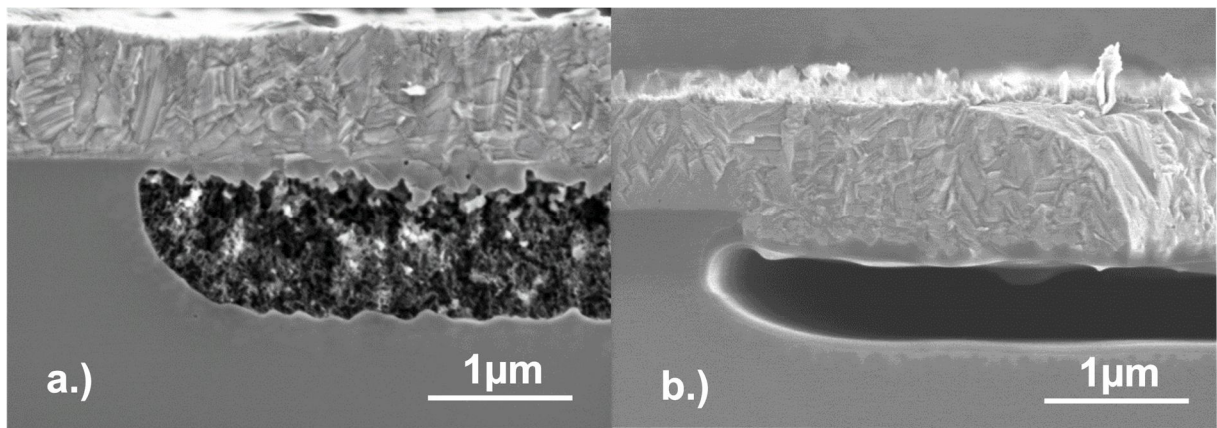


Figure 108: Polycrystalline SiC covering an area of porous SiC after annealing. a.) Only the pores from the active zone vanish b.) Complete reorganization of the porous layer.

These two possible outcomes are related to an oxide layer that forms on top of the polycrystalline SiC. Figure 109 shows complete cross-sectional views of the re-organized square porous SiC areas. In Figure 109a, it can be seen that there is a thin oxide layer on top of the polycrystalline SiC. This layer partially delaminated from the samples, hence this is not observed in Figure 108. However, a closer examination revealed, that re-organization takes place when the forming oxide layer comes into contact with the porous SiC layer as can be seen in Figure 109b. This issue has not been further investigated but it provides a suitable basis for the fabrication of membranes for pressure sensors. Furthermore the presented process can be used in general as a micromachining process, utilizing porous SiC as sacrificial layer.

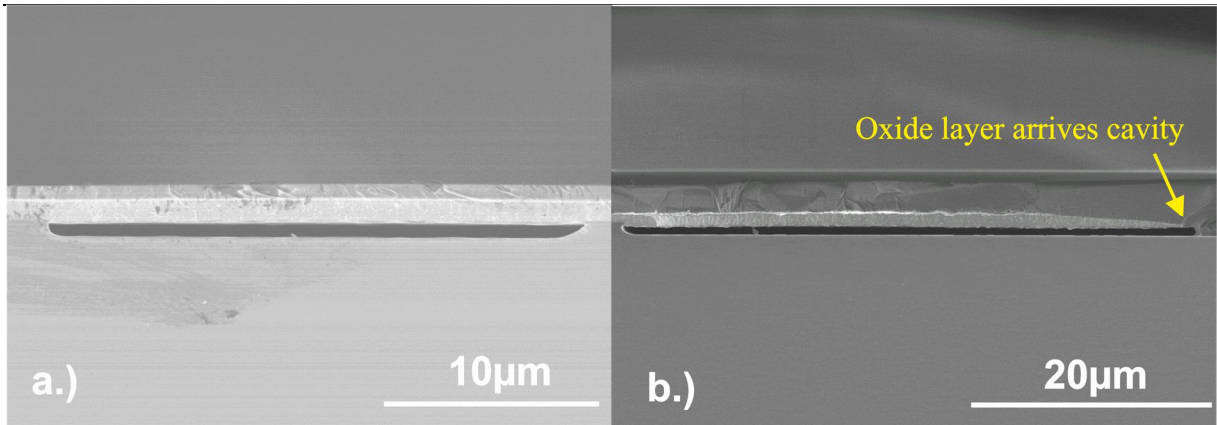


Figure 109: Examples of completely re-organized porous SiC layers after heat treatment. In both cases there is an oxide layer on top of the polycrystalline SiC layer. a.) Cross-sectional view of re-organized porous layer b.) The oxide layer reaches the etched layer causing re-organization.

5.1.2 Buckling approach

Beside the heat treatment approach for membrane fabrication, also the effect of membrane buckling was utilized. Clamped membranes show buckling, when they are under internal compressive stress and when this compressive stress exceeds the critical buckling value [117,118].

To fabricate such buckling membranes an effect discovered in section 4.3.1.1 was utilized. When MAPCE is done with H_2O_2 as oxidizing agent, a line of breakage underneath a highly porous layer can be generated. This is illustrated in Figure 110a, where a porous layer after etching for 150 minutes in a 0.15 M based H_2O_2 etching solution is shown. The experimental parameters for MAPCE in this section are the same as in section 4.3 and also square areas with side lengths of 50 and 100 μm were porosified.

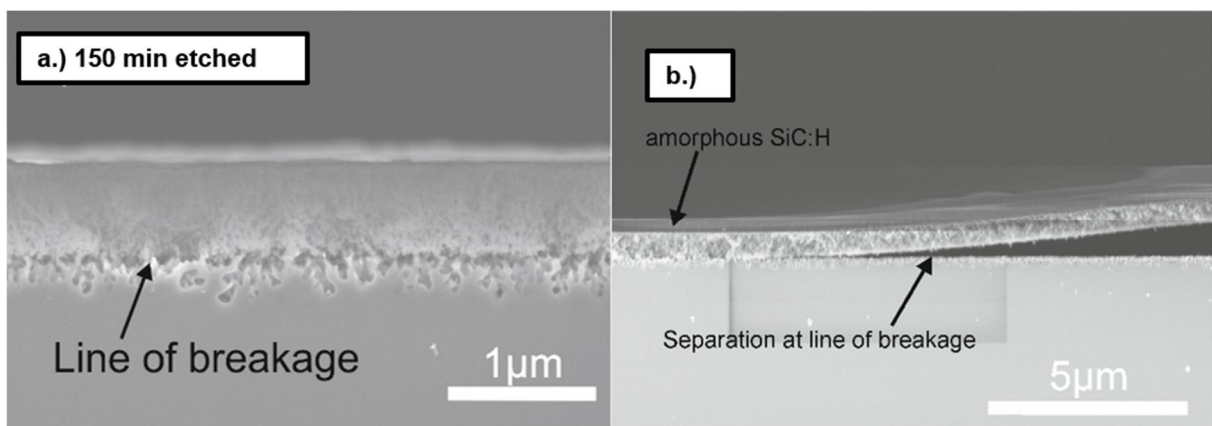


Figure 110: Porous SiC before and after a-SiC:H deposition a.) After etching with 0.15M H_2O_2 based etching solution for 150 minutes b.) After deposition of an a-SiC:H thin film.

After MAPCE the Pt was removed with boiling aqua regia and a $0.5\ \mu\text{m}$ thick a-SiC:H layer was deposited on the samples with PECVD. This is illustrated in Figure 110b. The amorphous SiC:H layer on top is under compressive stress of about $-770\ \text{MPa}$ predominantly due to the incorporated hydrogen [69]. The deposition parameters can be found in section 3.3. This causes membrane buckling, for the deposited thin film together with the porous layer can separate from the bulk material at the line of breakage.

Such buckling membranes were characterized with white light interferometry. Figure 111a shows the measured deflection of a square membrane with a side length of $100\ \mu\text{m}$, whereas red areas correspond to the highest deflection values. A corresponding cross sectional deflection curve is illustrated in Figure 111b, confirming that a buckling membrane has been fabricated. Such membranes may find potential application in MEMS devices, such as pressure sensors for harsh environments, since they are entirely made of chemically inert silicon carbide.

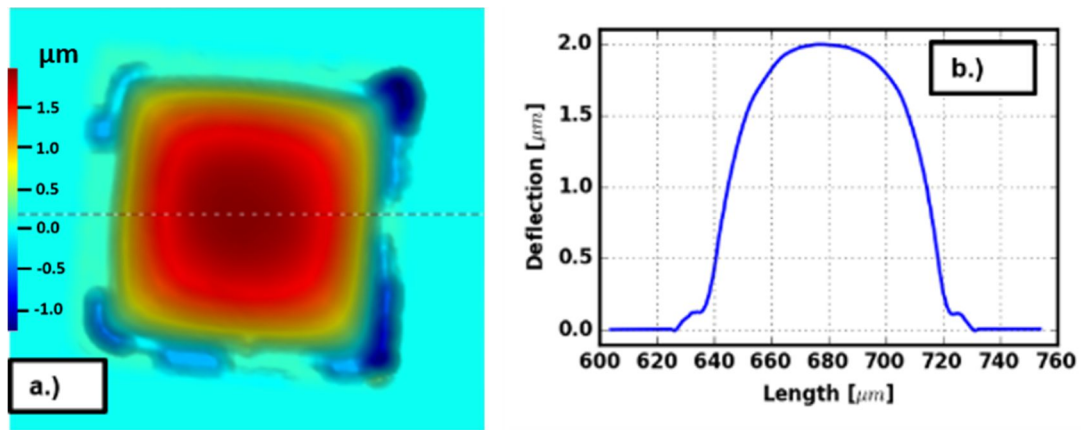


Figure 111: White light interferometry measurement of a buckling square sized membrane. a.) Membrane deflection distribution. b.) Cross-sectional deflection of the membrane.

5.2 Optical devices

In this section optical application scenarios for porous SiC layers are presented. First MAPCE generated porous layers are discussed and afterwards devices fabricated with PECE are presented.

5.2.1 Antireflective and homogeneous thin films

In section 4.3 it was found, that MAPCE allows the generation of porous SiC layers with a decreasing degree of porosity into the bulk. Such a layer is illustrated in Figure 112a; whereas the same experimental conditions were used as described in section 4.3.

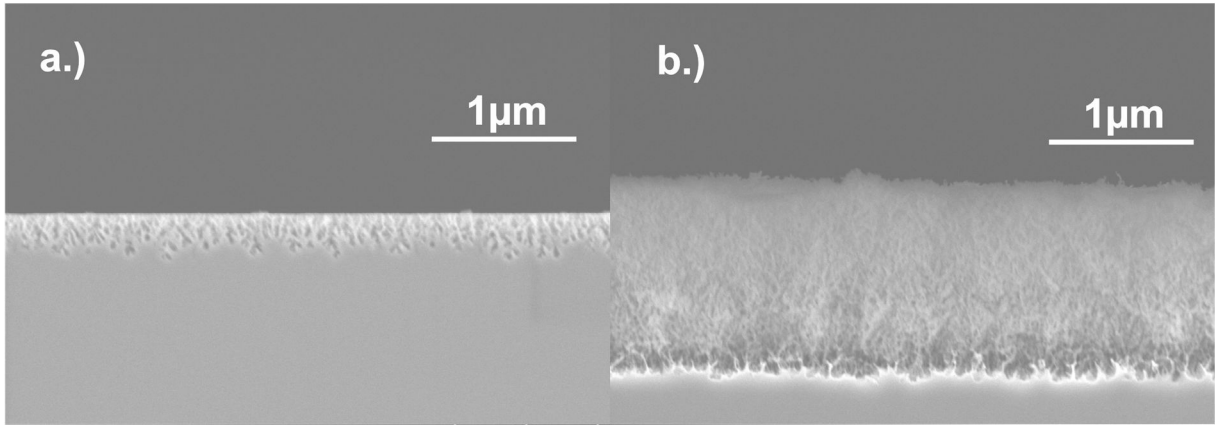


Figure 112: Porous SiC generated with MAPCE utilizing $\text{Na}_2\text{S}_2\text{O}_8$ as oxidizing agent. a.) After 15 minutes of etching (0.08 M $\text{Na}_2\text{S}_2\text{O}_8$) b.) After two etching steps of 120 minutes (0.08 M $\text{Na}_2\text{S}_2\text{O}_8$) and 90 minutes (0.04 M $\text{Na}_2\text{S}_2\text{O}_8$). The total etched area was 25 mm².

According to the Bruggeman effective medium theory, the effective refractive index is defined by the degree of porosity [60]. The higher the degree of porosity, the closer is the effective refractive index to the value of the pore filling medium and *vice versa*. When the surrounding medium is air (refractive index of 1), the effective refractive index corresponding to Figure 112a smoothly increases from the top of the wafer to the bulk substrate (refractive index of SiC is 2.64 at a wavelength of 603 nm) [119].

The ability to create such porous layers with a smooth increase of the effective refractive index allows the preparation of anti-reflection layers for SiC wafers. To explain this, a thin film with a refractive index lower than the substrate and of course higher than the top medium air is assumed, which is the case for a porous layer. Under such conditions a phase shift of π takes place at every interface and in summary does not contribute to interference phenomena. When the optical thickness of the film has a value of $\frac{\lambda}{4}$ destructive interference for the corresponding wavelength takes place.

Now when the refractive index increases linearly from the top of the wafer to the bulk substrate as assumed for the presented porous layer, many $\frac{\lambda}{4}$ sub-layers can notionally be placed in the refractive index profile (see Figure 113), provided the porous region is thick enough. Because of the continuous refractive index change, every plane in the increasing region creates a reflected wave. These waves destructively interfere with other waves, provided there are planes with an optical path distance of $\frac{\lambda}{4}$. Constructive interference effects do not take place like it is the case for a stack of discrete $\frac{\lambda}{4}$ layers. This discussion neglects multiple reflections but qualitatively explains why most of the reflectance is due to the boundary regions of the refractive index profile shown in Figure 113. The reflected waves at these boundary regions are also lower than from a sharp interface (obtained by removal of the gradient region in Figure 113) because the change in refractive index is significantly lower, thus leading to lower absolute reflection coefficients [58].

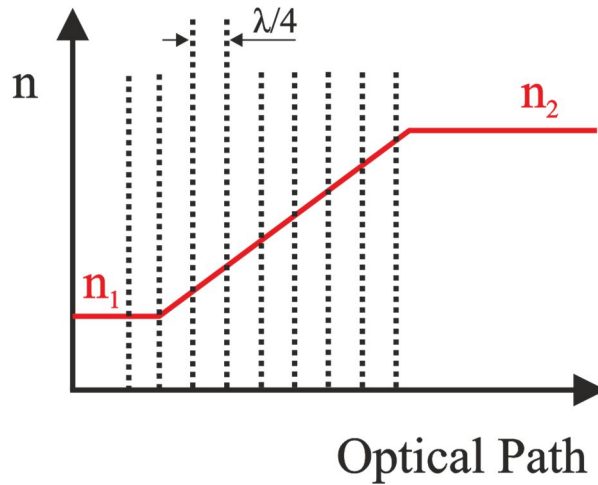


Figure 113: Increasing refractive index profile after [58].

So in summary two effects contribute to a decrease of the reflectance when an increasing refractive index profile is introduced in a substrate surface-near. First the reflected waves destructively interfere in the gradient region and at the boundaries the change in refractive index is significantly decreased compared to a sharp interface.

Now, after having discussed the basics of gradient index anti-reflection layers it has to be proven whether the porous layer shown in Figure 112a shows the expected decrease in reflectance. Corresponding measurements are shown in Figure 114. Indeed the reflectance is significantly decreased for a wafer that was etched for 15 minutes compared to a blank SiC substrate. This observation is attributed to a decreasing degree of porosity with depth and thus an increasing refractive index profile. Such porous anti-reflection layers could be used in light emitting

diodes reducing back reflection into the semiconductor [120] or UV sensors to decrease the amount of reflected UV light [121].

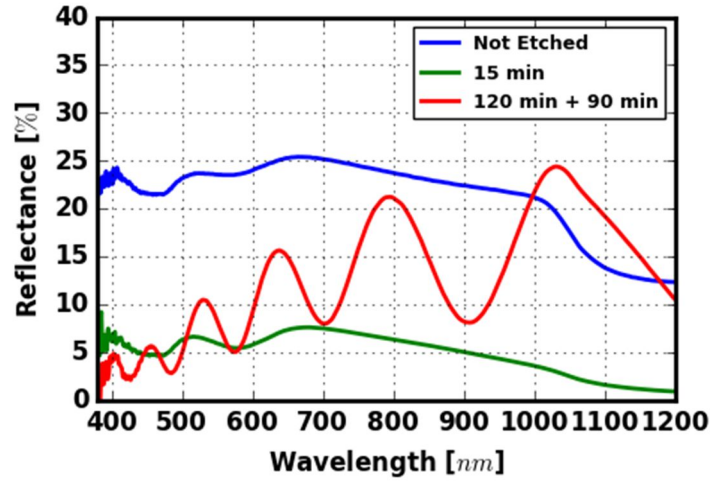


Figure 114: Measured reflectance curves corresponding to Figure 112. Additionally the reflectance of a not etched wafer is shown.

After having introduced anti-reflective coatings realized with MAPCE generated porous SiC, another application scenario has been investigated. MAPCE is also capable of producing highly uniform porous layers with a sharp interface to the bulk substrate. Such a layer is shown in Figure 112b. The corresponding reflectance spectrum is illustrated in Figure 114 by the red curve. In contrast to the not etched wafer and the anti-reflective coated substrate, minima and maxima are present. This is because the porous layer acts as a thin film with a rather homogeneous effective refractive index. The effective refractive index n as well as the degree of porosity p of the porous layer shown in Figure 112b can be determined by utilizing Equation [5-1]. The wavenumber $\frac{1}{\lambda_{min/max}}$ for which a minimum or a maximum in the reflectance spectrum occurs is determined by the effective refractive index and the physical thickness of the porous layer. The reflection order m takes on odd multiples of 0.5 for reflectance minima and integers for reflectance maxima.

$$\frac{1}{\lambda_{min/max}} = \frac{1}{2nd}m \quad [5-1]$$

Figure 115 shows a plot corresponding to [5-1] after inserting values obtained from the reflectance measurement of the homogeneous porous SiC layer while the numerical values are given in Table 8. As expected a linear relationship is obtained. The slope of the curve $\frac{1}{2nd}$ is determined to be $3.1048 \cdot 10^{-4} \text{ nm}^{-1}$ and the correlation coefficient of the fit was 0.995. The offset is due to an arbitrary choice of the reflectance order, which has no effect on the value of the slope. The physical thickness of the porous layer was measured, by utilizing SEM micrographs, to be

1.28 μm . Given this input, the effective refractive index was determined to be 1.25 which is substantially lower than that of the bulk material. Furthermore, the degree of porosity was calculated to be 79 % by utilizing Equation [5-3] (for further details see next section). Given these values, the effective refractive index was determined to be 1.26 which is substantially lower than that of the bulk material of 2.62 at 700 nm [119]. Such layers with a high degree of porosity and uniformity provide the basis for optical sensors utilizing a change in the refractive index profile, when the pores are filled with a different medium.

m	$\lambda_{\text{min/max}}$ [nm]	$\nu \cdot 10^3$ [nm^{-1}]
0.5	1032.2	0.97
1	909.0	1.10
1.5	795.5	1.26
2	702.5	1.42
2.5	638.2	1.57
3	575.5	1.74
3.5	531.1	1.88
4	485.6	2.06
4.5	457.6	2.19
5	425.0	2.35

Table 8: Reflection order, position of the minima and maxima in the reflectance spectrum for a homogeneous porous layer (Figure 112b and Figure 114 120 min. + 90 min.) and the corresponding wavenumbers.

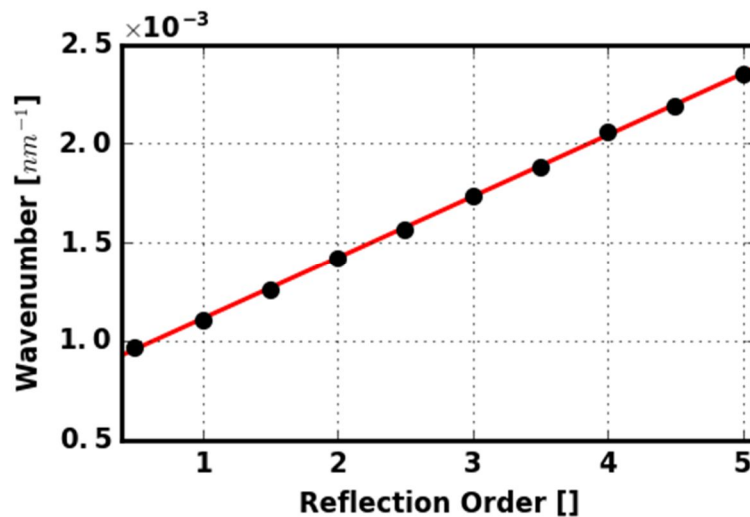


Figure 115: Wavenumbers for which reflectance minima and maxima occur versus the reflection order.

In summary, possible application scenarios of MAPCE generated porous SiC layers have been presented. Short etching times allow the preparation of anti-reflective coatings on SiC wafers which are of interest in light emitting diodes or UV sensors. Long etching times allow the fabrication of porous layers that behave like thin films with a constant refractive index. Such highly porous layers can potentially be used in optical sensors.

5.2.2 Porous, SiC based optical mirrors fabricated with PECE

Parts of this section have been published in [107].

In this section the fabrication of porous SiC optical mirrors with PECE is presented. Such mirrors show a periodic variation in the degree of porosity, which in turn leads to a periodic profile of the effective refractive index. Two mirror types have to be distinguished: Bragg mirrors with alternating sub-layers of high and low degree of porosity and rugate mirrors which show a sinusoidal porosity-depth profile.

The findings in section 4.4.3 showed that the resulting degree of porosity during PECE is mainly controlled by the applied voltage and unaffected by the current density. However, a decreasing current density reduces the thickness of each sub-layer.

To counterbalance this effect charge controlled PECE was utilized. This means that the applied voltage was switched after a certain amount of transferred charge rather than elapsed time. The porous thin film investigated with SIMS depth profiling in section 4.5.4 was already etched under such charge controlled conditions, aiming to fabricate a Bragg mirror. Its fabrication and optical properties are discussed in the following text.

In Bragg mirrors each sub-layer of the stack has to fulfil the condition shown in Equation [5-2], where n is the refractive index of the sub-layer, d is its thickness and λ_0 is the wavelength corresponding to maximum reflectivity. The reflection band of the filter is centered at the wavelength of maximum reflectivity [122].

$$nd = \frac{\lambda_0}{4} \quad [5-2]$$

The effective refractive index n_{eff} of a porous SiC sub-layer depends on its degree of porosity. A method to calculate n_{eff} is provided by Equation [5-3] which is based on the Bruggeman effective medium approach [123]. The refractive indices of SiC and the pores are denoted by n_{SiC} and n_{pore} , while p is the degree of porosity. Finally d represents the dimensionality of the system, which is set to 3 [124].

$$(1 - p) \frac{n_{SiC}^2 - n_{eff}^2}{n_{SiC}^2 + (d - 1)n_{eff}^2} + p \frac{n_{pore}^2 - n_{eff}^2}{n_{pore}^2 + (d - 1)n_{eff}^2} = 0 \quad [5-3]$$

To estimate the necessary thicknesses of the porous sub-layers for a Bragg filter with a wavelength of maximum reflectivity of 568 nm the corresponding effective refractive indices for porous layers with porosities of 38% and 15% (the porosity values for 11.5 and 8.5 V as found in section 4.5.2) were calculated with Equation [5-3]. The refractive indices of dense SiC and the pore volume filled with air were set to 2.72 [119] and 1, respectively. By using Equation [5-3], required thicknesses of 70 nm and 58 nm were calculated for the two individual porous sub-layers having either a degree of porosity of 38% or 15.

To realize a Bragg mirror with the calculated parameters a charge controlled experiment with alternating voltages (11.5 V and 8.5 V) was performed. The voltage was switched after a specific amount of transferred charge during the formation of an individual porous sub-layer. The corresponding charge values were calculated with the data shown in Figure 97, assuming there is a linear relationship between transferred charge and layer thickness. In particular, a phase with 11.5 V lasted until 0.6 C had been transferred. Then the voltage was switched to 8.5 V. The corresponding amount of charge was 0.12 C for the 8.5 V periods. This process was repeated until 300 sub-layers had been etched. Then a separation process was performed by rising the voltage to 60 V for 6 seconds. A cross-sectional SEM micrograph of the obtained freestanding porous layer (total thickness of 21.5 μm) is shown in Figure 116. In particular the bottom side of the freestanding film is shown. One can see that there are several porous sub-layers with alternating degree of porosity as had been intended. Figure 117 shows two reflectance measurements of the porous film. One can see that the two reflectance graphs show peaks at 570 nm and 538 nm which are close to the targeted value of 568 nm. The difference between the two curves is due to local variations immanent to electrochemical etching techniques. This shows that the preparation of porous 4H-SiC optical filters is possible with charge controlled PECE.

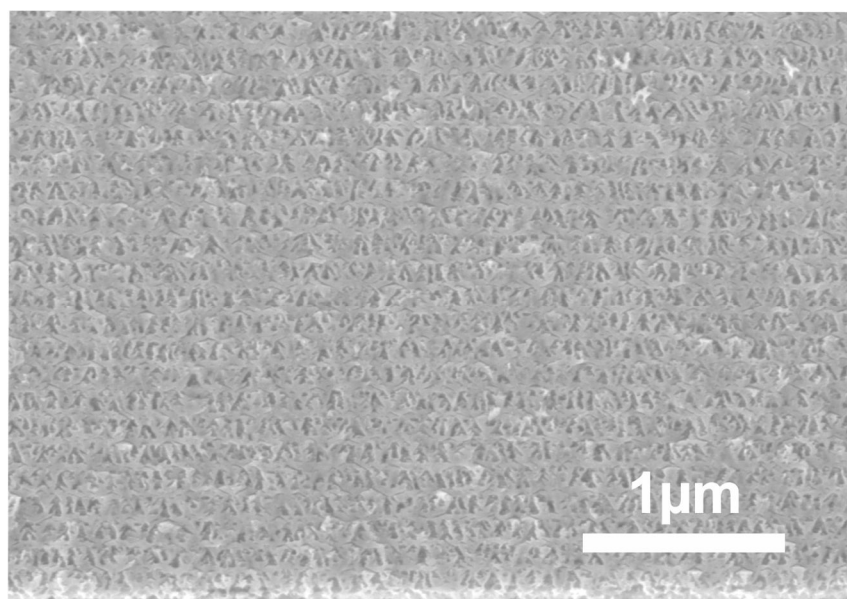


Figure 116: Cross-sectional SEM micrograph of a porous 4H-SiC film prepared on the dense 4H-SiC substrate with alternating voltages. The bulk resistivity of the sample is 0.02 $\Omega\cdot\text{cm}$.

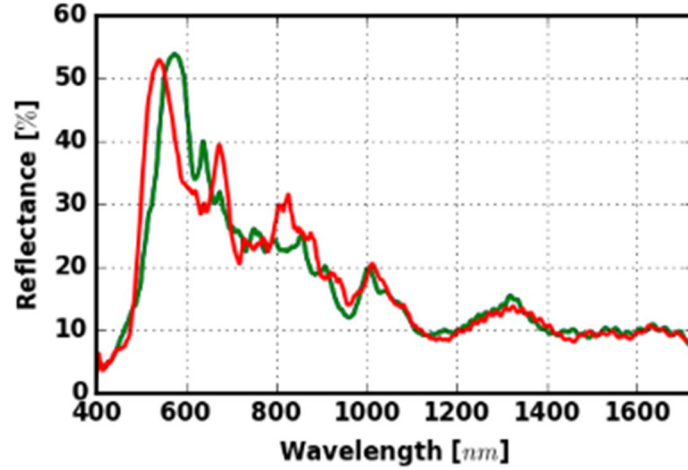


Figure 117: Reflection curves of a porous SiC film prepared with alternating voltages under charge controlled conditions. The bulk resistivity of the sample is $0.02 \, \Omega\text{-cm}$.

After this first successful experiment the fabrication of rugate mirrors having a sinusoidal porosity depth profile was aimed. Therefore, etching was again performed in a charge controlled mode, but the voltage was sinusoidally varied as is shown in Table 9. To obtain similar etching depths during each step the amount of charge per step is weighted such that more charge is transferred at a higher voltage, because under these conditions the resulting porosity is higher but the etching rate is decreased. During PECE this profile was executed 150 times after an initial phase of 11.5 V which lasted for 3 s. Finally two 60 V pulses, each lasting 6 seconds were applied to separate the porous layer from the bulk sample. This way the bulk sample can be re-used for mirror preparation by repeating the previous sequence of MAPCE and PECE steps.

All etching experiments for rugate mirror fabrication were performed on the Si-face of the 4H-SiC sample. Moreover an etching solution containing 0.04 mol/L $\text{Na}_2\text{S}_2\text{O}_8$ and 1.31 mol/L HF was used for these experiments. This was done to decrease the etching rate due to a decreased HF content and thus a better controllability of the whole process.

Voltage [V]	Cumulated Transferred Charge [C]
10.00	0.00
10.81	0.09
11.36	0.19
11.48	0.29
11.13	0.39
10.42	0.48
9.58	0.57
8.87	0.65
8.52	0.72
8.64	0.80
9.19	0.88
10.00	0.96

Table 9: First voltage profile during PECE for rugate mirror fabrication.

First the resulting pore morphology of the mirror was investigated by analyzing cross-sectional SEM micrographs. Figure 1 shows such a SEM micrograph with the corresponding black and white image which was obtained with adaptive Gaussian image thresholding (see Figure 118). The degree of porosity varies between low and high values, whereas the pore morphology varies between low and high porosity dendritic according to classification in literature [43]. The numerical value of the degree of porosity profile could be estimated from the black and white images as shown in Figure 119a. Additionally the distribution of the pore cross-sectional area contributing to the total degree of porosity is illustrated in Figure 119b. Pores with a cross-sectional area of approximately 350 nm^2 appear most often in this distribution. The porosity profile, in turn, allowed the calculation of the refractive index profile n_{eff} according to Equation [5-3]. The refractive index of SiC n_{SiC} was set to 2.62 being the corresponding value at a wavelength of 710 nm [125].

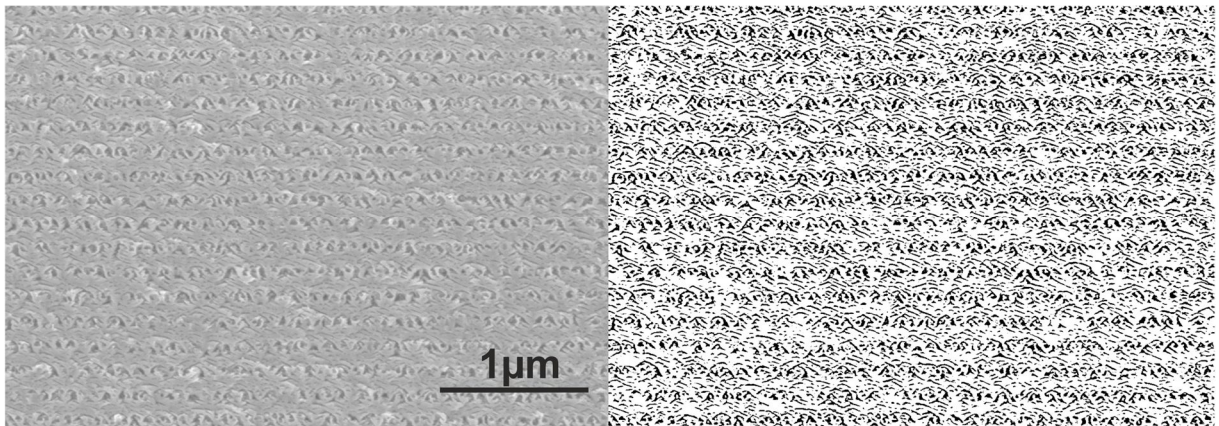


Figure 118: Cross-sectional SEM micrograph of a pSiC rugate mirror and the corresponding black and white image.

A section of the obtained refractive index profile is shown in Figure 119c. The refractive index varies periodically and the fast Fourier transform of the whole refractive index profile shows two peaks at $5.9 \mu\text{m}^{-1}$ and $11.8 \mu\text{m}^{-1}$ (see Figure 119d). This allows the prediction of the wavelengths of maximum reflectance in the reflectance of the mirror according to Equation [5-4].

$$\lambda_0 = 2z\langle n \rangle \quad [5-4]$$

Here $\langle n \rangle$ is the average refractive index of the mirror and z is the length of a period [58]. According to Equation 2 and the calculated data from the experiment ($z_1 = 0.0847 \mu\text{m}$; $z_2 = 0.169 \mu\text{m}$; $\langle n \rangle = 2.187$) two peaks are expected in the reflectance spectrum at rejection wavelengths of 370 and 739 nm. This was indeed found in reflectance measurements as is illustrated in Figure 120a. Three measurements of the prepared mirror are shown which exhibit peaks at 375 to 385 nm and 710 to 750 nm which correspond to the prediction from the refractive index profile.

A more rigorous calculation of the reflectance spectrum has also been performed with the program OpenFilters neglecting front and back side reflections [126]. The results are illustrated in Figure 120b, demonstrating that the rejection wavelengths are located at approximately 360 and 720 nm. Also, the physical appearance of the prepared mirrors is in accordance with the measurements as can be seen in Figure 120c. It appears in green, because in transmission one can see the complementary colors of the reflectance spectrum. This indicates that such mirrors can also be used in transmission mode.

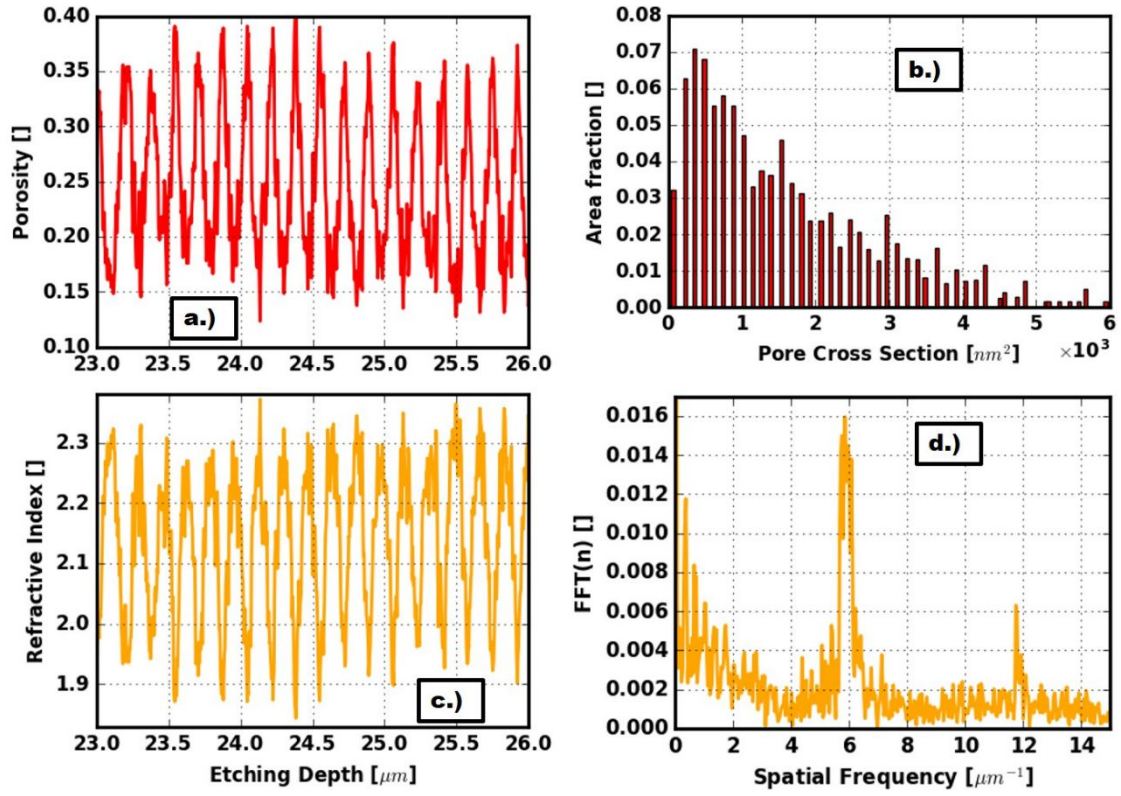


Figure 119: Refractive index profile and corresponding spatial frequency spectrum

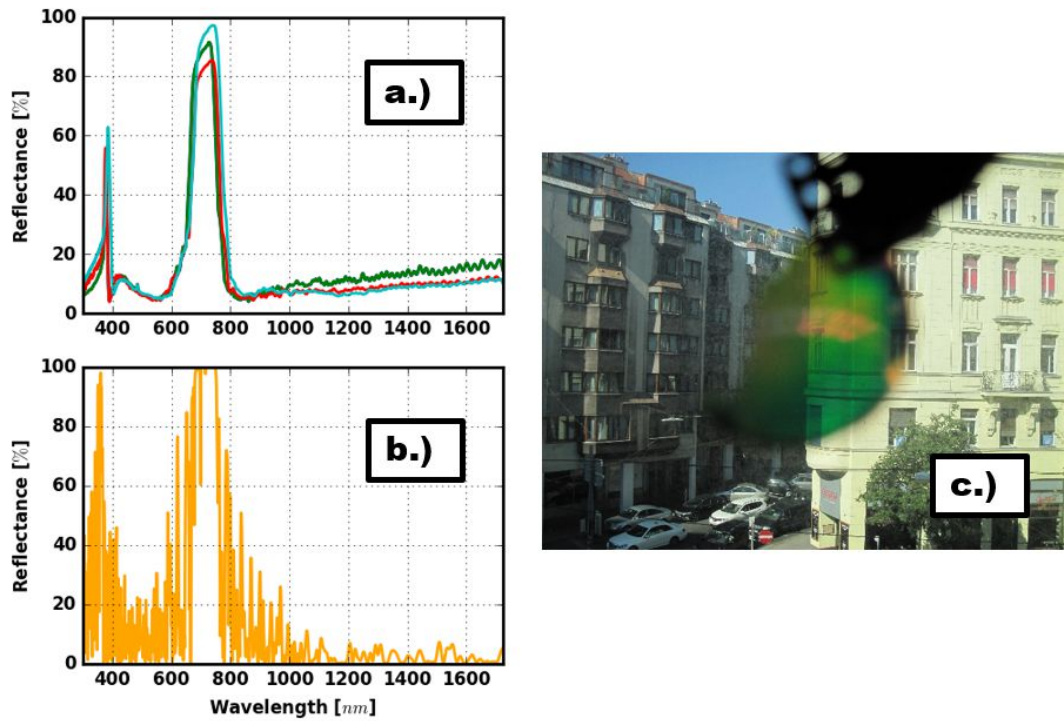


Figure 120: Properties of the novel porous SiC-based rugate mirror. a.) Reflectance measurements b.) Calculated reflectance spectrum. c.) Physical appearance.

Finally, the possibility to re-use the dense 4H-SiC sample for subsequent mirror fabrication is demonstrated. Therefore, the same etching procedure (i.e. MAPCE and PECE) was performed as used for the realization of the first rugate mirror element. Only the applied voltage profile was modified, such that the transferred charge during the porosification sequence was increased (see Table 1). This was done to show additionally, whether the peak positions in the reflectance spectrum can be shifted to higher values.

Voltage [V]	Transferred Charge [C]
10.00	0.00
10.81	0.11
11.36	0.23
11.48	0.36
11.13	0.48
10.42	0.60
9.58	0.71
8.87	0.81
8.52	0.91
8.64	1.0
9.19	1.1
10.00	1.2

Table 1: Modified voltage profile during PECE for rugate mirror fabrication.

The resulting reflectance spectra are illustrated in Figure 121a. As expected, the two reflectance peaks shifted to larger values of 440 to 460 nm and 810 to 920 nm compared to those illustrated in Figure 120a. In Figure 121b the calculated reflectance spectrum is shown proving on a theoretical basis the increase of the rejection wavelengths. Finally, it is worth mentioning that the physical appearance of the mirror changes when applying the modified parameters during PECE. Instead of green it appears now in yellow, being the complementary color of the minor peak located at 440 to 460 nm. Beside these observations also the total mirror thickness increased from about 28 to 35 μm .

In summary, the preparation of optical mirrors by utilizing PECE of 4H-SiC was successful and the properties of the mirrors could be adjusted by altering the process parameters during etching. In both cases the separation from the bulk substrate succeeded at the end of the etching sequence, so the etching depth equals the final mirror thickness.

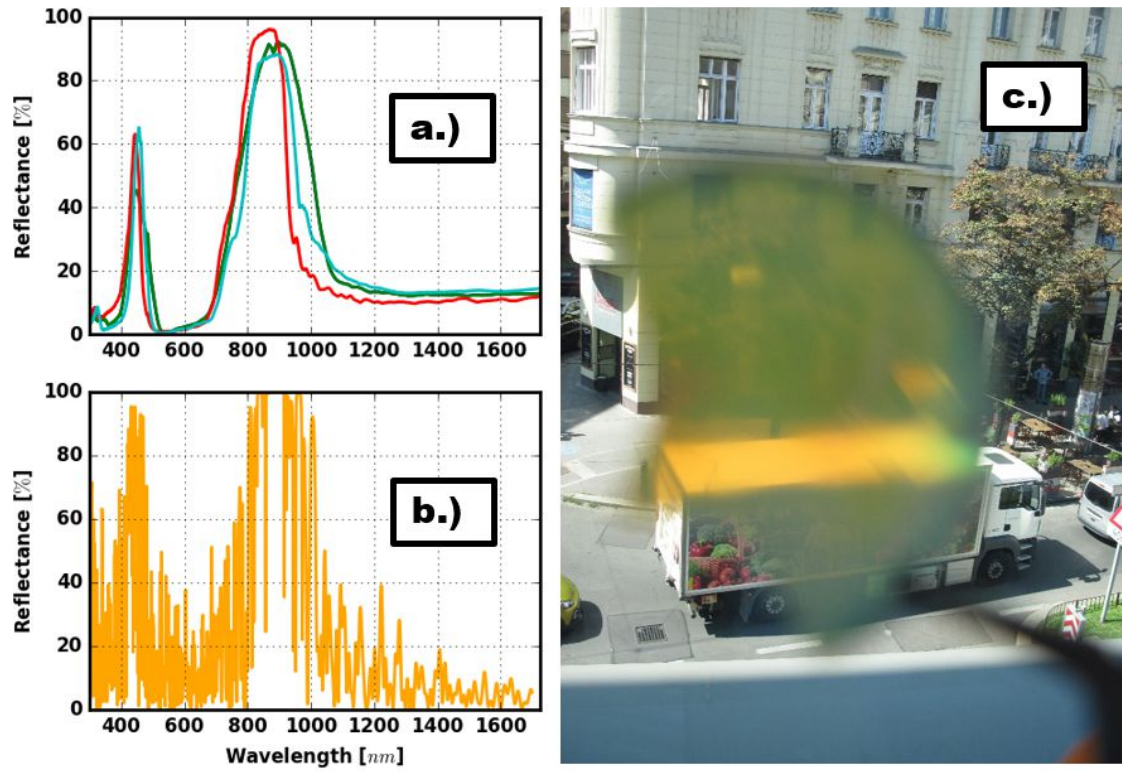


Figure 121: Properties of the modified rugate mirror. a.) Reflectance measurements b.) Calculated reflectance spectrum. c.) Physical appearance.

6 Summary and Outlook

In this thesis the fabrication of single crystalline porous silicon carbide (SiC) layers from a dense single crystalline 4H-SiC substrate using photoelectrochemical techniques is presented. Two different etching methods were investigated. The first is metal assisted photochemical etching (MAPCE) which utilizes sputter deposited platinum (Pt) as electrodes on the SiC substrate. UV light generates the necessary minority carriers (holes) which are necessary for etching, and an oxidizing agent in the etching solution takes up the electrons generated in the conduction band. By decreasing the contact resistance at the Pt/SiC interface, reliable porosification of substrates having different bulk resistivity values could be achieved.

These initial results allowed the enhancement of photoelectrochemical etching (PECE) of 4H-SiC. Before this thesis, only porous layers with an irregular porous structure had been reported in literature. Furthermore no reports were available, describing how to control and tailor the resulting degree of porosity. The first issue was addressed by generating a porous layer with MAPCE as a pre-treatment prior to PECE. By doing so, the homogeneity of the resulting porous structure was significantly increased because PECE pore growth started at the pore tips initially provided by the MAPCE porous layer. The second issue was addressed by evaluating the degree of porosity and varying the electrical parameters. It turned out, that the degree of porosity is mainly determined by the applied voltage and almost independent of the current density throughout PECE. This is an interesting result, considering that almost all electrochemical etching experiments done for the realization of porous silicon are performed under current controlled conditions. Finally it was also possible to separate thin porous films from a bulk substrate. Given the high cost of 4H-SiC wafers, this makes the developed combination of MAPCE and PECE economically interesting for the fabrication of MEM/NEMS, but also for power electronic devices.

Beside this basic investigations regarding PECE also the mechanisms governing MAPCE were further investigated. It could be shown that an already existing PECE layer levels out to a constant degree of porosity as a function of depth, when MAPCE is performed as a post-treatment. This shows that there is some limiting degree of porosity, which is explained with a space charge layer that fully covers the porous structure. Beside this, also no further etching into depth took place until the porous layer had a constant porosity-depth profile. This means that new pore initiation and etching of already existing pores are two different processes, with the latter one having a lower activation energy.

These findings inspired further MAPCE experiments with small volumes of etching solution. When the oxidizing strength of the etching solution decreases due to consumption of the oxidizing agent, thin films with a homogeneous degree of porosity should be obtained. Indeed this was demonstrated experimentally. Together with a cellular automaton simulation it could be

shown, that at the later stages of etching pore formation into depth ceases, and the etching of already existing pores becomes the dominant process. Beside these findings it could also be revealed, that total dissolution of the porous MAPCE layers is possible. A chemical analysis of the porous layers showed, that the passivating effect is closely related to functional groups at the surface generated during etching. When they are removed at high etching times, total dissolution takes place. This phenomenon also allowed to under-etch highly porous layers, by tuning the oxidation rate at the beginning of a MAPCE experiment.

In the end all these findings were utilized for the realization of novel device concepts. First membranes based on porous SiC were fabricated, either by a thermal re-organization of the porous layer or by covering a porous layer with a compressively stressed amorphous SiC thin film. In the latter approach a line of breakage was introduced during MAPCE, such that a buckling membrane was obtained. Both approaches are novel in the field of SiC, while the latter is a completely new concept for fabrication of MEMS devices. These membranes may find application in pressure sensors. Testing their response to external pressure and their long time stability are important tasks for the future.

A different field for possible application of porous SiC is optics. MAPCE allows to control whether there is a smooth or sharp interface between porous SiC and the bulk substrate. This is analogous to a smooth or abrupt change of the refractive index. This way anti-reflective coatings or optical thin films could be fabricated. The former have potential in light emitting diodes or UV sensors while the latter could be used e.g. in optical biosensors due to the observed interference phenomena.

Moreover more complex structure could be fabricated with PECE. The knowledge, that the degree of porosity is mainly determined by the applied voltage allowed the fabrication of stacked layers having alternating degree of porosity. When the thickness of each sub layer as well as the degree of porosity is chosen properly, a Bragg or rugate mirror is obtained. Indeed this could be achieved and the measured reflectance spectra are in excellent agreement with the calculated spectra obtained from the estimated degrees of porosity. Such mirrors have been produced with porous silicon, but need to be protected when it comes to application in harsh environments. Here porous SiC optical mirrors could replace porous Si. Further investigations are needed in the future to evaluate their full potential.

Altogether, in this thesis the theoretical basics of MAPCE and PECE were presented making it now possible to control the formation of porous SiC in a reliable way. With this knowledge porous SiC based MEMS devices were fabricated, thus hopefully stimulating the integration of porous silicon carbide in many other, future device concepts with increased robustness.

7 References

- [1] A. Uhler, Electrolytic shaping of germanium and silicon, *Bell Syst. Tech. J.* 35 (1956) 333–347. doi:10.1002/j.1538-7305.1956.tb02385.x.
- [2] L.T. Canham, Silicon quantum wire array fabrication by electrochemical and chemical dissolution of wafers, *Appl. Phys. Lett.* 57 (1990) 1046–1048. doi:10.1063/1.103561.
- [3] V. Lehmann, U. Gösele, Porous silicon formation: A quantum wire effect, *Appl. Phys. Lett.* 58 (1991) 856–858. doi:10.1063/1.104512.
- [4] F. Cunin, T.A. Schmedake, J.R. Link, Y.Y. Li, J. Koh, S.N. Bhatia, M.J. Sailor, Biomolecular screening with encoded porous-silicon photonic crystals, *Nat. Mater.* 1 (2002) 39–41. doi:10.1038/nmat702.
- [5] S.E. Lewis, J.R. DeBoer, J.L. Gole, P.J. Hesketh, Sensitive, selective, and analytical improvements to a porous silicon gas sensor, *Sens. Actuators B Chem.* 110 (2005) 54–65. doi:10.1016/j.snb.2005.01.014.
- [6] L. Oakes, A. Westover, J.W. Mares, S. Chatterjee, W.R. Erwin, R. Bardhan, S.M. Weiss, C.L. Pint, Surface engineered porous silicon for stable, high performance electrochemical supercapacitors, *Sci. Rep.* 3 (2013) 3020. doi:10.1038/srep03020.
- [7] G. Kaltsas, A.G. Nassiopoulou, Bulk silicon micromachining using porous silicon sacrificial layers, *Microelectron. Eng.* 35 (1997) 397–400. doi:10.1016/S0167-9317(96)00209-2.
- [8] S. Armbruster, F. Schafer, G. Lammel, H. Artmann, C. Schelling, H. Benzel, S. Finkbeiner, F. Larmer, R. Ruther, O. Paul, A novel micromachining process for the fabrication of monocrystalline si-membranes using porous silicon, *IEEE TRANSDUCERS Solid-State Sens. Actuators Microsyst. 12th Int. Conf. On.* (2003) 246–249. doi:10.1109/SENSOR.2003.1215299.
- [9] X. Li, P.W. Bohn, Metal-assisted chemical etching in HF/H₂O₂ produces porous silicon, *Appl. Phys. Lett.* 77 (2000) 2572–2574. doi:10.1063/1.1319191.
- [10] Z. Huang, N. Geyer, P. Werner, J. de Boer, U. Gösele, Metal-assisted chemical etching of silicon: a review, *Adv. Mater.* 23 (2011) 285–308. doi:10.1002/adma.201001784.
- [11] J. Salonen, E. Mäkilä, *Porous silicon for biomedical applications*, Woodhead Publishing London, 2014. <https://doi.org/10.1533/9780857097156.1.21>.
- [12] D.J. Díaz, T.L. Williamson, X. Guo, A. Sood, P.W. Bohn, Electroless deposition of gold and platinum for metallization of the intrapore space in porous gallium nitride, *Thin Solid Films.* 514 (2006) 120–126. doi:10.1016/j.tsf.2006.02.098.
- [13] H. Asoh, T. Yokoyama, S. Ono, Formation of periodic microbump arrays by metal-assisted photodissolution of InP, *Jpn. J. Appl. Phys.* 49 (2010) 046505. doi:10.1143/JJAP.49.046505.
- [14] J.S. Shor, A.D. Kurtz, Photoelectrochemical etching of 6 H–SiC, *J. Electrochem. Soc.* 141 (1994) 778–781. doi:10.1149/1.2054810.
- [15] P. Mélinon, B. Masenelli, F. Tournus, A. Perez, Playing with carbon and silicon at the nanoscale, *Nat. Mater.* 6 (2007) 479. doi:10.1038/nmat1914.

-
- [16] G.L. Zhao, D. Bagayoko, Electronic structure and charge transfer in 3C-and 4H-SiC, *New J. Phys.* 2 (2000) 16. doi:10.1088/1367-2630/2/1/316.
- [17] L. Latu-Romain, M. Ollivier, *Silicon carbide one-dimensional nanostructures*, John Wiley & Sons, 2015.
- [18] W.M. Haynes, *CRC handbook of chemistry and physics*, CRC press, 2014.
- [19] Dissertation Tesfaye Ayalew, (n.d.). <http://www.iue.tuwien.ac.at/phd/ayalew/mythesis.html> (accessed February 25, 2018).
- [20] C.-M. Zetterling, *Process technology for silicon carbide devices*, IET, 2002.
- [21] F. Bechstedt, A. Belabbes, Structure, energetics, and electronic states of III–V compound polytypes, *J. Phys. Condens. Matter.* 25 (2013) 273201. doi:10.1088/0953-8984/25/27/273201.
- [22] T. Kimoto, J.A. Cooper, *Fundamentals of silicon carbide technology: growth, characterization, devices and applications*, John Wiley & Sons, 2014.
- [23] M. Mehregany, C.A. Zorman, N. Rajan, C.H. Wu, Silicon carbide MEMS for harsh environments, *Proc. IEEE.* 86 (1998) 1594–1609. doi:10.1109/5.704265.
- [24] R. Memming, *Electron Transfer Theories*, *Semicond. Electrochem.* 2nd Ed. (2001) 127–168. doi:10.1002/9783527688685.ch6.
- [25] M.X. Tan, P.E. Laibinis, S.T. Nguyen, J.M. Kesselman, C.E. Stanton, N.S. Lewis, Principles and applications of semiconductor photoelectrochemistry, *Prog. Inorg. Chem.* Vol. 41. (1994) 21–144. doi:10.1002/9780470166420.ch2.
- [26] K. Rajeshwar, K. Rajeshwar, Fundamentals of semiconductor electrochemistry and photoelectrochemistry, fundamentals of semiconductor electrochemistry and photoelectrochemistry, in: *Encycl. Electrochem. Encycl. Electrochem.*, Wiley-VCH Verlag GmbH & Co. KGaA, Wiley-VCH Verlag GmbH & Co. KGaA, 2007. doi:10.1002/9783527610426.bard060001, 10.1002/9783527610426.bard060001.
- [27] G. Wedler, H.-J. Freund, *Lehrbuch der Physikalischen Chemie*, John Wiley & Sons, 2012.
- [28] S.H. Simon, *The oxford solid state basics*, Oxford University Press, Usa, Oxford, 2013.
- [29] H. Reiss, The Fermi level and the redox potential, *J. Phys. Chem.* 89 (1985) 3783–3791. doi:10.1021/j100264a005.
- [30] C. Kittel, The way of the chemical potential, *Am. J. Phys.* 35 (1967) 483–487. doi:10.1119/1.1974154.
- [31] H. Gerischer, Electron-transfer kinetics of redox reactions at the semiconductor/electrolyte contact. A new approach, *J. Phys. Chem.* 95 (1991) 1356–1359. doi:10.1021/j100156a060.
- [32] W.W. Gärtner, Depletion-layer photoeffects in semiconductors, *Phys. Rev.* 116 (1959) 84. doi:10.1103/PhysRev.116.84.
- [33] K.W. Kolasinski, Etching of silicon in fluoride solutions, *Surf. Sci.* 603 (2009) 1904–1911. doi:10.1016/j.susc.2008.08.031.
- [34] Y. Shishkin, W.J. Choyke, R.P. Devaty, Photoelectrochemical etching of n-type 4H silicon carbide, *J. Appl. Phys.* 96 (2004) 2311–2322. doi:10.1063/1.1768612.

-
- [35] Y. Shishkin, Y. Ke, R.P. Devaty, W.J. Choyke, Fabrication and morphology of porous p-type SiC, *J. Appl. Phys.* 97 (2005) 044908. doi:10.1063/1.1849432.
- [36] Y. Ke, R.P. Devaty, W.J. Choyke, Comparative columnar porous etching studies on n-type 6H SiC crystalline faces, *Phys. Status Solidi B.* 245 (2008) 1396–1403. doi:10.1002/pssb.200844024.
- [37] J. Senthilnathan, C.-C. Weng, W.-T. Tsai, Y. Gogotsi, M. Yoshimura, Synthesis of carbon films by electrochemical etching of SiC with hydrofluoric acid in nonaqueous solvents, *Carbon.* 71 (2014) 181–189. doi:10.1016/j.carbon.2014.01.028.
- [38] A.P. Sutton, *Electronic structure of materials*, Clarendon Press, 1993.
- [39] R.L. Smith, S.D. Collins, Porous silicon formation mechanisms, *J. Appl. Phys.* 71 (1992) R1–R22. doi:10.1063/1.350839.
- [40] X.G. Zhang, Morphology and formation mechanisms of porous silicon, *J. Electrochem. Soc.* 151 (2004) C69–C80. doi:10.1149/1.1632477.
- [41] A.O. Konstantinov, C.I. Harris, E. Janzen, Electrical properties and formation mechanism of porous silicon carbide, *Appl. Phys. Lett.* 65 (1994) 2699–2701. doi:10.1063/1.112610.
- [42] Y. Ke, Formation and characterization of columnar porous sic fabricated by photo-electrochemical etching, PhD Thesis, University of Pittsburgh, 2007. http://d-scholarship.pitt.edu/9656/1/Dissertation_Yue_Ke_JAN10_2008.pdf.
- [43] P. Newby, J.-M. Bluet, V. Aimez, L.G. Fr  chette, V. Lysenko, Structural properties of porous 6H silicon carbide, *Phys. Status Solidi C.* 8 (2011) 1950–1953. doi:10.1002/pssc.201000222.
- [44] D. Dimova-Malinovska, M. Sendova-Vassileva, N. Tzenov, M. Kamenova, Preparation of thin porous silicon layers by stain etching, *Thin Solid Films.* 297 (1997) 9–12. doi:10.1016/S0040-6090(96)09434-5.
- [45] G. Bianchi, F. Mazza, T. Mussini, Catalytic decomposition of acid hydrogen peroxide solutions on platinum, iridium, palladium and gold surfaces, *Electrochimica Acta.* 7 (1962) 457–473. doi:10.1016/0013-4686(62)80034-6.
- [46] C.M.A. Ashruf, P.J. French, P. Bressers, J.J. Kelly, Galvanic porous silicon formation without external contacts, *Sens. Actuators Phys.* 74 (1999) 118–122. doi:10.1016/S0924-4247(98)00340-9.
- [47] T.L. Rittenhouse, P.W. Bohn, I. Adesida, Structural and spectroscopic characterization of porous silicon carbide formed by Pt-assisted electroless chemical etching, *Solid State Commun.* 126 (2003) 245–250. doi:10.1016/S0038-1098(03)00130-3.
- [48] T.L. Rittenhouse, Formation of porous silicon carbide and its suitability as a chemical and temperature detector, Dissertation, Illinois Univ at Urbana Dept of Chemistry, 2004. <http://www.dtic.mil/cgi-bin/GetTRDoc?Location=U2&doc=GetTRDoc.pdf&AD=ADA428124>.
- [49] T. Hossain, I. Khan, I. Adesida, P.W. Bohn, T.L. Rittenhouse, Nanoporous silicon carbide for nanoelectromechanical systems applications, (n.d.). <https://ntrs.nasa.gov/archive/nasa/casi.ntrs.nasa.gov/20030037184.pdf> (accessed August 24, 2017).

-
- [50] A. Bsiesy, J.C. Vial, F. Gaspard, R. Herino, M. Ligeon, F. Muller, R. Romestain, A. Wasiela, A. Halimaoui, G. Bomchil, Photoluminescence of high porosity and of electrochemically oxidized porous silicon layers, *Surf. Sci.* 254 (1991) 195–200. doi:10.1016/0039-6028(91)90652-9.
 - [51] B. Gelloz, H. Sano, R. Boukherroub, D.D.M. Wayner, D.J. Lockwood, N. Koshida, Stabilization of porous silicon electroluminescence by surface passivation with controlled covalent bonds, *Appl. Phys. Lett.* 83 (2003) 2342–2344. doi:10.1063/1.1613812.
 - [52] F. Namavar, H.P. Maruska, N.M. Kalkhoran, Visible electroluminescence from porous silicon np heterojunction diodes, *Appl. Phys. Lett.* 60 (1992) 2514–2516. doi:10.1063/1.106951.
 - [53] T.L. Rittenhouse, P.W. Bohn, T.K. Hossain, I. Adesida, J. Lindesay, A. Marcus, Surface-state origin for the blueshifted emission in anodically etched porous silicon carbide, *J. Appl. Phys.* 95 (2004) 490–496. doi:10.1063/1.1634369.
 - [54] V. Petrova-Koch, O. Sreseli, G. Polisski, D. Kovalev, T. Muschik, F. Koch, Luminescence enhancement by electrochemical etching of SiC (6H), *Thin Solid Films.* 255 (1995) 107–110. doi:10.1016/0040-6090(94)05632-N.
 - [55] H. Mimura, T. Matsumoto, Y. Kanemitsu, Blue electroluminescence from porous silicon carbide, *Appl. Phys. Lett.* 65 (1994) 3350–3352. doi:10.1063/1.112388.
 - [56] L. Schirone, G. Sotgiu, F.P. Califano, Chemically etched porous silicon as an anti-reflection coating for high efficiency solar cells, *Thin Solid Films.* 297 (1997) 296–298. doi:10.1016/S0040-6090(96)09436-9.
 - [57] J. Oh, T. G. Deutsch, H.-C. Yuan, H. M. Branz, Nanoporous black silicon photocathode for H₂ production by photoelectrochemical water splitting, *Energy Environ. Sci.* 4 (2011) 1690–1694. doi:10.1039/C1EE01124C.
 - [58] O. Stenzel, Introduction, in: *Opt. Coat.*, Springer, Berlin, Heidelberg, 2014: pp. 1–17. doi:10.1007/978-3-642-54063-9_1.
 - [59] P. Menna, G. Di Francia, V. La Ferrara, Porous silicon in solar cells: A review and a description of its application as an AR coating, *Sol. Energy Mater. Sol. Cells.* 37 (1995) 13–24. doi:10.1016/0927-0248(94)00193-6.
 - [60] M. Khardani, M. Bouaïcha, B. Bessaïs, Bruggeman effective medium approach for modelling optical properties of porous silicon: comparison with experiment, *Phys. Status Solidi C.* 4 (2007) 1986–1990. doi:10.1002/pssc.200674420.
 - [61] C. Pacholski, Photonic crystal sensors based on porous silicon, *Sensors.* 13 (2013) 4694–4713. doi:10.3390/s130404694.
 - [62] S. Soloviev, T. Das, T.S. Sudarshan, Structural and electrical characterization of porous silicon carbide formed in n-6H-SiC substrates, *Electrochem. Solid-State Lett.* 6 (2003) G22–G24. doi:10.1149/1.1534733.
 - [63] M.-G. Kang, H.J. Lezec, F. Sharifi, Stable field emission from nanoporous silicon carbide, *Nanotechnology.* 24 (2013) 065201. doi:10.1088/0957-4484/24/6/065201.
 - [64] J.-H. Tan, Z. Chen, W.-Y. Lu, Y. Cheng, H. He, Y.-H. Liu, Y.-J. Sun, G.-J. Zhao, Fabrication of uniform 4H-SiC mesopores by pulsed electrochemical etching, *Nanoscale Res. Lett.* 9 (2014) 570. doi:10.1186/1556-276X-9-570.

-
- [65] Porous silicon etching – AMMT, (n.d.). <http://www.ammt.com/products/porous-silicon-etching/mpsb/> (accessed September 26, 2017).
- [66] H. Biederman, Organic films prepared by polymer sputtering, *J. Vac. Sci. Technol. Vac. Surf. Films.* 18 (2000) 1642–1648. doi:10.1116/1.582399.
- [67] A. Fridman, *Plasma chemistry*, Cambridge University Press, 2008.
- [68] L. Stöber, J.P. Konrath, V. Haberl, F. Patocka, M. Schneider, U. Schmid, Nitrogen incorporation in sputter deposited molybdenum nitride thin films, *J. Vac. Sci. Technol. Vac. Surf. Films.* 34 (2016) 021513. doi:10.1116/1.4941141.
- [69] T. Frischmuth, M. Schneider, I. Bogdanovic Radovic, Z. Siketic, D. Maurer, T. Grille, U. Schmid, Low temperature deposition of a-SiC:H thin films applying a dual plasma source process, *Thin Solid Films.* 616 (2016) 164–171. doi:10.1016/j.tsf.2016.07.030.
- [70] A. Stoffel, A. Kovács, W. Kronast, B. Müller, LPCVD against PECVD for micromechanical applications, *J. Micromechanics Microengineering.* 6 (1996) 1. doi:10.1088/0960-1317/6/1/001.
- [71] B. Hafner, *Scanning electron microscopy primer*, University of Minnesota-Twin Cities (2007), n.d. http://www.charfac.umn.edu/sem_primer.pdf.
- [72] R.H. Fowler, F.R. S, D.L. Nordheim, Electron emission in intense electric fields, *Proc R Soc Lond A.* 119 (1928) 173–181. doi:10.1098/rspa.1928.0091.
- [73] G. Bradski, A. Kaehler, *Learning OpenCV: computer vision with the OpenCV library*, O'Reilly Media, Inc., 2008.
- [74] OpenCV: OpenCV modules, (n.d.). <https://docs.opencv.org/3.4.0/index.html> (accessed February 25, 2018).
- [75] R. Niessner, D.A. Skoog, F.J. Holler, S.R. Crouch, *Instrumentelle Analytik: Grundlagen - Geräte - Anwendungen*, 6th ed., Springer Spektrum, Berlin, 2013.
- [76] D.A. McQuarrie, J.D. Simon, *Physical chemistry: a molecular approach*, 1997th ed., University Science Books, Sausalito, Calif, 1997.
- [77] J. Zakel, *Tiefenprofiluntersuchungen an ionenleitenden Gläsern mittels Flugzeit-Sekundärionen-Massenspektrometrie (ToF-SIMS)*, PhD Thesis, Philipps-Universität Marburg, 2014.
- [78] G. Holzlechner, M. Kubicek, H. Hutter, J. Fleig, A novel ToF-SIMS operation mode for improved accuracy and lateral resolution of oxygen isotope measurements on oxides, *J. Anal. At. Spectrom.* 28 (2013) 1080–1089. doi:10.1039/C3JA50059D.
- [79] P. Hariharan, Chapter 2 - two-beam interference, in: *Opt. Interferom.* Second Ed., Academic Press, San Diego, 2003: pp. 9–34. doi:10.1016/B978-012311630-7/50003-4.
- [80] M. Leitgeb, A. Backes, C. Zellner, M. Schneider, U. Schmid, Communication—the role of the metal-semiconductor junction in Pt-assisted photochemical etching of silicon carbide, *ECS J. Solid State Sci. Technol.* 5 (2016) P148–P150. doi:10.1149/2.0021603jss.
- [81] L.M. Porter, R.F. Davis, A critical review of ohmic and rectifying contacts for silicon carbide, *Mater. Sci. Eng. B.* 34 (1995) 83–105. doi:10.1016/0921-5107(95)01276-1.
- [82] U. Schmid, R. Getto, S.T. Sheppard, W. Wondrak, Temperature behavior of specific contact resistance and resistivity on nitrogen implanted 6H-SiC with titanium silicide ohmic contacts, *J. Appl. Phys.* 85 (1999) 2681–2686. doi:10.1063/1.369628.

-
- [83] S. Mendis, C.-C. Tin, I.G. Atabaev, B.G. Atabaev, The method of solid state impurity diffusion and doping in 4H-SiC, *Fundam. J.* 3 (2013) 75–78. doi:10.14331/ijfps.2013.33005 9.
- [84] C.-C. Tin, S. Mendis, M.T. Tin, T. Isaacs-Smith, J.R. Williams, A new approach in impurity doping of 4H-SiC using silicidation, *J. Appl. Phys.* 114 (2013) 244502. doi:10.1063/1.4854816.
- [85] M. Leitgeb, C. Zellner, M. Schneider, U. Schmid, A combination of metal assisted photochemical and photoelectrochemical etching for tailored porosification of 4H SiC substrates, *ECS J. Solid State Sci. Technol.* 5 (2016) P556–P564. doi:10.1149/2.0041610jss.
- [86] R. Memming, Mechanism of the electrochemical reduction of persulfates and hydrogen peroxide, *J. Electrochem. Soc.* 116 (1969) 785–790. doi:10.1149/1.2412052.
- [87] G. Gautier, J. Biscarrat, T. Defforge, A. Fèvre, D. Valente, A. Gary, S. Menard, Investigation of direct current electrical properties of electrochemically etched mesoporous silicon carbide, *J. Appl. Phys.* 116 (2014) 223705. doi:10.1063/1.4904085.
- [88] W. Lu, Y. Ou, P.M. Petersen, H. Ou, Fabrication and surface passivation of porous 6H-SiC by atomic layer deposited films, *Opt. Mater. Express.* 6 (2016) 1956–1963. doi:10.1364/OME.6.001956.
- [89] M. Leitgeb, C. Zellner, M. Schneider, S. Schwab, H. Hutter, U. Schmid, Metal assisted photochemical etching of 4H silicon carbide, *J. Phys. Appl. Phys.* 50 (2017) 435301. doi:10.1088/1361-6463/aa8942.
- [90] V.J. Pereira, H.S. Weinberg, K.G. Linden, P.C. Singer, UV degradation kinetics and modeling of pharmaceutical compounds in laboratory grade and surface water via direct and indirect photolysis at 254 nm, *Environ. Sci. Technol.* 41 (2007) 1682–1688. doi:10.1021/es061491b.
- [91] Y. Gao, N. Gao, Y. Deng, Y. Yang, Y. Ma, Ultraviolet (UV) light-activated persulfate oxidation of sulfamethazine in water, *Chem. Eng. J.* 195 (2012) 248–253. doi:10.1016/j.cej.2012.04.084.
- [92] M.P. McLaughlin, A compendium of common probability distributions, Michael P. McLaughlin, 2001. http://causascientia.org/math_stat/Dists/Compendium.pdf.
- [93] L.-C. Chang, H.-N. Wu, C.-Y. Lin, Y.-H. Lai, C.-W. Hu, K.-C. Ho, One-pot synthesis of poly (3, 4-ethylenedioxythiophene)-Pt nanoparticle composite and its application to electrochemical H₂O₂ sensor, *Nanoscale Res. Lett.* 7 (2012) 1–8. doi:10.1186/1556-276X-7-319.
- [94] S. Yae, Y. Morii, N. Fukumuro, H. Matsuda, Catalytic activity of noble metals for metal-assisted chemical etching of silicon, *Nanoscale Res. Lett.* 7 (2012) 1–5. doi:10.1186/1556-276X-7-352.
- [95] J. Yu, L. Qi, M. Jaroniec, Hydrogen production by photocatalytic water splitting over Pt/TiO₂ nanosheets with exposed (001) facets, *J. Phys. Chem. C.* 114 (2010) 13118–13125. doi:10.1021/jp104488b.
- [96] S.A. Alekseev, V.N. Zaitsev, J. Botsoa, D. Barbier, Fourier transform infrared spectroscopy and temperature-programmed desorption mass spectrometry study of surface chemistry of porous 6H-SiC, *Chem. Mater.* 19 (2007) 2189–2194. doi:10.1021/cm0629107.

-
- [97] S. Dhar, O. Seitz, M.D. Halls, S. Choi, Y.J. Chabal, L.C. Feldman, Chemical properties of oxidized silicon carbide surfaces upon etching in hydrofluoric acid, *J. Am. Chem. Soc.* 131 (2009) 16808–16813. doi:10.1021/ja9053465.
- [98] L. Patrick, W.J. Choyke, Lattice absorption bands in SiC, *Phys. Rev.* 123 (1961) 813. doi:10.1103/PhysRev.123.813.
- [99] A. Grill, D.A. Neumayer, Structure of low dielectric constant to extreme low dielectric constant SiCOH films: Fourier transform infrared spectroscopy characterization, *J. Appl. Phys.* 94 (2003) 6697–6707. doi:10.1063/1.1618358.
- [100] W. Peng-Fei, D. Shi-Jin, Z. Wei, Z. Jian-Yun, W. Ji-Tao, L.W. Wei, FTIR characterization of fluorine doped silicon dioxide thin films deposited by plasma enhanced chemical vapor deposition, *Chin. Phys. Lett.* 17 (2000) 912. doi:10.1088/0256-307X/17/12/020.
- [101] A.A. Langford, M.L. Fleet, A.J. Nelson, S.E. Asher, J.P. Goral, A. Mason, Determination of the fluorine content in a-Si: H: F by infrared spectroscopy, electron probe microanalysis, x-ray photoelectron spectroscopy, and secondary ion mass spectrometry, *J. Appl. Phys.* 65 (1989) 5154–5160. doi:10.1063/1.343168.
- [102] I. Lauermann, R. Memming, D. Meissner, Electrochemical properties of silicon carbide, *J. Electrochem. Soc.* 144 (1997) 73–80. doi:10.1149/1.1837367.
- [103] A.O. Konstantinov, A. Henry, C.I. Harris, E. Janzen, Photoluminescence studies of porous silicon carbide, *Appl. Phys. Lett.* 66 (1995) 2250–2252. doi:10.1063/1.113182.
- [104] T.A. Cao, Luong, Truc Quynh Ngan, T.C. Dao, Green synthesis of a carbon-rich layer on the surface of SiC at room temperature by anodic etching in dilute hydrofluoric acid/ethylene glycol solution, *Green Process. Synth.* 5 (2016) 491–498. doi:10.1515/gps-2016-0020.
- [105] S. Wolfram, Statistical mechanics of cellular automata, *Rev. Mod. Phys.* 55 (1983) 601–644. doi:10.1103/RevModPhys.55.601.
- [106] L.J. Reed, J. Berkson, The application of the logistic function to experimental data, *The Journal of Physical Chemistry.* (1929) 760–779. doi:10.1021/j150299a014.
- [107] M. Leitgeb, C. Zellner, C. Hufnagl, M. Schneider, S. Schwab, H. Hutter, U. Schmid, Stacked layers of different porosity in 4H SiC substrates applying a photoelectrochemical approach, *J. Electrochem. Soc.* 164 (2017) E337–E347. doi:10.1149/2.1081712jes.
- [108] A.J. Rosenbloom, D.M. Sipe, Y. Shishkin, Y. Ke, R.P. Devaty, W.J. Choyke, Nanoporous SiC: A candidate semi-permeable material for biomedical applications, *Biomed. Microdevices.* 6 (2004) 261–267. doi:10.1023/B:BMMD.0000048558.91401.1d.
- [109] L. Niemeyer, L. Pietronero, H.J. Wiesmann, Fractal dimension of dielectric breakdown, *Phys. Rev. Lett.* 52 (1984) 1033–1036. doi:10.1103/PhysRevLett.52.1033.
- [110] H.J. Wiesmann, H.R. Zeller, A fractal model of dielectric breakdown and prebreakdown in solid dielectrics, *J. Appl. Phys.* 60 (1986) 1770–1773. doi:10.1063/1.337219.
- [111] L. Papula, Gaußsches Fehlerfortpflanzungsgesetz, in: *Math. Formelsammlung Für Ingenieure Naturwissenschaftler*, Vieweg+Teubner Verlag, Wiesbaden, 2000: pp. 294–296. doi:10.1007/978-3-322-94377-4_65.

-
- [112] A. Andrews, M. Herrmann, M. Sephton, C. Machio, A. Michaelis, Electrochemical corrosion of solid and liquid phase sintered silicon carbide in acidic and alkaline environments, *J. Eur. Ceram. Soc.* 27 (2007) 2127–2135. doi:10.1016/j.jeurceram-soc.2006.07.011.
- [113] O. Pluchery, J.-M. Costantini, Infrared spectroscopy characterization of 3C–SiC epitaxial layers on silicon, *J. Phys. Appl. Phys.* 45 (2012) 495101. doi:10.1088/0022-3727/45/49/495101.
- [114] L.M. Johnson, L. Gao, C.W. Shields IV, M. Smith, K. Efimenko, K. Cushing, J. Genzer, G.P. López, Elastomeric microparticles for acoustic mediated bioseparations, *J. Nanobiotechnology*. 11 (2013) 22. doi:10.1186/1477-3155-11-22.
- [115] D.S. Kim, Y.H. Lee, Deposition of fluorinated a-SiC:H films at room temperature, *J. Electrochem. Soc.* 141 (1994) 3562–3571. doi:10.1149/1.2059370.
- [116] M. Leitgeb, C. Zellner, G. Pfusterschmied, M. Schneider, U. Schmid, Porous silicon carbide for MEMS, *Proceedings*. 1 (2017) 297. doi:10.3390/proceedings1040297.
- [117] R.A. Lake, R.A. Coutu, Variable response of a thermally tuned MEMS pressure sensor, *Sens. Actuators Phys.* 246 (2016) 156–162. doi:10.1016/j.sna.2016.05.018.
- [118] R.A. Lake, R.A. Coutu, Tunable pressure sensing applications of a MEMS buckled membrane, in: 2015 Natl. Aersp. Electron. Conf. NAECON, 2015: pp. 228–231. doi:10.1109/NAECON.2015.7443072.
- [119] P.T.B. Shaffer, Refractive index, dispersion, and birefringence of silicon carbide polytypes, *Appl. Opt.* 10 (1971) 1034–1036. doi:10.1364/AO.10.001034.
- [120] Patent US7087936 - Methods of forming light-emitting devices having an antireflective layer ... - Google Patentsuche, (n.d.). <https://www.google.com/patents/US7087936> (accessed September 19, 2017).
- [121] P. Li, Y. Wei, Z. Zhao, X. Tan, J. Bian, Y. Wang, C. Lu, A. Liu, Highly efficient industrial large-area black silicon solar cells achieved by surface nanostructured modification, *Appl. Surf. Sci.* 357 (2015) 1830–1835. doi:10.1016/j.apsusc.2015.10.035.
- [122] O. Stenzel, Heterogeneous coatings: general remarks, in: *Opt. Coat.*, Springer, Berlin, Heidelberg, 2014: pp. 245–258. doi:10.1007/978-3-642-54063-9_9.
- [123] C. Pickering, M.I.J. Beale, D.J. Robbins, P.J. Pearson, R. Greef, Optical properties of porous silicon films, *Thin Solid Films*. 125 (1985) 157–163. doi:10.1016/0040-6090(85)90408-0.
- [124] T. Jalkanen, Porous silicon optical filters in gas sensing applications, University of Turku, 2012. <https://www.doria.fi/bitstream/handle/10024/84837/AnnalesAI448Jalkanen.pdf?sequence=1> (accessed August 30, 2017).
- [125] S. Singh, J.R. Potopowicz, L.G. Van Uitert, S.H. Wemple, Nonlinear optical properties of hexagonal silicon carbide, *Appl. Phys. Lett.* 19 (1971) 53–56. doi:10.1063/1.1653819.
- [126] S. Larouche, L. Martinu, OpenFilters: open-source software for the design, optimization, and synthesis of optical filters, *Appl. Opt.* 47 (2008) C219–C230. doi:10.1364/AO.47.00C219.

8 Abbreviations

Description	Abbreviation	Abbreviation	Value
Absolute temperature	T	Kelvin	
Absorption	A		
Absorption coefficient or median	α	$\text{L} \cdot \text{mol}^{-1} \cdot \text{cm}^{-1}$ or nm^{-2}	
Amount of particles	N		
Amount of substance or refractive index	n	mol	
Area	A	cm^2	
Attenuated total reflection	ATR		
Average amount of needed holes	h_{avg}		
Band gap energy	E_{gap}	eV	
Boltzmann's constant	k_b	eV/K	$8.617 \cdot 10^{-5} \text{ eV/K}$
Built in voltage	V_{BI}	V	
Bulk or free electron concentration	n_b	cm^{-3}	
Cellular automaton	CA		
Charge	Q	C	
Chemical potential or reduced mass	μ	eV or kg	
Chemical vapour deposition	CVD		
Concentration	c	mol/L	
Concentration of a species A	[A]	cm^{-3}	
Conduction band edge	E_C	eV	
Current or intensity	I	A or W/cm^2	
Degree of porosity	P		
Degree of porosity	p		
Dielectric constant	ϵ	F/m	
Dielectric constant of free space	ϵ_0	F/m	8.854 F/m
Diffusion length	L_h	cm	
Dissolved volume fraction	V_{diss}		
Donator dopant atom concentration	N_D	cm^{-3}	
Dots per inch	dpi		
Electric potential	φ	V	
Electrical resistivity or mass density	ρ	Ohm or g/cm^3	
Electrochemical potential	$\tilde{\mu}_e$	eV	
Electrolyte particle	El		
Electron affinity	χ	eV	
Electron transfer rate constants	k_{et} k_{et}^{-1}	cm^4/s	
Electron volt	eV		
Elementary charge	q	C	$1.602 \cdot 10^{-19} \text{ C}$
Energy or electric field strength	E	eV or V/cm	
Exchange current or initial intensity	I_0	A or W/cm^2	
Externally applied voltage	V_{ext}	V	
Faraday's constant	F	As/mol	96485 As/mol

Abbreviations

Free energy	F	eV	
Frequency	ν	s^{-1}	
Frequency factor	Z	s^{-1}	
Inductively coupled plasma	ICP		
Infrared	IR		
Initial oxidation rate	Ox ₀	Particles/step	
Intrinsic electron concentration	n _i	cm ⁻³	
length	d	cm	
Length	L	cm	
Low pressure CVD	LPCVD		
Molarity, molar mass or magnification	M	mol/l or g/mol	
Mass	m	kg	
Metal assisted photochemical etching	MAPCE		
Microelectromechanical system	MEMS		
Modulu operator	mod		
Optical path difference	Δ_{path}	cm	
Oxide particle or oxidation rate	Ox	Particles/step	
Phase jump factor	Δ_{phase}	cm	
Phase shift factor	δ		
Photocurrent	I _{photo}	A	
Photoelectrochemical etching	PECE		
Planck's constant	h	Js	6,626·10 ⁻³⁴ Js
Plasma enhanced CVD	PECVD		
Porous silicon	pSi		
Porous silicon carbide	pSiC		
Potential energy	W _{pot}	eV	
Incident photon flux	ϕ	cm ⁻² s ⁻¹	
Radial frequency	ω	rad/s	
Radio frequency	RF		
Reduced Planck's constant	\hbar	Js	1.0545·10 ⁻³⁴ Js
Secondary ion mass spectrometry	SIMS		
Shape parameter	β		
Space charge layer	SCL		
Spot size	d _B	cm ²	
Spot size on sample	d _p	cm ²	
Steepness of logistic function	k	1/Steps	
Surface electron concentration	n _s	cm ⁻³	
Surface concentration of species A	[A] _s		
Surface electron concentration in equilibrium	n _{s,eq}	cm ⁻³	
Thickness of cuvette or dimensionality of system	d	cm	
Time of flight	ToF		
time	t	s	
Transmission	T		

Abbreviations

Transmission coefficient	κ	cm^4
Turning point of logistic function	t_0	Steps
Ultraviolet	UV	
Valence band edge	E_v	eV
Valence band hole	h^+	
Voltage	V	
Wavelength or reorganization energy	λ	nm or eV
Work function	W	eV

9 Appendix

9.1 SEM micrographs of PECE transition regions from section 4.5.1

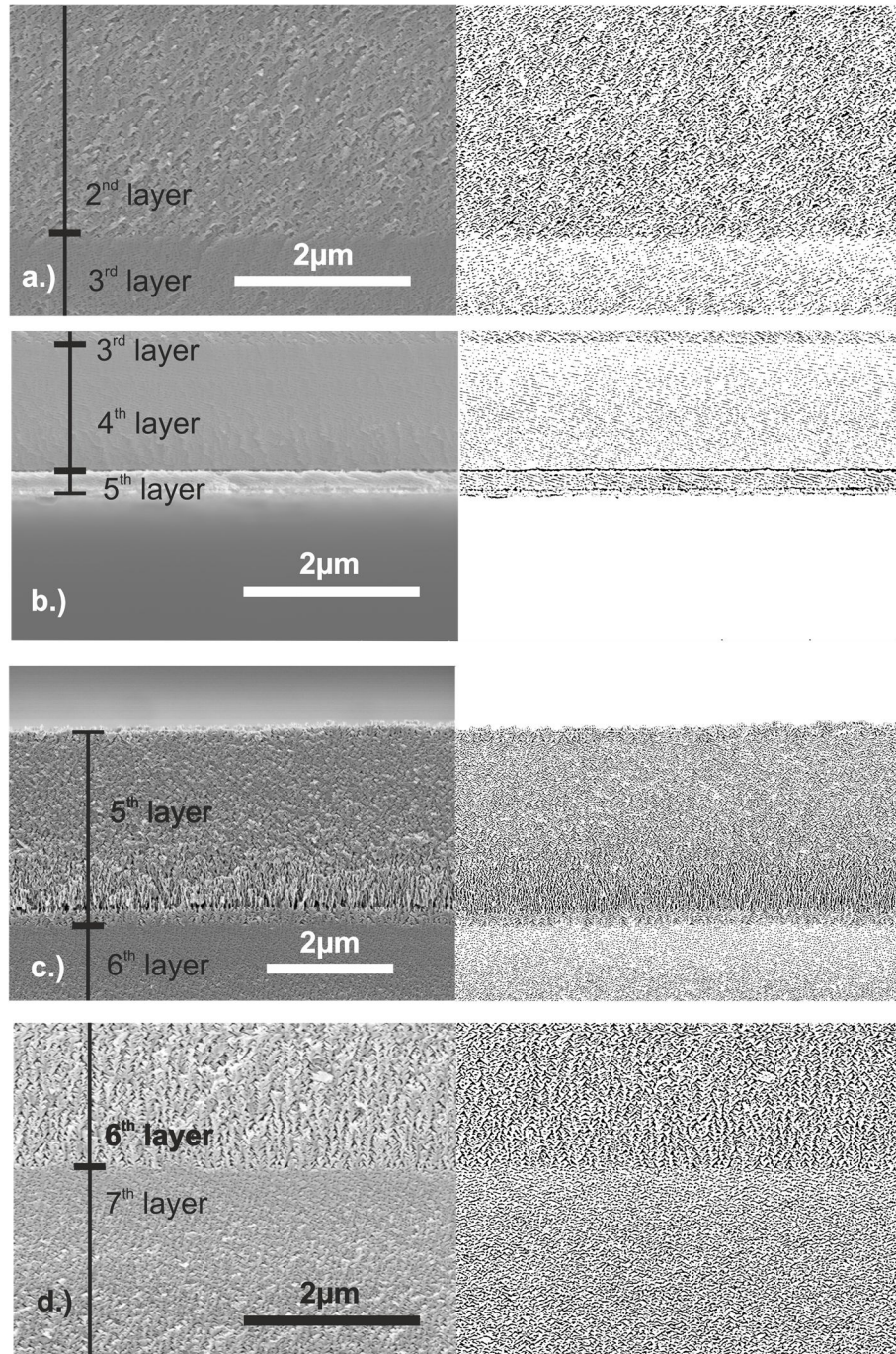


Figure 122: SEM micrographs of a 4H-SiC sample with a bulk resistivity of $0.02 \Omega\text{-cm}$ after MAPCE and PECE with corresponding black and white images obtained with image processing. a.) Transition from period 2 to 3. b.) Transition from period 3 to 4 and 4 to 5. c.) Transition from period 5 to 6. d.) Transition from period 6 to 7.

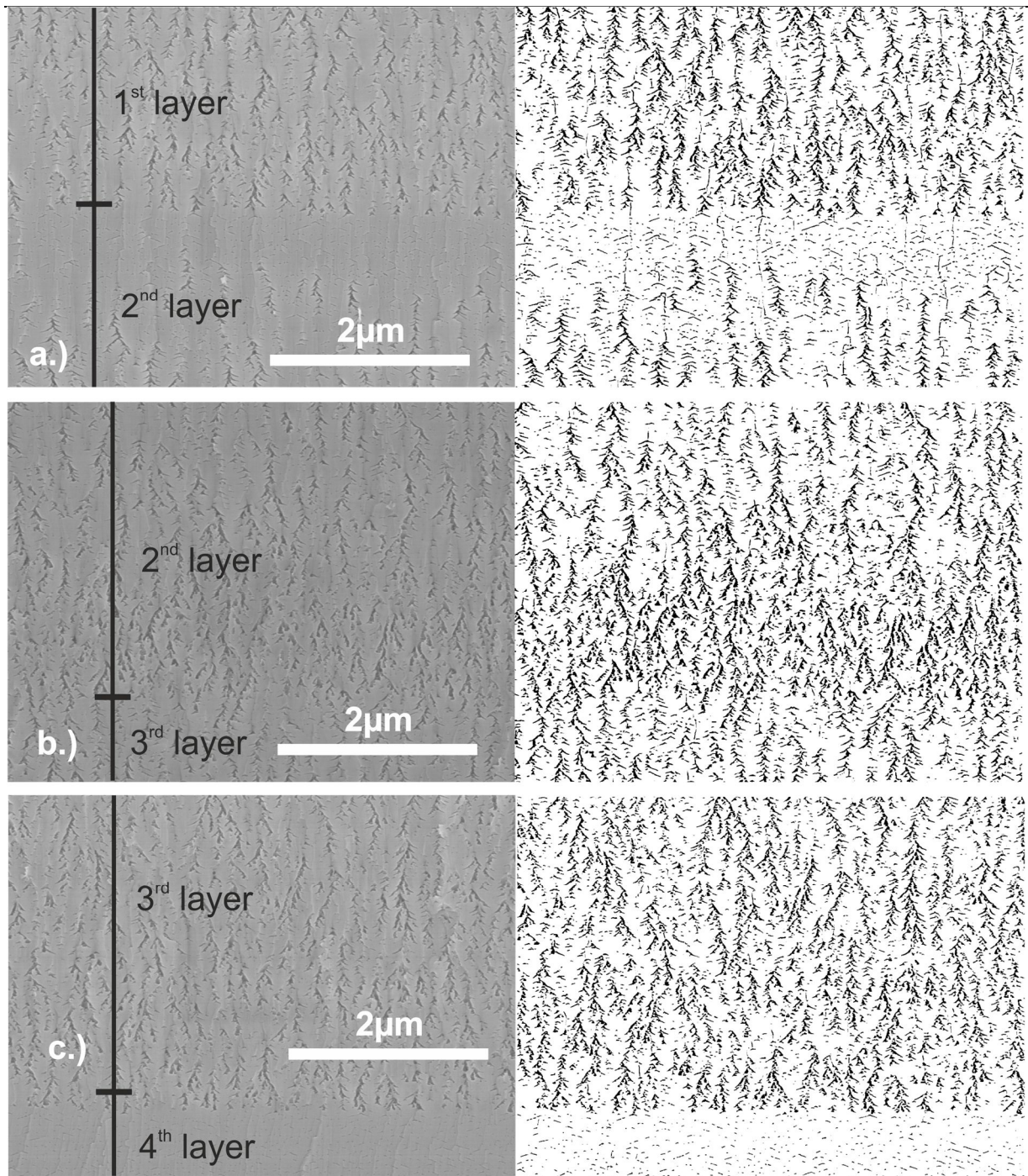


Figure 123: SEM micrographs of a 4H-SiC sample with a bulk resistivity of $0.106 \Omega\text{-cm}$ after MAPCE and PECE with corresponding black and white images obtained with image processing. a.) Transition from period 1 to 2. b.) Transition from period 2 to 3 c.) Transition from period 3 to 4.

9.2 Curriculum Vitae

Markus Leitgeb

Date of Birth: 4th of September, 1984

Place of Birth: Feldbach, Austria

Nationality: Austria

Education

03/2014 – 04/2018	Doctoral program in Engineering Science in Electrical Engineering PhD Candidate in Microsystems Technologies Technische Universität Wien, Austria
09/2011 – 03/2014	Master program Materials Science Technische Universität Wien, Austria
03/2008 – 09/2011	Bachelor program Technical Chemistry Technische Universität Wien, Austria
07/2007	Matura - Higher education entrance qualification Chemical Engineering School Graz, Austria and bfi Fürstenfeld, Austria
09/2000 – 02/2004	Apprenticeship as laboratory assistant AT&S Fehring, Austria

Work experience

01/2005 – 05/2008	Laboratory Assistant and Process Engineer AT&S Fehring, Austria
07/2011 – 09/2011	Laboratory Assistant Collini Wien
05/2013 – 01/2014	Master's Thesis – Roll to Roll Nanoimprint Lithography Joanneum Research Weiz, Austria

Publications:
Journal papers as first author:

- Leitgeb, M., Nees, D., Ruttloff, S., Palfinger, U., Götz, J., Liska, R., ... & Stadlober, B. (2016). Multilength scale patterning of functional layers by roll-to-roll ultraviolet-light-assisted nanoimprint lithography. *ACS nano*, 10(5), 4926-4941.
- Leitgeb, M., Backes, A., Zellner, C., Schneider, M., & Schmid, U. (2016). Communication—The Role of the Metal-Semiconductor Junction in Pt-Assisted Photochemical Etching of Silicon Carbide. *ECS Journal of Solid State Science and Technology*, 5(3), P148-P150.
- Leitgeb, M., Zellner, C., Schneider, M., & Schmid, U. (2016). A Combination of Metal Assisted Photochemical and Photoelectrochemical Etching for Tailored Porosification of 4H SiC Substrates. *ECS Journal of Solid State Science and Technology*, 5(10), P556-P564.
- Leitgeb, M., Zellner, C., Hufnagl, C., Schneider, M., Schwab, S., Hutter, H., & Schmid, U. (2017). Stacked Layers of Different Porosity in 4H SiC Substrates Applying a Photoelectrochemical Approach. *Journal of The Electrochemical Society*, 164(12), E337-E347.
- Leitgeb, M., Zellner, C., Schneider, M., Schwab, S., Hutter, H., & Schmid, U. (2017). Metal assisted photochemical etching of 4H silicon carbide. *Journal of Physics D: Applied Physics*, 50(43), 435301.
- Leitgeb, M., Zellner, C., Schneider, M., & Schmid, U. (2017). Porous single crystalline 4H silicon carbide rugate mirrors. *APL Materials*, 5(10), 106106.

Journal papers as co-author:

- Gerstl, M., Navickas, E., Leitgeb, M., Friedbacher, G., Kubel, F., & Fleig, J. (2012). The grain and grain boundary impedance of sol–gel prepared thin layers of yttria stabilized zirconia (YSZ). *Solid state ionics*, 225, 732-736.
- Backes, A., Bittner, A., Leitgeb, M., & Schmid, U. (2016). Influence of metallic catalyst and doping level on the metal assisted chemical etching of silicon. *Scripta Materialia*, 114, 27-30.
- Backes, A., Leitgeb, M., Bittner, A., & Schmid, U. (2016). Temperature Dependent Pore Formation in Metal Assisted Chemical Etching of Silicon. *ECS Journal of Solid State Science and Technology*, 5(12), P653-P656.

Conference talks:

- Leitgeb, M., Zellner, C., Pfusterschmied, G., Schneider, M., & Schmid, U. (2017, August). Porous Silicon Carbide for MEMS. In *Multidisciplinary Digital Publishing Institute Proceedings* (Vol. 1, No. 4, p. 297).